Direct Femtosecond Laser Inscription in Transparent Dielectrics

MYKHAYLO DUBOV

Doctor of Philosophy

ASTON UNIVERSITY

03 July 2011

To my parents and family for all their help and support

Abstract

Since 1996 direct femtosecond inscription in transparent dielectrics has become the subject of intensive research. This enabling technology significantly expands the technological boundaries for direct fabrication of 3D structures in a wide variety of materials. It allows modification of non-photosensitive materials, which opens the door to numerous practical applications.

In this work we explored the direct femtosecond inscription of waveguides and demonstrated at least one order of magnitude enhancement in the most critical parameter - the induced contrast of the refractive index in a standard borosilicate optical glass. A record high induced refractive contrast of 2.5×10^{-2} is demonstrated. The waveguides fabricated possess one of the lowest losses, approaching level of Fresnel reflection losses at the glass-air interface. High refractive index contrast allows the fabrication of curvilinear waveguides with low bend losses. We also demonstrated the optimisation of the inscription regimes in BK7 glass over a broad range of experimental parameters and observed a counter-intuitive increase of the induced refractive index contrast with increasing translation speed of a sample. Examples of inscription in a number of transparent dielectrics hosts using high repetition rate fs laser system (both glasses and crystals) are also presented.

Sub-wavelength scale periodic inscription inside any material often demands supercritical propagation regimes, when pulse peak power is more than the critical power for self-focusing, sometimes several times higher than the critical power. For a sub-critical regime, when the pulse peak power is less than the critical power for self-focusing, we derive analytic expressions for Gaussian beam focusing in the presence of Kerr non-linearity as well as for a number of other beam shapes commonly used in experiments, including astigmatic and ring-shaped ones.

In the part devoted to the fabrication of periodic structures, we report on recent development of our point-by-point method, demonstrating the shortest periodic perturbation created in the bulk of a pure fused silica sample, by using third harmonics ($\lambda = 267$ nm) of fundamental laser frequency ($\lambda = 800$ nm) and 1 kHz femtosecond laser system. To overcome the fundamental limitations of the point-by-point method we suggested and experimentally demonstrated the micro-holographic inscription method, which is based on using the combination of a diffractive optical element and standard micro-objectives. Sub-500 nm periodic structures with a much higher aspect ratio were demonstrated.

From the applications point of view, we demonstrate examples of photonics devices by direct femtosecond fabrication method, including various vectorial bend-sensors fabricated in standard optical fibres, as well as a highly birefringent long-period gratings by direct modulation method.

To address the intrinsic limitations of femtosecond inscription at very shallow depths we suggested the hybrid mask-less lithography method. The method is based on precision ablation of a thin metal layer deposited on the surface of the sample to create a mask. After that an ion-exchange process in the melt of Ag-containing salts allows quick and low-cost fabrication of shallow waveguides and other components of integrated optics. This approach covers the gap in direct fs inscription of shallow waveguide.

Perspectives and future developments of direct femtosecond micro-fabrication are also discussed.

Acknowledgments

I am grateful to my supervisor Prof. Ian Bennion, who gave me the opportunity to work on this topic, and for his constant attention and support during my work at Aston University as a Research Fellow. I was delighted to work at Aston.

I would like to express my gratitude to my co-supervisor and colleague Dr. Vladimir Mezentsev, for sharing his knowledge and expertise in plasma physics, nonlinear optics, and especially in numerical simulation. I would like also to thank Dr. Holger Smitz and Dr. Jovana Petrovich for their highly professional help in numerical solution of the NLSE model. The results obtained by them were used in my thesis in Figures 3.2, 3.2, and 6.6, as well as in a number of our joint publications. I am grateful to Dr. V. Mezentsev, Dr. E. Podivilov, Prof. M. Fedoruk, Prof. A. Rubenchik and Prof. S. Turitsyn for pointing out the direction in which to go and help with an analytic treatment of a "simplified" NLSE model. This allowed me to consider all particular cases, which are explored in Chapter 3 on a similar basis, and to retrieve the analytical results, which were used later in Chapter 6.

I am grateful to Dr Alexander Turchin, for the idea of single-shot, on-line measurements of complex permittivity and his invaluable help with experiments. These results presented in Section 4.8.

Special thanks to Dr. Tomas Allsop for his invaluable help with the characterisation of the fs waveguides in BK7 glass (Chapter 5) and for the complete characterisation of all of the LPG-based vectorial bend sensors (Chapter 7).

I would like to express my gratitude to Dr. Amós Martinez for his help with all fibre alignments during the fabrication of almost all fibre devices, described in Chapter 7. Indeed we spent about 300 days per year in the very first fs laboratory which we have built together, exploring the new (for us) and very exciting field of direct femtosecond micro-fabrication in various optical fibres. I also acknowledge the help with programming for stabilisation of laser power provided by Dr Yicheng Lai, as well as his help during the characterisation of the FBG-based directional bend sensor (Chapter 7, Figure 7.5).

I am very grateful to Dr. S.R. Natarajan for our fruitful collaboration on the hybrid mask-less lithography method, and also for his help with polishing of the optical samples.

I would like to express my gratitude to Dr. Andrey Okhrimchuk for our long-lasting collaboration on direct femtosecond inscription in crystals, as well as experimental help with the measurements of the absorption, described in Section 3.4.

I am also grateful to all the colleagues and co-authors of all our joint papers and works - published and yet unpublished as they have taught me a great deal about many different things, and assisted during my work at Aston University. The friendly environment welcomed me in 2001 continues to encourage to the present day. This environment is created by the members and former members of the Photonics Research Group, a group which does not exist on paper, but which has become famous for a number of its world-record breaking results in photonics.

I acknowledge the support from secretarial and technical staff of both our Group and School of Engineering and Applied Science, and especially Mrs. Helen Yard and Mr. Herbert Biggs. They helped me so much on so many occasions, so I always will be grateful for their consolidating role in the Photonics Research Group.

Contents

List of Figures

6

List of Tables

0.1 Abbreviations and units

2D	Two-Dimensional
3D	Three-Dimensional
AO(m)	Acousto-Optics (modulator)
BB	Broad-Band
CPA	Chirped Pulse Amplifier
CPO	Chirped Pulse Oscillator
CL	Coupling Losses
CW	Continuous Wave (or continuous)
DIC	Differential Interference Contrast
EM	Electro-Magnetic (field)
FROG	Frequency Resolved Optical Gating
fs	femtosecond, 10^{-15} sec
FBG	Fibre Bragg Grating
GVD	Group Velocity Dispersion
HRR	High Repetition Rate
LBF	Life-Before Failure
LPG	Long-Period Grating
LRR	Low Repetition Rate
MFD	Mode-Field Diameter
MPA	Multi-Photon Absorption
MPI	Multi-Photon Ionisation
NIR	Near Infra-Red
NLSE	Non-Linear Schrödinger Equation
OPD	Optical Path Difference
OAPM	Off-Axis Parabolic Mirror
PDL	Polarisation Dependent Losses
PL	Propagation Losses
PM	Phase Mask
PLC	Planar Light-wave Circuits
PbP	Point-by-Point
QPm	Quantitative Phase microscopy
RNF	Refractive Near-Field (profilometry)
SMF	Single-Mode Fibre
TEE	Transport-of-Energy Equation
WBG	Waveguide Bragg Grating

0.2 Journal and conference papers directly related to this work

Fundamental aspects of femtosecond inscription were considered in the following papers:

[1] V. K. Mezentsev, S. K. Turitsyn, M. P. Fedoruk, M. Dubov, A. M. Rubenchik, and E. V. Podivilov, Modelling of femtosecond inscription in fused silica, in *Intern. Conf. on Transparent Optical Networks (ICTON)*, **4**, pp. 146 - 149, 2006.

[2] S. Turitsyn, V. Mezentsev, M. Dubov, A. Rubenchik, M. Fedoruk, and E. Podivilov, Nonlinear diffraction in sub-critical femtosecond inscription, in *CLEO/IQEC-Europe 2007 Conf. Digest*, **1**, p.CM2.2, 2007.

[3] S. K. Turitsyn, V. K. Mezentsev, M. Dubov, A. M. Rubenchik, M. P. Fedoruk, and E. V. Podivilov, Sub-critical regime of femtosecond inscription, *Optics Express* **15**, pp. 14750 - 14764, 2007.

[4] V. Mezentsev, M. Dubov, A. Martinez, Y. Lai, T. P. Allsop, I. Khrushchev, D. J. Webb, F. Floreani, and I. Bennion, Micro-fabrication of advanced photonic devices by means of direct point-by-point femtosecond inscription in silica, in *Proc. of SPIE*, **6107**, p. C1070, 2006.

[5] V. Mezentsev, M. Dubov, J. S. Petrovic, I. Bennion, J. Dreher, and R. Grauer, Role of plasma in femtosecond laser pulse propagation, in *Physics of Ionized Gases*," **876**, pp. 169 - 180, 2006.

[6] V. Mezentsev, J. S. Petrovic, M. Dubov, I. Bennion, J. Dreher, H. Schmitz, and R. Grauer, Femtosecond laser microfabrication of subwavelength structures in photonics, in *Proc.SPIE* **6459**, paper B4590, 2007.

[7] I. S. Petrovic, V. Mezentsev, M. Dubov, A. Martinez, and I. Bennion, Plasma assisted femtosecond laser inscription in dielectrics, in *Physics of Ionized Gases* **876**, pp. 216 - 223, 2006.

Measurement Techniques and Methods were published in:

[8] M. Dubov, V. Mezentsev, and I. Bennion, Method for characterisation of weakly guiding waveguides by measuring mode field diameter, in *Conf. on Lasers and Electro-Optics Europe - Technical Digest*, p. 565, 2005.

[9] A. Martinez, M. Dubov, I. Khrushchev, and I. Bennion, Photoinduced modificationsin fiber gratings inscribed directly by infrared femtosecond irradiation, *IEEE Photonics Technology Letters* **18**(21-24), pp. 2266 - 2268, 2006.

[10] A. V. Turchin, M. Dubov, and J. A. R. Williams, In situ measurement and reconstruction

in three dimensions of femtosecond inscription-induced complex permittivity modification in glass, *Optics Letters* **35**(17), pp. 2952 - 2954, 2010.

[11]   A. V. Turchin, M. Dubov, and J. A. Williams, 3-D reconstruction of complex dielectric function of the glass during the femtosecond micro-fabrication, in *Bragg Gratings, Photosensitivity, and Poling in Glass Waveguides*, paper BWD7, 2010.

Following papers deal with waveguide fabrication:

[12]   M. Dubov, I. Khrushchev, I. Bennion, A. Okhrimchuk, and A. Shectakov, Waveguide inscription in YAG:Cr4+ crystals by femtosecond laser irradiation, in *CLEO and IQEC 2004 Conf. Digest*, p. CWA49, 2004.

[13]   M. Dubov, T. D. P. Allsop, S. R. Natarajan, V. K. Mezentsev, and I. Bennion, Low-loss waveguides in borosilicate glass fabricated by high-repetition-rate femtosecond chirp-pulsed oscillator, in *CLEO-Europe and IQEC-2009 Conf. Digest*, paper CEP.4, 2009.

[14]   M. Dubov, T. Allsop, S. R. Natarajan, V. K. Mezentsev, and I. Bennion, Curvilinear low-loss waveguides in borosilicate glass fabricated by femtosecond chirp-pulse oscillator, in *OSA Trends in Optics: Femtosecond Laser Microfabrication*, paper LMTuC6, 2009.

[15]   I. Khruschev, A. Okhrimchuck, A. Shestakov, M. Dubov, and I. Bennion, Laser inscription of optical structures in crystals (*Patent WO 2005040874-A2*), 2005.

[16]   I. Khruschev, A. Okhrimchuck, A. Shestakov, M. Dubov, I. Bennion, and A. Martinez, Laser inscribed structures (*Patent WO 2005111677-A2*), 2005.

[17]   I. Khrushchev, A. Okhrimchuck, A. Shestakov, M. Dubov, and I. Bennion, Laser inscription of optical structures in crystals, (*Patent EP 1678535*), 2006.

[18]   T. Allsop, M. Dubov, V. Mezentsev, and I. Bennion, Inscription and characterization of waveguides written into boro-silicate glass by a high-repetition-rate femtosecond laser at 800 nm, *Applied Optics* **49**(10), pp. 1938 - 1950, 2010.

[19]   I. Bennion, V. Mezentsev, M. Dubov, A. Okhrimchuk, T. Allsop, and H. Schmitz, Single process femtosecond microfabrication of key components for integrated optics, in *Bragg Gratings, Photosensitivity, and Poling in Glass Waveguides*, (Invited talk) BWB3, 2010.

[20]   Y.-L. Wong, D. Furniss, V. K. Tikhorairov, E. A. Romanova, M. Dubov, T. D. P. Allsop, V. Mezentsev, I. Bennion, T. M. Benson, and A. B. Seddon, Femtosecond laser writing of buried waveguides in erbium iii-doped oxyfluoride glasses and nanoglass-ceramics, in *Proc. of 10th Anniv. Int.*

Conf. on Transparent Optical Networks (ICTON), **3**, pp. 234 - 238, 2008.

[21] A. G. Okhrimchuk, V. K. Mezentsev, H. Schmitz, M. Dubov, and I. Bennion, Cascaded nonlinear absorption of femtosecond laser pulses in dielectrics, *Laser Phys.* **19**(7), pp. 1415 - 1422, 2009.

[22] A. Okhrimchuk, V. Mezentsev, M. Dubov, H. Schmitz, and I. Bennion, Cascaded nonlinear absorption of laser pulse energy in femtosecond microfabrication: Experiment, numerics, and theory, in *OSA Trends in Optics: Femtosecond Laser Microfabrication*, p. LMTuA6, 2009.

[23] A. Okhrimchuk, V. Mezentsev, H. Schmitz, M. Dubov, and I. Bennion, Characterization of nonlinear absorption in femtosecond laser inscription, *CLEO-Europe and IQEC 2009 Conf. Digest*, p. EFP15, 2009.

[24] M. Ams, G. D. Marshall, P. Dekker, M. Dubov, V. K. Mezentsev, I. Bennion, and M. J. Withford, Investigation of ultrafast laser-photonic material interactions: Challenges for directly written glass photonics, *IEEE Journal on Selected Topics in Quantum Electronics* **14**(5), pp. 1370 - 1388, 2008.

[25] R. Graf, A. Fernandez, M. Dubov, H. Brueckner, B. Chichkov, and A. Apolonski, Pearl-chain waveguides written at megahertz repetition rate, *Applied Physics B: Lasers and Optics* **87**(1), pp. 21 - 27, 2007.

Point-by-point method and its developments were presented in:

[26] I. Khrushchev, M. Dubov, A. Martinez, Y. Lai, and I. Bennion, Point-by-point femtosecond laser inscribed structures in optical fibres and sensors using the same, (*Patent EP 1759229*), 2007.

[27] A. Martinez, M. Dubov, I. Khrushchev, and I. Bennion, Point by point FBG inscription by a focused NIR femtosecond laser, in *Conf. on Lasers and Electro-Optics(CLEO) Conf. Digest*, **1**, pages 2, 2004.

[28] A. Martinez, M. Dubov, I. Khrushchev, and I. Bennion, Direct writing of fibre Bragg gratings by femtosecond laser, *Electronics Letters* **40**(19), pp. 1170 1172, 2004.

[29] A. Martinez, M. Dubov, I. Khrushchev, and I. Bennion, Point by point FBG inscription by a focused NIR femtosecond laser, in *OSA Series: Trends in Optics and Photonics*, **96** A, pp. 393 394, 2004.

[30] A. Martinez, M. Dubov, I. Y. Khrushchev, and I. Bennion, Direct femtosecond inscription of fiber Bragg gratings, in *Proc. of the Materials Research Society Symposium*, **850**, pp. 137 142, 2005.

[31] A. Martinez, M. Dubov, I. Khrushchev, and I. Bennion, Structure of fiber gratings directly

written by infrared femtosecond laser, in *CLEO and IQEC 2006 Conf. Digest*, paper JTuD13, 2006.

[32] M. Dubov, V. Mezentsev, I. Bennion, and D. N. Nikogosyan, UV femtosecond laser inscribes a 300 nm period nanostructure in a pure fused silica, *Meas. Science & Technol.* **18**(7), pp. L15 - L17, 2007.

[33] M. Dubov, V. Mezentsev, I. Bennion, and D. Nikogosyan, Inscription of a 300-nm period nanostructure in a pure fused silica, in *Conf. on Lasers and Electro- Optics Europe - Technical Digest (Post-deadline papers)*, **1**, p. 1, IEEE, 2007.

[34] M. Dubov, V. Mezentsev, I. Bennion, and D. N. Nikogosyan, Demonstration of possibility of 300-nm-period Bragg grating inscription in a pure fused silica, in *Bragg Gratings, Photosensitivity, and Poling in Glass Waveguides*, p. BTuD5, 2007.

[35] M. Dubov, V. Mezentsev, I. Bennion, and D. Nikogosyan, Inscription of a 300- nm-period nanostructure in a pure fused silica, in *CLEO-Europe and IQEC-2007 Conf. Digest*, CP2.4, 2007.

[36] M. Dubov, I. Bennion, D. Nikogosyan, P. Bolger, and A. Zayats, Point-by-point inscription of 250 nm period structure in bulk fused silica by tightly focused femtosecond UV pulses, *J. of Optics A: Pure Applied Optics* **10**(6), p. 025305, 2008.

[37] M. Dubov, R. K. Nasyrov, D. N. Nikogosyan, A. G. Poleshchuk, V. Mezentsev, and I. Bennion, Micro-holographic methods for sub-micrometer grating fabrication in fused silica with UV femtosecond laser, in *Proc. SPIE* **7100**, p. T1000, 2008.

[38] D. N. Nikogosyan, M. Dubov, H. Schmitz, V. Mezentsev, I. Bennion, P. Bolger, and A. V. Zayats, Point-by-point inscription of 250-nm-period structure in bulk fused silica by tightly-focused femtosecond uv pulses: experiment and numerical modeling, *Cent. European Journal of Phys.* **8**(2), pp. 169 - 177, 2010.

Application examples, devices, and various sensors were described in following papers:

[39] M. Dubov, T. D. Allsop, A. Martinez, V. Mezentsev, and I. Bennion, Highly birefringent long period gratings fabricated with femtosecond laser, in *Optical Fiber Communication Conf. (OFC)*, vol. 1-6, pp. 663665 (paper OWI50), 2006.

[40] T. Allsop, M. Dubov, A. Martinez, F. Floreani, I. Khrushchev, D. Webb, and I. Bennion, Directional bend sensor based on an asymmetric modification of the fiber cladding by femtosecond laser, in *CLEO and IQEC-2005 Conf. Digest*, **3**, pp. 2179 2181, 2005.

[41] T. Allsop, M. Dubov, A. Martinez, F. Floreani, I. Khrushchev, D. J. Webb, and I. Bennion,

Long period grating directional bend sensor based on asymmetric index modification of cladding, *Electronics Letters* **41**(2), pp. 59 60, 2005.

[42] T. Allsop, M. Dubov, A. Martinez, F. Floreani, I. Khrushchev, D. J. Webb, and I. Bennion, A long period grating directional bend sensor incorporating index modification of the cladding, in *17th Intern. Conf. on Optical Fibre Sensors (OFS)*, **5855**, pp. 98 101, 2005.

[43] T. D. Allsop, M. Dubov, A. Martinez, F. Floreani, I. Khrushchev, D. J. Webb, and I. Bennion, Directional bend sensor based on an asymmetric modification of the fiber cladding by femtosecond laser, in *CLEO & QELS Conf. Techn. Digest*, paper CFG6, 2005.

[44] T. Allsop, M. Dubov, A. Martinez, F. Floreani, I. Khrushchev, D. Webb, and I. Bennion, Bending characteristics of fiber long-period gratings with cladding index modified by femtosecond laser, *J. Lightwave Technol.* **24**(8), pp. 3147 3154, 2006.

[45] T. Allsop, M. Dubov, H. Dobb, A. Main, A. Martinez, K. Kalli, D. Webb, and I. Bennion, A comparison of the spectral properties of high temperature annealed long period gratings inscribed by fs laser, uv and fusion-arc, in *Proc. SPIE*, **6193**, paper 61930M, SPIE, 2006.

[46] T. Allsop, K. Kalli, K. Zhou, Y. Lai, G. Smith, M. Dubov, D. J.Webb, and I. Bennion, Long period gratings written into a photonic crystal fibre by a femtosecond laser as directional bend sensors, *Optical Communications* **281**(20), pp. 5092 5096, 2008.

[47] A. Martinez, Y. Lai, M. Dubov, I. Y. Khrushchev, and I. Bennion, Vector bending sensors based on fiber Bragg gratings inscribed by an infrared femtosecond laser, in *CLEO & QELS Conf. Techn. Digest*, paper CFH1, 2005.

[48] A. Martinez, Y. Lai, M. Dubov, I. Khrushchev, and I. Bennion, Vector bending sensors based on fibre Bragg gratings inscribed by infrared femtosecond laser, *Elect. Lett.* **41**(8), pp. 472 474, 2005.

[49] A. Martinez, Y. Lai, M. Dubov, I. Khrushchev, and I. Bennion, Vector bending sensors based on fiber bragg gratings inscribed by an infrared femtosecond laser, in *CLEO & QELS Conf. Techn. Digest*, **3**, pp. 2185 2187, 2005.

Other examples, including hybrid and mask-less lithography:

 [50] Y. Lai, K. Zhou, M. Dubov, L. Zhang, and I. Bennion, Fabrication of micro-channels in optical fibers using femtosecond laser pulses and selective chemical etching, in *Optical Fiber Communication Conf. (OFC)*, **1-6** pp. 286 288 (paper OTuL4), 2006.

[51] M. Dubov, S. R. Natarajan, J. A. R.Williams, and I. Bennion, Mask-less lithography for fabrication of optical waveguides, in *Proc. SPIE* **6881**, paper 88110, 2008.

[52] M. Dubov, S. Natarajan, J. Williams, and I. Bennion, Optical structures (Application for Patent WO 2009007712), 2009.

Note that the re-distribution of the papers is, to certain extent, a matter of author's preferences.

Chapter 1

Introduction

1.1 Historic perspective

The modern era of information and communications demands increasing volumes of information to be transmitted per unit time. Despite the obvious requirements of energy supply to perform such communications, traffic is still growing exponentially. One example is the telephone calls: there were about a million overseas calls per year over the transocean copper cables in the mid-50s; in the mid-80s, it was already 200 million calls, and nowadays (based on a 2005 report by Federal Telecommunication Commission, USA) every person in the modern world, on average, makes more than a thousand calls per year. So, the Earth's population may already be approaching a trillion (10^{12}) telephone calls per year. Most of them are made using various network services, thus via optical fibres.

Since the Internet Revolution began in the 70-s, the demand for traffic has grown and keeps on growing significantly. A realistic margin for the amount of data transferred in the WWW-world is $10^{20\sim22}$ bits per year. It is expected that this will rise significantly when movies-on-demand, HD- and other holographic or 3D-television services become widely available. If just a pico-Joule (1 pJ = 10^{-12} J) is required to transfer a bit of information per 100 km, such traffic would demand several dozen modern power plants just to support this, all being used continuously. The view from the top on the infrastructure pyramid to support further progress during the Information Era may reveal the necessity for the optimal global designing of the fibre networks in order to minimize energy consumption by whole system.

This scale of "routine" optimisation and data-banks redistribution itself may require cloud- and super-computers and thus will contribute to fibre-optic traffic.

Video conferences and private video-calls, remote work and remote industrial process control, enormous (already existing, as well as future) data-banks, remote continuous medical diagnostics of every human being, web-commerce and other services will definitely stimulate if not drive the development of information technologies as well as ultrafast all-optical transmission and signal processing. Optical technologies are also expected to shake up the field of super-computers, traditionally controlled by electronics [53], as well as a number of sensing and many other applications.

In this thesis we focus on the lowest level of the Information Pyramid - the technology and components which lie at its foundation. It seems that Photonics is the only technology which can cope with growing traffic and energy demands at the same time. It would not be difficult to anticipate a supreme role for various elements and devices of integrated optics, especially ultrafast and telecommunication systems, as well as various sensor and control systems.

Each integrated optoelectronic circuit comprises a few basic elements:

- waveguides (WG) of various types (passive, active, nonlinear, coupled or arrayed, tapered, straight and curvilinear, etc.);

- wavelength and polarization sensitive elements (gratings, resonators, polarisation controllers and splitters);

- various devices to generate or change the properties of light (e.g. light emitting diodes, semiconductor DFB lasers, amplifiers, as well as other devices) to modulate, delay, split, combine, attenuate and/or manipulate the spectral content of a signal;

- and finally - the optical receivers, to convert the energy carried by photons into an electric current.

Optimisation of any component could bring enormous economic benefits as well as making significant improvements in the quality of people's lives. Thus, the main motivation for this work was to explore new and alternative technologies for the fabrication of photonic devices.

There are many well developed methods of fabricating planar lightwave circuits, as can be seen in the literature [54–59]. In most of the methods the waveguides are fabricated by some processes at the surface of the substrate, for example various deposition techniques (e.g. beam sputtering, plasma, thermal evaporation, pulsed laser, epitaxy (MBE), chemical-vapour deposition (MOCVD), sol-gel, etc.) when certain material is deposited (or grown) on the top surface of some substrate and later patterned; ion implantation or exchange, for example, bombardment, thermal in- and out-diffusion; change in the oxidation state; surface modification (by illumination, bombardment, and then etching); and also mechanical methods, for example, dicing, milling, moulding and various bonding techniques - for example, thermal or diffusion bonding etc.

In the absolute majority of technologies various types of lithography are being used. Lithography seems to be an *irreplaceable* method to pattern various photonic and electronic circuits. Any lithography involves the use of some photosensitive layer and its irradiation by UV light or an electron beam, especially when high spatial resolution is required. It is basically a multi-stage process, which typically includes: surface preparation (cleaning and drying), resist deposition (and its drying or pre-conditioning), UV or e-beam exposure, post-processing of the exposed resist layer (developing/removing exposed or unexposed areas and then drying again), then some physical or chemical etching through the pattern obtained, so in fact it can be effectively implemented only on a flat surface. Lithography can be challenged by other methods - various direct writing methods, e.g. focused beams. Most direct methods are sequential in contrast to lithographic ones, as they require beam scanning. Thus, the speed of material removal/deposition is the most important limiting factor for the direct methods. It is directly related to the process of energy deposition and its precision. In all cases good spatial and temporal control of the energy source is required, as well as high precision in sample translation or beam positioning.

There have been many attempts to develop methods to fabricate non-planar structures (which are not on a flat substrate surface). Examples include many types of advanced multistage lithography followed by material deposition stage(s); various chemical methods to change the properties of the top layer(s); and also induced photo-refraction and/or electro-optic refraction; also photo-chemical reactions triggered by multi-photon absorption - e.g. polymerization of transparent gels; thermo- or photo-modification of the refractive index of

the glass, initiated by photons in the bulk of some special glasses doped by metal ions; various bonding techniques to arrange stack of different layers often combined with traditional polishing, dicing etc.; ion-exchange methods - for example, electric field assisted ion diffusion could be used to make a buried non-planar light guiding circuits. However the best multi-layered structures are being fabricated by sequence of above mentioned *lithography* techniques.

Femtosecond laser inscription is arguably the only and thus the enabling technology to manufacture sophisticated 3D photonic devices during a single stage process. Its uniqueness and exceptional geometrical flexibility are based on local material modification triggered by multi-photon absorption in the bulk of transparent dielectrics. It can handle a wide range of materials, such as polymers, various doped and un-doped optical glasses and ceramics, pure and doped crystals, semiconductors, and even some liquids, such as polymerizing gels. In many of these media the method of direct femtosecond modification has been already demonstrated [60, 61] soon after the invention of ultrashort pulse lasers and the concept of Chirped Pulse Amplifiers (CPA) [62, 63] and the publication of pioneering papers on waveguide inscription in optical glass [64–66].

The direct fs method also allows a broad range of hybrid techniques , whose exploration is both promising and exciting. In every hybrid technique a combination of an fs laser irradiation with some other physical or chemical processes demonstrates significant advantages. Examples include:

- selective chemical etching of fs-irradiated glasses, which revealed significant anisotropy of the etching speed;

- laser plasma assisted surface etching of the hardest surfaces at atmospheric pressure in normal laboratory conditions;

- fs laser triggered gas deposition, which can be effectively used for metal deposition on any surface without a vacuum;

- precipitation of metal nano-clusters in the bulk of special optical glasses;

- stimulation of crystal growth by femtosecond laser irradiation;

22

- precision metal and/or dielectric film ablation without damage to any surrounding material, with consequent deposition or chemical reactions on unprotected areas;

- chemical reactions and physical transformations triggered by fs laser, for example, metal oxidation, phase transitions under direct fs illumination, or change of charge-state of RE-ions in crystal host, thermal diffusion of atoms or ions to/from focal spot region, and others.

In a majority of the above mentioned methods the process is due to multi-photon absorption (MPA), which is the key process in allowing good spatial control - down to a sub-micrometer in space, and precise energy deposition - down to a sub-nJ. We demonstrate below that this speed, as well as the density of deposited energy, can be superior to almost all methods previously used. It is this precision which allows the deposition of laser energy without damage, and enables almost all these applications.

Ultrashort laser irradiation quickly became a mainstream technology. It has facilitated a number of emerging technologies over the past 10 years or, in general, the **technology of direct femtosecond micro-fabrication** [60, 61, 67].

A wide range of photonic structures and devices has been recently demonstrated, including straight waveguides [64, 65, 68–73], curvilinear waveguides [74–79], which are often combined with couplers and/or interferometers, and many other components.

In optical fibres, applications of fs inscription originally included Long-Period Gratings (LPG) [80–84], and then Fibre Bragg Gratings as well as Waveguide Bragg Gratings (FBG and WBG respectively). These were fabricated initially by UV CW lasers [85], then higher harmonics of NIR fs laser [86], and finally at the fundamental wavelength of a Ti:Sapphire laser and optimised phase masks [87, 88]. Very recently, FBGs were fabricated by the Point-by-Point (PbP) method [27, 28, 89]. This method offers the most flexibility and one of the shortest fabrication times. Such fs inscribed FBGs possess unprecedented parameters, e.g. their thermal durability [90–92] when the grating can survive up to the melting temperature of glass; unprecedented spectral chirp [93] - when a 4 cm FBG covers all of the telecommunication bands as it has a few hundred nanometers spectral width; or grating selective reflection of more than 99.99% [94].

The polarisation properties of the gratings can be controlled by the inscription geometry, which we will illustrate in more detail below (in Section 7.2). The inscription through a

standard polymer/acrilic coating of the fibre is also possible [94], and it is unique to NIR fs inscription, as most plastics and polymers are UV-absorptive. Very recently fibre and waveguide lasers fabricated by direct fs inscription were demonstrated, with fs FBG and WBG being the key component for this - see for example, [95–99] - again, with sometimes unique properties, such as very narrow linewidth (less than 0.1 nm) at the output power of 100W in when laser operates in a CW mode. This was demonstrated in Yb-doped, CW fibre laser [100, 101] incorporating point-by-point femtosecond FBG. Other applications of direct femtosecond micro-fabrication include photonic band-gap structures, various sensors, and promising opto-fluidic devices [102]. Both the waveguides and the micro-channels can be fabricated on the same setup at the same time, eliminating the need for tedious device assembly and alignment stages. A number of applications of the method of direct femtosecond inscription are expected to be targeted on further development of femtosecond lasers. Altogether these factors indicate the great potential of this technology.

1.2   Principles

Alongside the versatility of direct femtosecond micro-fabrication comes complexity, due to the the inherently nonlinear processes involved in the fabrication stage, for example: high-peak-power fs-laser pulse propagation, multi-photon mechanisms of energy absorption and dissipation, and then, multiple stages for eventual material modification and possibly, phase transitions. The material modification stage itself includes a wide spectrum of physical phenomena, starting from laser interaction with plasma, heating such non-equilibrium plasma up to the stage when avalanche ionisation takes place, and later, sophisticated thermo-elastic material transformations, often beyond thermodynamic equilibrium and under unique conditions of both high pressure and temperature. Realistic physical models should include self-influence of the beam due to modified refractive index, strong thermal lensing and complex dynamics of permittivity (complex-valued dielectric function) of the media during and after the modification stage. Note that the equations of state of matter under exotic conditions are simply not available; moreover their solution, if they did exist may require significant effort both in terms of programming and as regards high-performance computing.

   It is important to recognize the limitations as well as the attractive features of a new

technology. Practical demands for fs direct inscription push laser pulse energies up to the limit of material damage. Modification of material without the optical damage can be achieved only through precise control over the deposition of the laser pulse energy. One can expect that a modification of the material may be transformed into damage, when the density of the absorbed energy becomes comparable with the density of energy already stored inside the bulk of material, so-called the density of cold bonds [103, 104]. This parameter can be estimated from the Young Modulus, **E**, which for most dielectrics ranges between $10 \sim 100\ GPa$ or $10 \sim 100\ kJ/cm^3$ respectively. Obviously, when the deposited energy density becomes comparable to these values, structural modifications are inevitable, which are believed to cause *damage*, or in other words *uncontrolled structural changes*. Direct femtosecond inscription is only possible if the density and speed of energy deposition are controlled within certain margins. In this sense it may be considered that it is the optical damage which is under control. The estimates for this are given in Chapter 5.

The main results reported in this work are:

- The technological processes for the direct femtosecond micro-fabrication method have been established, including the setting-up of a number of laboratories at Aston University.

- The margins for low-loss waveguide fabrication in BK7 glass and initial trials in some other transparent dielectrics were explored. Record high refractive index contrast (more than $2.5 \cdot 10^{-2}$) was demonstrated, which is more than an order of magnitude above the results obtained by low-repetition rate fs systems.

- This result was confirmed by calibration of the method of QPm used, and by exploring the mode-field distributions for these waveguides (both numerically and experimentally). Such high refractive index is obtained at the translation speed of the sample of about $30mm/s$, which is three orders of magnitude more than for LRR systems. The energy utilisation, productivity and an estimated cost for directly inscribed waveguides make this method attractive for industry.

- Total insertion losses in optimised HRR fs waveguide can be minimised below 1 dB per 2 cm structure. These include Fresnel losses (0.35 dB), as well as coupling and propagation (2 cm) losses.

- Curvilinear tracks can also be fabricated with extra $1 \sim 2$ dB/cm bend losses when the radius of curvature $R = 10$ cm.

- The point-by-point method for fibre Bragg gratings fabrication was suggested for NIR fs laser irradiation. This method enabled us to demonstrate unique components directly fabricated in non-photosensitive optical fibres: directional bend sensors, overlapped Bragg gratings, highly birefringent long-period gratings (which can be used as a polarisers in high-power applications) and others.

- The limitations of the NIR PbP method as regards short-period inscription and their transverse dimensions were addressed by using UV fs radiation (third harmonics of 800 nm fs laser). Short periods - down to 250 nm - were demonstrated experimentally by the UV PbP method. This opens the possibility for a number of new applications at the wavelength below or about 1 μm.

- To increase the transverse size in the PbP method we suggested and demonstrated experimentally the micro-holographic method, which is based on a combination of the diffractive optical element (or its simplest realisation - binary phase mask) and a standard reflecting micro-objective. The focal spot is patterned as a result of the two-beam interference, and the inscription occurs when this patterned focal spot is translated between the laser shots, similar to the PbP method. The aspect ratio can be improved by at least one order of magnitude, thus making potentially stronger gratings.

- Finally, shallow waveguides can be fabricated by the mask-less lithography method suggested, which is one of the hybrid methods: direct fs laser ablation is used in combination with ion-exchange process in a multicomponent glass. This express and low-cost method can be used both for prototyping planar photonics circuits and for mass production, and it matches the demand for a number of plasmonic sensors and other applications.

1.3 Thesis structure

The thesis is structured according to the following scheme (journal papers and conference presentations with direct author's contribution are mentioned below):

Chapter 2 is a brief historic and literature review describing the state-of-the-art of direct fs fabrication of waveguides and the inscription of periodic perturbation in various fibres - the fibre Bragg Gratings (FBG) and Long-Period Gratings (LPG).

Chapter 3 describes the fundamentals of the direct fs inscription method. It begins with a general model of fs pulse propagation, and demonstrates some numerical results for the basic model based non-linear Schrödinger equation (NLSE). Then we demonstrate the NLSE reduction in the case where the pulse peak power is below the critical power for self-focusing. Rather different cases can be treated in a similar way, including non-Gaussian ring-shaped and astigmatic beams. Further comparison with experiments for the case of Transport-of-Energy-Equation (TEE) reveals that a revision of the NLSE model may be required. After a brief discussion of post-energy-deposition scenarios, we stress the importance of direct experimental methods to stimulate the development of a realistic theoretical model of femtosecond inscription. Some of the materials in this Chapter were reported in [1–7].

Chapter 4 describes both femtosecond laser systems, auxiliary and diagnostics equipment, and provides a review of methods for waveguide characterisation. The method of quantitative phase microscopy (QPm) turned out to be the key one, which enabled us to quantify numerous experimental results. This method was calibrated on a standard fibre with approximately the same dimensions and refractive index (RI) contrasts. A numerical procedure for index reconstruction by means of Abel inversion, using accumulated phase measured by QPm software was developed. The results from this chapter have been reported in the following papers: [8–11].

Chapter 5 presents the experimental results for fs waveguide fabrication by the LRR laser system and then demonstrates a radical improvement in fs inscription and a superior quality of fs waveguides, obtained by the HRR Chirped Pulse Oscillator (CPO), operated at the repetition rate of 11 MHz. We optimise experimentally the regimes of HRR fs inscription for the case when our structures will be coupled with a standard optical fibre SMF-28. With this optimal regime the waveguides obtained are low-loss, with propagation losses are of the order of the Fresnel reflection losses, both at HeNe laser wavelength and at 1550 nm, super-high RI index contrast is achieved (with the max-

imum of 0.025), and there is excellent mode matching to SMF-28 fibre. Based on this, low-bend-losses curvilinear waveguides with the bend losses about 1 dB/cm for the radius of curvature of 1 cm were demonstrated. This paves the way to a variety of integral optics applications and components. The experimental results presented in this Chapter were published in the following papers: [4, 8, 12–24].

Chapter 6 describes our point-by-point method, starting with its first realisations. Then we discuss the intrinsic difficulties of PbP method and suggest two approaches to improve it. First, we demonstrated experimentally PbP inscription by third harmonics ($\lambda = 267\ nm$) of NIR laser, with the shortest ever periodic perturbation obtained in the bulk of fused silica sample. Second, the micro-holographic method also suitable for short-period FBG fabrication was suggested. Both results have been obtained using the LRR laser system. The direct modulation method, which can produce sub-0.5 μm periodically modulated waveguide Bragg gratings, was demonstrated on the HRR system as well. Such flexibility enables the widest variety of applications of the method of direct fs inscription. Most of the results of this Chapter have been published in papers [9, 26–38, 105].

Chapter 7 describes a few applications of direct femtosecond inscription in optical fibres: highly birefringent LPG and various bend sensors, inscribed in a standard telecom fibre. For all cases presented we utilize the 3D flexibility of the fs direct inscription method. These results were published in [105], [40–49].

Chapter 8 addresses the issue of shallow waveguide fabrication by femtosecond laser. We suggested and demonstrated experimentally a practical technique for the fabrication of planar integrated optical circuits by combining precision ablation of pre-deposited Al film with a subsequent ion-exchange applications in prototyping and flexible small-scale production [51, 52, 106].

In Conclusion section we summarise our results as well as discussing possible directions of future work on fs micro-fabrication.

Chapter 2

Direct femtosecond inscription - state-of-the-art

The main motivation for this work was to explore alternative methods for manufacturing integrated optics elements and circuits, apart from those based on lithography, and to explore the routes and margins for direct fs micro-fabrication technology. In this Chapter, after an overview of methods for waveguide fabrication, there is a review of direct femtosecond inscription of waveguides. A brief review of methods for fibre gratings fabrication is also provided.

2.1 Literature review

The best traditional methods of fabrication for Planar Light-wave Circuits (PLC) set important benchmarks for any emerging technology. However, the field of PLC has matured over more than forty years since its emergence. The key parameters for any light guiding circuit may be extracted from the books [55, 107] and reviews [108–110]. First, following the paper by Teysuo Miya (NTT Photonics Labs) [108] we classify the refractive index contrast and other parameters in accordance with the following table 2.1. For example, by this classification the fibre with a refractive index contrast of 0.36% or $5.3 \cdot 10^{-3}$ has an index contrast between *Low* and *Medium* . Note that this classification was initially introduced in relation to flame hydrolysis deposition method [108], deployed routinely at NTT photonics labs nowadays. A more recent review was produced by Louay Eldada (DuPont Photonics Tech-

Parameter				
RI contrast, %	Low 0.25	Middle 0.45	High 0.75	Super-High 1.50
Propagation Loss, dB/cm	< 0.01	0.02	0.04	0.75
Fibre Coupling Loss, dB/cm	< 0.1	0.1	0.2	2-SMF, 0.4-DSF
Minimum Bending Radius, mm	25	10	5	2
Application Field	Small-Scale PLC	Medium-Scale PLC	Large-Scale PLC	Very Large-Scale and High-Density PLC

Table 2.1: Basic characteristics of waveguides for integrated optics PLC.

Material System	Prop. Loss (dB/cm)	Coupl. Loss (dB)	Refr. Index	RI Contrast $(\%)$	Birefrin- gence	Passive/ Active (Y/N)	Fabr. time $(h/min.)$
Silica fibre	$2 \cdot 10^{-6}$ $(SMF-28)$	0.1 $(splice)$	1.47	0.4	$10^{-7} - 10^{-5}$	Y/Y	
Silica-on-Si [Si]	0.1	0.5	1.44-1.47	1.5	$10^{-4} - 10^{-2}$	Y/Y	hh
Silicon-on-insulator	0.1	1.0	3.47	70	$10^{-4} - 10^{-2}$	Y/N	hh
Silicon oxy-nitride [SiO_xN_y]	0.1	1.0	1.44-1.99	30	$10^{-6} - 10^{-3}$	Y/N	hh
Sol-gel	0.1	0.5	1.2-1.47	1.5	$10^{-4} - 10^{-2}$	Y/Y	h
Polymers [$acrylate$, $polyimide$]	0.1	0.5	1.3-1.7	35	$10^{-6} - 10^{-2}$	Y/Y	h
Lithium Niobate [$LiNbO3$]	0.5	2.0	2.13-2.21	0.5	$10^{-2} - 10^{-1}$	Y/Y	hh
Indium Phosphide [InP]	3	10	3.1	3	10^{-3}	Y/Y	hh
Gallium Arsenide [$GaAs$]	0.5	2	3.37	14	10^{-3}	Y/Y	hh
Magneto-Optic materials [YIG]	0.5	2	2.2	12	$10^{-5} - 10^{-4}$	Y/Y	hh
Direct fs-tab:b**inscription**	$0.1 - 0.2$	≈ 1	$1.44 - 2.3$	1.5	n/a	Y/Y	minutes

Table 2.2: Basic characteristics of PLC fabrication technologies.

nologies) [109], where the technologies for both passive and active waveguide fabrication were compared. Some data in table 2.2 are extracted from Table I, p.577 of the paper [109]. For comparison we added the direct fs fabrication technology at the end of the table.

An alternative review of the WG fabrication method has been provided by Dr. S.Kobtsev (Novosibirsk State University, Russian Federation), which is presented in Table 2.3. This review is more focused on methods and properties of waveguide fabrication as well as on the characteristics of fabrication methods themselves [111].

Analysis of tables 2.1-2.3 and the literature on waveguide fabrication methods and their properties revealed:

- acceptable propagation losses for most practical applications could be 0.5 dB/cm and below;

- coupling losses to standard optical fibre from 0.5 to 1 dB can be tolerated;

- the lowest propagation losses appeared typically when high-temperature, post-deposition annealing of the glass film took place, the waveguides without annealing always have higher losses;

- for methods suitable for high-speed signal modulation (from *Polymers* and below in Table 2.2) the losses are usually higher than for passive technologies;

- the higher the average refractive index of the material used, the greater the coupling and propagation losses, which can be explained by both elevated Fresnel losses and increased scattering losses, as the Rayleigh scattering losses are proportional to n_0^4, where n_0 - is the bulk RI;

- refractive index contrast above 0.5% is acceptable for simple PLC, while more dense photonics lightwave circuits require RI contrasts of 1.5 % or more.

Note that capital and infrastructure investments in the direct femtosecond method seem to be comparable or even lower than for other methods, especially those that utilize lithography and photoresist-based stages in a clean room environment.

No	Waveguides fabrication methods	Type of WG	Wave-guide Border	Host materials	Typical propagation loss, dB/cm	Maximum Refr. Index Contrast	Maximum Depth, μm	Fabrication Time
1.	Vacuum evaporation	P	DoP	glass, SiO_2	0.3~3	0.6	~5	hours (1nm/s)
2.	Ion sputtering	P	DoP	amorphous	0.2	10^{-3}~1	~2	hours or day
3.	Deposition from liquid solution	P	DoP	glass	0.15~0.3	-2~$3\ 10^{-2}$	~5	hours
4.	Chemical vapor deposition	P	DoP	silica, doped silica	0.01~0.06	1~$2\ 10^{-2}$	~5	hours
5.	Flame hydrolysis deposition	P	DoP	glass	0.01~0.8	10^{-2}	several	hours
6.	Pulsed laser deposition	P	DoP	crystals, M/C films S/C, hetero-struct.	1 down to 0.1	0.1~1	≤ 135	hours
7.	Ion exchange ($Na^+ \leftrightarrows K^+, Ag^+$)	CnS	U	M/C special glasses	0.1 or less	up to 0.13	5~10	2 hours
8.	Proton exchange	CnS	U	$LiNbO_3$, $LiTaO_3$, PPLN	0.15~0.5	up to 0.145	5~10	several hours or days (poling)
9.	Waveguiding by lowering concentr. of free carriers	P	U	S/Cond. (e.g. GaAs)	9	$5\ 10^{-3}$	~3	a day
10.	Electrooptical waveguides	P	U	($In_{1-s}Ga_sAs_tP_{1-t}$)	n/a, high	10^{-2}	~0	10^{-12} s
11.	Epitaxy (LPE or MBE)	P	S	crystals	0.1 or 1.0	10^{-3}	1~100	several hours
12.	Thermal bonding	P	S	cryst., oxides	0.2~0.5	1	up tp mm	several days
13.	Direct proton beam writing	ChS	U	polym., photoresist	0.2~1	n/a (etching)	~5	0.5 hour
14.	Laser ablation	ChS	S	crystals	very high	n/a (etching)	2.5~5	several min
15.	UV-writing	CnS	U	UV-ph.sens. glass	0.7~2	0.01 to 0.15	~3	several hours
16.	Ion beam etching	C	U	S/Cond., Sapph.	2~3	n/a (etching)	2~3	hours
17.	I/B impalatation & Chem. Etch.	C	U	cryst., $LiNbO_3$	high	n/a (etching)	1~2	hours
18.	I/B or p^+ implantation	P&C	U	cryst., glasses	down to 0.7	$\pm 10^{-2}$	~10	2-4 hours
19.	Soft-lithography & rapid phototyp.	3D & C	S	PDMS	0.4	$2\ 10^{-2}$	125	2-4 hours
20.	Direct fs writing	3D&C	U	glasses, cryst.	<0.1	$10^{-2} \sim 10^{-1}$	~mm	minutes

Table 2.3: Comparison of different WG fabrication methods (courtesy of S. Kobtsev). Notes on data presented: (P) planar; (CnS) Channel, near-Surface; (C) channel; (3D-c) 3D-channel; (DoP) Depends on subsequent etching process; (U) un-sharp; (S) sharp; (S/Cond.) semiconductors; (M/C) multi-component.

It is difficult to provide a complete review of the literature on direct femtosecond micro-fabrication as, for example, the paper by K.M. Davis et al. (the pioneering and, possibly, a contradictory one) published in 1996 [64], has been cited more than 900 times since then, despite the fact that the main experimental results in this paper seem to be questionable. The claim that the achieved refractive index contrast was 0.035 has not been confirmed by the same group of authors [65], [66] or by other researchers. Moreover, this value of induced index contrast would imply that the phase transition to, perhaps, *tridymite*, a form of SiO_2, high-temperature polymorph of quartz, metastable under normal pressure, had taken place. Taking into account the method of ellipsometry was used for RI characterisation, as well as significant ellipticity (6×180 μm) of the tracks obtained after ten scans over the same path in a 3% Ge-doped Si-glass, and considering possible errors in the micro-ellipsometry, which is estimated by authors to be ± 0.01), and also the birefringence which was possibly induced in the *damaged* [66] glass, it would be reasonable to assume that the induced RI contrast was less than reported.

The literature on fabrication of waveguides in glasses may be reasonably classified on the basis of the repetition rate of the inscription laser. The boundary at pulse repetition rate of about 100 or 200 kHz naturally arises when one compares the time for heat diffusion with the interval between laser pulses.

Low repetition (typically, kHz) CPA systems were available before their HRR counterparts and thus were tested first. kHz laser systems tend to create elliptical or elongated modified areas in the bulk of material, which if guiding the light do exhibit high coupling and propagation losses. This problem has been addressed in many experiments and described in the literature.

It was suggested in 2003 by Osellame et al. [71], that a telescope built of cylindrical lenses in front of MO may be used to astigmatically shape the laser beam. The obtained structures indeed have a more circular shape at least at optimal conditions. What was also achieved in the abovementioned paper is that the diameter of the waveguide could be made few times larger, thus the waveguide itself could be stronger. Additionally, this approach allows good utilization of laser energy when optics with AR-coatings are used: no energy loss, as for example with a slit method, described below. The disadvantages of the suggested method are: i) a larger focal area demands higher laser pulse energies, which can damage

focusing optics (in particular, MO), if they are made of glass; ii) the higher peak power of the pulse brings an additional problem: the non-linear beam propagation; there are no analytical models or numerical packages to calculate accurately the task for propagation of fs beam which is arbitrarily shaped: it is still largely unexplored area; iii) the involvement of non-linearity makes focusing dynamics intensity dependent, and thus being subject to laser pulse energy instabilities; iv) the sample translation speed typically remains slow for any beam shaping method, significantly diminishing the practical applicability of the method of direct fs fabrication; v) in our experiments, we have found the tracks produced by this method are typically modulated along the direction of scan; vi) in practice, the alignment of the cylindrical optics is complex and time consuming.

A similar approach was developed by M.Ams et al. [70]. In their method only one (and much simpler) optical element is used: the optical slit in front of the MO. Using similar materials both groups achieved quasi circular waveguides with induced RI contrast of about $3 \cdot 10^{-3}$ and quite high propagation losses of about 1 dB/cm, which are possibly due to longitudinal modulation of the parameters of the waveguide and induced losses (imaginary part of permittivity) in the material.

A third approach which overcomes the problem of the elliptical shape of the waveguide is a multiple scan approach. A number of parallel tracks can together form a guide for a super-mode or the mode which only exists if the tracks are combined/brought together. The intriguing possibility to control both the shape of the mode and its dispersion (which is not trivial) was confirmed by numerical simulations. Examples of such structures were demonstrated in fused silica [39] and laser crystals [12, 15, 112]. This approach will be mentioned in Section 5.1.4. However it cannot resolve the issue of the very long inscription time for the LRR system either.

A very unusual result was presented in the paper by Zhang et al. in 2006 paper [113]. A much longer pulse duration (1 ps) than was commonly believed to be the optimum (< 250 fs) was used to inscribe a low-loss ($< 0.25\ dB/cm$) type-II waveguide in fused silica. Similar results were described in the paper by Graf et al. [25] with the difference that in the LRR case each of the spots was made by a single shot, while in the paper [25] pearl-chain waveguides were fabricated by $\approx 10^3$ laser pulses per each bubble, or even more.

In general, the waveguides obtained by LRR systems have RI contrast from 0.1×10^{-3} to

3.5×10^{-3} [70], with propagation losses of 0.39 dB/cm [70] or 0.25 dB/cm [99]; both were obtained in phosphate glass doped by $Er^{3+}$and Yb^{3+}. Usually one can obtain propagation losses of the order of 1 dB/cm.

When much lower losses are required, as for example in some laser crystals, an alternative method with astigmatic laser beam has been suggested by Okhrimchuk et al. [15], [21]. In our method the inscription spot is expanded *along* the direction of scan, not perpendicular to as it was used in the experiments by Osellame and Ams cited above. More details are given in Section 5.3.

The work by Zhang et al. [114] also reports on quite low losses of $0.25 dB/cm$ obtained by 1 kHz but this was demonstrated in (*Corning* 7890) fused silica; however the method used for loss estimation is ambiguous, as the microscopic photo from the top of the waveguide in this paper exhibits a damaged track, so it is hard to believe that the quality of the waveguide was good and thus it had low losses. The last reference is the only paper on 1 kHz inscription, where the sample translation speed approaches or exceeds 1 mm/s. The coupling losses to a standard optical fibre (losses associated with mismatch of mode-field diameters) at telecom bands are about 1 dB per joint. This remarkable result definitely requires further investigation.

There are also journal papers and conference proceedings where record-low propagation losses are reported [115]. The authors of the paper claim that by optimizing the duration of the laser pulse (from 120 to 650 fs) they achieved 0.1 and, soon after, 0.05 dB/cm, this time after additional thermal annealing. In reflection such a low level corresponds to the best (state-of-the-art) thin-film Anti-Reflection (AR) coatings [116] and this makes us believe that loss figures could be due to the erroneous substraction of coupling losses and, possibly, originated due to the subtraction of the Fresnel losses, which are 4 to 8 times higher (0.36 dB). Moreover, the bright-field microscope images provided in the papers [115, 117] reveal average visual quality of fs waveguides, and thus it raises some questions about possible systematic errors in their experiments. However, the main point of this paper - that by controlling the pulse duration one may affect the focal volume where the energy is deposited - was recently confirmed in experiments by other groups, see for example paper by Ferrer et al. [118].

HRR fs inscription systems [13, 18, 25, 66, 72, 74, 119–121] offer significant advantages

with respect to kHz ones. These advantages are:

- sample translation speed can be at least 3 orders of magnitude more than by LRR systems; this makes direct femtosecond inscription interesting for practical applications;

- the laser energy utilisation and fraction of absorption energy from the pulse train are much higher in the case of HRR systems;

- RI contrast obtained with HRR systems is much higher than in the case of kHz systems;

- coupling losses with standard fibres are much lower, due to the naturally occuring circular cross-section of HRR waveguides and their larger dimensions;

- propagation losses are lower, perhaps due to the effect of heat accumulation and annealing;

- the stability of the pulse train after the CPO is much better than after the CPA due to deep gain saturation of the active media and the fact that a more stable pump is used.

This makes the investigations into direct femtosecond inscription by HRR lasers very timely indeed.

Our narrow selection of literature on fs waveguide fabrication is dictated by the scope of the present thesis. Perhaps a better overview can be found now in journal reviews and books: see, for example [60], [67], [122], [24], as well as in the PhD theses by Shane M. Eaton (2008), Martin Ams (2008), Rafael R. Gattas (2006), as well as others from research groups in Europe and beyond.

To summarise all the abovementioned data we compiled comparison Table 2.4.

Laser system [k/M Hz; fs; nm]	Type of glass	RI $\times 10^3$ contrast	Propagation (Coupling) Losses [dB/cm] @λ [nm]	Year [Ref.]
	Low	**Repetition**	**Rate**	
20 kHz; 40fs; 800nm	Fused Silica	5	n/a	2002 [123]
1 kHz; 150fs; 790nm	Phosphate	< 3	1.5 @ 1550	2003 [71]
0.238 kHz; 150fs; 790nm	several	0.15	0.51 @1550	2003 [75]
1 kHz; 120fs; 800nm	Phosphate	< 3.5	0.39 @1550	2005 [70]
1-100 kHz; 50fs; 800nm	various	$-4 \sim +5$	12 in IOG-1 glass	2005 [124]
1 kHz; <5000fs; 800nm	Fused Silica	0.5	0.25 @ 1ps; 1mm/s	2006 [113]
1 kHz; 140fs; 800nm	**Fused Silica**	**0.5**	**>(3 dB)@633**	**2006 [39]**
1 kHz; 120fs; 800nm	Foturan	1.7	0.8	2007 [125]
1 kHz; 100fs; 800nm	Baccarat	1	0.9 (0.7dB)	2009 [126]
	High	**Repetition**	**Rate**	
200 kHz; 120fs; 810nm	Fluoride	3	n/a	1998 [66]
80 MHz; 25fs; 400nm	Fused Silica	4.5	n/a	2001 [74]
200 kHz;150fs;800nm	Fused Silica	n/a	0.5	2005 [115]
26 MHz; 30 fs; 800 nm	*Corning* 0211, IOG10	$3 \sim 4$	0.5 (0.9) in IOG10	2005 [127]
25 MHz, 60fs; 800nm;	B-silicate 0215	n/a	≈ 0.1	2006 [128]
26 MHz; 30fs; 1070 nm;	IOG10; [0211]	$3 \sim 6$	0.5(0.9); [0.5(2.9)]	2006 [129]
1 MHz; 350fs, 1070 nm;	Borosilicate	8	0.4 (0.1 dB)	2006 [121]
1 MHz; 300fs, 1045 nm;	Borosilicate	<6	0.6	2008 [130]
1.5 MHz; 300fs; 1045nm	Phosphate QX	<9	0.3	2008 [72]
11 MHz; 48fs; 792nm	**BK7**	**25**	**0.2-0.3**	**2009 [13]**
1 MHz; 220fs; 532nm	Fused Silica	$10 - 15$	$0.3 - 0.6$ at 1550 nm	2009 [131]

Table 2.4: Review table for refractive index contrast and insertion losses archived by different femtosecond laser systems. The results discussed in the present work are highlighted.

The comparison of the induced RI contrast and the insertion losses are presented in Table 2.4. There are two groups in this table. The first group represents results obtained by LRR systems, the second is for HRR systems.

The conclusions which follow from analysis of the data in this table are: i) the coupling and propagation losses are lower for HRR systems; ii) the induced RI contrast is higher for HRR inscription; iii) these advantages may depend on the repetition rate of the laser.

More importantly from the instrumental point of view, the traditional fs laser systems (regenerative CPA and multipass amplifiers) have almost reached their limits in terms of pulse repetition rate. Further progress may require novel CPO designs, so the research on direct fs inscription with this laser sources is extremely important. Given the explosive interest and recent developments in femtosecond high-power, high-repetition rate fibre oscillators, it is very timely. Such laser systems may pave the way for future direct fs laser methods, as well as methods for engineering of material properties.

Bragg gratings are ubiquitous components in many composite devices where wavelength selectivity is required. Manufacturing of the FBG or WBG in the bulk of any material is a challenging technological problem involving precise periodic perturbation of the refractive index within or in the vicinity of the waveguide or a fibre core. We demonstrate below how they both can be fabricated during the same microfabrication stage. The major problem with FBG is the diffraction limit, as sub-μm pitch size for variation of the refractive index is required for first order Bragg grating even at NIR wavelengths. For example, an application wavelength of $\lambda = 1550$ nm implies a grating period of $2\lambda/n_0$ or about 535 nm to satisfy the first order Bragg reflection condition in standard fibres. Thus, such constraint requires a pitch size of about 1/4 μm. In Chapter 6 we describe fs-fabrication of periodic structures with the period of 250 nm, first demonstrated in the bulk of fused silica, which we believe to be the shortest period directly inscribed by fs pulses. It should be remembered that after the possibility of such inscription was demonstrated in the bulk of fused silica sample [39] it became possible to inscribe 535 nm period in various fibres [132], [133]. Twice shorter period of 250 nm has been achieved by UV-femtosecond inscription. The nonlinear temporal and spatial evolution of the femtosecond pulse was proved to play a key role in focusing of fs laser light below the diffraction limited spot size [38].

The fabrication of LPGs by NIR fs laser was first reported in the paper by Yuki Kondo

et al. in 1999 [80]. Subsequently, fibre Bragg gratings by interferometric method using NIR femtosecond laser were demonstrated in 2001 by K. Oi et al. [85]. In spite of the simplicity of this method there were few publications on this. The first reproducible femtosecond LPGs and FBGs were fabricated by Prof. D. Nikogosyan's group (Ireland) [82], [134], [135] by using higher harmonics (264 nm, and later, 211 and 352 nm) of lamp-pumped Yb^{3+}-glass "Twinkle" femtosecond laser (Light Conversion, Lithuania) and mask methods with both amplitude and phase masks. Later on the mask method was demonstrated by using NIR (800 nm) laser in Prof. S. Mihailov's (Canada) group [87], [136], [137], followed by multiple examples of fs inscription in various fibres and planar waveguides. The femtosecond mask fabrication method is now widely adopted and very recently FBGs with record-wide spectral width were demonstrated by this approach [93].

An alternative method for FBG fabrication by NIR fs laser was that developed at Aston University. This is the Point-by-Point (PbP) method [138], [27], [28], which consists of the consecutive inscription of a series of individual groves, with typically a single laser pulse per pitch. It allows the best control over the position and, in principle, the arbitrary amplitude apodisation coefficient of Bragg grating, and yet still possesses full 3D capability of femtosecond inscription. Further details and earlier results were published in the PhD thesis of A.Martinez (Aston University, 2005) [139]. The multiphoton excitation by NIR fs inscription creates a non-sinusoidal profile of the FBG grove [9], thus allowing the fabrication of Bragg gratings of multiple order(s) (second and higher). For example, the second order FBG by NIR fs laser can produce in a transmission spectrum the attenuation of a depth of about -60 dB, at 1550 nm, for a second order Bragg grating about 20 mm long [94]. The PbP method was adopted by other groups, for example it has been widely used by researchers from Macquarie University (Australia), so it was fairly quickly developed up to the stage when first order Bragg gratings at telecom wavelength were demonstrated [132].

Further progress in PbP inscription required some fundamental problems to be solved. Firstly, it is not likely that shorter than 0.5 μm periods can be fabricated by NIR fs laser irradiation, and moreover, the shorter the FBG period the more evident the second drawback: the laser affected/modified area occupies only a small fraction of the fibre core, so it limits the overlap of the propagating mode and the grating pitch and thus the strength of the grating's response. Thus, more pulse energy may be required if a stronger FBG is needed, but

higher laser pulse energy would create larger voids in the fibre core, as was demonstrated by Martinez et al. in [9], which prohibits the fabrication of short periods simultaneously with good strength gratings. Additionally, the PbP gratings often demonstrate high off-resonant losses, which are associated with the Rayleigh scattering on small-size non-uniformities of the refractive index - see, for example papers by Aslund et al. [140], [141]. These gray losses seem to be an intrinsic property of the PbP FBGs, especially the higher order gratings. Finally, the PbP FBGs suffer from the laser pulse instabilities, as a 5-photon mechanism of absorption is involved. The alternative to the PbP method [37] with a multi-pulse illumination for each grove of the grating could potentially resolve this particular problem, as described in Chapter 6. Thus, it would be advantageous to have a photo-induced modification with a cross-section whose size is more than the core diameter and, if possible, with multiple laser shots arriving at the same area. It seems this can be achieved by the interferometric method, however the application of such method for ultrashort pulsed laser inscription is complicated. In Chapter 6 we report on such a development of the PbP method by suggesting micro-holographic femtosecond inscription, using the third harmonics of fs NIR laser.

Chapter 3

Fundamentals of femtosecond inscription

As an electromagnetic phenomenon ultrashort laser pulse propagation as well as its interaction with dielectrics and plasma can be described by the system of Maxwell equations for two basic fields - the electric field $\mathbf{E}$ and the magnetic induction $\mathbf{B}$ and the derived fields, the electric displacement $\mathbf{D}$ and the magnetic field $\mathbf{H}$:

$$\nabla \times \mathbf{E} = -\frac{\partial \mathbf{B}}{\partial t}$$

$$\nabla \times \mathbf{H} = \frac{\partial \mathbf{D}}{\partial t} + \mathbf{J}$$

$$\mathbf{D} = \varepsilon\mathbf{E} \qquad \mathbf{B} = \mu\mathbf{H} \,,$$

coupled to equations for plasma:

$$\mathbf{J} = -e\rho\mathbf{v_e}$$

$$\frac{d\mathbf{v_e}}{dt} = -\tau_e^{-1}\mathbf{v_e} - \frac{e}{m_e}e\mathbf{E}$$

$$\frac{d\rho}{dt} = W_{ionisation\ sources},$$

where $\mathbf{J}$ is an electron current density, ρ is the density of free electrons, $\mathbf{v}_e$ is the average speed of a free electron oscillating in EM field, $\mathbf{m}_e$ is the mass of free electrons and τ_e is the shortest electron collision time. The description of plasma is based on relaxation dynamics of the electron, driven by the electromagnetic wave. All sources of free electrons (combined term $W_{ionisation\ sources}$ in the last equation) are, in general, intensity dependent. The major source of plasma in a strong electromagnetic field is thought to be the multiphoton ionisation mechanism with the speed, proportional to $\sim I^K$ [142], where the K is the

41

number of photons involved in the act of absorption, as well as avalanche ionisation, with the speed which depends both on electron density and instantaneous intensity distribution ($\sim I \cdot \rho$). These have to be included in the continuity equation.

Despite the fact that the relaxation of plasma occurs on a very short time-scale, it is still longer than the laser pulse duration and can be excluded from the last equation.

The envelope approximation [143] can be used to describe the evolution of a quasi-monochromatic pulse in a paraxial approximation [144–146]. Finally, Kerr nonlinearity must be taken into account for strong laser field $n = n_0 + n_2 \cdot I$. Such an approach was originally suggested by Feit and Fleck [147] and later developed into fairly complex models, see for example references [146, 148–154]. For our purposes a simplified model is used, which is essentially similar to the one described by Feng et al. [155]:

$$i\mathcal{E}_z + \frac{1}{2k}\Delta_\perp \mathcal{E} - \frac{k''}{2}\frac{\partial^2 \mathcal{E}}{\partial t^2} + k_0 n_2 |\mathcal{E}|^2 \mathcal{E} = -\frac{i\sigma}{2}(1 + i\omega\tau)\rho\mathcal{E} - i\frac{\beta^{(K)}}{2}|\mathcal{E}|^{2(K-1)}\mathcal{E} \quad (3.1)$$

$$\frac{\partial \rho}{\partial t} = \frac{1}{n_0^2}\frac{\sigma_{bs}}{E_g}\rho|\mathcal{E}|^2 + \frac{\beta^{(K)}}{K\hbar\omega}|\mathcal{E}|^{2K} \quad (3.2)$$

The terms on the left-hand side of Equation (3.1) describe effects of beam diffraction with $k = n_0 k_0 = n_0 \omega/c$ is the propagation vector, group velocity dispersion (GVD), with $k'' = \partial^2 k(\omega)/\partial\omega^2$ to be the GVD parameter, and $n_0(\omega)$ is a linear refractive index of the bulk medium, and n_2 is the nonlinear RI coefficient describing the Kerr nonlinearity and self-modulation, such that $n_2|\mathcal{E}|^2$ is a nonlinear contribution to the refractive index. The latter is responsible for a catastrophic self-focusing but only in the case of paraxial approximation [156], which in our case would be limited anyway by the effects described by other terms on the right-hand side of Eq.(3.1), namely plasma and multi-photon absorptions.

This equation is essentially a reduced paraxial approximation of the wave equation for the complex electric field envelope $\mathcal{E}$ with a carrier frequency ω, in the moving frame of coordinates: along Z direction with the group velocity v_g.

In the right-hand side of Equation (3.1) the σ_{bs} is the cross section for inverse Bremsstrahlung, τ is the electron relaxation time, E_g is the ionisation energy, and the quantity $\beta^{(K)}$ is the K-photon absorption coefficient.

Equation (3.2) implements the Drude model for electron-hole plasma in the bulk of silica and describes the evolution of the electron density ρ. The first term on the right-hand side is responsible for the avalanche impact ionisation and the second term $\beta^{(K)} \cdot |\mathcal{E}|^{2K}/(K \cdot \hbar\omega)$

for the ionisation resulting from MPA. Equation (3.2) is suitable for description of the sub-picosecond laser pulses when plasma diffusion is negligible.

Thus, the wave equation describing the evolution of the focused optical beam in the form of Non-Linear Shrödinger Equation (NLSE). The terms on the left-hand side in Eq.3.1, include plasma generation by the interaction of the laser pulse with the plasma, and multi-photon ionisation term: these two terms have correspondent ones on the right-hand of Eq.(3.1).

Group velocity dispersion included in Eq.(3.1) has been shown to lead to a pulse splitting and arrest of the beam collapse.

The initial conditions used for the numerical solution of Eqs. (3.1, 3.2) are the beam with Gaussian distribution both spatial and temporal. These can be defined either through the beam parameters on the top surface of the sample:

$$\mathbf{A}(r, z = 0, t) = \sqrt{\frac{E_{in}}{\pi \sqrt{\pi} \tau a_s^2}} \exp\left(-\frac{(1 + iC_s)r^2}{2a_s^2} - \frac{t^2}{2\tau_p^2}\right), \tag{3.3}$$

here index s denotes the values taken at the surface, a_s is the beam radius at the surface of the sample, τ_p is the pulse duration, and the parameter C_s is defined by focal distance f of spherical lens used as:

$$C_s = \frac{a_s^2 k}{f}, \tag{3.4}$$

or, for all numerical simulations we define the Gaussian beam in a slightly different way:

$$\mathcal{E}(r, z = -(f - S), t) = \sqrt{\frac{2P_{in}}{\pi r_0^2}} \exp\left(-\frac{r^2}{2\omega_0^2} - \frac{ikr^2}{2f} - \frac{t^2}{2\tau_p^2}\right), \tag{3.5}$$

where ω_0 is the beam radius on the lens. In our calculations fixed single values for $\omega_0 = 2.5$ mm and $\tau_p = 60$ fs were used. The variable S represents focal shift inside the sample, so that the depth of the structure positioning is about $n_0 \cdot S$. The pulse width τ_p together with peak power P_{in} define the pulse energy.

The important threshold for the pulse peak power is when it equals the critical power of self-focusing:

$$P_{cr} = \lambda_0^2 / 2\pi n_0 n_2. \tag{3.6}$$

This parameter depends on the material, and in a fused silica with a linear RI of 1.453 and the non-linear index $n_2 = 3.2 \times 10^{-16}$ cm^2/W the critical power for self-focusing is about 2.3 MW. So the pulse peak power will be equal to the critical power for self-focusing when pulse energy equals to 116 nJ (for pulse duration of $\tau_p = 60$ fs).

Critical power is proven to be a crucial parameter to determine the evolution of both the collapsing beam and the beam with *sub-critical* peak power (see section 3.2). In all numerical simulations the laser wavelength λ_0 was 800 *nm* unless otherwise specified, as, for example in Section 6.2, and the focusing lens has the focal distance f, with the corresponding numerical aperture *NA*.

Other parameters for fused silica used in simulations are: GVD coefficient $k'' = 361$ fs^2/cm, inverse Bremsstrahlung cross section $\sigma_{bs} = 2.78 \times 10^{-18}$ cm^2, multi-photon absorption coefficient $\beta^{(K)}$ can be expressed as $\hbar\omega\sigma_K\rho_{at}$, with $\rho_{at} = 2.21 \times 10^{22}$ 1/cm^3 being a SiO$_2$ molecules concentration and $\sigma_K = 1.3 \times 10^{-55}$ $cm^{2K}W^{-K}s^{-1}$ is the 5-photon absorption cross-section, as the band-gap in fused silica is $E_g = 7.6$ eV, so the $K = 5$.

Equations 3.1, 3.2 can be transformed into a dimensionless form:

$$\frac{\partial}{\partial t}\frac{\rho}{\rho_{BD}} = \frac{1}{n_b^2}\frac{\sigma_{bs}}{E_g}\frac{\rho}{\rho_{BD}}|\mathcal{E}|^2 + \left(\frac{|\mathcal{E}|^2}{I_{MPA}}\right)^K \tag{3.7}$$

where

$$I_{MPA} = \left(\frac{K \cdot \hbar\omega \cdot \rho_{BD}}{\tau_P \cdot \beta^{(K)}}\right)^{1/K} \tag{3.8}$$

Equation 3.8 naturally defines the threshold of MPA, as the plasma creation rate becomes very steep when the intensity exceeds I_{MPA}.

$\rho_{BD} = 1.7 \times 10^{21}$ is a plasma breakdown density, which corresponds to the density of plasma when plasma frequency - ω_p becomes equal to the optical frequency of a laser:

$$\omega_p = \sqrt{\frac{\rho \cdot e^2}{4\pi^2 \cdot \varepsilon_0 \cdot m_e}}. \tag{3.9}$$

As is known from plasma physics, such dense plasma absorbs laser radiation in the thin layer with a thickness of a few tens of *nm*. Being important physical thresholds, both I_{MPA} and ρ_{BD} were used for a general normalization of physical variables to perform the numerical simulations. Note that the threshold value for MPA obtained from Equation 3.8 is quantitatively close to the experimental values for the MPA threshold intensity and the threshold of permanent material modification.

The average kinetic energy of free electrons in plasma (equivalent to the temperature) can be estimated from the analysis of the electron oscillations in high frequency EM-field [157] as:

$$E_{osc} = \left\langle\frac{e^2 \cdot \mathcal{E}(t)^2}{4 \cdot m_e \cdot \omega^2}\right\rangle_t = 9.31 \times 10^{-14} \cdot I \cdot \lambda^2 \tag{3.10}$$

where e and m_e are electron charge and mass respectively, $\mathcal{E}$ is an envelope amplitude of the electric field, ω is a carrier angular frequency of the laser. If I, its intensity is in W/cm^2 and λ - the wavelength is in μm, then numerical expression in (3.10) on the right hand side gives a value of the kinetic energy in eV.

Typical values of electron kinetic energy versus laser intensity are given in Table 3.1. It

Intensity, W/cm^2	$1 \cdot 10^{13}$	$2.5 \cdot 10^{13}$	10^{14}	10^{15}
Kinetic Energy, eV	0.59	1.49	5.95	59.5

Table 3.1: Kinetic energy of oscillations of electrons in laser fields of different intensity.

is worth to note that at the intensity, corresponding to I_{MPA}, the average oscillation energy for electron oscillation is approaching the energy of a single photon or $\hbar\omega$.

The system of equations 3.1, 3.2 can be solved numerically as we demonstrated in [6], using the adaptive mesh refinement approach described in [158]. The main problem for the numerical solution of stiff differential equations is the left-hand side of the equation, which in stationary cases describes the collapse of the arbitrary intensity distribution of the input pulse, when the pulse power is high enough, or above the critical power for self-focusing, P_{cr}. It is known that in extended models [159], such collapses will be arrested, for example by dispersion, resulting in rather complex pulse propagation dynamics, and with both temporal and spatial splitting of the pulse. In our model the MPA-ionisation as well as plasma terms may also deplete the pulse and should arrest the collapse. Such temporal and spatial splitting of the pulse demands the use of fine mesh, which is still challenging for computing. Thus in the simulation of a single pulse propagation and residual plasma distribution an effective mesh resolution of 16384^3 ($4 \cdot 10^{12}$ points) was reached [158].

3.1 Post-deposition scenarios, limitations of the NLSE model

The numerical solution of the system of Equations (3.1, 3.2) allows one to find a spatial distribution of the plasma cloud resulting from intense laser focusing. If the average oscillation energy (Eqn. 3.10) is attributed to every electron in the valence band, this creates a source of energy which is assumed to be translated into the distribution of the local material

a)

b)
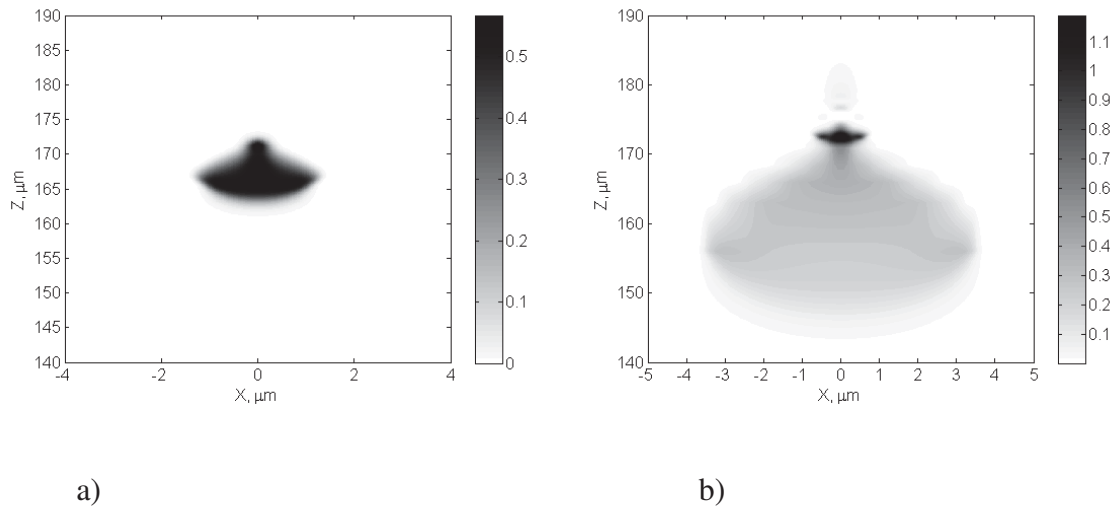
Figure 3.1: Plasma density contours after the electric field is vanished, for two different values of input power, a subcritical $P_{in} = 0.5 \, P_{cr}$ (a) and supercritical, $P_{in} = 5 \, P_{cr}$ (b).

a)

b)
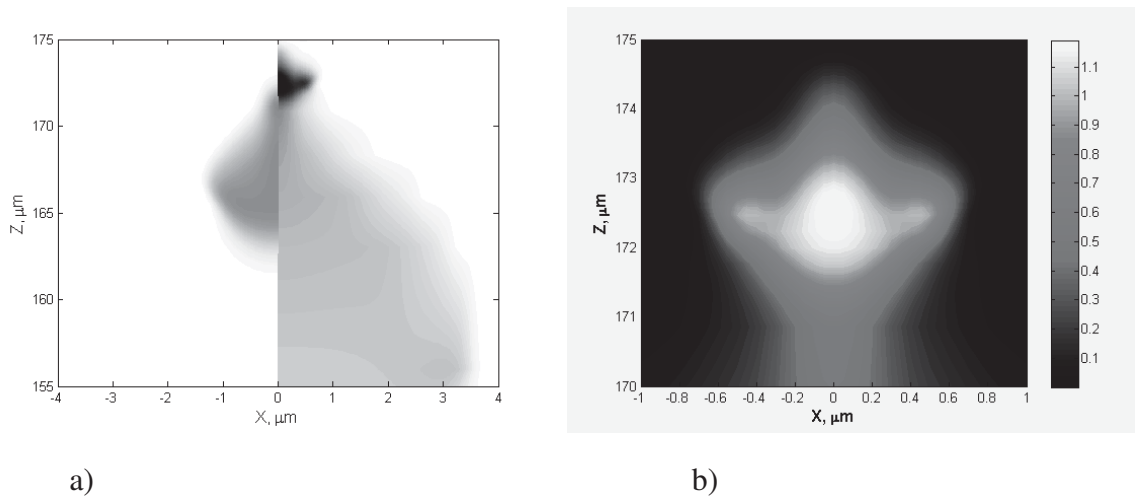
Figure 3.2: Back-to-back comparison (a) of the plasma produced in subcritical and supercritical regimes with the parameters as in Figure 3.1. Closeup of the plasma profile in supercritical case (b).

temperature since the deposited energy density is proportional to the plasma density. As the thermal relaxation takes place on a much longer scale (of a few picoseconds), no heat diffusion will take place. Extrapolation of the results of the numerical modeling of the irreversible thermo-elastic dynamics [160] suggests that the resulting diameter of the domain with modified refractive index will be half that for the temperature profile. Unfortunately, the thermo-elastic stage requires knowledge of numerous material parameters (such as elastic modulus, temperature dependencies of all material parameters, the equation of states for the case of phase transitions, including ones for non-equilibrium conditions, the data on radiation effects at elevated temperatures, knowledge of interband and intraband crossections, including all of these under high pressure conditions), which are typically not known. Thus, it is not likely that the system of equation can be made closed, so that it would be possible to predict the residual RI of mechanical stress analytically or numerically. So it would be impossible to consider the effects of self-influence of the beam on its own focusing by closing this loop.

Besides this, there are some problems with the NLSE model itself. These include:

• the paraxial approximation, used during the derivation of the Eq. (3.1). Initially this is assumed to be valid if the fields do not change significantly over the scale of a wavelength - both along the direction of propagation and in transverse direction [144]. The validity of such approximation was confirmed numerically up to these scales, however we have obtained even more compact solutions for intensity and plasma distributions (see, for example Figures 3.1, 3.2);

• slowly varying approximation. Initially it was thought that the second order dispersion term describes the temporal effects well down to the pulse duration of about $40-50$ fs. If even shorter pulse fragmentation occurs, this requires higher order dispersion terms to be included;

• sub-wavelength-scale effects, including the EM-field coupling to plasma, excitation of plasma waves, as well as back-scattered and reflected light. All these effects are completely omitted from consideration.

• the model of MPI is rather phenomenological, based on pioneering work by Keldysh in 1969 [142] which is still subject to intense scientific discussion;

• simplified treatment of nonlinear effects, as most of them are just excluded from

consideration;

- very basic kinetics of hot electrons, when they all are being prescribed an average oscillation energy instead of a proper distribution function;

- macroscopic plasma motion is not considered, which excludes the effects, similar to the ones observed during the experiments on voids formation (Coulomb explosion). Furthermore, microscopic plasma motion may be essential even for moderate laser pulse energies: for example, at the intensity of 10^{14} W/cm^2 the (quiver) oscillation energy of electrons is about 10 eV, and the electron density is 10^{21} cm^{-3}. The electron thermal velocity may reach 2.5 nm/fs which facilitates the passage of electron during the pulse duration (100 fs) to be about 250 nm - which is comparable with the whole radius of a plasma cloud;

- no memory on the inscription process or any kind of hysteresis is allowed. Free electrons could be trapped (auto-localised) after they lose their kinetic energy at the outer part of the irradiated volume. These trapped electrons would create strong local electrostatic fields, which must change the band-gap and thus the multi-photon absorption (MPA), for example for next laser pulse;

- neither thermal lensing effect nor dependence of E_g on temperature T are considered;

- there are no consistent physical models for the refractive index change, thus it is, in principle not possible to incorporate self influence into the model that describes changes in the RI.

In conclusion, we seem to be at the very beginning of the understanding of fundamental processes during and after femtosecond irradiation and the following modification of transparent dielectrics. Much more research is required. It seems unlikely that such tasks can be modeled in near future. The NLSE model described by Equations (3.1, 3.2), can be used on earlier stage of light propagation only, to account for contributions by MPA and avalanche ionisations. Meanwhile, further simplifications of the NLSE model are possible for the case before the inscription takes place. This is the subject considered in the next few sections.

3.2 Reduction of the NLSE model in the case of sub-critical peak power

In spite of numerous revisions, corrections and limitations of the NLSE model, as was mentioned at the end of the previous section, this approach allows some important simplifications, which were found in the process of the numerical integration of the system of Equations (3.1, 3.2). We found that below the femtosecond modification threshold, the contributions of right-hand side terms in the Equation (3.1) are small. In view of the relatively negligible inscription depth, the dispersion term is also insignificant for the range of pulse durations typically used in our experiments.

Then, as was demonstrated in paper [3], one can use an exact mathematical theorem (by Vlasov et al.) to describe the evolution of the beam parameters, before the fs modification begins. In such cases the Kerr nonlinearity is the only effect which would contribute to the focusing dynamics of laser pulses of different shapes. This is valid as long as the multiphoton absorption is weak, so the pulse energy remains almost constant. In this case the plasma is absent, so it does not affect the propagation of the pulse and Eq.(3.1) is reduced to:

$$i\mathcal{E}_z + \frac{1}{2k}\Delta_\perp \mathcal{E} + k_0 n_2 |\mathcal{E}|^2 \mathcal{E} = 0 \qquad (3.11)$$

According to Vlasov et al. [161], the evolution of the transversal root-mean-square width of the laser beam is described by the following analytical expressions:

$$\langle R^2(z) \rangle = \frac{\int_S \overrightarrow{r_\perp}^2 \cdot |\mathbf{A}|^2 \cdot d\overrightarrow{r_\perp}}{\int_S |\mathbf{A}|^2 \cdot d\overrightarrow{r_\perp}} = C_1 z^2 + C_2 z + R(0)^2,$$

where z-independent constants C_1 and C_2 are determined by the parameters (shape) of the incident beam, the beam power, $P = P(t)$, is normalized as in Eq. (3.5):

$$P = P(t) = \int_S |\mathbf{A_0}|^2 \cdot d\overrightarrow{r_\perp}, \qquad (3.12)$$

and the parameters C_1 and C_2 are defined by the EM-field wave-front through the following equations:

$$C_1 = \frac{\lambda_0^2}{4\pi^2 n_0^2} \frac{\int_S |\nabla_\perp \mathbf{A}|^2 \, d\overrightarrow{r_\perp}}{P} - \frac{n_2}{n_0} \frac{\int_S |\mathbf{A}|^4 d\overrightarrow{r_\perp}}{P} \qquad (3.13)$$

$$C_2 = \frac{\lambda_0}{\pi n_0} \frac{\int_S (\overrightarrow{r_\perp} \cdot \overrightarrow{\nabla_\perp} arg(\mathbf{A_0})) \cdot |\mathbf{A_0}|^2 \, d\overrightarrow{r_\perp}}{P} \qquad (3.14)$$

This result is very general, since no assumptions about the beam shape have been made so far. It is valid until the simplified Equation 3.11 can be used. Other parameters used throughout this section are: critical power for self-focusing in the case of Townes soliton [162]:

$$P_{cr} \simeq 0.93 \frac{\lambda_0^2}{2\,\pi\,n_0\,n_2} \tag{3.15}$$

and quite close to the previous one - the critical power for self-focusing in the case of axially-symmetrical Gaussian beam:

$$P_{cr}^{(G)} = \frac{\lambda_0^2}{2\,\pi\,n_0\,n_2} \tag{3.16}$$

The approach suggested by Turitsyn et al. [3], allows the inclusion of Kerr self-focusing effect into equation describing not only the Gaussian beam, but an arbitrary shaped one. As was demonstrated in [3], it is very interesting to re-examine the diffraction of the beams in the context of fs laser processing in so-called "sub-critical" regime, when input power is less than the critical power for self-focusing. It turns out that self-focusing formally removes some restrictions such as minimal achievable beam size at the focus during linear focusing; it also relaxes the need for tight pre-focusing to inscribe small-size objects and effectively can help to produce sub-wavelength structures. Essentially, this approach can be applied to a variety of spatial beam forms, if some conditions are met: the Equation (3.11) can be used to describe beam evolution, or there is no absorption, dispersion, and the effects due to plasma generation.

Substitution of the particular form of input beam leads to the analytical description of the beam focusing, which we illustrate below, considering several particular examples of input laser beam distributions. The experimental evidences supporting this approach are discussed in Sections 3.4. They are based on measurements of the fraction of laser pulse energy [21] which has been absorbed. It turned out, that until fairly high laser pulse energy is used, the absorbed energy constitutes a small fraction of it. First of all, we consider Gaussian distribution as an important benchmark, and in the limiting case of low peak power we shall arrive the well known formulas of Gaussian beam optics.

3.2.1 Gaussian beam in the Kerr nonlinear media

For a radially symmetric Gaussian beam we use an electric field in the form:

$$\mathbf{A}(r, z = 0, t) = \sqrt{\frac{E_{in}}{\pi \sqrt{\pi} \, \tau \, a_s{}^2}} \, \exp\left(\frac{(1 + iC_s)r^2}{2a_s{}^2} - \frac{t^2}{2\tau^2}\right), \tag{3.17}$$

where a_s is the radius at the sample surface, τ is the pulse duration, and the parameter C_s is connected to the wavefront curvature, imposed by a spherical lens with the focal distance f:

$$C_s = \frac{a_s{}^2 \, k}{f}, \tag{3.18}$$

while k is a wavevector.

Note that C_s within the factor of 2π is identical to the Fresnel number, a dimensionless number often used in scalar diffraction theory. It can be expressed in terms of experimental parameters: lens focal distance f, numerical aperture NA of the micro-objective (or effective NA) and the distance d from lens to the sample surface, so that the difference $S = f - d$ represents the inward shift of the micro-objective, the last one is most often referred to in publications:

$$C_s = \frac{\pi \, (f - d) \, NA^2}{\lambda \, (1 - NA^2)}, \tag{3.19}$$

Note that the real position of the structure inscribed beneath the surface is expected to be at the depth of about $n_0(f - d)$ due to the refraction. Using Eqs. (3.12-3.14), (3.17) one can arrive [3] at the following:

$$\langle R(z,t)^2 \rangle = R_{min \ NL}^2 \left(1 + \frac{(z - z_{min \ NL})^2}{Z_{R \ NL}{}^2}\right), \tag{3.20}$$

which resembles the classic formulae for the beam-waist for a Gaussian beam, but with important corrections, namely, substitutions of the classic parameters with their non-linear counterparts: $R_{min} \rightleftarrows R_{min \ NL}$, $Z_R \rightleftarrows Z_{R \ NL}$ and $z_{min} \rightleftarrows z_{min \ NL}$, which are: the minimum radius of the beam, confocal parameter and z-coordinate of the minimum respectively.

$$(R_{min \ NL})^2 = \frac{a_s{}^2}{\left(1 + C_s{}^2 - \frac{P(t)}{P_{cr}^{(G)}}\right)} \cdot \left(1 - \frac{P(t)}{P_{cr}^{(G)}}\right), \tag{3.21}$$

$$(Z_{R \ NL})^2 = \frac{k^2 \, a_s^4}{\left(1 + C_s{}^2 - \frac{P(t)}{P_{cr}^{(G)}}\right)^2} \cdot \left(1 - \frac{P(t)}{P_{cr}^{(G)}}\right) \tag{3.22}$$

$$z_{min\ NL} = \frac{k\,a_s^2\,C_s}{\left(1 + C_s^2 - \frac{P(t)}{P_{cr}^{(G)}}\right)} \tag{3.23}$$

These equations generalise linear (low power case) expressions - in the case of $P << P_{cr}$:

$$(R_{min})^2 = \frac{a_s^2}{\left(1 + C_s^2\right)} \tag{3.24}$$

$$(Z_R)^2 = \frac{k^2\,a_s^4}{\left(1 + C_s^2\right)^2} \tag{3.25}$$

$$z_{min} = \frac{k\,a_s^2\,C_s}{\left(1 + C_s^2\right)} \tag{3.26}$$

The necessary condition for the femtosecond inscription to occur is that peak intensity exceeds the threshold I_{th}, which will initially occur in the beam center, when the power $P(t) \simeq exp(-t^2)$ reaches its maximum value at $t = 0$. The shape of the area of energy deposition may be estimated by resolving the equation:

$$I(\vec{\mathbf{r}}, z, t = 0) = I_{th} \tag{3.27}$$

Assuming that a relaxation of plasma takes place with an average oscillation energy E_{osc}, this provides an energy/heat source for further thermo-elastic modelling. In conclusion, the analytic expressions for the Gaussian beam focusing in the case of sub-critical pulse peak power (3.24), (3.22) reveal the possibility for beam compression in both transverse and longitudinal directions.

3.2.2   Ring-shaped beams

Further, we consider a family of axis-symmetric beams, where an electric field distribution is in the form of a ring, with zero intensity on the optical axis:

$$\mathbf{A}(r, z = 0, t) = \sqrt{\frac{E_{in}}{\pi\,\sqrt{\pi}\,\tau\,a_s^{2+2\,M}}} \cdot r^M \cdot \exp\left(\frac{(1 + iC_s)r^2}{2a_s^2} - \frac{t^2}{2\tau^2}\right), \tag{3.28}$$

Similarly to the expression obtained earlier, the beam evolution can be presented in the form described by Eqs. (3.20) where one has to substitute the expressions for $R_{min} \rightleftarrows R_{min\ M}$, $Z_R \rightleftarrows Z_{R\ M}$ and $z_{min} \rightleftarrows z_{min\ M}$, obtained for a ring-shaped beam with the index $M \geq 0$, corresponding to different specific shapes of the beam from this family. The following are the expressions

for mean-square radius of the beam, confocal parameter and its position. We have omitted the sub-index NL for simplicity of records.

$$(R_{min\ M})^2 = \frac{(1+M) \cdot a_s{}^2}{\left(1 + (1+M) \cdot C_s{}^2 - \frac{P(t)}{P_{cr_M}}\right)} \cdot \left(1 - \frac{P(t)}{P_{cr_M}}\right), \tag{3.29}$$

$$(Z_{R\ M})^2 = \frac{k^2 \ (1+M)a_s^4}{\left(1 + (1+M)C_s{}^2 - \frac{P(t)}{P_{cr_M}}\right)^2} \cdot \left(1 - \frac{P(t)}{P_{cr_M}}\right) \tag{3.30}$$

$$z_{min\ M} = \frac{k \ (1+M)a_s^2 \ C_s}{\left(1 + (1+M)C_s{}^2 - \frac{P(t)}{P_{cr_M}}\right)}, \tag{3.31}$$

where critical power for self-focusing $P_{cr\ M}$ increases by the numerical factor > 1 compared to the case of the Gaussian beam, Eq. (3.15):

$$P_{cr\ M} = \frac{2^{(2\ M)} \ (M)!^2}{(2\ M)!} \cdot P_{cr\ G} \tag{3.32}$$

These equations generalise the propagation of the ring-shaped beam in the case of Kerr nonlinearity of the medium. One conclusion could be drawn immediately from Eq. (3.32): in the case of the ring-shaped beam the critical power for self focusing is few times the $P_{cr\ G}$. This factor equals 2 for lowest order ring ($M = 1$), and to 5.1 when $M = 8$.

Analysis of Eqs. (3.29 - 3.31) in the case $C_s \gg 1$ suggests:

- the area of the beam-waist has no or little dependence on the particular shape of the ring beam (defined by M), and it can be estimated by Eq. (3.21);

- the shift in the beam position or $z_{min\ M}$ is negligible in practice, and does not depend on the specific shape of the ring-beam (or M). The shift is comparable to the case of the Gaussian Beam (see Eq. 3.23);

- and, most important, the confocal parameter of the ring-shaped beam is shorter than that for the Gaussian beam even in non-linear case and does depend on the shape of ring beam (index M).

Thus, using some special types of objectives (e.g. reflective ones), a higher threshold for self-focusing can be achieved, leading to a higher density of the deposited energy, than by using the Gaussian beam and a standard focusing. This approach could be of great importance in the case of high-repetition-rate systems, when the possibilities of shortest pulse engineering are being exhausted.

3.2.3 Gaussian beams with spherical aberration

Direct femtosecond inscription is often used with samples that have a flat surface. In the case where focusing optics are being corrected for aberrations in air, after refraction on a flat surface the spherical aberration can be introduced. Note that some of the advanced (and more expensive) micro-objectives allow compensation of this effect, by introducing an adjustable shift in one or a group of lenses. It would be instructive to consider another type of non-Gaussian beam, namely, the one with a spherical aberration. In this case the laser beam can be described as:

$$\mathbf{A}(r, z = 0, t) = \sqrt{\frac{E_{in}}{\pi \sqrt{\pi} \, \tau \, a_s{}^2}} \, \exp\left(\frac{(1 + iC_s)r^2}{2a_s{}^2} - \frac{ibr^4}{4a_s^4} - \frac{t^2}{2\tau^2}\right), \tag{3.33}$$

where the parameter b describes the phase deviation of the wavefront of the field A at the distance of a_s from the beam axis. In this case the Eqs. 3.21 - 3.23 will be transformed into:

- the analogue of the beam-waist:

$$(R_{min \ SA})^2 = \frac{a_s{}^2 \cdot \left(1 + 2b^2 - \frac{P(t)}{P_{cr}^{(G)}}\right)}{\left(1 + 2b^2 + (C_s + 2b)^2 - \frac{P(t)}{P_{cr}^{(G)}}\right)}, \tag{3.34}$$

- the "confocal parameter":

$$(Z_{R \ SA})^2 = \frac{k^2 a_s{}^4 \cdot \left(1 + 2b^2 - \frac{P(t)}{P_{cr}^{(G)}}\right)}{\left(1 + 2b^2 + (C_s + 2b)^2 - \frac{P(t)}{P_{cr}^{(G)}}\right)^2}, \tag{3.35}$$

- and its position:

$$z_{min \ SA} = \frac{k \, a_s{}^2 \cdot (C_s + 2b)}{\left(1 + 2b^2 + (C_s + 2b)^2 - \frac{P(t)}{P_{cr}^{(G)}}\right)}, , \tag{3.36}$$

where critical power for self-focusing is the same as for the case of Gaussian beam $P_{cr}^{(G)}$, see Eq. 3.15.

The relation between the phenomenological parameter b and the numerical aperture NA, parameter C_s, shift S and refractive index of the material n could be found if one compares the focus position as a function of radius of the beam on the lens, using the Equation (3.18):

$$\frac{\Delta f(r)}{f_0} = \frac{b}{2 \, C_s} \cdot \left(\frac{r}{a_s}\right)^2, \tag{3.37}$$

where the value $\Delta f(r)$ represents the focus shift as a function of the radius. This is to be compared with the shift of focus by Snell's law for some "ideal" lens, which provides aberration-free focusing in the air:

$$\frac{\Delta f(r)}{f_0} = \sqrt{1 + \left(\frac{r}{S}\right)^2 \cdot \left(1 - \frac{1}{n^2}\right)} - 1 \qquad (3.38)$$

Comparing the last two expressions, one can express the parameter b as following:

$$\frac{b}{C_s} = \left(\frac{NA^2}{1 - NA^2}\right)\left(\frac{n^2 - 1}{n^2}\right) \qquad (3.39)$$

The conclusions from Eqs. (3.34) and (3.35) are the following: spherical aberration can arrest the non-linear beam compression obtained for Gaussian beam in the sub-critical regime. It is necessary to use focusing optics, corrected for spherical aberration, in order to minimize the threshold power for femtosecond inscription especially when $NA \geq 0.1 \sim 0.2$.

3.2.4 Gaussian Beam with astigmatism

In this case of astigmatism the Gaussian shape of EM-field can be defined as:

$$\mathbf{A}(r, z = 0, t) = \sqrt{\frac{E_{in}}{\pi \sqrt{\pi} \tau (a_x a_y)}} \exp\left(\frac{(1 + iC_x)x^2}{2a_x^2} + \frac{(1 + iC_y)y^2}{2a_y^2} - \frac{t^2}{2\tau^2}\right), \qquad (3.40)$$

where for the sake of simplicity we omitted all sub-indices s in all variables (all variables are taken at the surface of a sample in this section).

For this shape there are three important cases:

- $C_x = C_y$, $a_x \neq a_y$, which may correspond to an elliptically shaped stigmatic Gaussian beam, focused by a micro-objective;

- $C_x \neq C_y$, $a_x = a_y$ - this is the case when a cylindrical lens is installed in proximity to the micro-objective, so there is no change in beam dimensions, but only an alteration in wavefront curvature;

- A general case, when both $C_x \neq C_y$, $a_x \neq a_y$, so both dimensions and focal positions are different.

The first and second cases were explored experimentally, although not in detail. The justification of the analytic results obtained below could be accomplished thorough numerical

simulation. The astigmatic beams turns out to be important in producing smooth waveguides with low-repetition rate laser systems, especially in laser crystals [15]. We did find experimentally that without controlled astigmatism the inscription of smooth and low-loss tracks was not possible in almost all laser crystals when the kHz fs-laser system was used. One can obtain the positions of minimum beam-waist, mean-square beam radius (or beam area), as well as a "confocal parameter".

$$\left(r_{min}^A \right)^2 = \frac{\frac{(C_x a_y{}^2 - C_y a_x{}^2)^2 + (a_x{}^2 + a_y{}^2)^2}{a_x a_y} - 2\left(a_x{}^2 + a_y{}^2\right)\frac{P}{P_{cr}}}{4\left(\frac{(1+C_x{}^2)\frac{a_y}{a_x} + (1+C_y{}^2)\frac{a_x}{a_y}}{2} - \frac{P}{P_{cr}}\right)} \tag{3.41}$$

$$\left(Z_R^A \right)^2 = \frac{2\,k^2\,a_x a_y\left(a_x{}^2 + a_y{}^2\right)\cdot\left(\frac{(C_x\,a_y{}^2 - C_y\,a_x{}^2)^2}{2\,a_x a_y\left(a_x{}^2 + a_y{}^2\right)} + \frac{a_x{}^2 + a_y{}^2}{2\,a_x\,a_y} - \frac{P}{P_{cr}}\right)}{4\left[\frac{(1+C_x{}^2)\frac{a_y}{a_x} + (1+C_y{}^2)\frac{a_x}{a_y}}{2} - \frac{P}{P_{cr}}\right]^2} \tag{3.42}$$

$$Z_{min}^A = \frac{k\,a_x\,a_y\,(C_x + C_y)}{2\left(\frac{(1+C_x{}^2)\frac{a_y}{a_x} + (1+C_y{}^2)\frac{a_x}{a_y}}{2} - \frac{P}{P_{cr}}\right)} \tag{3.43}$$

The meaning of these results is not straightforward, so we provide a simplified formula only for the second case mentioned above. In this case of practical interest when both a_x and a_y are equal (to a), while $C_x \neq C_y$ the last expressions read:

$$\left(r_{min}^A \right)^2 = a^2\,\frac{\frac{(C_x - C_y)^2}{4} + 1 - \frac{P}{P_{cr}}}{\frac{(C_x{}^2 + C_y{}^2)}{2} + 1 - \frac{P}{P_{cr}}} \tag{3.44}$$

$$\left(Z_R^A \right)^2 = k^2\,a^4\,\frac{\frac{(C_x - C_y)^2}{4} + 1 - \frac{P}{P_{cr}}}{\left[\frac{C_x{}^2 + C_y{}^2}{2} + 1 - \frac{P}{P_{cr}}\right]^2} \tag{3.45}$$

$$Z_{min}^A = \frac{k\,a^2\,(C_x + C_y)}{2\left[\frac{C_x{}^2 + C_y{}^2}{2} + 1 - \frac{P}{P_{cr}}\right]} \tag{3.46}$$

Thus, in this case of astigmatism, the compression of the non-linear beam waist (Eq. 3.44) and confocal (Eq. 3.45) parameter may occur, only when the parameters C_x and C_y are close to each other.

The experiments reveal that only when a long focal distance, negative, cylindrical lens was used the astigmatic scheme produces smooth tracks. The pulse energies were well above the critical power for self-focusing - for the case of radially symmetric Gaussian beam.

3.2.5 Threshold for fs-Inscription

The multi-photon absorption of the ultrafast laser pulse is very sensitive to the intensity of the laser and starts only when this exceeds the threshold value I_{th} (Eq. 3.8). A semi-empirical approach suggested by Zhang et al. in [160], which was confirmed by numerical simulations, can be used. This results in the shape of the area with a modified refractive index following the spatial distribution of the generated electron plasma and thus, the volume, where the intensity exceeds the threshold value. In other words, because of the sharp dependence of the multiphoton ionisation process on the field intensity, the spatial form of the inscribed structure can be well approximated by resolving an Equation 3.27 on the field intensity [3]:

$$I_{th} = \frac{P_{in}}{\pi R_{min}^2} = \frac{P_{in}\left[1+C_s^2-\frac{P_{in}}{P_{cr}}\right]}{S_s\left[1-\frac{P_{in}}{P_{cr}}\right]} \tag{3.47}$$

the last equation can be resolved for P_{in}/P_{cr} in order to estimate the minimal power required:

$$\frac{P_{in}}{P_{cr}} = \frac{1}{2}\left(1+C_s^2+\frac{I_{th}\cdot S_s}{P_{cr}}-\sqrt{\left(1+C_s^2+\frac{I_{th}\cdot S_s}{P_{cr}}\right)^2-\frac{4\cdot I_{th}\cdot S_s}{P_{cr}}}\right) \tag{3.48}$$

or, when $\frac{P_{in}}{P_{cr}} \ll 1+C_s^2$, and with $S_l = S_s/(1+C_s^2)$ - the focal spot area in linear theory, and $S_{cr} = \frac{P_{cr}}{I_{th}}$ - which we call "critical focal area", this last equation becomes:

$$\frac{P_{in}}{P_{cr}} \approx \left(\frac{\frac{S_l}{S_{cr}}}{1+\frac{S_l}{S_{cr}}}\right) \tag{3.49}$$

At the phenomenological "modification threshold", the inscription occurs in a single point ($\overrightarrow{\mathbf{r}} = 0$, Z_{min}) in a single moment in time: $t = 0$. To find the shape of the modified area the Equation (3.27): $I(\overrightarrow{\mathbf{r}},z,t=0) = I_{th}$ has to be solved. If a more accurate or 3D solution is required, then the numerical integration of the system of Eqs. (3.1), (3.2) has to be carried out. Once the density of electrons $n(\overrightarrow{\mathbf{r}},Z,t \gg \tau_p)$ after the laser pulse is found, one has to prescribe some oscillation energy to each electron within this volume. The energy can be either taken from the experiment, or estimated by E_{osc} through Eq. (3.1). This approach, being an obvious simplification, is nevertheless justified by an important physical observation: there are several different characteristic time scales in fs laser inscription processes. At the first stage, the laser pulse energy is deposited through the multi-photon absorption mechanism, creating an electron plasma cloud with a shape that follows the spatial field intensity

distribution. Next, the created plasma locally transfers a fraction of its energy to the lattice causing irreversible changes in the material. However, the latter process takes place during a much longer time scale as compared with the duration of the ultra-short fs pulse. It is assumed that the shape of the resulting area with a modified refractive index that is formed during the slower second-stage processes should reflect an initial boundary condition in the form of the electron cloud produced by the fast first-stage multiphoton ionisation, and perhaps avalanche ionisation. Therefore the spatial distribution of the generated electron plasma can be used as a first simplified approximation of the shape of the inscribed structures.

The applicability of the analytic results, obtained in Section 3.2.1 has been confirmed by solving numerically the system of light-plasma equations [163], [3]. It was observed that for a pulse peak power $P < 0.6 \sim 0.7 P_{cr}$ the analytic results are in good agreement with the numerical solution. The deviation is due to a violation of the major assumption regarding a self-similar beam shape. In fact, at laser peak powers approaching the critical power for self-focusing the beam shape may change significantly.

3.3 Limits for femtosecond inscription without optical damage

The estimate of the threshold of laser-induced damage can be made on the basis of the density of cold bonds [103], which is about of 100 kJcm^{-3} or 100 nJ·μm^{-3} in more practical units. Then in a typical focal volume of 10~15 μm^3 the damage will most certainly occur if about 1~1.5 μJ is absorbed.

The damage threshold may be estimated from the thermodynamic viewpoint as well. Assuming adiabatic conditions or no heat exchange between this volume and the surrounding medium, and taking the parameters for fused silica glass as the following: heat capacity C_V=0.7 $J/(g \cdot K)$, density ρ=2.2 g/cm^3, and temperature change ΔT=1600 K (a softening point), one can find the energy required for melting of such 15μm^3 volume to be about 36 nJ, with the absorbed fraction of pulse energy of 30~50% this corresponds to 70~100 nJ of laser pulse energy. The second estimate provides a threshold less on one order of magnitude, perhaps due to the fact that we assumed no energy exchange (or its dissipation).

Let us compare these estimates with the energy required to trigger the absorption. When

a NIR fs laser (λ)=800 nm is used and the band-gap (e.g. fused silica) is about E_g =7.6 eV, the 5-photon absorption takes place ($K = 5$), with the threshold intensity to be about $2 \sim 2.5 \cdot 10^{13}$ W/cm^2. Laser pulse energy, which corresponds to that intensity threshold, depends on the duration of the laser pulse. For example, for Gaussian in time pulse-shape ($exp(-t^2/\tau^2)$) peak intensity is reached at $t = 0$. Let us assume a tight focusing into a focal area A with a radius of about the laser wavelength, when pulse duration τ is 100 fs ($\tau_{FWHM} = 60$ fs). Thus the energy required to reach the threshold intensity is $E_{th} \approx \sqrt{\pi}(I_{th} A \tau)$ or 89 nJ. The last estimate stresses the importance of careful energy balance, its distribution and paths of its dissipation, as even the pulse with the threshold intensity could lead to an absorbed energy density sufficient for melting. For longer laser pulses the energy required to reach the intensity threshold is higher, so the energy absorbed in the material will also increase and thus may even cause damage.

This observation has been confirmed in experiments by Guo et al. [164] and Hnatovsky et al. [165], that ≈ 250 fs laser pulses and longer could damage even fused silica - the hardest glass with a wide band-gap. In our experiments we found [21] that the fraction of energy absorbed in the bulk is between 30 and 40 % for the beam with radial symmetry and up to 60 % for an astigmatic beam. These findings have been confirmed by other groups as well [123, 166].

It is worth noting that at higher repetition rate the fraction of energy fs laser energy absorbed can reach 90 % as was reported by Eaton et al. [167]. From this we may conclude that:

- higher repetition rate laser may need even shorter laser pulses *at* focus;

- most tight, aberration-free focusing is required, however this is subject to routes of energy dissipation;

- sample translation speed may need to be increased significantly in the case of direct fs inscription by HRR systems in order to avoid thermo-elastic and hydrodynamic instabilities, which are quite general (RayleighTaylor instability, Rayleigh-Bernard, thermo-capillary or Bernard-Marangoni convection and others);

- laser beam shaping may be the key controlling the absorbed energy density;

- it seems not likely to develop the thermo-elastic model of material modification without detailed knowledge of both material and physical properties involved.

3.4   Energy dissipation equation, numerical modelling, results and interpretation

The NLSE model given by equations 3.1, 3.2 allowed essential simplification in the case of weak absorption - below or near the ionisation threshold. Ignoring all terms related to plasma, and by using the equations to describe the non-linear evolution of the Gaussian beam with the parameters $\langle R^2 \rangle$ defined by Eq. (3.21), the changes in the intensity of the beam during propagation can be obtained by directly integrating the analytic expression obtained in the previous section:

$$\int_0^z I_z(z)dz = I(z) - I(0) = \Delta I(z) = -\int_{-\infty}^z \int_{S_\perp} \beta^{(k)} \left(A(\mathbf{r}_\perp, z)\right)^{2k} d^2\mathbf{r}_\perp dz \qquad (3.50)$$

By substitution A in a similar form to 3.17 and integrating it over transverse area, it is possible to obtain the following relations for transmission T as a function of input laser pulse energy [21]:

$$T(E_{in}) = T_0 \left(1 + (K-1) \cdot \alpha(K) E_{in}^{(K-1)}\right)^{-\frac{1}{K-1}}, \qquad (3.51)$$

$$\alpha(K) = \left(\frac{2}{\pi}\right)^{3 \cdot (K-1)/2} \cdot \frac{\pi \cdot \mu(K) \cdot \beta^{(K)} \cdot n_0}{K^{3/2} \cdot \lambda \cdot \tau_p^{(K-1)} \cdot \omega_0^{2(K-2)}} \qquad (3.52)$$

$$K = \{2, 3, 4, 5, 6\}, \quad \mu(K) = \pi \cdot \{1, 1/2, 3/8, 5/16, 35/128\}, \qquad (3.53)$$

where n_0-refractive index of the medium, λ - laser wavelength, $2\tau_0$ - pulse duration at $1/e^2$ level, K - multiphoton index (number of photons required for multi-photon ionisation), ω_0 - beam waist radius in linear theory. The only unknown parameter, $\beta^{(K)}$ is the multi-photon absorption coefficient, which could be determined experimentally by finding the slope coefficient of the transmittance curve, (proportional to E_{in}^K). The multiphoton cross-sections were not known for a number of materials, including for example doped YAG crystals and some others. To measure absorbed energy we set up the optical scheme, which is plotted in Fig. 3.3 based on a two-channel, single shot, power-meter, which simultaneously records both input and transmitted pulse energies, using two identical photodiode heads. The threshold

a)   b)
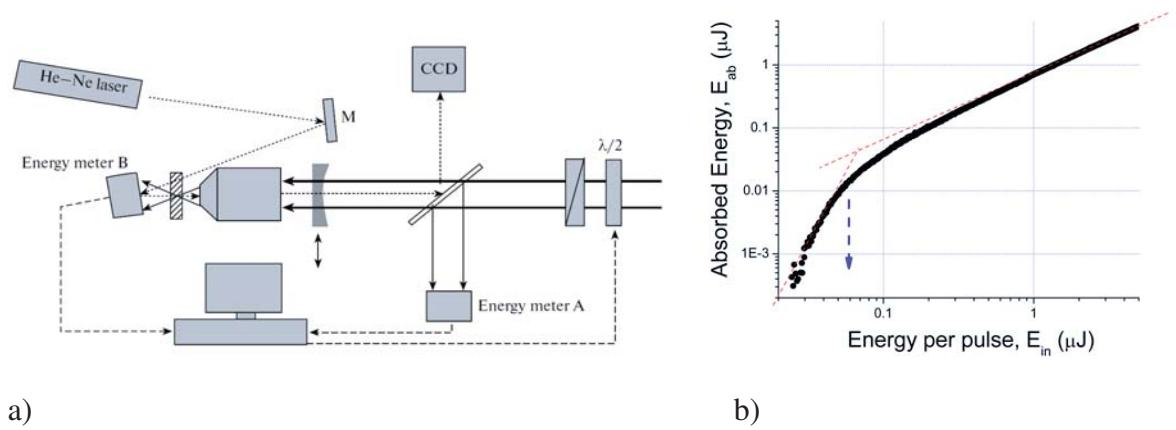
Figure 3.3: Experimental arrangement (a) and absorption for YAG crystal as function of laser pulse energy (b). Arrow indicates the threshold for permanent RI change.

for permanent induced change in RI was determined visually by monitoring the scattered (He-Ne) laser radiation. Only when the modification of the RI occurs, an image on the focal area is observed on the monitor, surrounded by rings, which appear due to interference with residual part of the probe beam. When the rings remained after we blocked the inscription laser, we assumed that the threshold was reached. In fact, it depends on the sensitivity of the CCD-camera used. Using the setup presented in Fig. 3.3 we measured multiphoton coefficients for different materials. The data are summarised in papers [21], [22] and in Table 3.2.

When we compared the experimental results with the results of numerical simulations we found that: i) the slope of the transmittance could not be determined uniquely - for example, in the case of BK7 glass there are three different values of K, which could provide a satisfactory fit with the experimental data. This may indicate the inaccuracy of the model used, or perhaps more complex intra-zone transition absorption dynamics, which are completely ignored in the NLSE model; ii) sometimes the best parameters to fit the experimental result demand values with no physical sense. For example, electron collision time, τ_e may have to be selected very short, less or about 0.1 fs. Such collision times imply energy exchange of the order of a few tens of eV (due to energy-time uncertainty principle); iii) there was strong influence of spherical aberration which resulted in systematic errors in determining the threshold for permanent RI change. This revealed itself as a shift of the absorption/transmittance curve towards the lower energies for shallow depths (right plot in Fig. 3.4). It is not possible to consider such effects in the framework of Equations (3.1,

61

Material	MPA order, K	MPA coefficient, $\beta^{(K)}$	Thresholds			Transmittance at the threshold	
			w/o cyl. lens	with cyl. lens	Intensity,	w/o cyl.	with cyl.
			nJ	nJ	TW/cm^2	lens	lens
YAG	5	3.1×10^{-51} cm^7/W^4	61	610	48	0.64	0.49
YAG:Nd^{3+}			55	580	45	0.66	0.54
YAG:Cr^{2+}			46	1200	40-90		
PbRb$_2$Cl$_5$:Dy^{3+}				9	6.6		
ZnSe:Cr^{2+}	2		10^4		8500		
ZnSe (polycryst.)	2		not reached	not reached		-	-
Fused Silica	5	1.2×10^{-51} cm^7/W^4	44	460	36	0.83	
	6	2.7×10^{-65} cm^8/W^5					
BK7	3	2.7×10^{-24} cm^3/W^2	55	550	44	0.71	0.55
	4	6.9×10^{-38} cm^5/W^3					
	5	1.9×10^{-51} cm^7/W^4					

Table 3.2: Cumulative data for multiphoton absorption coefficients, thresholds for permanent RI change, and transmittance at threshold.

a)   b)
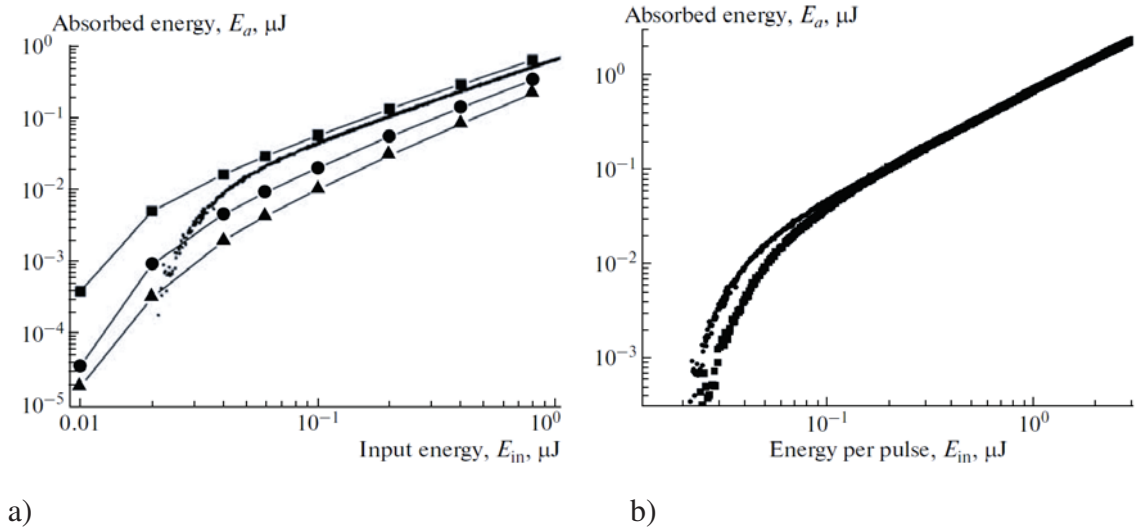
Figure 3.4: Absorbed energy *vs.* input pulse energy for YAG crystal (a). Experiment (small circles) and numerical simulations for MPA coefficient $\beta^{(K)} = 3 \cdot 10^{-51}$ cm^7/W^4, and electron collision time τ_e is: 0.3 fs (squares), 3 fs (large circles), and 10 fs (triangles). b) - absorbed energy dependence for YAG crystal when the focal is spot positioned 100 μm (circles), and 200 μm (squares) beneath the sample surface. In both cases the laser beam was focused by MO objective alone (no cylindrical lens was used).

3.2); iv) a very narrow window for the applicability of the analytic formulae 3.53 demands more than one fitting parameter, otherwise the value of the fitting parameter may become meaningless. Overall, this reduces the accuracy with which β and τ_e are determined, so they may be considered to be known within the order of magnitude.

To conclude this section, we demonstrated that the simplified NLSE model which is described by Equations (3.1, 3.2) can provide a reasonably good description for the laser beam focusing stage, especially in a single shot regime. We found that this model allows significant simplification when laser peak power is below the critical power for self-focusing. Such a model may be useful for simple estimates of the fs inscription thresholds in various materials. The comparison of the observed dependency of the absorption as a function of laser pulse energy revealed significant deviations from the results of numerical simulations, using NLSE model. It is not likely that a complete model of femtosecond modification can be produced at this stage, before fundamental questions have been answered and all relevant processes identified. The only way to proceed might be through direct experiments with inscription, in order to find reproducible regimes for direct fs laser modification as well as to establish margins for this technology.

Chapter 4

Experimental set-up and procedures

This chapter describes the experimental set-up used for direct inscription by Low Repetition Rate (LRR, 1 *kHz*) and High Repetition Rate (HRR, 11 *MHz*) systems in a planar configuration, as well as in optical fibres by using a transverse inscription geometry. A set of diagnostics equipment was used for the output pulse train of these lasers. The diagnostic of the structures created by fs laser (e.g. measuring the refractive index (RI) induced by fs laser) is of great importance, as it can provide the only feedback which allows one to optimize the inscription process. A-posteriori feedback of the results of femtosecond inscription was done by the optical microscope, equipped with precision Z-stage and Quantitative Phase microscopy (QPm) software. The present work leads us to the conclusion, that on-line diagnostics enables significant improvement in optimisation of the inscription regimes. The on-line feedback was also implemented.

4.1 Low repetition rate chirped pulse femtosecond amplifier system

The LRR system used is one of the first commercially available - Spitfire CPA (by *Positive Light* and *Spectra-Physics*), which includes the following modules:

- Tsunami - the femtosecond mode-locked oscillator, pumped by;

- Millenia - the DPSS laser with intra-cavity frequency doubling which provides CW output of 10 W at the wavelength of 532 nm;

- the pulse stretcher, based on 1200 mm^{-1} diffraction grating and also a compressor with identical grating;

- *Evolution*-7.5 separate DPSS, Q-switched, laser to pump the amplifier;

- auxiliary equipment includes: AO mode-locker built into the Tsunami cavity - for external or active mode-locking, synchronisation and delay generator (SDG-1), which synchronizes the moment of Q-switch to pump the amplifier with the only optical clock: the pulse train from the Tsunami. Note that this clock is subject to external conditions. It was the SDG-1 which made the point-by-point method feasible.

The optical layout for the fs oscillator is presented in Fig. 4.1. Tsunami has a traditional 4-prisms design of intra-cavity dispersion compensation, and can produce average power of up to 1.2 W at maximum 10 *W* pump at the wavelength of 532 nm. Typically we pump the Tsunami by $7 \sim 7.5$ W. Then the output from this oscillator is a train of pulses with a 82 MHz repetition rate, which has an average power of up to 700 mW at the pump levels used, or about $8 \sim 9$ nJ per pulse; the pulses are transform limited with a maximum spectral width of about 16 nm (the maximum observed is ≈ 18 *nm*), and the shortest pulse duration of 60 fs (FWHM). In day-by-day operations we typically have pulses of $90 \sim 100$ fs (FWHM), unless shorter ones are required. It is worth noting that there is a possibility of using a pulse train from the oscillator with 3 times stretched cavity and with the RR of 25 MHz for direct fs inscription, as was reported in [119], [128]. As the threshold is about 10 nJ, it would be necessary to minimize the energy losses, and take care on pulse duration. Note that a few auxiliary components would be needed anyway in such a system, after the output window of the oscillator. These are: the optical isolator, which seems to be a "must have" device, as any back reflection can easily destroy the mode-locking of such extended cavity oscillator. Obviously, after an isolator made of crystal with a thickness of ≈ 10 *cm*, one has to add a compressor, in order to compensate the frequency chirp introduced by the isolator and, possibly, precompensate the frequency chirp acquired in MO, and the compressor itself should not introduce any losses. Also, one has to use a telescope in order to match the diameters of the beam at the oscillator output and input pupil of standard MO and thus minimize the losses associated with the objective. For such a low threshold direct femtosecond inscription a high-NA focusing is required. In total this makes the energy close to or even less than
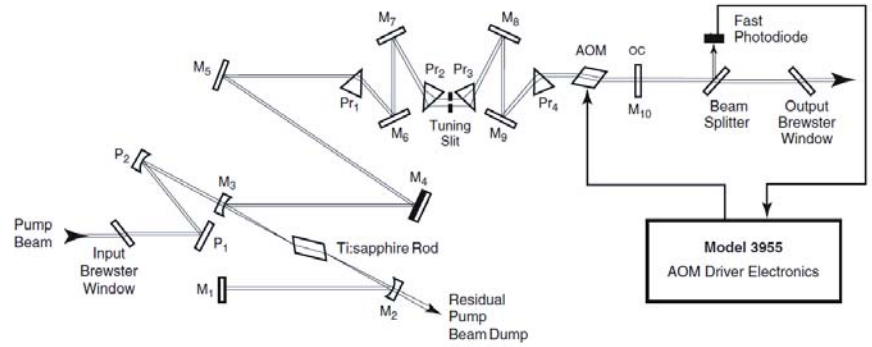
Figure 4.1: Photo (a) (from *Spectra-Physics* web-page), and optical layout (b) of Tsunami oscillator .

that required for waveguide inscription. Additionally, it is not clear what is the best pulse duration for waveguide fabrication by a fs oscillator. All these make WG inscription by an extended cavity fs oscillator challenging.

To address the problem of low pulse energy the only way is to increase the length of the cavity, for example, by using a cavity damping technique [168], [169]. Increasing the length of the laser cavity brings additional problems, such as stability of the pulse train, which can be addressed as was described in the paper by Fernandez et al. [170]. In this paper a stretched-cavity oscillator operated with a net positive dispersion regime in the cavity; this was achieved by BB multilayered chirped mirrors. This regime is opposite to the one used in standard Ti:Sa Kerr-lens mode-locked fs laser, as the pulse generated possesses high spectral chirp. It allows the generation of highly chirped pulses inside the oscillator cavity, and thus makes much better use of the CW pump, as well as giving deeper saturation in the active media. Overall, such a CPO system provides more output power, better pump power utilization and, simultaneously, significantly reduces the possibility of laser damage and other non-linear effects, all due to the fact that the pulse is stretched inside the cavity, so that it has less peak intensity. Moreover, CPO approach paves the way to high repetition rate, high power lasers. Indeed, such systems were quickly scaled up to a 1 μJ level [171], [172], whilst maintaining record short pulse duration, sometimes of the order of 25 fs. Such solid-state lasers have been commercially available since 2009. Subsequently, this approach has been chosen for advanced femtosecond fibre lasers as well as hybrid laser systems.

Only a small percentage of the output power of Tsunami is needed to seed the CPA. Tsunami has transform-limited pulses with a time-bandwidth product of 0.44. As no chirp is present at the oscillator output, first the pulse has to be stretched, which is achieved in the stretcher by four reflections from a diffraction grating in the Littrow configuration (Fig. 4.2). After that, the pulses enter the regenerative amplifier, with the help of the polarisation rotation in-gate, which is based on Pockels cell No1. It operates at 1 kHz repetition rate, while the high-voltage pulse which drives the cell is provided by the synchronisation and delay generator SDG-1. The amplifier has a separate pump, a DPSS Yb:YLF laser with intra-cavity frequency doubling in a temperature controlled LBO crystal - the "Evolution" (Positive Light). This laser is actively Q-switched by the AO-modulator and it operates at the wavelength of 540 nm and is capable of generating pulses with the energy of up to 10 mJ. The Q-switch and Pockels cells are synchronised with the Tsunami pulse train by means of the synchronisation and delay generator SDG-1 (together with AO mode-locking unit, both are by *Spectra Physics*). The SDG-1 has a timing jitter of less than 1 ns. The amplifier runs under deep saturation, so the variations in the moment of pump arrival will not be significant, provided that the output pulse energy of the "Evolution" is stable. Due to these circumstances - stability in time and stability in energy of the output pulse train - it was possible to fabricate fibre Bragg gratings by direct point-by-point inscription [29], [28], and [16].

The optical scheme for CPA is presented in Figure 4.2:
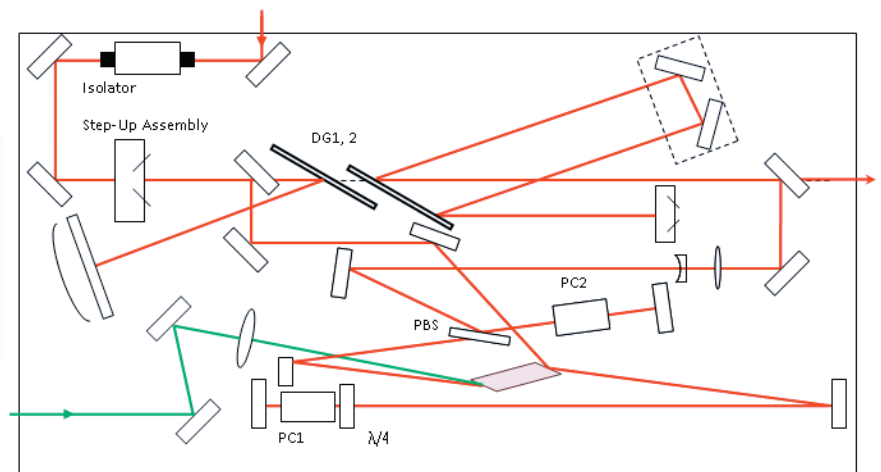
Figure 4.2: Photo (a) (from *Spectra-Physics* web-page), and the optical layout of the Spitfire CPA regenerative amplifier (b).

The quality of the laser beam is controlled by M^2 meter $M^2 - 200S$ (Laser Lines). A well aligned CPA system typically demonstrates M^2 parameters of $1.05 \sim 1.08$ in the vertical and horizontal directions respectively, which is slightly better than the specifications for the system.

4.2 High repetition rate femtosecond laser system

The laser system comprises commercial ultrafast CPO, based on a highly-doped Ti:Sapphire crystal of 3 mm length [170] and broad-band (BB), chirped intracavity mirrors design, which in contrast to LRR case generates a train of pulses at the repetition rate of 10.82 MHz. Typical laser pulse duration is below 50 fs (FWHM) when the saturated Bragg reflector (SBR) is used and can be reduced to approximately 26 fs if the laser operates without the SBR. In the case of 50 fs pulse duration the spectral width is about 30 nm, and the spectrum is centered at 796 nm. The laser has compact design (a single box solution) due to the Heriott cell used (the cell consists of two concave spherical mirrors with two auxiliary flat mirrors to steer the laser beam in and out of the cell). This cell is designed and built in such a way that the beam-waist dimensions remain unchanged. To a certain extent all 16 reflections on both spherical mirrors can be represented as a laser beam passage through the periodical lens waveguide - a chain of positive lenses, which compensate for the divergency of the beam. The state-of-the-art CPO system described in [170] was used in our work [173]. It had two times shorter pulse duration with approximately two times higher energy per pulse, due to the absence of spectral limiting and reflection losses imposed by SBR, when replaced by a BB mirror. Note that it is much more difficult to start and operate a laser of such a type without the SBR, due to the fact that both cavity length and its dispersion have to be changed continuously without destroying the mode-lock operation, as mode-lock regime can be more easily achieved with net negative dispersion in the cavity. Then a slow change by shifting the end mirror in a short arm of the cavity (see Fig. 4.3) with a precision screw may change the regime of operation without destroying the mode-locking. To do this, the cavity had to be aligned in such a way as to preserve the mode-locking which occurred during this shift. Another complexity brought by the SBR-less CPO system was its very high sensitivity to a back-scattering of the laser radiation from any (AR- or un-coated) surface of optical

components or even a sample, sometimes positioned a few meters away. This sensitivity, which is undesirable, can be eliminated by introducing an optical isolator in front of the prism compressor (Fig. 4.3), however this requires the re-design of the compressor and a re-configuring of its optical layout. More advanced pulse compressor design, which is based on a combination of chirped mirrors and a small-scale prism compressor allows this modification to be done more easily. Note that advanced design is also preferable due to a higher third order dispersion left uncompensated by standard, large scale, prism compressors.

In the case of the commercial CPO system (Scientific-XL) we managed to fit the Faraday optical isolator (LINOS) into the current design, after the laser cavity but in front of the compressor. The measured pulse duration remained almost unchanged at about $50fs$. As the pulses are chirped at the isolator input, there was no danger of damaging the material of the isolator (10 cm long TGG crystal). Non-linear effects such as self-phase modulation were not observed either. However, due to the compact design of the laser itself this approach cannot be used in a system without the SBR, as due to much shorter laser pulse duration and thus stronger dispersion a longer optical path would be necessary in a modified prism compressor. There is no space left for this inside a standard laser case, so in practice the SBR-less option would be less stable.

Remarkable recent progress in the field of fs all-fibre lasers has created an explosively growing market in high-energy CPOs. This makes them one of the best candidates for direct fs inscription, as well as making the method of direct fs fabrication very competitive. Currently, bulk CPO systems, commercially available since 2009 (e.g by Femtolasers), are capable of delivering more than 1 μJ per pulse in a multi-MHz regime with a pulse duration of or below 50 fs. At the same time there are reports on fibre-based oscillators combined with a large-mode-area fibre amplifiers, which can now deliver more than 220 nJ, at a pulse duration of 50 fs and with the repetition rate of up to 80 MHz [174], while the record average power of such fs "fibre" lasers approaches kW level at MHz repetition rate [175].

The optical layout of our CPO system is presented in Figure 4.3. The output chirped pulse is compressed down to 50 fs in a prism compressor outside the laser cavity. In front of the telescope and prism compressor we inserted the AO-modulator. This is the most suitable place in the laser cavity, since the longest pulse duration and the smallest beam diameter are here. Next Fig. 4.4 shows spectrum and FROG trace of the CPO in a femtosecond mode.
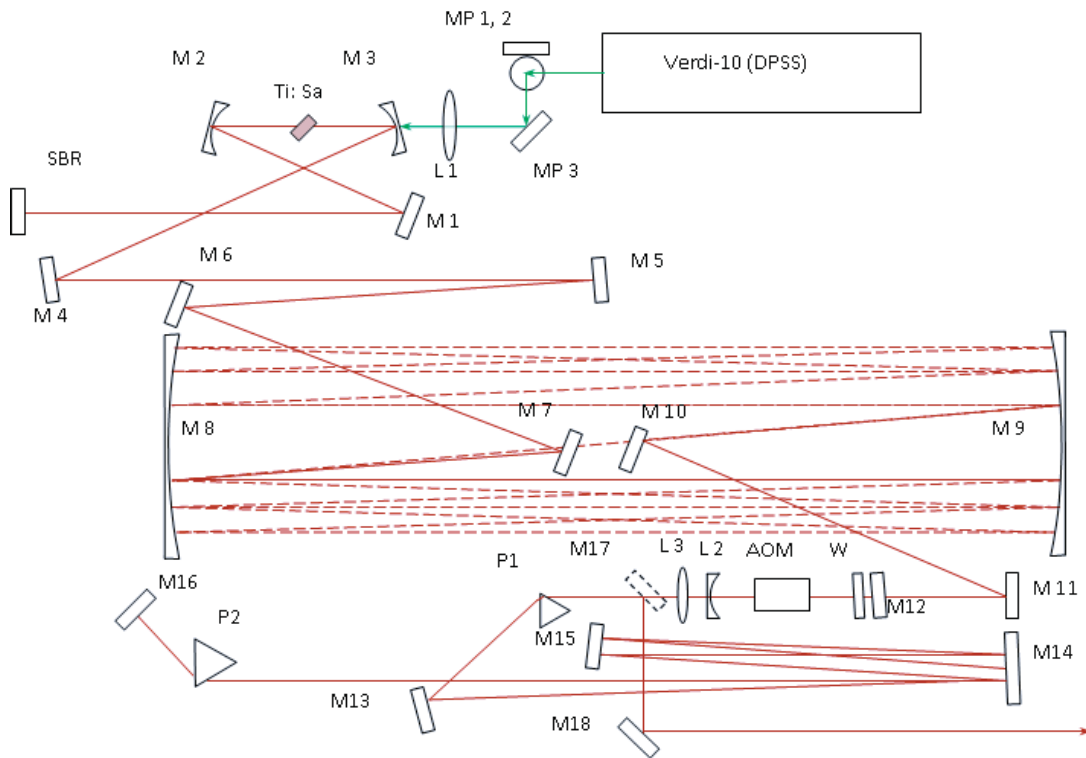
Figure 4.3: Scientific-XL optical layout. The specifications for this chirp-pulse oscillator are the following: pulse duration - less than 50 fs; spectral width about 30 nm; the spectrum is centered at 796 nm; output average power - 1100 mW; pulse repetition rate - 11 MHz; output beam diameter - 5 mm (M^2 parameter is less than 1.1). Note that similar version of the system, without semiconductor Saturable Bragg Absorber can deliver 26 fs pulses with 240 nJ per pulse, all at the same repetition rate of 11 MHz. The spectrum of such system is shown on Fig. 5.9.
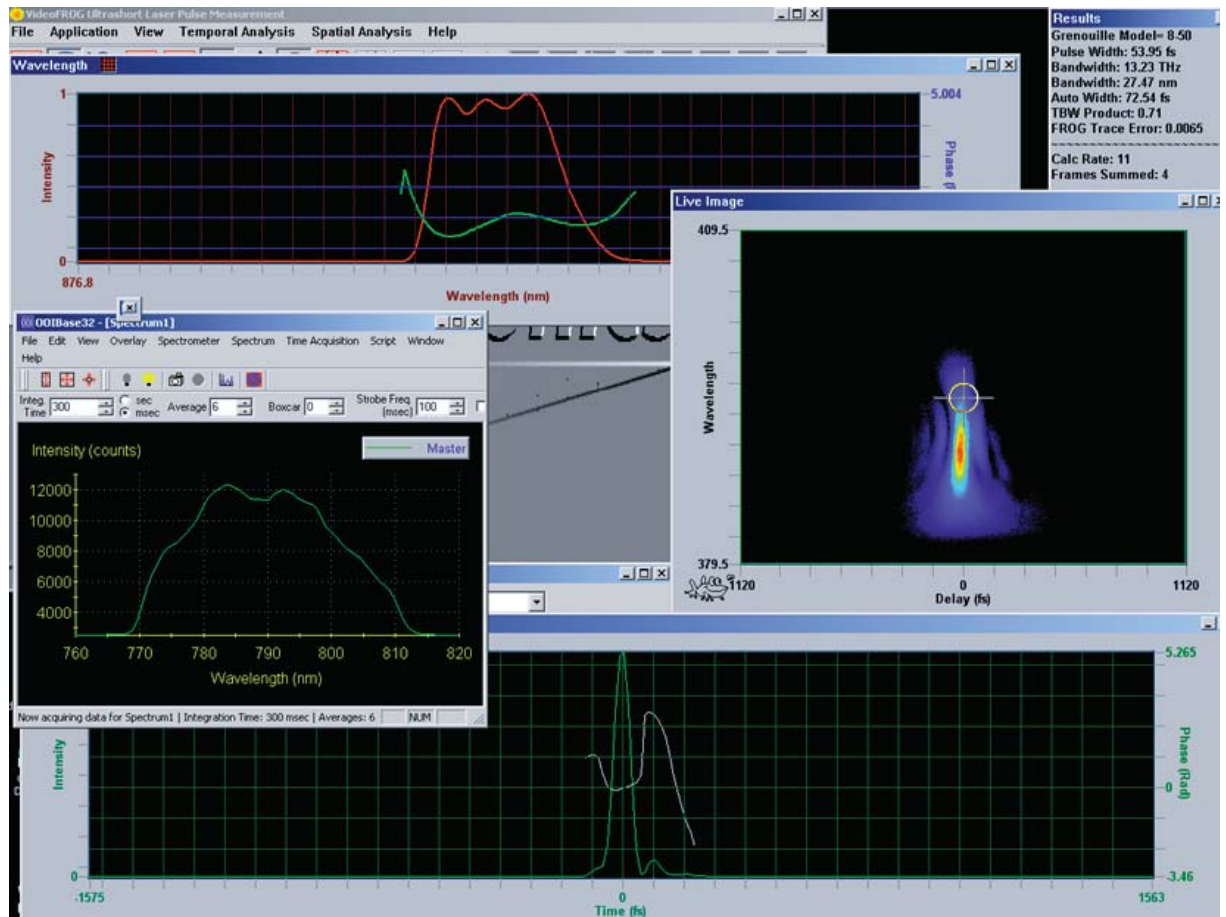
Figure 4.4: The snapshot window with Scientific-XL laser diagnostic information.

4.3 Experimental setup for planar inscription using 1 kHz system

The experimental setup for direct femtosecond fabrication of planar light-guiding structures is presented in Figure 4.5. The microscopic objective is installed on a separate 3D mechanical stage, which can be adjusted with micrometer precision. The setup includes: (1) electronic shutter (Uniblitz), a zero-order half wave-plate (2) and a thin-film polarising beam-splitter (3) - these are for coarse attenuation of the laser pulse energy. The usage of the thin-film polariser allows the avoidance of damage, inevitable at the peak powers of $10\ GW/cm^2$ or when pulse energy approaches the mJ level. If a Glan laser prism is used instead, it becomes damaged at a few hundred μJ. After the laser pulses were first coarsely
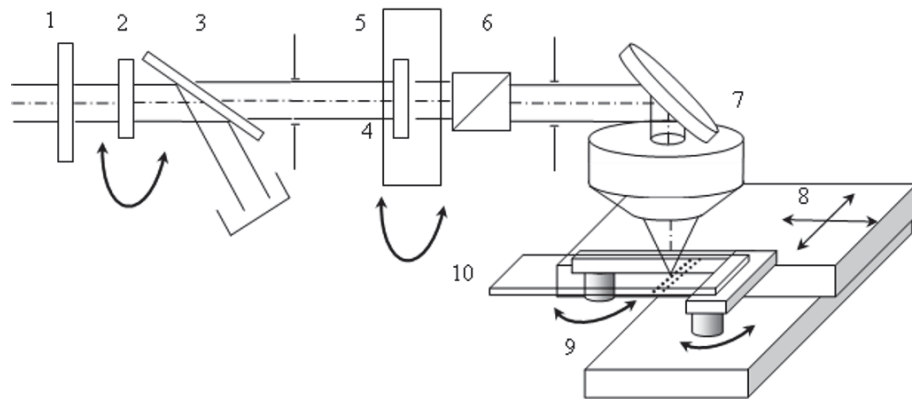
Figure 4.5: Experimental setup for direct femtosecond inscription using LRR CPA laser system.

attenuated (Fig. 4.5), fine adjustment was done by a second half-waveplate installed on a precision rotator under computer control and a polariser - in our case, the Glan prism polariser (6). In general, in view of the dispersion introduced by the Glan prism with the dimensions of $10 \sim 20$ mm, it would be better to operate using two thin-film-polarisers, so that transmittance through the glass will be completely avoided. This approach is used in our HRR inscription setup. Although this configuration is more difficult for alignment, after two reflections the beam can retain its direction and has a well-defined polarisation state because of two polarisation-selective reflections.

For inscription in planar sample (10), it is positioned horizontally by modified optical mount (9) to exploit the advantages of the 2D patterning in a transverse inscription geometry

with 2D (X,Y) air bearing translation stage. An auxiliary He-Ne laser (not shown in the Figure) is used for sample alignment in the horizontal plane by monitoring the reflection from the top and/or bottom surfaces of a sample during translation. A similar setup to the one in Fig. 4.5 is used for fabrication of Bragg gratings in fibres by the point-by-point method [28]. For this, two mechanical 3D stages with two rotational clamps on top are used. Initially no immersion liquids were used, and acrylic coatings were removed prior to the bare fibre alignment. The setup allows independent alignment of the fibre on both ends. The fibre was stretched a little when loaded into rotational clamps in order to make it straight. In both of our setups the state of polarisation of the attenuated beam can be changed by an additional half-wave plate (not shown in Fig. 4.5). Steering mirrors with high-reflectivity and minimal Group Delay Dispersion (GDD) are used. The compressors in both laser systems can be tuned in order to induce proper pre-chirp into the pulse. Such pre-chirp can be used to compensate for temporal elongation of the pulse after passage through a microobjective made of glass. For example, in the 1 kHz CPA setup, a laser pulse with 106 fs (FWHM) pulse duration was pre-chirped so it becomes 140 fs in duration. In this case the inscription threshold can be minimal after passage through the $100\times$ Apo-SL microobjective (Mitutoyo). Thus elongation of the pulse in the Mitutoyo objective is about 30% for a 105 fs pulse. Optimal pre-chirp was found experimentally for all microobjectives used by monitoring the continuum generated, when the laser beam is focused inside the bulk of the sample. This was possible since at the threshold the continuum appears before permanent modification occurs.

Two CCD cameras were used to monitor the alignment in the case of inscription in fibre samples. For inscription in planar samples an additional beam-splitter and a CCD camera were added. Some tension can be introduced by micrometer screws operating in the direction of the fibre axes, which may allow fine tuning of the period of FBG. There were no other controls than this over the tension. In fact, in our first design of the PbP inscription setup the fibre must have had a more complex shape than the chain line, due to obvious uncertainty in the fibre clamp alignment on both ends. This and other issues were addressed in our second version of the PbP inscription setup.

In order to perform the experiments on UV-fs inscription we built the optical setup for harmonics generation; this is based on two BBO crystals cut for optimal phase-matching condition. Both crystals were cut for collinear (o-o-e) sum-frequency generation: the first, for

frequency doubling ($800 + 800 \Rightarrow 400$ nm), and the second crystal for slightly non-collinear sum-frequency generation ($800 + 400 \Rightarrow 267$ nm). More details on this are given below, in Section 6.2.

4.4 Setup for inscription by high repetition rate femtosecond chirped pulse oscillator

The setup for HRR femtosecond inscription is shown in Figure 4.6. It includes the air-bearing, 2D-stage ABL10050, while the translation along the third (Z) axis is accomplished by the independent mechanical, roll-bearing stage of ABS-100 type (all by Aerotech). This is to be carefully positioned along the vertical direction of the laser beam by use of the tip-tilt platform (Ekspla, Lithuania), capable of carrying a heavy load. All the computer-controlled stages are synchronized through the NPAQ controller (Aerotech), which is capable of handling up to 6 different stages.

We use a transverse inscription geometry whereby a femtosecond laser pulse train is delivered and focused in Z-direction, perpendicular to the sample translation (X,Y) plane. The sample is mounted by a modified mirror mount with precision screws.

The microscope objective is fixed to Z-stage by a micro-objective holder, which has 6 degrees of freedom for alignment (*Thorlabs*). The system incorporates an electronic shutter (Uniblitz), which is computer controlled through the digital output port of the NPAQ controller.

The CPO oscillator provides moderate output pulse energies, thus the design of the attenuation and beam delivery systems has to be done with broadband, highly reflective, polarisation insensitive, dielectric mirrors, with low group-velocity dispersion (GVD) (20 fs^2) and high reflection coefficient of 99.9% (*Layertech*).

By optimizing the alignment of the laser cavity and the expanding telescope in front of the compressor a beam with either circular Gaussian or slightly elliptical profiles can be obtained. The beam diameter at the input of the MO matches its input pupil diameter. The ellipticity of the beam can be adjusted between 1 (almost circular) and about 0.9 (with the elongation always in the horizontal direction), as presented in Figure 4.7. To focus the ultrashort pulse with a spectral width of about 30 nm without adding an extra chirp due to
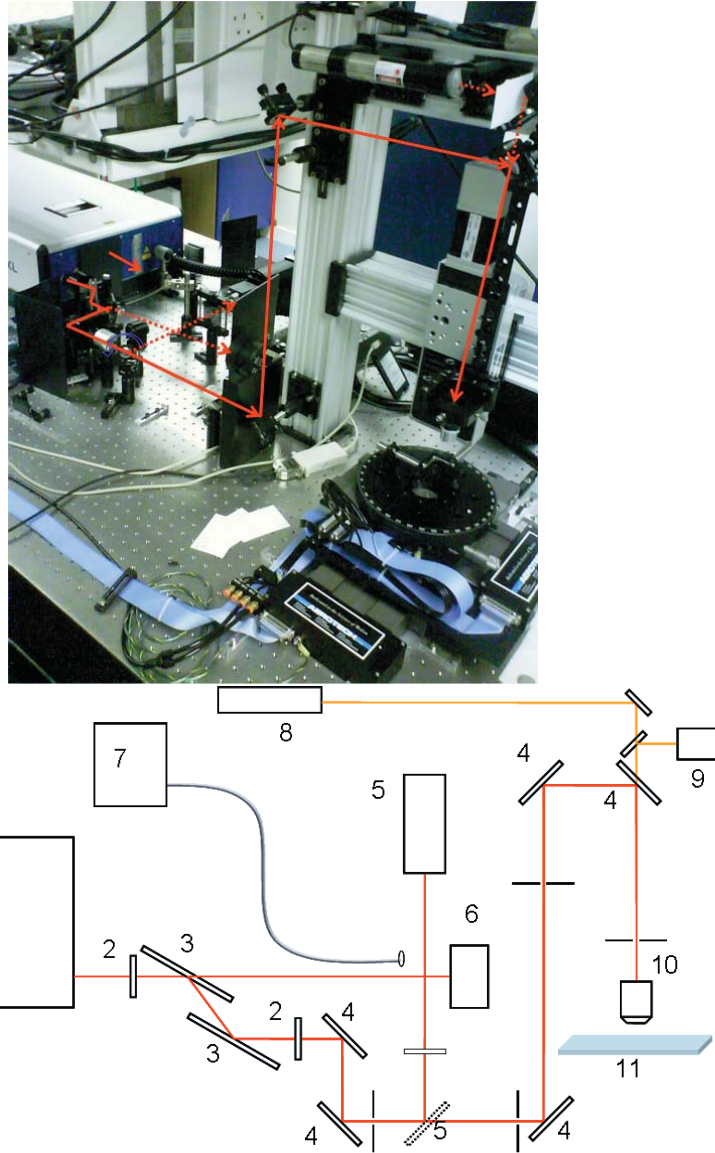
Figure 4.6: Photo (top) of the experimental set-up for HRR inscription, and its optical layout (bottom). The output of the laser (1) after the first half-wave plate (2) is attenuated by two Brewster angle polarisers (3), then its polarisation can be changed by a second waveplate. Steering mirrors (4) deliver the laser beam through the MO (10) to the sample (11) installed on 2D air-bearing stage. Diagnostic equipment includes: beam profiler (6), FROG (5) and fibre coupled speedometer (7). Auxiliary He-Ne laser (8) and CCD camera (9) are used for alignment.
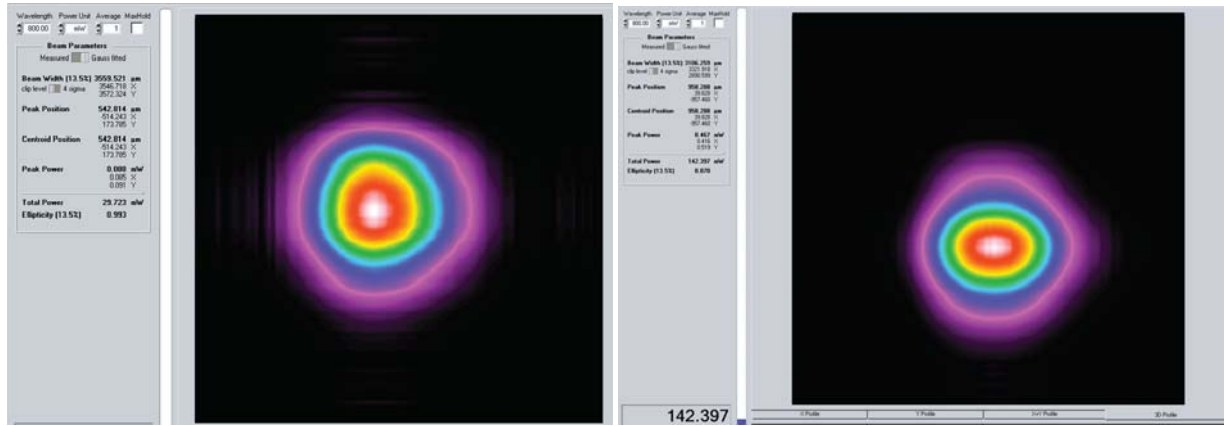
a)   b)

Figure 4.7: Beam-profiles at the microobjective. Almost circular (a) and slightly elliptical (b) profiles; the second one has been used for the inscription of smooth waveguides.

the glass dispersion, the reflecting microobjective would be preferable, however it cannot be used due to high obscuration as well as the fact that the quality of classic objectives made of glass is typically much better. Thus there is an unavoidable trade-off between the dispersion introduced by MO and low-losses if a sharp focusing optics have to be used. Note that the dispersion may be partially pre-compensated by the compressor adjustment.

A few micro-objectives were tested for inscription by the HRR CPO fs laser system. The best results (among Nikon micro-objectives) were found with the classic CFI $60\times$, $NA = 0.8$ micro-objective (Nikon), which has working distance of just 0.3 *mm*. Newer designs of such objectives include a correction ring to compensate spherical aberration up to a depth of 450 μm, the last figure depends on the glass used.

We also tested the Plan Neofluar objectives (by *Zeiss*) with the magnifications from $40\times$ to $63\times$, and $NA =0.6$ and $NA =0.85$ respectively. These objectives are corrected not only for spherical aberration but also for the distortion and other aberrations. However they have higher losses than CFI objective, as well as other objectives by Leica - with magnifications from $50\times$ to $100\times$, and $NA = 0.55$ to $NA = 1.3$ (in oil).

Finally, the optimised design of the inscription set-up and choice of the micro-objective allowed overall losses, including beam delivery, attenuation and focusing, of less than $25 \sim 30\%$. The maximum laser pulse energy on target can be as high as $70 \sim 80$ nJ. It turned out that the maximum energy was required only for inscription in the hardest materials, such as $Nd^{3+} : YAG$ crystals with a slightly astigmatic beam.

In a majority of transparent dielectrics, in visible range, the refractive index drops gradually with increasing wavelength [143–145]. This effect is a manifestation of the presence of strong absorption bands at shorter wavelengths. In the case of ultrashort pulse propagation in such media this leads to a number of effects due to the dependence of the both phase- and group- velocities on wavelength [176], [143]. These effects are:

- CW chromatic aberration of the glass used in MO may be considered as a dispersion of phase velocity $c/n(\lambda)$. It results in a shift of focus of the lens, unless the lens or MO is designed to be achromatic (achromatisation means the independence of the focal position for at least two different wavelengths) or apochromatic (when achromatisation is done minimum at a minimum of three different wavelengths).

- Dispersion of group velocity $v_g = c/(n(\lambda) - \lambda \cdot dn/d\lambda)$, which is a velocity of energy propagation for the ultrashort pulse. The group delay always takes place even in some achromats, unless special rules were implemented [176] at the stage of MO design. In most glass-made micro-objectives there is a dependence of the group delay vs the radial position of the ray [177].

The chromatic dispersion introduced by different (compound) lenses inside the MO can be compensated to a certain extent by an appropriate pre-chirp introduced in the compressor. This was adjusted by visual monitoring of the brightness of the inside of a glass sample at or below the inscription threshold. In this experiment we noticed that the super-continuum threshold does depend on the depth of focusing inside the glass. So initially the range of depths for "minimum threshold" was determined. Minimum threshold was found at about 50 μm for the case of CFI MO, mentioned above (magnification $60\times$, aperture $NA = 0.8$), however this MO was designed to compensate spherical aberration at a focusing depth of 170 μm. To a certain extent, an arbitrarily chosen microobjective can be used in this way, however with a limited flexibility as to the inscription depth.

Thorough investigation and optimisation of the focusing conditions could reduce the inscription threshold and perhaps provide a more circular shape of the modified area [143, 176–179]. During such optimisation it is necessary to consider all parameters, such as design of a particular MO (aberrations), and also to include the pulse duration into the optimization. It is not clear how the complex interplay between chromatic and group-delay dispersions, aberrations, spectral chirp, and other wavefront distortions may affect the final density and

distribution of the deposited energy around the focal area, in particular when the non-linear effects in lens material would affect the wavefront of the beam inside the MO.

Systematic numerical studies of fs pulse dynamics in the MO glass plus sample material have not been done even for the axially symmetric case, as the wavefront distortions due to Kerr nonlinearity are more difficult to explore and correct. They affect the refractive index of glass, especially where the beam diameter shrinks to a fraction of *mm* - as, for example, in the output lens of almost all high-NA microscopic objectives. Even for objectives where the beam remains quite big in diameter (such as the ones by Mitutoyo), characteristic filamentation or damage patterns (or damage in the form of filamentation) occur, which are typical for the case of self-focusing. For example, in the Mitutoyo Apo-SL 100× MO the effect of filamentation with subsequent damage took place at a laser pulse energy of about 20 μJ.

Although the choice of focusing optics is most critical for direct fs inscription, the design information and detailed specifications for most of MO are typically not available, so the most reliable method is direct observation of the results of focusing, for example, by monitoring radiation from plasma created at focus. This approach has been chosen in our work and has also been used by others [118]. This monitoring of intermediate results is still far from the final goal of direct fs inscription. Only the measurement of the residual RI or complex permittivity dynamics with both temporal and spatial resolution [11], [10] would completely resolve all these issues and provide unambiguous feedback. In order to do this the first step would be to find proper on-line monitoring technique. Then one has to arrange closed-loop feedback in order to maximise the resultant RI contrast, possibly by using an adaptive-shape mirror as a wavefront corrector, as well as other adjustments.

In practice, the alignment of the objective in HRR set-up starts with the adjustment of the MO. There are several degrees of freedom to consider. First, the MO has to be installed perpendicular to the incident beam. This is done by monitoring the back reflection on a remote diaphragm, and by using the tilt adjustments of the 6-axis MO holder. The same beam-profiler was used before for Z-stage alignment in order to make the translation along the Z-axis collinear to the laser beam. To do this the beam profiler was installed on the Z-stage. The deviation of the beam center of the laser beam was kept below 30 μm over 100 mm - the whole travel range of the Z-stage. Then the MO centering was accomplished by monitoring the beam diameter below the MO again by the beam profiler, when the MO

was translated up and down by Z-stage. The MO installed was adjusted by translating in two perpendicular directions. The position of the beam without the MO served as a reference. Finally, when the MO is properly aligned the beam spreads and collapses symmetrically with Z-shifts, while it remain centred.

There are no commercial products available, which take into account the non-linear effects, apart from an adaptive mirror combined with Hartman wavefront sensor. The only universal method introduced so far seems to be the adaptive optics/mirrors, when coupled with the feedback of supercontinuum generation. Otherwise the MO of special design, following the recommendations of paper [177], is available, but this option seems to be very expensive. These are being built using the general requirements for such design for linear focusing [143].

4.5 Auxiliary laser diagnostics equipment

In order to monitor and keep the parameters of the fs lasers within the specs on a daily basis the following auxiliary diagnostics equipment was used:

- beam profiler BP109-IR (*Thorlabs*),

- spectrometer QE65000 (*Ocean Optics*),

- single-shot autocorrelator/FROG (Model 8-50 Grenuville, *Swamp Optics*),

- power meter FieldMaxII-TO (*Coherent*) equipped with a PM3 (1mW - 3W) thermal head,

- pulse-energy meter USBI or LaserStar, equipped with one or two PD10 pyroelectric heads respectively (all by *Ophire*),

- single-shot intensity autocorrelator AFS-20 (by *Avesta*) which is capable of measuring pulse duration in the range 20-200 fs,

- $M^2 - 200S$ meter (by *Laser Lines*),

- IR-viewer and IR visualisation cards.

Unlike the LRR inscription system, the balance of intra-cavity dispersion is critical for optimal laser operation, thus a single-shot FROG (Grenuville, *Swamp Optics*) was used for periodic checks of the pulse duration and during the alignments. For the LRR system a single-shot autocorrelator AFS-20 (by *Avesta*) was routinely used. The advantage of the AFS-20 model is that it is truly a single-shot version. It could measure a pulse duration with the speed limited by the CCD readout time. Such speed was required, for example, during the alignment and optimisation of the Tsunami oscillator and the intra-cavity AOm, installed before the compressor in Spitfire CPA.

The beam profiler BP109-IR belongs to the class of slit-scanning devices. A single photodiode with good linearity and dynamic range is used as a detector. This type of beam profiler has a disadvantage in that its readings depend on the size and the orientation of the laser beam, and so it requires extra care, e.g. additional measurements when the profiler is rotated by 90 degrees. It was very useful to monitor and exclude any beam clipping at the edges of the optical components.

The M^2-meter was used during all major realignments on both systems, again when AO-modulators were introduced, and during the laser cavity realignment.

Auxiliary equipment used in this work for sample preparation and waveguide characterisation includes:

- dicing, grinding and polishing equipment, including disk and wire saw Model-15, and polishing machine LP-50 (both by *Logitech*);

- vacuum deposition equipment and thermal evaporator (*Kurt Lesker*);

- optical microscope laboratory, which includes *Zeiss* Axio MOT-2M bright-field and differential interference contrast (DIC) microscope, equipped with the QPm software, which is described below in Section 4.6;

- A diagnostics laboratory for waveguide characterisation and loss measurement has been built. It has a few precision, multi-axis, translation stages to manipulate the sample and to couple light in/out of the waveguides, as well as various light sources and cameras, including visible and IR InGaAs cameras (this is described in detail below, in Section 4.7.

4.6 Refractive index visualization and measurements

The induced variations of the refractive index (RI) due to fs laser irradiation is the most important or target parameter for any inscription. Microscope-based techniques are required for measurements of the spatial dimensions of the modified area and the magnitude of the refractive index changes. We commissioned the Axioscope-2 MOT (*Zeiss*), a bright-field and differential interference contrast (DIC) optical microscope. It can resolve the index variation of less than 10^{-4} in a sub-cubic-micrometer volume. In other words, its sensitivity to phase excursion is better than 10^{-3} rad, or 0.1 nm, in terms of the optical path difference (OPD).

The microscope is equipped with a set of Plan-Neofluar and Achroplan micro-objectives with magnifications and numerical apertures ranged from $5\times$, $NA = 0.1$ and up to $100\times$ $NA = 1.4$ (in oil). It includes a high-NA condenser with variable aperture up to 1.4 (when immersion is used). It also has a polariser and an analyser, as well as a set of Wollaston prisms for the DIC (or Nomarsky) technique. These prisms are designed and manufactured to match the micro-objectives used. Each of them introduces a spatial separation between the two orthogonally polarised beams, with spatial separation a few times less than the resolution of the corresponding objective, which is close to the diffraction limit. It was this fact which allowed us to detect 250 nm-periodic perturbations in the bulk of fused silica [36] by DIC technique, as described in Chapter 6. A high-resolution CCD camera with 10 Mega-pixels, and 16-bit dynamic range in gray or 12-bit per colour is interfaced with the desktop computer by a fibre-optic link in order to allow minimal electric noise. The Axioscope-2 MOT has computer controlled, precision Z-stage, with an accuracy of about 50nm, so it enables the acquisition of Z-stacked images. Such resolution makes feasible the method of Quantitative Phase microscopy (QPm) by *IATIA*. Commercially available QPm software is capable of measuring the phase retardation by a thin non-absorbing phase object. The method is based on a solution of the transport-of-intensity (TIE) equation [180, 181]. Experimentally, it requires a sequence of intensity distributions, measured with small offsets of the MO or the object between this. When the shift is within the depth of focus of the MO, and the paraxial approximation is valid, the TIE equation reads:

$$\frac{\partial I(r_\perp, z)}{\partial z} = -\frac{\lambda}{2\pi} \cdot \nabla_\perp \left[I(r_\perp, z) \cdot \nabla_\perp \phi(r_\perp) \right]. \tag{4.1}$$

Resolving the Eq. (4.1), one can obtain the phase retardation, acquired by the beam after

passing the sample, over the whole field of view of the microscope [182], [183]. Here the $\perp$-subscript indicates vectors and operators which are acting in the plane, perpendicular to the optical axis (Z), ϕ denotes the phase, I stands for the intensity distribution on camera, when the MO is focused at position z, λ is a "central" wavelength of the spectrum of light source. The phase can be determined completely by the algorithm described, for example in [184], where it was shown that there is no phase unwrapping problem. The algorithm implemented in the QPm software package, is essentially based on a calculation of Fourier transforms (denoted by bold letters $\widehat{\mathbf{F}}$ and $\widehat{\mathbf{F}}^{-1}$ for forward and inverse operators respectively)

$$\overrightarrow{\nabla}_{\perp}(\phi(r_{\perp})) = \frac{\partial\phi(x)}{\partial x} = -\frac{i \cdot k}{I(r_{\perp})}\left(\widehat{\mathbf{F}}^{-1}\left[\frac{k_x}{k_{\perp}^2}\widehat{\mathbf{F}}\left[\frac{\partial I}{\partial z}\right]\right] \cdot \overrightarrow{\mathbf{e}}_x + \widehat{\mathbf{F}}^{-1}\left[\frac{k_y}{k_{\perp}^2}\widehat{\mathbf{F}}\left[\frac{\partial I}{\partial z}\right]\right] \cdot \overrightarrow{\mathbf{e}}_y\right)$$

(4.2)

so that the solution of equation 4.2 is generated by the QPm. The output data of the QPm we will refer to below as a 2D phase retardation map. This incorporates all the information about the sample. A number of digital pseudo-microscopic images can be generated numerically based on the phase retardation map. These are Zernike phase-contrast, Nomarsky (DIC), Hoffman modulation contrast and others. Note that these numerically generated microscopic images can reveal some peculiarities, which are difficult, if not impossible, to observe with the naked eye either under the microscope or by CCD camera. It is also worth noting that we have found some drawbacks with our system and in our version of the software, the majority of them was found experimentally. The QPm software should preferably be integrated with the image acquisition process in order to allow image averaging and thus noise reduction. If not, there is a need to use some digital image filtering, which may diminish the accuracy of the phase measurements. In addition, there is almost no control over the input data; for example, at short acquisition times there are significant variations in the average intensity of the images among the same Z-stack. Another difficult problem, which could be addressed in future versions, is related to an uncertainty in the "true-focus" position for distributed structures without sharp edges. The parabolic dependence of the measured phase *vs* focus offset was demonstrated in [185]. This may allow one of the major problem of QPm to be resolved uniquely, rather than relying on operator's experience. Otherwise visual detection of the "in-focus" position is not trivial in the case of thick objects, and if not done properly the QPm software can underestimate the phase retardation. This issue may be resolved by computing the phase retardation for each of the multiple planes of the Z-stack, assuming it

is a "true in-focus" one. Then a simple fitting by parabola provides a unique answer. Other problems of QPm-software may appear when:

- high-magnification MO is used, so the object under investigation could not be considered as optically thin;

- the illumination condensor is not positioned correctly, so a sample is illuminated by a convergent or divergent wavefront. Similarly, when one attempts to measure the modification in the fibre core without immersing the fibre in the index-matching oil;

- there are some aberrations, with a typical example of misuse being an attempt to measure the object with oil-immersion MO without using the oil;

- attempts are made to measure under-resolved objects;

- the material is birefringent, so polarisation effects are involved.

- the material is absorbing, thus assumptions of the QPm method are violated.

In order to be sure, one has to cross-calibrate the method by measuring reference or test objects, which have both similar dimensions and RI contrasts. For the calibration we chose a standard optical fibre, as presented on the following Figure 4.8, where the insert describes the geometry and defines some of the parameters used. The $SMF - 28$ fibre is immersed in the oil between two planes, which are formed by a microscope slide and thin cover slip. In accordance to the specifications by *Corning*, this fibre has a core diameter of 8.2 μm and a refractive index contrast of 0.37% or $5.3 \cdot 10^{-3}$ and thus a maximum optical path difference (OPD) of $\Delta n \cdot d = 42.64$ nm in the center. This corresponds to the maximum accumulated phase of 0.7 rad (in the center of the core) at a wavelength of $387nm$. The QPm measures phase retardation $\phi(r)$ in a few dozen points across the fibre core - see Figure 4.8, which sometimes creates problems for calculations. For example, if a differentiation of the accumulated phase is to be done, it may suffer from poor resolution and possibly noise. After the accumulated phase is found, we use the Abel inversion to determine the profile of the refractive index, as described in [186]. There are many numerical techniques for calculating the Abel integral (which is an ill-posed problem with the integrand diverging at integration limit); in all of them it is assumed that i) no absorption takes place, ii) the object
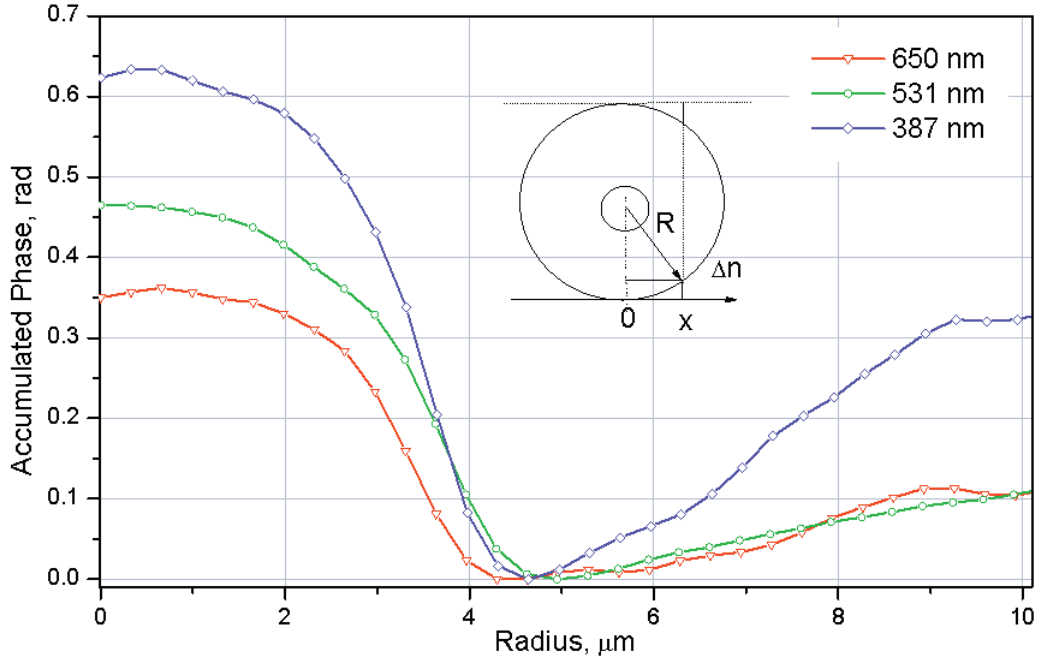
Figure 4.8: The measured accumulated phase (cross-section) for standard optical fibre SMF-28.

has axial symmetry, and iii) the phase excursion is small. If so, the radial distribution of the RI can be found as follows:

$$\triangle n(r,\, y) \;=\; -\frac{\lambda}{2\pi^2} \int_r^R \frac{\partial \phi(x,\, y)}{\partial x} \frac{1}{\sqrt{R^2 - x^2}} dx \tag{4.3}$$

Note that it would be natural to incorporate the Abel inversion into the QPm software package, as an intermediate result of phase reconstruction - $\partial\phi/\partial x$, Eq. (4.2), can be used in the Equation (4.3). In order to develop the most stable procedures for Abel inversion we have developed a MathCad program, based on a Fourier series expansion, which we describe below. First of all we interpolated the phase obtained by QPm package, using cubic splines and generating up to a few hundred points. The comparison of raw QPm data and the results of interpolation was found to be good. After that we calculated the coefficient of the Fourier expansion, which may now include up to a few hundred coefficients of expansion,

$$\phi(x,y) \;=\; a_0(y) + \sum_{m=1}^{M} a_m(y) \cdot cos\left(\frac{\pi \cdot x \cdot m}{R}\right) \tag{4.4}$$

here $M \gg 1$ is a reasonably big number, R stands for the cladding radius of the fibre (or maximum of all dimensions of the structure). The differentiation of ϕ from Eq. (4.4) is then
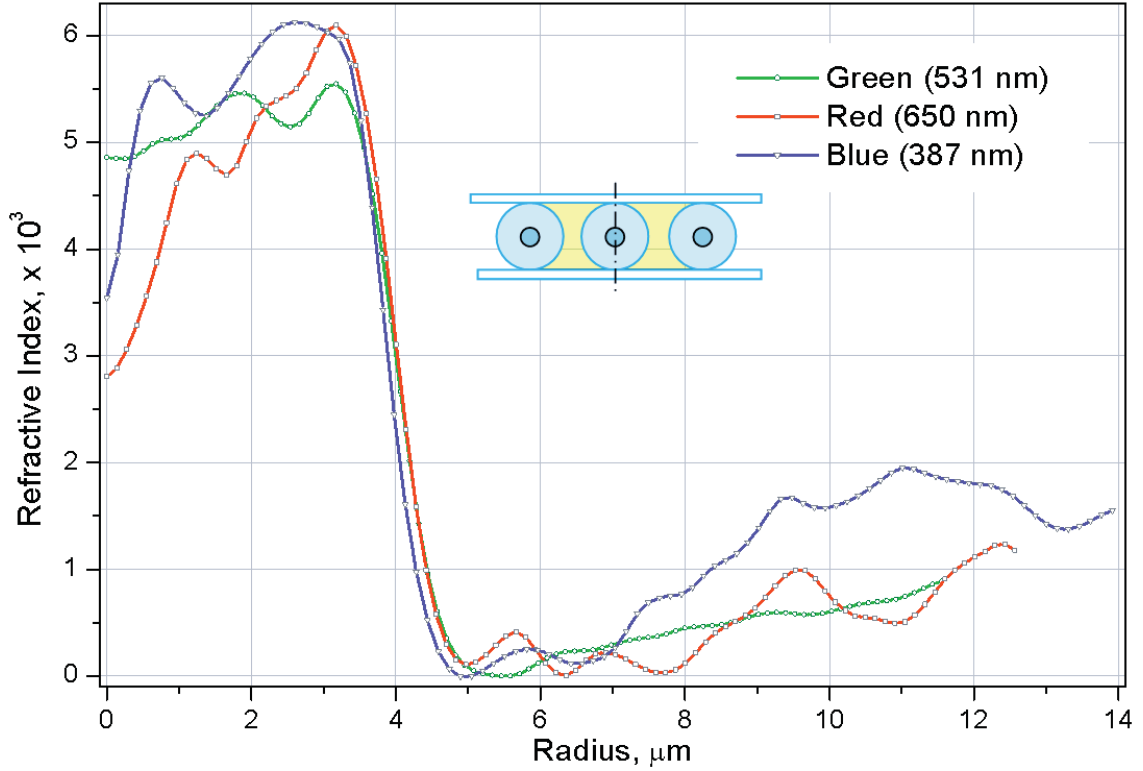
Figure 4.9: Calibration of the QPm method - reconstruction of the core-cladding refractive index contrast for single-mode optical fibre SMF-28e (by Corning), which has core diameter of 8.2 μm and core-cladding contrast of the refractive index of 0.00536.

straightforward:

$$\frac{\partial \phi(x,y)}{\partial x} = -\frac{\pi}{R} \sum_{m=1}^{M} m \cdot a_m(y) \cdot sin\left(\frac{\pi \cdot x \cdot m}{R}\right). \tag{4.5}$$

After that the expression (4.5) is to be inserted into integral (4.3) for numerical evaluation at a number of points across the fibre, in order to produce a radially symmetric distribution of the RI. Such a reconstruction for the case of $SMF-28$ fibre is presented in Figure 4.9. The comparison with manufacturer's data allows us to conclude that the method of QPm together and the software developed are calibrated. The calibration results, presented in Figure 4.9 revealed a refractive index contrast of about $5.3 \cdot 10^{-3}$ for three different wavelengths, with the core diameter of about 8.2μm. Further examples of reconstruction can be found in Chapter 5.

However, there is a discrepancy of the RI profile outside the core boundary, which seems to be due to non-complete matching of refractive indices for the immersion liquid (based on a solution of Glycerine, $n \approx 1.46$) and fused silica cladding ($n \approx 1.445$). A simple

formula which allows the estimation the refractive index contrast between the cladding and the immersion liquid can obtained from a geometric consideration (for notation of variables see the insert in Figure 4.8).

The dependence of phase $\Delta\phi$ vs x - a distance from the center of the fibre is connected to the index mismatch Δn, between the fibre with the cladding of radius R, for the wavelength λ as:

$$\Delta\phi(x) \approx \frac{2\pi}{\lambda} \cdot \frac{\Delta n}{R} \cdot x^2, \quad for \ x \ll R \tag{4.6}$$

An analysis of the data using Eq. (4.6) reveals: i) the dispersion of RI of the oil used is high at blue wavelength; ii) for green and red illumination the phase excursion is about 0.1 rad at the distance of $\mathbf{x} = 10 \ \mu$m, which corresponds to the cladding-oil index mismatch Δn of about 0.006.

Thus we arrived at the following **conclusions**: a simple and quick method for measuring the refractive index variations in solid samples, for example in optical fibres and planar samples with fs inscribed waveguides, can be built using a commercial microscope and a QPm software. Its realisation allowed refractive index measurements with an error of about 10% or better. There are no issues associated with the immersion liquids for planar samples, so the QPm method may be even more accurate. Further improvements require careful choice of the image acquisition hardware (high resolution camera, low noise, with linear response over the wide dynamic range) and significant efforts in re-programming the image processing part. The results of calibration of the QPm method with standard fibre, may have revealed the presence of chromatic dispersion in the Neofluar objective and/or immersion liquid at blue wavelengths. Cross-calibration of the QPm-based technique with other methods may be required for better than 10% precision. The implementation of the QPm method with absorbing samples is still an open question.

It is obvious that the QPm method can be modified in order to provide time-resolved measurements, as was demonstrated by Horn in [187]. This was done without any scanning of the sample or micro-objective, simply by combining three identical CCD cameras with the help of two beam-splitters. The cameras have to be offset from the "in-focus" position with high precision. Thorough calibration of the cameras' positions as well as scaling and intensity calibration factors was required [187]. Moreover, these separations have to be variable in order to provide the maximum resolution/sensitivity and be applicable with different

micro-objectives. This makes the design of such a set-up a challenging engineering task. The dynamic QPm method cannot produce true 2D reconstruction of the RI profile from a single-side projection. However, such modifications of QPm with ultrashort pulse as a light source possess the best temporal resolution.

For the sake of completeness, we will mention **other methods for refractive index measurement** of embedded waveguides, some of which may be used for on-line monitoring.

Shadowgraphy [188], which is also based on the TIE, requires low-aperture imaging optics with consequent insufficient spatial resolution for the typical micro-fabrication applications, but only a single shot of laser/illuminating source (as a background measurement can be done in advance). As it demands almost no optics, this method can be used with very short-wavelength radiation sources, which could improve its spatial resolution - at the cost of an additional (and, sometimes expensive) pulsed source. The method can produce a distribution of permittivity for axially symmetric objects only after reconstruction, and after a few assumptions have been made.

The first and most reliable, truly 2D method for RI reconstruction is the Refractive Near-Field (RNF) profilometry, with the Rink Electronik machine being a typical example of such types of devices. It allows the measurement of the index of an arbitrary profiled waveguide by micro-objective scanning across the polished slice of the sample. With sensitivity approaching the level of $2 \sim 3 \cdot 10^{-5}$ this method provides a true 2D map of the RI. However, it is not clear how it will cope with absorptive samples. Being most reliable (but expensive), this direct method is extremely slow and very time- and labour-consuming, as two manual polishings of the sliced sample are required. For this reason it cannot be applied for on-line diagnostics. Its substitution or simplification seems to be possible with a near-field surface profilometry of a polished and then chemically etched edge of the sample using, for example some water solution of hydrofluoric acid (HF). This is proved to work with fused silica. Other materials would require a cross-calibration by other methods (e.g. RNF).

The second family of methods may be grouped under the name of Digital Holographic Microscopy (DHM) [189], [190], which usually involves at least two beams, one of which is scattered on the object of interest. In DHM, a second or reference beam interferes with the scattered one, so a digital CCD camera records an off-axis interferogram (or digital hologram), which after reconstruction may produce the distribution of the refractive index [191].

The reconstruction is done by scalar Fresnel diffraction integrals, so DHM enables reconstruction of the phase of a wave front just after the transmission of the probe beam through the object, so this can be related to the object's permittivity [189]. That object is assumed to be optically thin. In order to achieve diffraction-limited resolution with DHM, it is necessary that both reference and scattered beam experience the same optical aberrations and this typically requires duplicate high-NA optics in both paths of the interferometer thus greatly increasing complexity and also creating problems with alignment. The method can use pulsed laser illumination, however the minimal pulse duration is limited by phase excursion on hologram. Alternative versions of DHM have been used for refractive index measurements of fs-inscribed waveguides, details can be found in [127].

There is also classic interferometric technique which can provide quantitative time-resolved diagnostics on small volumes which includes Mach-Zehnder interferometer, followed by Fourier filtration of fringes to determine accumulated phase retardation, and then the inverse Abel transform (e.g. [192]). It can provide only qualitative measurements in real time from the interferometric fringes. The reconstruction itself relies on a series of approximations, which may not be valid in the case when high spatial resolution is required or dense plasma cloud is created inside the dielectrics.

We would like to mention the method of tomographic ellipsometry as well, which has been developed by Limberger et al. [193], [194]. This method involves multiple acquisitions of data on polarisation rotation of probe laser at different angles or directions, similar to tomographic approach. The method is capable of extracting the information on stress distribution inside the optical fibre after the fs inscription of various gratings, for example the LPG inscribed by femtosecond laser at the wavelength of 254 and 352 nm [194], [84]. The method is very time-consuming, but allows one to measure objects with the volume down to a few $\approx \mu m^3$. The ellipsometry, being quite a general approach, requires careful analysis of experimental data in the case of absorbing and/or birefringent materials.

Record-low RI contrasts measurement inside optical glass can be done by another method, based on measurements of the diffraction of the probe beam on "as-long-as-required" tracks, potentially with arbitrary low refractive index contrast [164]. A simple consideration reveals that the phase accumulated by diffracted probe beam is proportional to the product of Δn and L - the length of the structure along the direction of the probing laser. These tracks

have to be inscribed in advance, so they can be made sufficiently long. When the length L is known one can evaluate the phase retardation, and thus the induced RI contrast using the approach described in [164]. This method can be applied for resolving the refractive index distribution in the single waveguide (grove). It can be obtained as a result of Fourier filtering of diffracted light distribution, using a phase diffractive grating made of a number of such identical waveguides. The greater the number of waveguides used to form the diffraction grating, the better spatial resolution can be achieved for a single track. Unfortunately, being potentially very sensitive as well as very general, this diffraction method is not applicable for on-line diagnostics and on-line optimisation of the inscription.

As the on-line monitoring and feedback are very important for both understanding of physics processes and optimization of regimes of direct femtosecond inscription, we re-examined various microscopic, diffraction-based and scattering-based techniques to i) visualise and ii) measure the RI changes induced by fs laser irradiation. An advanced method has been suggested, the experimental setup has been built and numerical procedures have been developed to solve the inverse scattering problem, without any assumptions, but first order scattering (Born) approximation. As was demonstrated in our papers [10, 11], the method is capable of measuring *both* the real and the imaginary part of permittivity, with sub-ps temporal resolution and on a sub-μm scale. It is this method which allowed us to observe the moment when various phase transitions take place, during and after fs laser irradiation of the sample. It is discussed below in relation to underlying physics of fs inscription and in Section 4.8.

Finally, there is a number of high spatial resolution imaging techniques in use which provide only a qualitative indication of induced refractive index distribution including pump-probe transmission microscopic imaging [195]; time-resolved photography [196]; ultrafast transient absorption spectroscopy [197], [198]; and also a static DIC-microscopy [36] or dynamic version of DIC described in detail in the dissertation by Alexander Horn, 2003 (Aachen, Germany) "Time-resolved analysis of interaction of ultrashort-pulse laser radiation with dielectrics" ("Zeitaufgeloste Analyse der Wechselwirkung von ultrakurz gepulster Laserstrahlung mit Dielektrika").

4.7 Waveguide diagnostics tools and equipment

The structures fabricated were explored under the *Zeiss* microscope and the accumulated phase maps were measured as described in Section 4.6.

The light guiding is an ultimate test of their quality. In order to measure coupling, propagation, polarisation-dependent and bend losses both edge surfaces of the samples have to be gridded and polished, because the waveguides do not normally terminate at the side of the sample, but rather end at a distance of a few dozen micrometers inside the bulk.

The refractive index distribution left after the fs irradiation and the maximum RI contrast induced seem to be most important parameters. For RI distribution the Abel inversion could be used in the case of almost circular, non-absorbing waveguides.

If these conditions are not met, a simpler but less reliable technique could be used. We refer to the method in which the side scattering of coupled laser radiation is observed by the top-view CCD camera. If the waveguide is uniform along its length, and all the energy at the input is coupled into it rather than into the slab substrate, one can deduce the level of propagation loss by monitoring the decay in intensity of the scattering light along the WG image, obtained by a camera from the perpendicular direction. This method is best suited to strong, high-loss structures, but not for low-loss ones. It could easily lead to misleading conclusions, when the radiation propagates into the slab almost without losses. The greatest advantage of this method is its speed.

There are characterisation techniques to measure the effective NA of the waveguide, and thus induced RI contrast. They were considered in several papers by Streltsov, et al. [74], Tong, et al. [128] and others. This method utilizes the expression for NA for a circular axi-symmetric step-index waveguide:

$$NA = sin(\alpha_{max}) = \sqrt{n_1{}^2 - n_0{}^2}. \qquad (4.7)$$

In the case of non-step-index WG, one can determine the effective numerical aperture and thus make an estimate of the RI contrast simply by measuring the maximum angle of light diffracted out of the waveguide, or by measuring the dependence of total propagation losses as a function of *NA* of the launching MO, equipped with a variable diameter diaphragm, as was suggested by Tong, et al. [128]. There is a typical experimental problem associated with this method, which is in measuring weak intensity at the wings of the diverging beam

diagram.

A slightly more reliable method is to fit the distribution obtained by numerical calcula-
tions of the WG mode and the shape of the output mode-field diameter, measured by CCD
camera. Obviously, for such calculations some model distribution of the refractive index has
to be chosen in advance. A more advanced technique, capable of true 2D-reconstruction
of the refractive index is based on rigorous analysis of the shape of the 2D mode-field dis-
tribution, as described by Florea, et al. [75]. In this approach the Helmholtz equation for
fundamental eigen-mode reads:

$$\Delta_\perp E(x,y) + \left[k_0^2 \cdot (n_0 + \Delta n(x,\ y))^2 - \beta^2 \right] \cdot E(x,y) = 0. \tag{4.8}$$

assuming that the distribution $E(x,y)$ is known (or measured) one can invert the equation 4.8
to determine the $\Delta n(x,\ y)$ as:

$$\Delta n(x,\ y)\ =\ \frac{1}{2\ n_0\ k_0^2} \left[\beta^2 - \frac{\Delta_\perp E(x,\ y)}{E(x,\ y)} \right] - \frac{n_0}{2}, \tag{4.9}$$

which essentially has all the information on the spatial distribution of the refractive index
across the waveguide in its second term in brackets, while the knowledge of β, the propa-
gation constant and n_0, background refractive index can provide the absolute value of the
refractive index. This approach requires low-noise, high dynamic range imaging cameras
with linear response characteristics, and some numerical image processing (e.g. noise fil-
tering). Indeed, the calculation of second derivative of noisy data $E(x,\ y)''_{xx}$ is at least prob-
lematic. It corresponds to a multiplication on $-\ k_x^2$ in **k**-space. The white noise at higher
frequencies will then be significantly enhanced, so some accurate filtering (or fitting) of the
experimental mode-field distribution is required. These numerical filters have to be carefully
tested for absence of spurious oscillation, typically associated with numerical filtering in the
spectral domain; also, ideally, it should not modify the mode-field distribution.

There is a less complex technique, which occupies an intermediate place between com-
plete 2D RI reconstruction and effective NA measurements. The method suggested in our
paper [8] is based on an approximation of the dependence of the Mode-Field Diameter
(MFD) on other parameters, for example the wavelength of the light source. It requires
measurements of the MFDs at several different wavelengths, and can be made more accurate
if a tunable laser source is used [8]. The idea can be understood by inspecting the Marcuse
approximation for step-index circular fibres with the core radius a, which expresses the ω

- the $(1/e)$ half-width of electric field distribution as a function of normalized frequency, $V = 2\pi\, a/\lambda \cdot \sqrt{n_{co}{}^2 - n_{cl}{}^2}$:

$$\omega = a \cdot \left(0.65 + 1.619 \cdot V^{-3/2} + 2.879 \cdot V^{-6} \right). \tag{4.10}$$

By measuring the mode-field diameters at different wavelengths, the unknown parameters can be found by numerical fitting of MFD-curve at different wavelengths.

Finally, if the mode-field distribution is known, one can calculate the overlap integral and estimate the coupling losses (CL):

$$C.L. = \frac{\int \int E_f(x,\, y) \cdot E_{WG}^*(x,\, y)\, dx\, dy}{\sqrt{\int \int |E_{WG}(x,\, y)|^2\, dx\, dy \cdot \int \int |E_f(x,\, y)|^2\, dx\, dy}} \tag{4.11}$$

Note that the information on phase of the waveguide mode(s) cannot be extracted from a single intensity distribution, so it may not be possible to calculate CL by using Eq. 4.11 in the case of a multi-mode waveguide.

The Propagation Losses (PL) are the most difficult to measure accurately. One can potentially measure them by the "cut-back" method, when the waveguide is sliced into pieces with progressively decreasing lengths and all pieces are side-polished to identical optical quality [115]. The PL are determined by the slope of the fitting curve (losses *vs* length), so that a small experimental error can change significantly the value of PL obtained. This method is sensitive to experimental errors because progressively decreasing PL are measured typically along with CL and other losses.

The most reliable and commonly used method is based directly on the definition of total losses (TL), in dB/cm:

$$TL\,[dB/cm] = 10 \cdot \log_{10}\left(P_{out}/P_{in}\right)/\Delta L\,[cm]\,, \tag{4.12}$$

where P_{in}, P_{out} are the input and output powers respectively, and ΔL is the length of the structure. This method has been used in our work for all waveguides obtained by the HRR CPO system. The experimental setup for loss and mode-field distribution measurements is depicted in Fig. 4.10. It includes two six-axis NanoMax stages (*Thorlabs*) to control positions by virtue of three coordinates: $X,\, Y,\, Z$, and three tilt angles: $\theta_X, \theta_Y, \theta_Z$ by means of either manual or piezo-drivers. It enables easy butt-coupling from a standard fibre to the waveguide of interest by using the top-view stereo-microscope shown in Fig. 4.10, a).
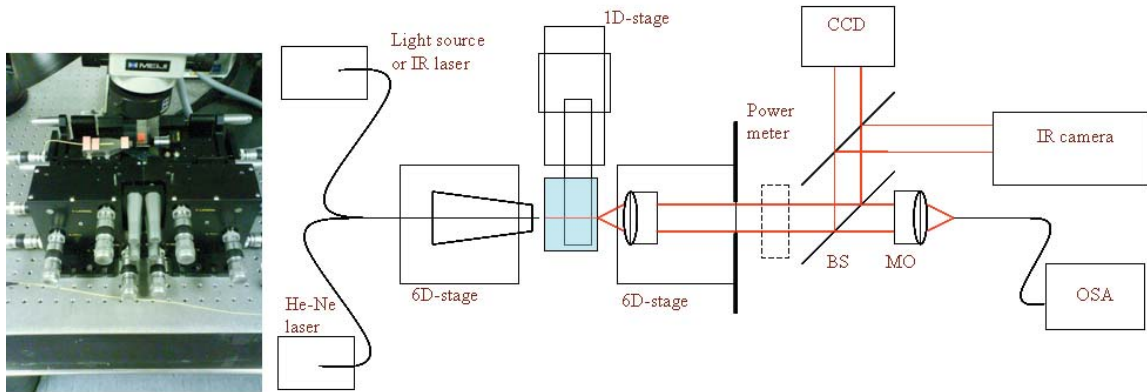
Figure 4.10: Waveguide characterisation setup.

The sample is mounted on a separate 1D-stage with sufficient range of translation and semi-automatic position control. Precise sample positioning is essential because it is hard to locate the waveguide even with the top-view microscope, especially when the propagation and/or scattering losses are small.

The near-field intensity distributions at the output facet of the sample (or fibre) were recorded by both visible CMOS, 12-bit camera (by *PhotonFocus*) and near-IR InGaAs CCD camera *Goodrich*-IRS by *Laser Lines* (UK), and the software for *Spiricon* cameras. The calibration of the resolutions for both cameras was done by transverse shifting of the micro-objective by known distance using precision piezo-drivers of the *NanoMax* stages. Scaling factors for both imaging systems were derived by comparing images of the same object. Using a proper WDM-or X-coupler two different lasers can easily be combined at the WG input.

The loss-measuring setup also includes two power-meters: model 840-C with two different optical heads incorporated Si, and Ge calibrated diodes, and also some fixed attenuator and filters (by *Newport*), and all-fibre M9001A power-meter by *Anritsu*, as well as the optical spectrum analyzer with 0.1 nm resolution (*Hewlett Packard*). This set-up was used for loss measurements and spectral characterisation of the waveguides. The diaphragm installed after the projection MO (to the right in Figure 4.10) was kept in the same position for the rest of the experiments, until the next calibration. The power-meter head inserted for power measurements always had the back reflection from its front surface at the same spot, and its position was always kept the same in order to avoid effects associated with variable sensitivity across the area of the detector.

To calibrate the power measurements and the magnification on this setup the sample was initially removed by moving it in the direction perpendicular to the direction of light propagation. The output power of the freshly cleaved *SMF-28* fibre was measured by the power meter, when the fibre was translated into the position of the output facet of the waveguide. By doing so, we observe the most compact and brightest image on a camera. These positions were slightly different for different laser sources, due to insignificant chromatic aberration of the $20\times$ projection micro-objective used. Measured power from the output of the optical fibre provides the reference level or P_{in}.

The mode-field distributions were measured at the same time by virtue of two imaging cameras, mentioned above. The output distribution of the *SMF-28* fibre $\sqrt{I_f(x,\,y)} \simeq E_f(x,\,y)$ served as additional proof for calculations of the coupling loss by Eq. 5.3. After that the sample was put in place and the fibre was scanned across the input port of the sample until we launched some light into the waveguide of interest. The edge of the sample has to be aligned to be parallel to the direction of translation, so that the lateral shift to the next waveguide does not introduce a displacement along the optical axis. This allowed easy switching between nearby waveguides in future, by simple translation of the sample in transverse direction over the known distance. This makes the alignment procedure (to the next waveguide in each group) quick. It can be made even more easily by observing the image of the output facet of the sample on a camera or even on a white screen. In doing so, we have measured the total insertion losses for all waveguides under investigation. These losses include:

- Fresnel losses on two glass-air interfaces (approximately 4% on each, or 0.36 dB on both surfaces);

- coupling-in losses from the fibre to the waveguide. This is estimated by virtue of equation 5.3 after measuring the mode-field distribution from the waveguide of interest;

- and finally, the propagation losses for the 20mm-long sample.

The waveguide mode-field distributions were measured and quantified for all tracks both at 633 nm and 1550 nm, using the LBA software (*LaserLines*). Only a few were used to measure losses at 1550 nm. The major difficulty was in the alignment of the sample during its

a)   b)
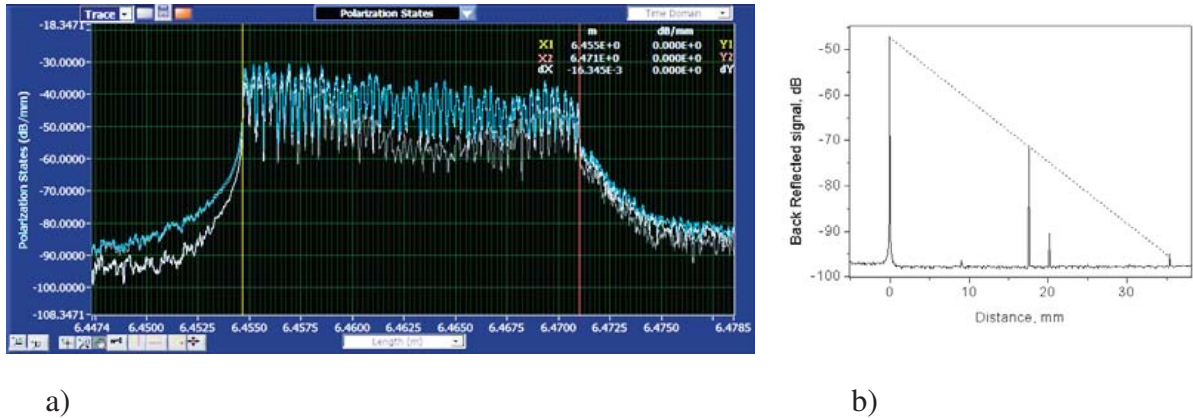
Figure 4.11: The work screen (a) of the $OBR-4400$ when femtosecond LPG is monitored. Note the significant rise in the back reflection far before the first grove of the LPG. Back reflection signal from the 18 mm long planar BK7 waveguide (b) could be used to monitor the propagation losses.

translation in a lateral direction without proper computer control, especially if observation of light scattering becomes problematic, as in the case of high-quality or low-loss structures. From the loss measurements at 1550 nm we concluded that they often reproduce the tendencies observed at 633 nm, but with some offset of less than or about -2 dB. Our estimations of CL at 1550 nm as well as numerical modelling of coupling losses by FimProp software (*Photon Design*) confirmed that this is due to higher coupling losses at NIR wavelength, where all of the waveguides become single-mode.

For completeness, we should mention one of the most advanced techniques for loss measurements. An optical backscatter reflectometer of the OBR-4400 type (by *Luna Technologies*) is the "industry's first" ultra-high resolution device for testing of distributed components or systems. The device uses swept-wavelength coherent interferometry with narrow linewidth frequency-swept laser to measure minute reflections (down to $3 \cdot 10^{-13}$) in an optical system as a function of length along the waveguide. This technique allows the measurements of spectrally resolved delays, group velocity, return loss, propagation loss and dispersion, as well as some spectral-selective characteristics. The maximum measurable optical path in the model we tested was 70 m, resolving individual features down to 10 μm, versions for up to 2 km long fibre spans may also be ordered. The OBR measures group delay up to 150 ns, and provides 70 dB of dynamic range with -120 dBm sensitivity. The $OBR-4400$ system was tested on some of fs-inscribed devices, namely with fs-LPGs and 18 mm long waveguide. Figure 4.11 provides two examples of such measurements.

95
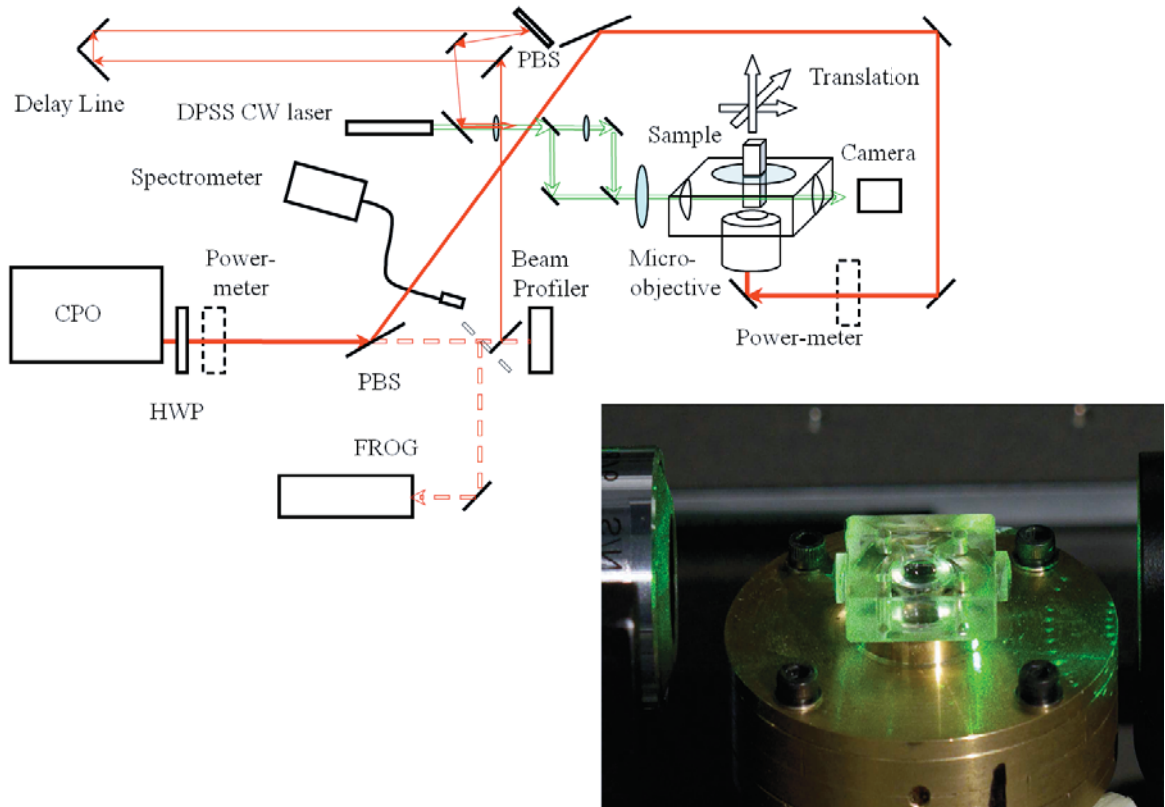
Figure 4.12: Experimental arrangement for on-line measurement and optimisation of the induced RI contrast, as well as for visualisation of the fs inscription process.

4.8 On-line monitoring of inscription process

It is advantageous to have on-line feedback for direct femtosecond inscription, but it comes with a drawback: one should choose in advance the parameters of interest to monitor, as well as the time slot during which the corresponding processes are observed. For example, the dynamics of the RI can be observed after the inscribing pulse at different time slots; the continuum or luminescence generated during fs inscription, as described in Chapter 5, or perhaps the acoustic signal generated inside the sample at some specific frequency can be monitored. The choice is not trivial, given that the time-scales for the different processes involved vary significantly.

We suggested using a fairly general approach based on a scattering of a probe light (laser radiation), in a transverse direction to the femtosecond laser. For this an optical scheme and special cuvette have been designed and manufactured as shown on the insert of Figure 4.12.

Figures 4.12,4.13 explain the optical layout used. In our design both the reference and probe beams originate in a symmetric MachZehnder interferometer (Fig. 4.13), so that they

96
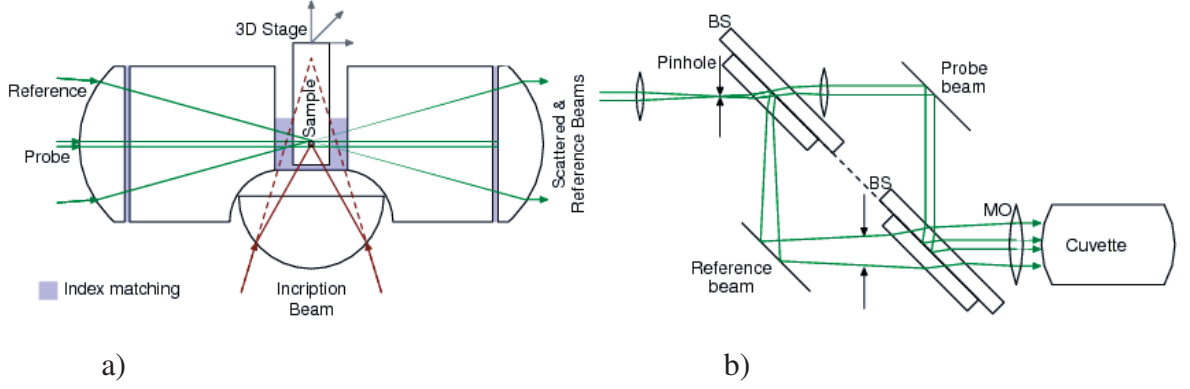
Figure 4.13: Side-view on the cuvette with the sample (a), and top view on the Mach-Zehnder interferometer (b). The slight tilt between the probe beam (the narrow one) and reference beam (the wide one) axes allows us to focus the reference beam outside the area affected by inscribing fs laser, which comes from the bottom on figure (b).

have identical propagation time in both arms, and they traverse almost the same optical path inside the cuvette, such that they match in polarisations at the detector plane. Additionally, they have almost identical wavefronts in terms of aberrations, as they a) both refract at the same optical components, and b) we implemented aplanatic design for input and output "windows" of the cuvette. Our configuration eliminates the need for a duplicate separate set of optics for each beam as is necessary in digital holographic microscopy [189] and the resulting complexity of alignment that it introduces. Off-the-shelf optical elements can be used even for a sub-picosecond probe pulse. Surprisingly, in our current setup presented in Figure 4.12, with just a $5\times$ magnification, long working distance probing MO in front of the cuvette we achieve a sub-micrometer spatial resolution when measuring the refractive index.

In addition to improvements in the optical configuration, the theoretical analysis was re-examined from first principles starting from Maxwell's equations and considering the scattering problem in the first order (Born) approximation, taking into account the vector nature of EM-fields used to form the interference pattern. It could be shown that, assuming axial symmetry along the inscription beam direction and a probe beam perpendicular to this axis of symmetry, the complex permittivity change can be determined from the measured single interferogram using the following relation for the Fourier component of permittivity in wave vector space:

$$\varepsilon(\vec{q}_{n,m}) = \frac{4\pi}{k_0^3} \frac{\sqrt{k_0 k} \rho_0}{G_{n,m}} \frac{W_{n,m}^{\text{int}}}{\sqrt{W_{n,m}^{\text{ref}} W_{\text{sum}}^{\text{ref}}}} e^{-ik_1 \left(R_{n,m}^s - R_{n,m}^{\text{ref}} \right)}, \tag{4.13}$$

$\vec{q}_{n,m}$ is the wave vector corresponding after refraction to the direction to the (n, m) indexed

detector pixel. k_0, k and k_1 are the wave numbers of the probe light in vacuum, the glass and in air respectively. ρ_0 is the half width $(1/e)$ of the probe beam assuming Gaussian beam profile. $G_{m,n}$ is a geometric factor taking account of angles of the beams onto the sensor and beam refraction. $W_{n,m}^{\mathrm{ref}}$ is the intensity of the reference beam at pixel (n,m), which will have been previously recorded and $W_{\mathrm{sum}}^{\mathrm{ref}}$ is the normalisation factor or sum of the intensity for whole detector area for the reference beam.

In scalar approximation, the measured interferogram $W_{n,m}^{\mathrm{total}}$ is expressed in terms of the reference beam, scattered beam $W_{n,m}^{\mathrm{scattered}}$ and two interference terms - $W_{n,m}^{\mathrm{int}}$ and its complex conjugate $\overline{W_{n,m}^{\mathrm{int}}}$, as follows:

$$W_{n,m}^{\mathrm{total}} = W_{n,m}^{\mathrm{ref}} + W_{n,m}^{\mathrm{scattered}} + W_{n,m}^{\mathrm{int}} + \overline{W_{n,m}^{\mathrm{int}}}. \tag{4.14}$$

For the case of off-axis interference, the last three terms are well separated in the Fourier domain. Thus the term $W_{n,m}^{\mathrm{int}}$, the measured interference amplitude term required for Equation (4.13), may therefore be obtained by filtering the measured interferogram in the Fourier domain to remove the unwanted probe, reference beam and conjugate components.

The complex phase term in the aforementioned Eq. (4.13) $exp(-i \cdot k_1 \cdot (R_{n,m}^s - R_{n,m}^{\mathrm{ref}}))$ originates due to the difference in optical paths to the sensor between the scattered beam from the object and the reference beam. It is difficult to determine this term precisely, however it can be determined a posteriori using an optimisation technique on the measured interference patterns [10]. It is for this reason that Equation (4.13) is difficult to use for real time online reconstruction of $\varepsilon(\vec{q}_{n,m})$.

For the purpose of real time monitoring, our analysis shows that the scattering amplitude $\mathbf{S}_{n,m}$ can be used to provide online feedback or qualitative indications of the permittivity profile in real time:

$$\mathbf{S}_{n,m} = \frac{4\pi}{k_0^3} \frac{\sqrt{k_0 k}\rho_0}{G_{n,m}} \frac{W_{n,m}^{\mathrm{int}}}{\sqrt{W_{n,m}^{\mathrm{ref}} W_{\mathrm{sum}}^{\mathrm{ref}}}}. \tag{4.15}$$

Alternatively, one can use so-called interference image $\mathbf{P}_{n,m}$ defined as:

$$\mathbf{P}_{n,m} = |\mathbf{F}^{\mathrm{filtered}}\left[W_{n,m}^{\mathrm{total}} - W_{n,m}^{\mathrm{ref}}\right]| = |\mathbf{F}\left[W_{n,m}^{\mathrm{int}}\right]| \tag{4.16}$$

Superscript $^{\mathrm{filtered}}$ indicates that the part of the Fourier spectrum in the vicinity of the region of interest is taken.

Figure 4.13 shows the optical cuvette arrangement used to enable inscription and the in-situ interferometric measurements. The inscription beam was pre-focused onto the bottom spherical lens of the cuvette using a 0.55 NA (*Mitutoyo* 100× LWD) microscope objective. The target sample used in these experiments was 1.5×1.5×15 mm optically polished BK7 glass which could be accurately positioned inside the cuvette using a 3D-translation stage (*Aerotech*).

In the initial demonstration of the technique, a 532 nm single frequency CW diode pumped solid state laser was used for the measurements. This beam was divided to provide probe and reference beams using a Mach-Zehnder interferometer (figure 4.12) which employed broadband beam-splitters (BS) with the reflecting surfaces optically contacted between two thick (9.5 mm) glass slabs. Both beams focused through a long working distance (5×, NA=0.14) micro-objective installed in front of the cuvette. In the cuvette the probe beam is collimated and centered on the inscribed target region, while the reference beam is transmitted over nearby unmodified glass and is tightly focused to enable even illumination and almost parallel interference fringes on the detector plane. Since the two interfering beams experience virtually the same optical path and optical aberrations, their electric field vectors are parallel when they interfere on the detector, thus a scalar approximation can be used.

The cuvette (Figure 4.13, a) was constructed from the same BK7 glass as our sample, which was embedded into index-matched oil, thus minimising parasitic internal reflections. The arrangement satisfies the aplanatic conditions for focusing the inscription, as well as probe and reference beams. In this way Seidel aberrations were minimised. An additional advantage, when the aplanatic conditions are also met for the inscription laser, is that the effective numerical aperture is also increased. This can be seen as the difference between dashed and solid red lines in Figure 4.13, a). This enables aberration free focusing more deeply into the sample than would be possible using a standard microscope objective alone. In our configuration the effective numerical aperture of the inscribing optics was increased from 0.55 to approximately 1.26, enabling inscription at depths of up to a few mm. At the same time the long working distance of the *Mitutoyo* MO has almost been preserved.

In order to demonstrate the technique, interferograms were recorded at 18 frames per second during the exposure of the glass sample by the inscription laser. Figure 4.14 shows a sequence, labelled by sequential frame number, for an inscription power of 700 mW. At each

a)   b)
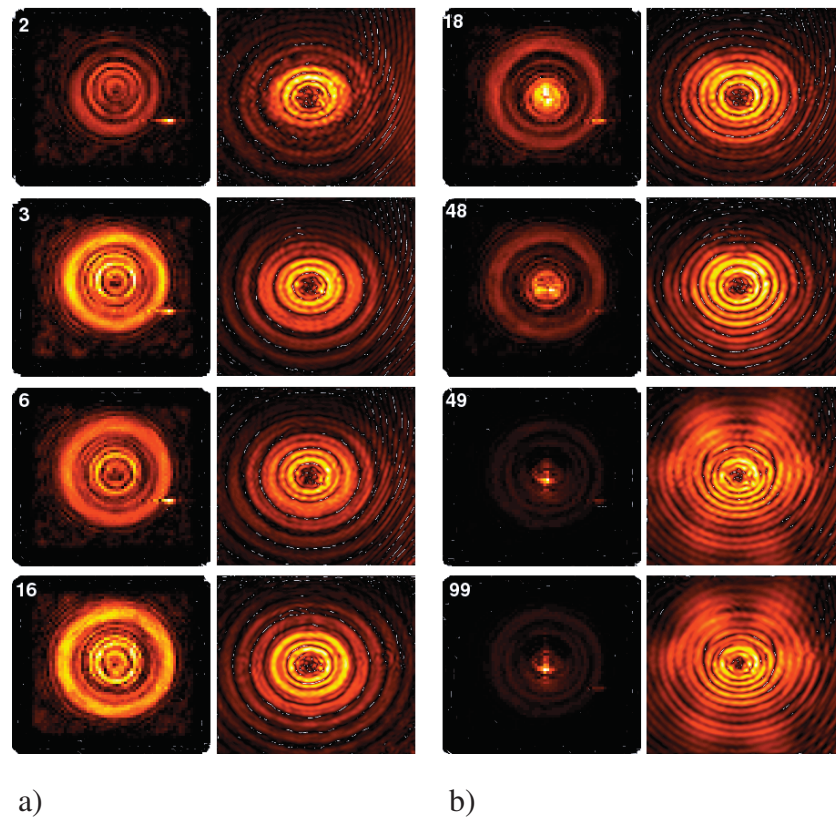
Figure 4.14: Sequence of plots of absolute value of interference image(a): $\mathbf{P}_{n,m}$ and the scattered amplitude (b) $\mathbf{S}_{n,m}$ with 700 mW exposure. Labels correspond to multiples of $1/18$ sec.

a)   b)
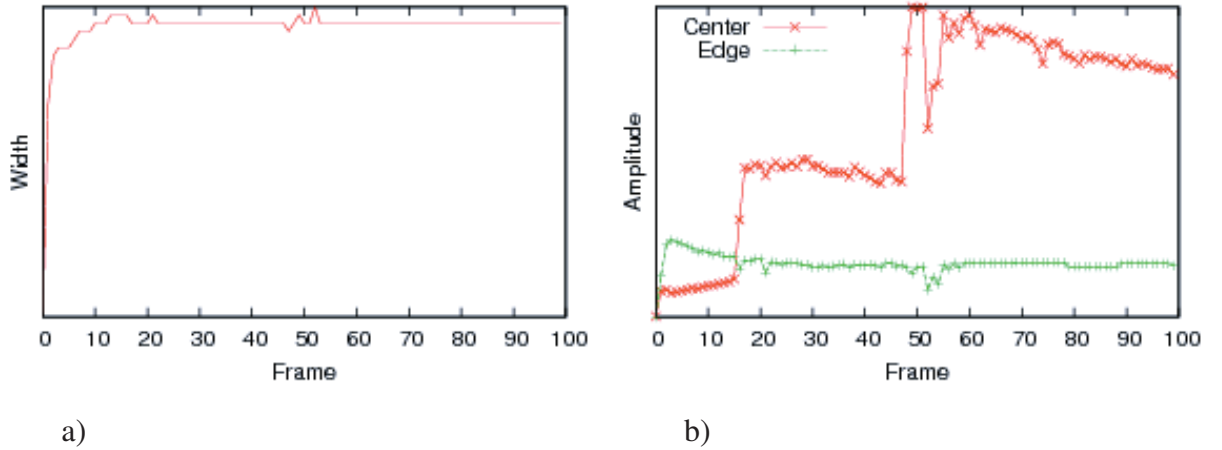
Figure 4.15: Diameter of the outer annulus of $\mathbf{P}_{n,m}$ versus frame number (a), and change in the amplitudes for the central peak and outer ring versus frame number (b).

frame, the interference image $\mathbf{P}_{n,m}$ (as referred to in Equation 4.16) is plotted on figure a) and the modulus of the measured scattered amplitude $\mathbf{S}_{n,m}$ is plotted on figure b) in each column. The scattered amplitude $\mathbf{S}_{n,m}$ is calculated from the filtered single interference term in the Fourier transform of the change in the interferogram induced by the inscription, and could be also monitored in real time. In Figure 4.14, frame 2 corresponds to the first frame after the inscription laser was turned on, and the laser was turned off between frames 48 and 49. Frame 99 was recorded much later and corresponds to the "equilibrium" state of the change in permittivity. The concentric ring patterns observed are indicative of a bubble shape in the index change with a sharp edge.

Analysis of images in Fig. 4.14 show the change in the radius of the central ring (Figure 4.15, a) and the changes in peak amplitude of the central peak and outer annulus (Fig. 4.15, b) versus frame number. It is apparent that the size of the inscription region increases rapidly but only up to frame number 3 and then does not change much with further exposure or even when the laser was turned off. Figure 4.15 (a) however shows that the amplitude of the central region undergoes a sudden increase at the 16th frame during exposure and again when the laser is turned off at the 48th frame. Shortly after the inscription laser is turned off there appear to be some other sudden changes in index before it settles (cools) down and gradually decays to the equilibrium value. We believe that these sudden jumps in scattered amplitude and thus refractive index correspond to phase transitions in the material. It is assumed that the first transition between frames 15 and 16 may be due to a microscopic
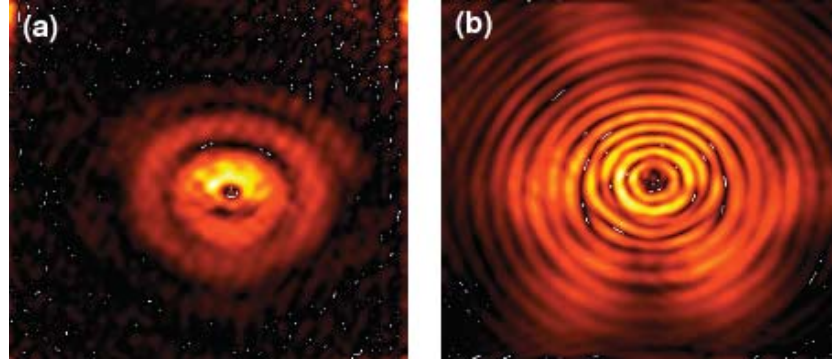
Figure 4.16: Plot of absolute value of the scattered wave $\mathbf{S}_{n,m}$ for inscription at 475 mW after 5 seconds exposure (a) and 700 mW after 2.5 seconds exposure (b).

rearrangement of the material when a build up of mechanical stress is released due to the melting, accompanied by a macroscopic motion of the inner volume of the melted material as has been proposed to take place under the heat accumulation regime in glass [60,67,199]. The second transition corresponds to the solidification and structural rearrangement of the central part of the bubble when it is squeezed by the cold outer shell of the bubble. There is also a characteristic 6-fold symmetry, which can be observed in scattering amplitude in frames 49-99, which appeared only after the inscription laser (a heat source) was turned off.

Figure 4.16 shows the measured absolute amplitude of the scattered wave calculated from the interferograms at average laser powers of 475 mW and 700 mW once equilibrium state has been reached after exposure. The differences between the two different inscription powers can be clearly seen: in the case of "low-power" irradiation during 5 seconds. The inscription beam direction is vertical in these figures. The mirror symmetry in the horizontal direction confirms the validity of our assumption of axial symmetry along the beam direction, while the asymmetry in the vertical direction implies that the change in epsilon must have both real and imaginary components.

Indeed, Figure 4.17 shows the calculated quantitative values for the real figure 4.17 (a) and imaginary figure 4.17(b) parts of the reconstructed distribution of $(\Delta\varepsilon_{\tau})$ - the modified permittivity in real space corresponding to Figure 4.16(a). The shape of the real component (a central peak surrounded by lower trough and raised ring) agrees with that in our previous studies [25]. The positive imaginary component of this indicates that there is an induced absorption in the exposure process as well as the induced refractive index. Negative values of $\Im(\Delta\varepsilon_{\tau})$, which would be unphysical, give an estimate for errors in both experimental and
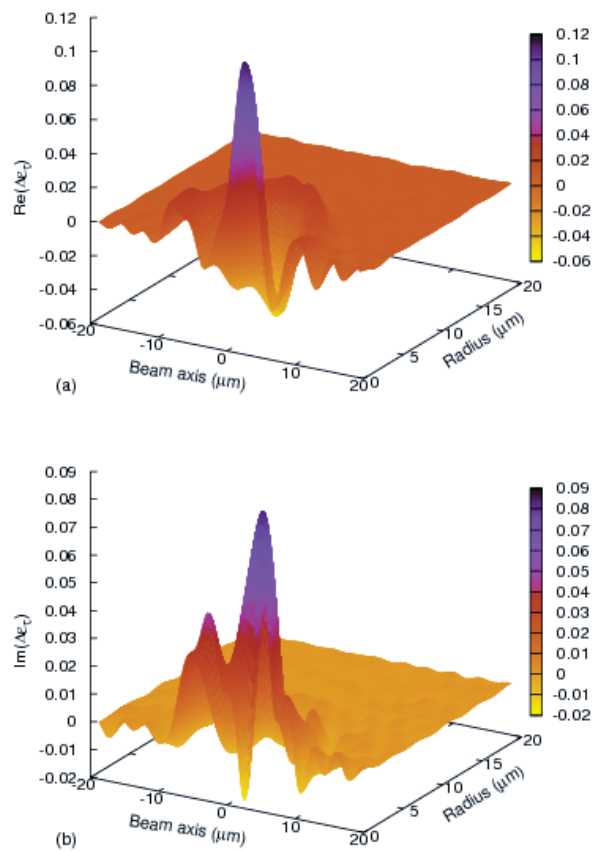
Figure 4.17: Plot of axially-symmetric reconstructed real part, $\Re(\Delta\varepsilon)$, (a) and imaginary part of permittivity (b), $\Im(\Delta\varepsilon)$, in cylindrical coordinates at an inscription laser power of 475 mW.

reconstruction procedures.

To conclude this section, we have developed a practical experimental technique to enable on-line measurements, in real time and on micrometer scales, the change in complex permittivity in materials under femtosecond laser pulse irradiation. Analytic solution of the EM scattering problem beyond the paraxial approximation has enabled development of a numerical technique to solve the inverse scattering problem for the case of transverse imaging of the modified volume under the assumption of axial symmetry along the inscription beam axis. We have used this to observe the development of induced permittivity during and after high repetition rate femtosecond laser irradiation. The observed maximum induced changes of $\Re(\Delta\varepsilon_\tau)$ and $\Im(\Delta\varepsilon_\tau)$ were 0.1 and 0.06 respectively, at a laser pulse energy of 20 nJ and a repetition rate of 11 MHz. We have also been able to observe sudden changes in the permittivity during the inscription process, which we believe corresponds to phase transitions in the material. This technique may improve our understanding of the physical processes involved. It also provides on-line control and enables an optimisation of inscription regimes during femtosecond modification in transparent dielectric materials.

Chapter 5

Direct femtosecond inscription of low-loss waveguides

In this Chapter we present experimental results for direct femtosecond inscription of low-loss waveguides in various transparent dielectrics, using both low- and high- repetition rate laser systems, and demonstrate that HRR inscription has significant advantages for waveguide fabrication. The maximum refractive index (RI) contrast achieved in borosilicate glass is 2.5×10^{-2}; to the best of our knowledge, this is the maximum ever reported for a low-loss, uniform waveguide. The optimisation of the inscription regimes allowed us to obtain total losses for a 2 cm sample of about 0.6 dB. The last figure includes both propagation and coupling (to a standard fibre) losses.

5.1 Inscription using a low repetition rate femtosecond system

5.1.1 Historical perspective

Initially the experiments were carried out on the LRR CPA laser system, described in Sect. 4.1. Intensive experimental trials were undertaken in order to fabricate a waveguide that was of a "good" quality or "visually free from damage". The last observation correlates very well with low propagation losses, as we found over a few years exploring both a wide variety of

materials and a broad range of experimental parameters, such as laser pulse energies, spectral chirps, sample translation velocities, focusing depths, different focusing optics, state of polarisation of laser radiation, etc. We found in most cases that the WGs fabricated were either too weak, had low RI contrast or were damaged.

It turned out that our system has excessive laser pulse energy, so it has to be dumped or attenuated significantly for any kind of meaningful inscription. However, we very soon recognised that the CPA system is well suited when higher laser pulse energy is required, such as:

- FBG and LPG fabrication in any fibre [16], as described in Ch. 6;

- generation of harmonics of NIR fs laser and their usage for periodic structures fabrication [36], Ch. 6;

- laser ablation with subsequent ion-exchange process, described in more detail in Ch. 8;

- inscription by use of astigmatic laser beams [15, 21] described below in this chapter;

- inscription by the micro-holographic method, when two or more beams have to be delivered simultaneously into focus, as described in Sect. 6.3 [200];

- fibre Bragg grating fabrication by the mask method;

- as well as for fs nano-structuring of the glass for the subsequent selective chemical etching, as described in [50, 201],

and some others.

In spite of the difficulties with waveguide fabrication using the LRR CPA system, in 2005 we succeeded in fabricating smooth structures in fused silica as well as in other wide-band-gap materials [12], [4]. These WGs were with low RI contrast, so that the maximum V-parameter was just about 1 [8], while in a standard telecommunication fibre V is $\approx$2.1. During these trials it was found that the WGs can be reliably fabricated on our system only by using a reflective micro-objective rather than traditional objectives made from various optical glasses. Additionally, the laser pulse duration had to be kept as short as possible, preferably less than 150 fs.

At that time there were promising reports in the literature, published by researchers from Politecnico di Milano (Italy), Harvard University (USA) and Macquarie University (Sydney, Australia) [70, 99, 202, 203], however, we decided to stop the search for and optimisation of inscription schemes, focusing conditions and regimes for LRR fs laser inscription.

Our decision was made on the basis of the following considerations and experimental findings:

- regardless of the optical layout, the inscription speed (0.01 $\sim$ 0.1 mm/s) cannot be increased significantly when a kHz fs system is used. Faster translation speeds require higher laser pulse energies, but there is an upper limit for this, imposed by the damage threshold of the material or the glass micro-objective itself. This limit is ranged between 1 and 10μJ, depending on a the material or objective;

- a very low inscription speed would significantly increase the manufacturing cost for any photonic device apart from basic ones, which would not be acceptable for the majority of applications of the fs method;

- the stability of the output pulse train of the laser for longer lasting inscription sessions also becomes a serious issue;

- at high laser pulse energy the beam is distorted by nonlinear effects such as self-focusing, this prevents control over the energy deposition and requires more efforts to optimise the focusing conditions;

- the induced refractive index contrast was typically low, regardless of chosen inscription method or focusing optics, making it impossible to produce curvilinear waveguides. This circumstance seems to restrict the applicability of the LRR fs inscription to straight waveguides only;

- to avoid self-focusing and to fabricate the waveguide with a circular cross-section, the beam had to be shaped, for example by introducing some astigmatism by means of cylindrical lens telescope [71] or optical slit [70]. There are no analytic or rigorous numerical simulation tools to describe the evolution of the beam for the case of non-symmetric beams, or beyond axial symmetry. Furthermore, the slit method makes poor laser energy utilisation for kHz systems even worse, while the telescope-based

approach is complex in practice. In our experiments on fs inscription with astigmatically shaped beams, when the long axis of the beam was perpendicular to the direction of scan, we always observed stochastically modulated tracks. This phenomenon has not yet been understood and thus is beyond control. Also the propagation losses are higher for such a modulated track than for a smooth one. We also found that in this case the telescope has to be optimised (lens positions have to be changed and re-aligned) for each particular level of laser pulse energy. The alignment of a cylindrical telescope is complex, more complex than, for example, the alignment of a slit [70]. None of the astigmatic beam inscription methods allows complete control over the cross section of the fs waveguides. Indeed, it was later found that for astigmatic fs beams the cross-section of the waveguide may vary with the laser pulse energy. Figure 5.1 reproduces Figure 5.10 a), from the PhD thesis "Fabrication of optical waveguide devices in bulk material using femtosecond laser pulses" by Martin Ams [204]. One can see that the shape of the waveguides becomes triangular instead of round at higher pulse energies.

However, we managed to find regimes for inscription with astigmatic beams, capable of producing smooth tracks even inside the hardest materials such as YAG or other crystals [15]. Despite the fact that the induced refractive index change in the WG core becomes negative or the refractive index is lower than for the surrounding material in this case, the light guiding structure can still be made by inscribing a cladding. This "depressed cladding" is formed by virtue of multiple scans, starting from the bottom in the transverse inscription geometry. These tracks surround the core, which can now be arbitrarily shaped [112, 205]. But the fabrication of such a structure takes a significantly longer time, up to N times, where N≈20∼40 is the number of tracks which surround a core. Although the translation speed of a sample can be slightly increased, the fabrication of each WG still takes a few hours. The induced RI contrast remains low, limiting applications to straight waveguides only.

After analysis of the available alternatives for laser systems, we have undertaken experimental trials on direct inscription using two newly emerged HRR fs systems, both operated at the repetition rate of more than 1 MHz.

One set of experiments has been performed at the research laboratory of *IMRA* (Freemont, USA), and a second set was carried out in the Max-Plank Institute of Quantum Optics (Munich, Germany). First, we tested a hybrid, Yb fibre-based laser system, μJewel D-400-
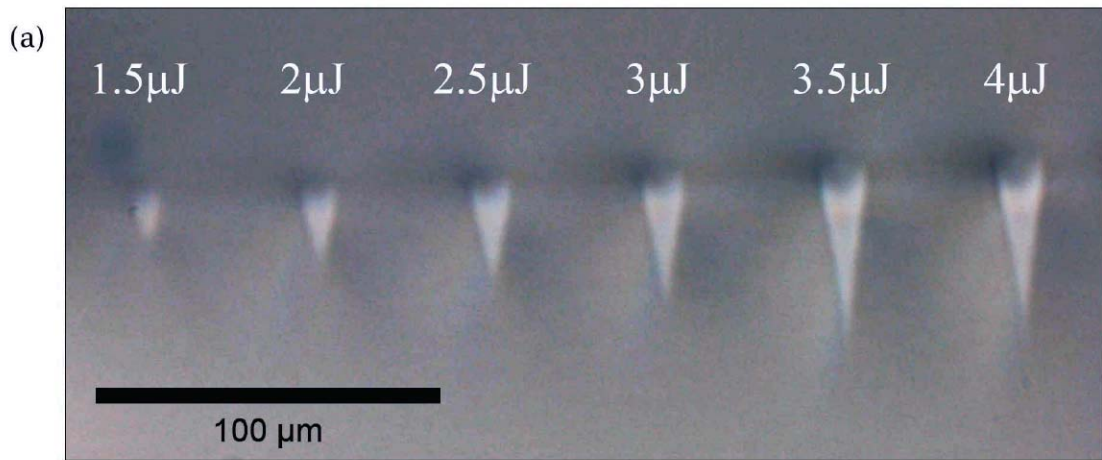
Figure 5.1: Transverse cross-section of the waveguide written in fused silica by LRR laser system vs. function of laser pulse energy. Note the change in shape at higher energies. This photo is reproduced from *Fig.5.10 a)*, from page *128* of the PhD Thesis of M.Ams.

VR by *IMRA*, which had 300 fs pulse duration at the wavelength of 1046 nm and 1 MHz repetition rate, while during the second set of trials we attempted to fabricate fs waveguides by 11 MHz RR, operated at 800 nm CPO with sub-30 fs pulse duration.

In the first set of experiments we observed that strong smooth waveguides with a circular cross-section can be fabricated in pure fused silica samples only when second harmonic of fundamental frequency (λ=525 nm) was used. In the second set of experiments we did observe a record-high induced refractive index contrast, but not in the form of smooth tracks, albeit we used continuous scans of the sample with a speed of a few mm/s, and the repetition rate was even higher: 11 MHz. The waveguides were in the form of a periodic chain of pearls or bubbles [25]. However, in some small sections between the bubbles we found strong and very well defined smooth parts which, if they can be made continuous, would create an "ideal" waveguide.

Based on the analysis of the experimental data obtained, we chose an 11 MHz, Ti:Sa based, CPO fs laser system. The only commercially available version at that time, similar to the one used in Munich, was the *Scientific-XL* laser by *Femtolasers* (Austria), which is described in Chapter 4. For this system a new femtosecond laboratory was designed and

built at Aston in 2006-2007; a photo of it can be seen in Figure 4.6.

In order to characterize inscribed waveguides we designed, built and commissioned a diagnostics lab. Earlier, in 2004, our group deployed a dedicated brightfield/differential interference contrast (DIC) microscope *Axioscope-2 MOT* (by *Zeiss*), for which we adopted the software for measurements of the refractive index: quantitative phase microscopy (QPm) by *IATIA* (Australia). More details are given in Chapter 4 and in particularly Section 4.6.

Advanced optical microscopy combined with the quantitative measurements using the QPm technique were the key to success, not only for the optimisation of WGs fabrication described in this thesis, but also for a number of other projects undertaken by the Photonics Research Group since then, see for example papers [18, 38, 112, 133, 206].

5.1.2 Femtosecond inscription by sharp focusing glass micro-objectives

To fabricate a smooth waveguide in transverse inscription geometry by LRR CPA system, the well-known sharp focusing approach was initially tested. We found that a smooth waveguide can be produced in silica glasses only by pulses shorter than $\approx$150 fs. In the majority of cases the reflective 36× objective was used (by *Davin Optronics*). The maximum refractive index contrast achieved in this configuration was $5 \cdot 10^{-4}$ [207]. It was obtained for the sample translation speed of 10 μm/s. The inscription window, or the ratio of pulse energy at the inscription threshold (80~90 nJ) to the pulse energy at damage (140~150 nJ), was found to be very narrow, just about 50% for the pulse duration of 120±10 fs. For a longer pulse the inscription window becomes even narrower. This contrasts with approximately 600 % windows reported by Guo et al. in [164]. We believe that there are two reasons for this. First, researchers often report their tracks to be waveguides without the damage, as in the above mentioned paper by Guo et al. The conclusions they arrived at depend on the visualisation procedures used. The second reason, which seems to be relevant to our case, is that the microscopic objectives used are not common. Usually an unknown design of these micro-objectives and, especially, heavy types of glass may change the focusing dynamics even inside the MO, which is often made of a few different types of glass in order to remove chromatic and other aberrations. The chromatism, aberrations and accumulated non-linear phase changes may affect the later focusing in the sample, as explained in Sections 3.2.1-3.2.3. Despite the importance of wavefront control, commercial tools for this are not available or
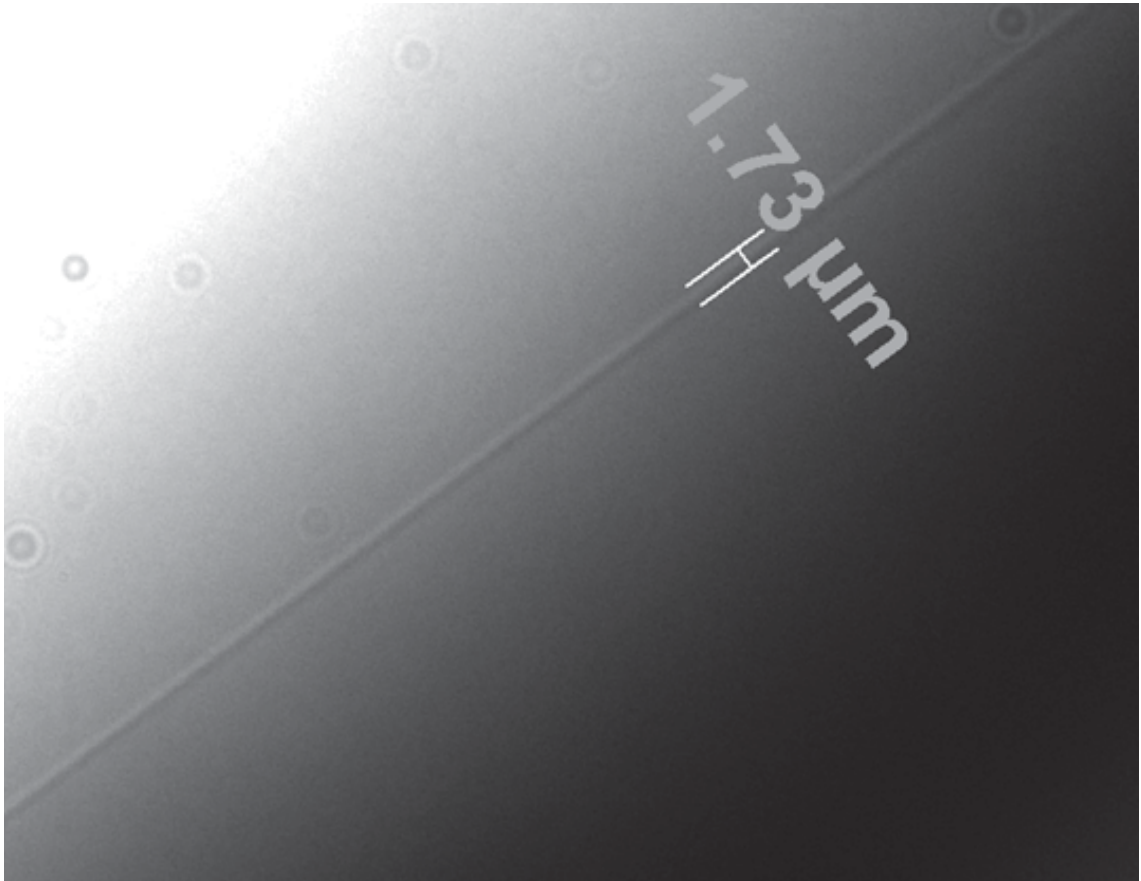
Figure 5.2: DIC microscopic image of smooth waveguide formed at sample translation speed of 10 μm/s, with pulse duration of 120 fs (FWHM); and reflecting microscopic objective 36× (NA=0.5); focusing depth is 200 μm.

are rather expensive, as well as special objectives for femtosecond micro-machining. Thus we had to carry out extensive experimental trials in order to find proper focusing conditions/optics and to optimise the regimes of inscription for each particular layout.

A typical waveguide obtained by LRR fs laser and sharp focusing has an elliptical cross-section with the dimensions of 2×6∼12 μm, almost regardless of the type of micro-objective used. This elongation of the modified area in the direction of laser propagation is mostly due to the spherical aberration (and chromatic one - in the case of glass MO), as well as the non-linear effects, such as beam filamentation. Due to the elliptical shape and low RI contrast usually obtained by LRR systems, even the best waveguides were found to be weak, with the V-parameter of less than 1 at telecommunication wavelengths [8]; they also have high bend, coupling and propagation losses.

One of the most serious drawbacks for LRR systems is the duration of the inscription process. Taking into account a multi-hour inscription time and the cost of the laser system and auxiliary equipment, it is difficult to consider the method of direct fs inscription to be practical in this case. The stability of the laser system also becomes an issue: conditions in the laboratory may change during the long processing time, so the interference of an operator may be required for minimisation of the pulse duration by compressor adjustment, for beam steering and its alignment into the input pupil of the micro-objective, etc.

There are some issues with our laser system as well, which appeared after shorter intervals. We noticed some variations in the output power of our laser during periods of about 4∼5 min. It was found that these cycles are due to the change in the temperature of the cooling liquid (of less or about 0.1°C) in the laser chiller reservoir. Since we intended to keep the induced RI contrasts quite close to its maximum value, such variations may cause damage, which can harm the quality of the individual waveguide and thus devices made of them. Note that $\pm2\%$ variation in the laser pulse energy corresponds to at least $\pm10\%$ variation in the rate of the multi-photon ionisation.

As a result feedback and control over laser pulse energy were necessary, so the scheme for on-line laser power monitoring and automatic corrections was designed (and built by Yicheng Lai). Its implementation allowed a closed loop stabilization (Figure 5.3), which addressed the issue of output power instability.

Usually the LRR inscription produces structures with a small lateral size. In the case of limited RI contrast, the only option left is to increase the "diameter" of the waveguide in order to make it stronger. There are a few approaches to do this: the first approach consists of inscription of a "bundle" of tracks positioned close to each other; the second is to shape a beam-waist to inscribe wider tracks. For example, astigmatic shaping of the laser beam attempts to increase the V-parameter by increasing its diameter. As was mentioned above, this can be done by using either an optical slit, as described in the paper by Ams et al. [24], or a cylindrical telescope, as suggested by Oscellame et al. in [71]. This could resolve both the issue of small WG diameter and its elliptical shape. However, there are some problems with both approaches, which are still to be addressed.

Generally, for any type of astigmatic beam one has to use an objective without the obscuration of a central area. Such MO are typically made of glass. An astigmatic shaping

a)   b)
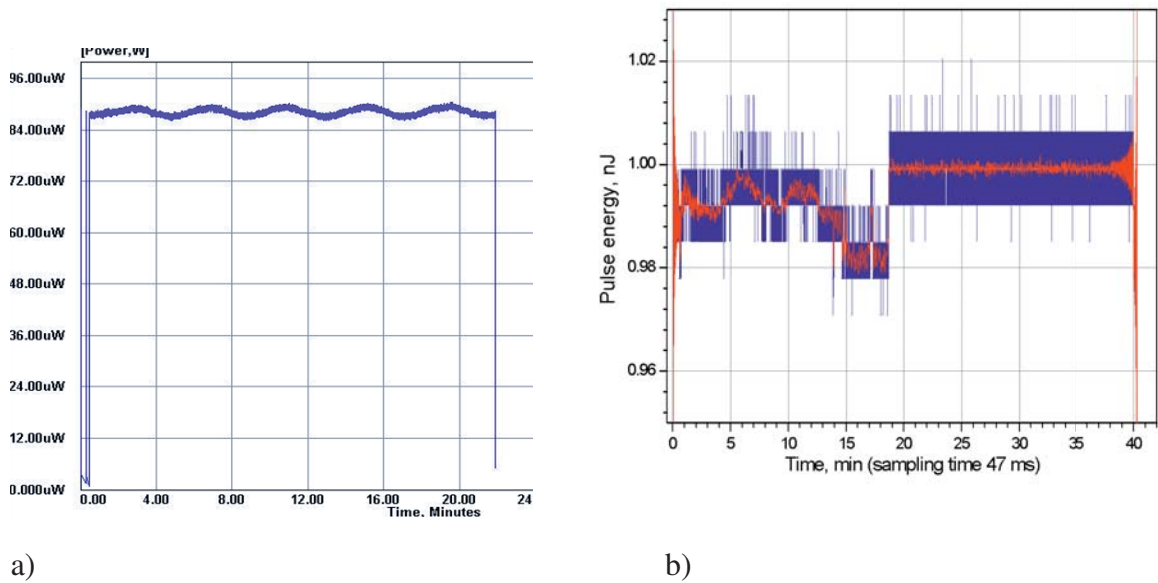
Figure 5.3: Laser pulse energy, measured in each pulse over a period of 20 min without (a) and with active feedback (b). Note the suppression of slow changes (period about 5 min).

demands much higher laser pulse energies on target, thus various non-linear effects (including MO damage) are inevitable.

In our realization, the set-up for inscription with astigmatic beam had a telescope, made of two plano-convex cylindrical lenses. When the elongated axis of the focal spot was perpendicular to the direction of translation of the sample, we observed a self-modulation of the refractive index along the track. This modulation causes elevated scattering losses, and this process was beyond our control. We tested a number of standard MO to focus collimated Gaussian beam with elliptical cross section. In all cases we observed a self-modulation effect; the phenomenon, which resembles a cumulative nonlinearity, has also been observed during the inscription of type-II fibre gratings by NIR femtosecond lasers in [88].

The astigmatic shaping seems to be less problematic when the optical slit method is used, but the method has very low efficiency, as a significant fraction of the laser pulse energy is dumped by the slit. Also periodic and a-periodic perturbations during the fs inscription tend to be the rule rather than the exception. Self-organization processes of various types occur in all dielectrics we have dealt with, starting from polymers and up to the hardest laser crystals.

Despite all these difficulties, fs beam shaping is far from being exhausted, although its successful application requires at least two conditions to be met: good quality focusing optics

113
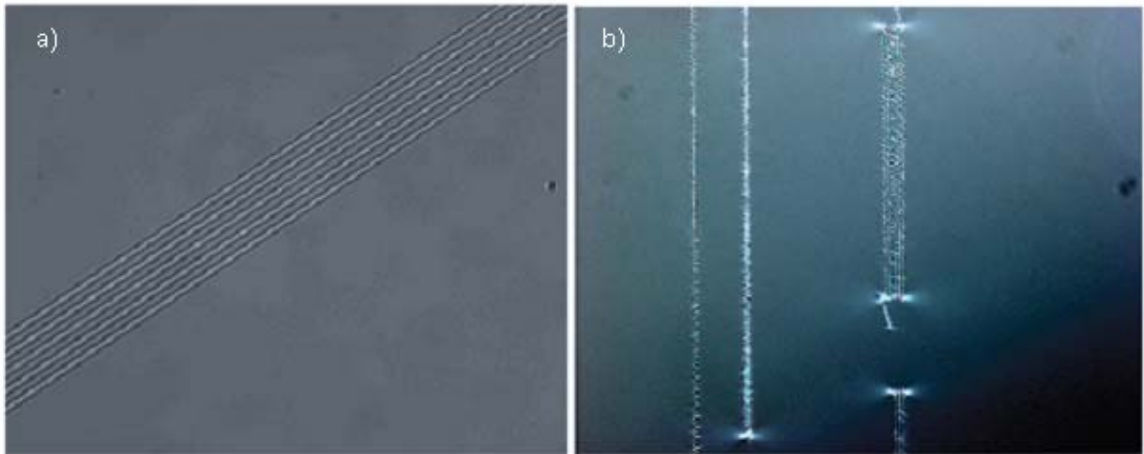
Figure 5.4: Bundle of five waveguides (a) and dark-field microscope image (a visualisation of locked stress under crossed polarisers, (b).

with a high damage threshold; and the wavefront monitoring tool with, possibly, adaptive control over this wavefront.

We also found that the inscription of "bundles" made by multiple tracks inscribed close to each other can produce strong cross-talk between the closest tracks in fused silica and other materials, most probably due to long-ranging mechanical stresses in the glass surrounding the fs WG. This phenomenon does not allow low-loss waveguides to be fabricated by LRR fs laser. Every successive scan makes these stresses even more pronounced. This seems to be a feature of both the LRR fs inscription with sharp focusing itself, and fused silica as a material.

5.1.3   Inscription by astigmatic beams. Concept of depressed cladding.

The need to increase both induced refractive index contrast and sample translation speed demands higher laser pulse energies. When the power exceeds the critical power for self-focusing, nonlinear self-focusing leads to elongation of the filament, and out-of-control energy deposition process and thus waveguide parameters, which are strongly dependent not only on the material but also on laser energy and pointing instabilities and wavefront quality. This is more important for a wide-band-gap optical material which has a high inscription threshold, as for example fused silica or YAG-crystals.

a)   b)
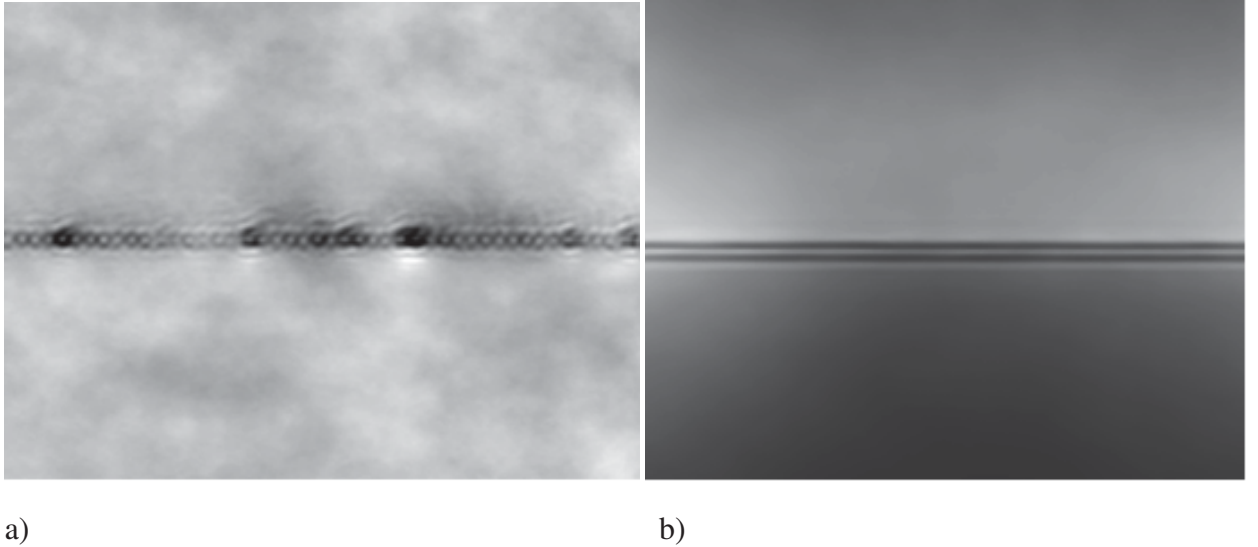
Figure 5.5: Example of inscription with sharp focusing in YAG:Nd^{3+} without a cylindrical lens (a) and with the cylindrical lens of $F = -350$ mm at the depth of $150\,\mu$m (b).

To suppress self-focusing we found experimentally how to use an astigmatic beam. As follows from the analysis for the sub-critical case in Sect. 3.2.4, there are a few ways of introducing astigmatism. The case we are referring to is identical to the one considered in Section 3.2.4, when beam dimensions of the laser beam remain the same $a_x = a_y$, but a wavefront has different curvatures in orthogonal directions $C_x \neq C_y$. As was found experimentally, the introduction of a negative cylindrical lens in front of the microscopic objective enables one to produce smooth tracks [21]. It is essential that the translation speed may be at the same time 10 times greater than the one used with sharp focusing (about $10\,\mu$m/s). The absolute value of the refractive index contrast induced also slightly higher, reaching values of about $1{\sim}3{\times}10^{-3}$. We found that in most crystals the sign of the induced refractive index change is negative. This seems to be a common feature for crystals, as they have a dense arrangement of atoms, so that disorder introduced by a fs laser could only decrease the density by introducing some defects, for example non-bridged or broken chemical bonds, thus creating new absorption bands. Our approach is simple and robust, as the alignment of a single plano-convex cylindrical lens is simple due to its long focal distance. Additionally, we found that energy utilisation increases to about 50% as compared to the case of an axially symmetric beam [21].

This approach has enabled the fabrication of low-loss structures, which were described in patents [15] and a number of papers [19], [112], [205].

115

5.1.4 Inscription with low-NA focusing

In this section we describe experiments with focusing using low- or medium-NA optics. Below NA<0.3 the area of the focal spot is larger than S_{cr}, so the nonlinear effects might contribute significantly to the focusing dynamics of the beam. The details on the different focusing optics used are combined in Table 5.1.

NA	0.8	0.65	0.5	0.45	0.36	0.08
F, mm	3.	4.	1.6	2.5	8.6	25.
WD, mm	0.6	0.9	13	2.5	8.6	25.
MO losses, %	30	15	85 [1]	5	15 [2]	2 [3]
Comment	Plan-Apo	Plan-Apo	LD Plan-Apo	Asph.Opt.	Refl.MO	Refl.Mirr.
Made by	*Zeiss*	*Zeiss*	*Mitutoyo*	*Newport*	*Davin*	*Edmund*

Table 5.1: Focusing optics used in experiments on direct inscription with LRR system. Notes on data presented: [1] the attenuation is due to a mismatch of beam and input pupil diameters; [2] in this case an obscuring of the central part of the beam occurs; [3] this small attenuation is due to the reflection loss of gold-covered off-axis parabolic mirror.

In the first set of experiments an off-axis parabolic mirror (OAPM) with both diameter and effective focal length of 25 mm was used. Focusing by OAPM completely eliminates damage and nonlinear effects in the optics. In the second set of experiments we explored medium-NA focusing when the HRR CPO laser was focused using a short-focal-length aspheric lens (by *Newport*) [25].

In the first case the radius of the beam at $1/e$ intensity level, measured by the closing apertures method, was 2.5 mm. So the effective NA in this case was $\approx$0.08. The analytic formulas obtained earlier in Section 3.2 emphasize the importance of self-focusing and beam filamentation for input peak pulse powers below the critical power P_{cr}. In contrast to this, in experiments we almost always exceeded this threshold, sometimes significantly.

The reason is that the necessary condition for inscription to occur (Section 3.2.1) is not sufficient. As was observed in the experiments, the multiphoton absorption does not guarantee permanent modification of the refractive index. It may be that the MPA produces free electrons close to the bottom of the band-gap, so that their (radiational) relaxation could not generate a sufficient deposited energy density in the material. Only after the "avalanche stage" begins, its possible for the amount of energy deposited and its density to reach the
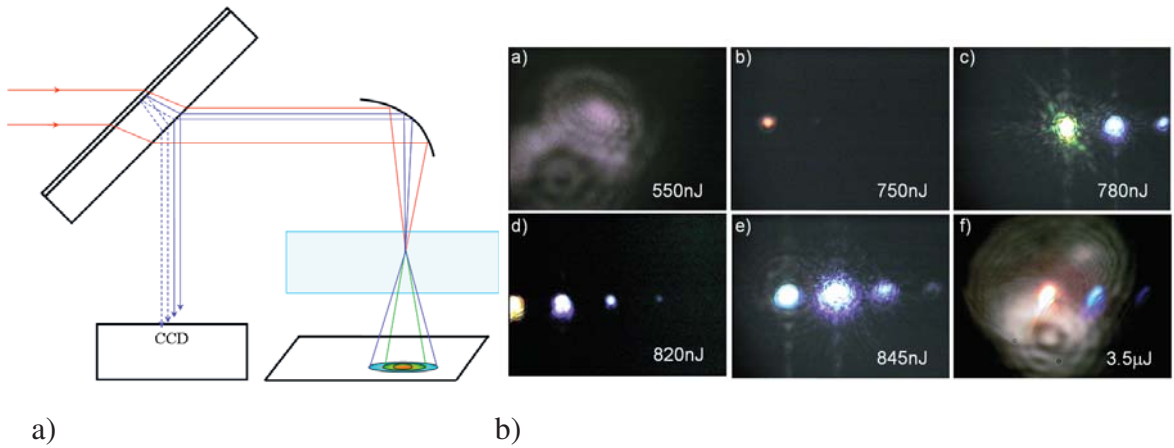
Figure 5.6: Optical layout for low NA inscription and continuum observation (A). The dichroic beam-splitter has AR-coating for 800 nm but highly reflective for green and blue wavelengths on output surface. And images of the continuum observed (colour online) at different laser pulse energies as marked on the corresponding frames. The CCD image in the case of small astigmatism was introduced (B, frame f).

modification threshold. The radiation quanta produced by energetic electrons can have shorter wavelengths than the band-gap, so they will be re-absorbed in close proximity to the emission point. In such a way the energy deposition is more localized than for "cold" free electrons, which are created after the MPA stage.

When the pulse energy is so high that the peak power is above the critical power for self-focusing, a super-continuum generation can be observed, which is a manifestation of the Kerr nonlinearity. Indeed, with the experimental arrangement described in Figure 5.6 we managed to observe multi-coloured radiation, conically emitted and with different colours at different angles. Its appearance was strongly dependent on the pulse energy and the focusing depth, as presented in figure 5.6, b). The sample alignment becomes an issue in this case due to extended confocal length.

Surprisingly, the inscription window was the widest for all the different methods. The distinct feature of this method is: in order for permanent RI modification to occur, the laser has to be focused deeper inside the material than in other cases. This can be explained by the fact that the longer distance travelled over the glass strengthens the non-linear effect, while allowing damage at the surface to be avoided.

The best inscription was found with the orange to green continuum, see frames a) to d) in figure 5.6 b), when the laser pulse energy ranged between 750 and 820 nJ. At much higher pulse energies (1,500 nJ) and if the beam did not exhibit any aberrations in reflection from

117

the sample surface, the formation of multiple filaments can be observed.

However, when a small astigmatism was introduced by an angular tilt of OAPM, we observed an inscription of smooth tracks again, with pulse energies up to 3,600 nJ. Thus the inscription window can be made much wider in this case than by sharp focusing, by controlling the astigmatism of the beam.

The maximum refractive index in such smooth tracks obtained by a single scan with low-NA focusing can be obtained at a depth of about 600 μm, when the speed of inscription is 50 μm/s, and pulse energies are ranged between 600 and 780 nJ. We found that this regime allows for both multiple scans over the same track, sometimes up to sixteen times, and bundles of waveguides with practically no separation or even overlapping (Fig.5.7). In both cases neither residual mechanical stress nor damage have been observed under cross-polarisation examination. The most characteristic features of the inscription with "low-NA" focusing are: a strong white or multicolored super-continuum with a conical radiation diagram, which strongly depends on pulse energy and is sensitive to the depth of focusing; the widest inscription window, exceeding a hundred percent; and no residual stress or self-modulation left in the material under crossed polarisers.

The individual core of the WG after a single scan has dimensions of about $5\times30\mu$m, with the maximum QPm-measured phase four times less than for a standard fibre, thus the RI contrast has to be below 0.4×10^{-4} for a single scan. After eight consecutive scans over the same path the phase retardation across the waveguide can reach $0.2\sim0.3$ rad (see figure 5.7, a); thus, the contrast of RI reaches the value of $0.8\sim0.9\times10^{-3}$.

These waveguides can guide visible radiation mainly due to their dimensions. Indeed we did observe a good coupling of CW laser (532 nm) and lowest propagation loss for a dual-core waveguide inscribed at 650 nJ (top structure in figure 5.8, a)). This experiment revealed that two parallel tracks separated by a gap (of 5 μm) produce stronger guiding than two consecutive scans over the same region, as expected. Even the two-core guide still has an elliptic-shape mode (see Fig.5.8, b). In order to make it match better the circular mode of the standard fibre, a structure made of three tracks has to be inscribed (see Fig. 5.8, c)).

Analysis of the inscription results with the OAPM revealed that the inscription regime strongly depends on mirror alignment, for example, when the mirror is slightly tilted and an astigmatism is introduced. This can manifest itself on a monitoring camera after reflection

118

a)   b)
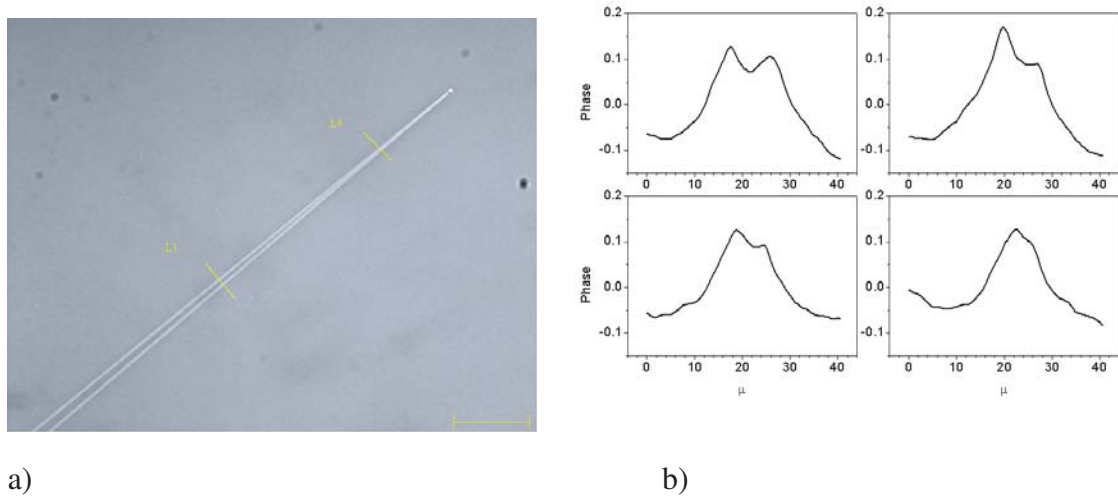
Figure 5.7: Phase retardation map of the structure obtained by low-NA focusing (a). RI contrasts at different cross-sections (b) after 8 consecutive scans over the same pattern.

a)   b)
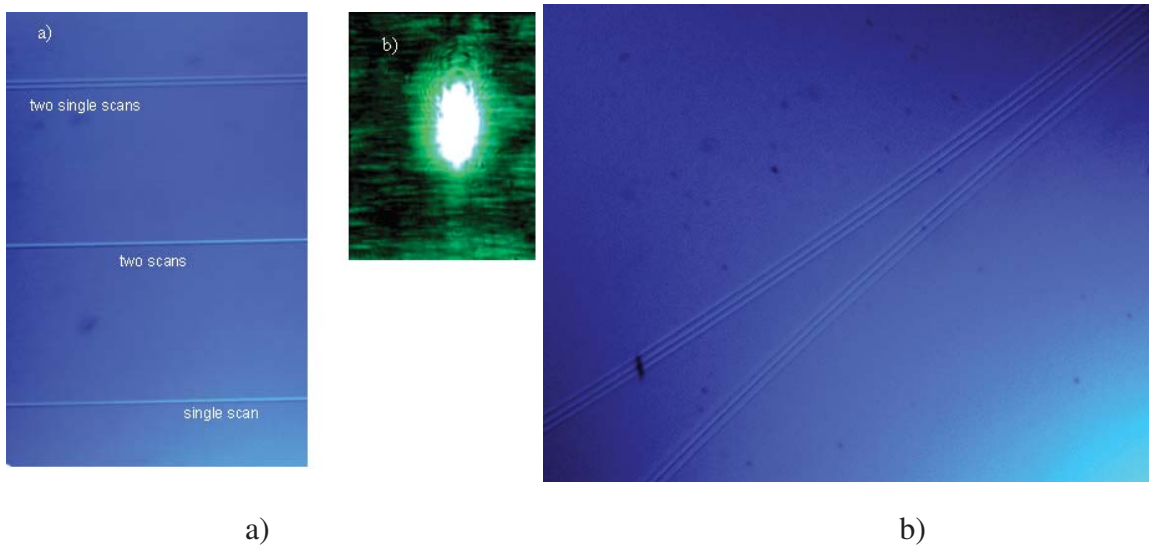
Figure 5.8: Femtosecond waveguides inscribed with low NA focusing optics (a). All tracks obtained with 650 nJ pulse energy and 10 μm/sec translation speed. Two non-overlapping scans (a, top), two scans on top of each other (c), and a single scan (bottom track) were done respectively. The strongest output is observed for the double-core (top) track. The output mode (b), and a coupler (a) made by such low-NA fs inscription.

119

from the sample surface as an elongation of the round focal spot. More importantly, we found an increase in the damage threshold for such astigmatic (or "distorted") beams, namely that the damage can be postponed for up to 3.600 nJ. However, no reliable procedures could be found for day-to-day OAPM alignment, so inscription regimes were not completely reproducible. An upgrade of the set-up in terms of beam wavefront monitoring was required. The only reliable experimental method which can be derived consists of achieving similar colours for a continuum, generated in glass (orange to orange-green). This is difficult to quantify, and thus to use in practice. When a blue or white continuum appears it signals the proximity of the damage. Any wavefront distortions may change previously optimised regimes and would require the operator's interference. Given the slow sample translation speed, the stability of the output power, pulse duration and wavefront divergency has to be better than a few percent. Unfortunately this was beyond the specifications of the LRR CPA system.

We found that the continuum occurs only at a certain depth, for a particular pulse. The chirp does depend on the amplifier gain and saturation, and thus is extremely sensitive to variations in the pump energy provided by the Q-switched DPSS laser (Evolution) as well as its beam-shape. With the changes in the temporal chirp the optimal inscription depth also varies. More importantly, the design of the 1 kHz CPA laser system and its complexity do not allow effective interference in order to stabilise its output. Additionally, with such loose focusing it is not possible to align the sample with the tolerance required without use of an auxiliary laser with sharp focusing optics. This inevitably makes the inscription system even more complicated. In our realisation, the continuums' colour serves as an indicator of the optimal depth. This requires a lengthy "trial" inscription in order to align the sample strictly perpendicular to the laser beam.

As regards periodic structures, using $34\times$ reflecting MO a 530 nm periodic perturbation can be inscribed in the bulk of a fused silica sample [39]. Such periods enable the fabrication of components for applications at the telecom range [132]. Unfortunately with loose focusing we were able to fabricate periods shorter than 1.5 μm. The final remark is on the uniformity of the waveguides. It was found that more uniform structures can result from multiple overlapping scans, and the losses are also lower, possibly due to the effect of the induced RI saturation. However, propagation and especially bend losses remain unacceptably high.

Overall, a method of direct inscription by "loose focusing" possesses the major drawbacks of the LRR inscription, such as low RI contrast, high bending losses and slow inscription speed.

In the second case, we used a CPO system and explored focusing using a single aspheric lens [25] as well as standard micro-objectives, following the earlier publications by Herman's group and the IMRA research labs [208]. However, in our case the laser had a sub-30 fs pulse duration, and a step-wise spectrum of about 70 nm in width (Figure 5.9). The conclusion we reached at the end of this work was that a thick, aspheric, single lens cannot be used due to strong chromatic aberrations of the glass. In the experiments we produced tracks with highly elliptic cross-sections [25]. There was a tendency for self-arranged structures to appear at laser powers above certain values, which is quite common to both LRR and HRR systems.
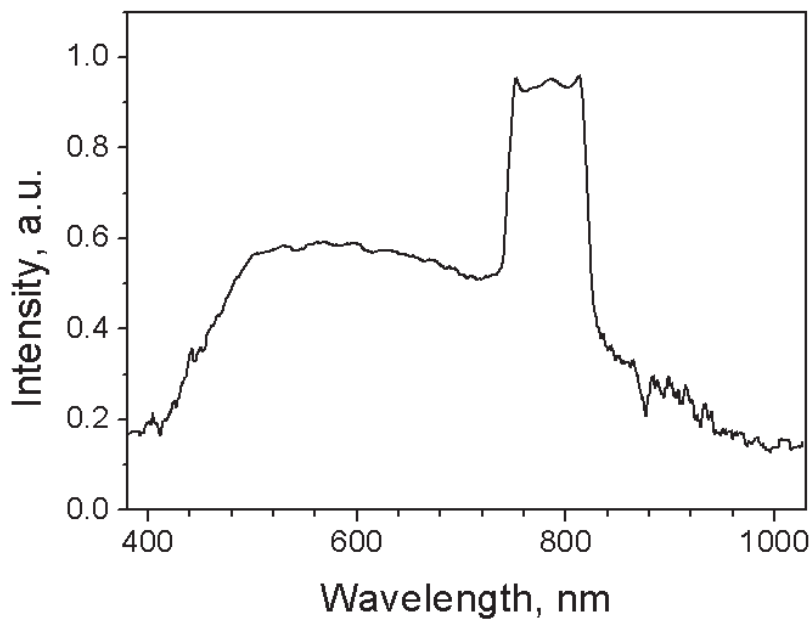
Figure 5.9: Broadband spectrum of the emitted continuum radiation when a self-arranged pearl-chain structure is formed. Note almost square-shape laser spectrum at about 800 nm.

It was found that smooth but weak waveguides can be inscribed with lower pulse energies below 26 nJ (recall that the laser has 11 MHz repetition rate). However, the attempt to increase the RI contrast revealed a sharp threshold at about 1.7 MW. Note that the pulse peak power is below $P_{cr} \cong 2.3$ MW. Above the threshold of 1.7 MW a bright white continuum

appeared (its spectrum is in Figure 5.9), and the waveguides suddenly became self-modulated (Figure 5.10) in width, almost regardless of the translation speed and laser pulse energies used [25]. We believe that the effect was due to a self-influence of the beam, which is often triggered by aberrations of the wavefront [209]. These were imposed by achromatism of an aspheric lens in our case. Strong sensitivity to wavefront distortions has been observed both in our experiments (Section 5.2) and by other groups, see for example the bibliography in the abovementioned paper by Kazansky et al. [209].

a)   b)
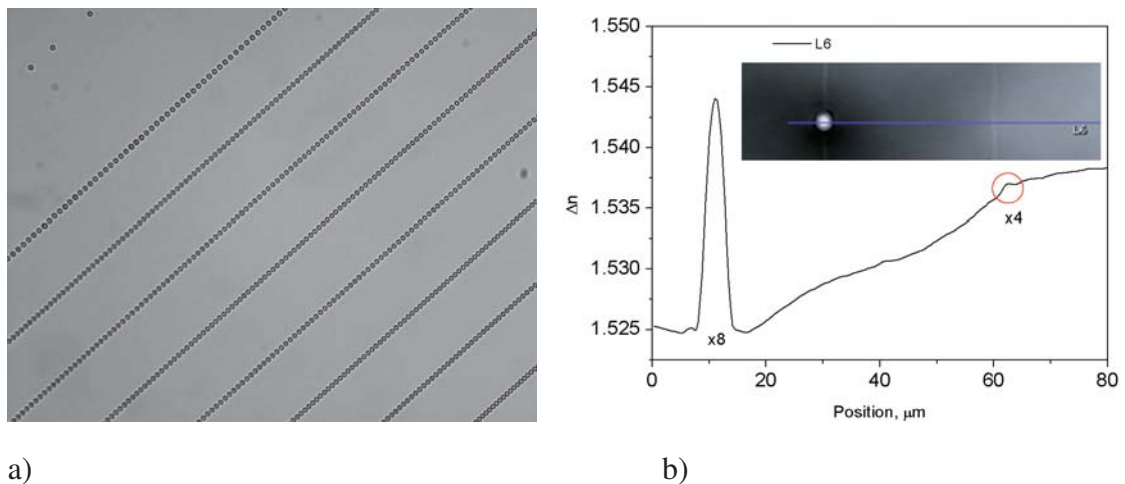
Figure 5.10: Example of self-organization in fused silica (a), and a comparison of the induced RI contrast in the pearl and across a smooth waveguide after 4 scans (b) and across the pearl.

We believe that the main reason for this sudden transition from smooth to modulated waveguide is due to a change in linear absorption of fused silica with temperature, which is referred to as "regime of heat accumulation" [72]. The very broad continuum observed (Figure 5.9) supports this conclusion, and it corresponds to a black-body radiation with the temperature of more than 4000 K.

Finally, in Table 5.2 we summed up the results for LRR inscription with different methods and focusing optics used. For comparison the last row provides results for HRR fs inscription, which we describe in the next Section. The undoubted superiority of HRR fs inscription is evident.

Method	Waveguide quality, shape	Dimensions, [μm]	Refr. Index ($\times 10^4$) (V-param.)	Losses- propagat., coupling, bending	Multi-Scan	Bundles	Grating with min. period, [nm]	Inscription Speed [mm/sec]	Energy of the Pulse [nJ]	Commentets
A. LRR and sharp focusing	smooth, elliptical, AR (8:1)	1×10	2 to 6 very weak ($V \lesssim 0.6$)	high high high	not possible, irregular, (due to stress)	irregular	535 (Λ=250 nm) (with TH)	0.01	30 to 500	locked residual stress in all materials
B. LRR and astigmatic beam shaping	smooth, modulated can be circular	3 to 10	5 (10) due to size	low, avrg., high	not possible irregular (due to stress)	possible	900	0.01 up to 0.1	$>10^3$ up to $10\,\mu J$	one of the best LRR method; glass optics often get damaged
C. LRR and non-linear beam shaping	smooth, elliptical AR (6:1)	2×15	5 (10 - bundle)	avrg., avrg. high	possible	possible	2000	0.1	500 up to 3500	promising technique for LRR systems
D. HRR, and sharp focusing single lens	smooth pearl-chain first AR (10:1)	1×10	<10 ($V<1$)	high high high	possible at low energy	possible	870	0.1 up to 1	<26 or pearls	at multiple scans often damaged
E. HRR system, achromatic sharp focusing	almost circular, has a core & cladding, W-shaped	5/25 μm (core/cladd.)	>250 ($V \lesssim 7$) very strong	low low low	possible up to 16 times	possible	480 up to 10^4	$>$ 5mm/s up to 100	16 up to 52	the best technique so far, for both waveguides & WG gratings

Table 5.2: Comparison of different inscription methods with Low Repetition Rate system. AR - aspect ratio, TH - third Harmonic (of 800 nm).

5.2 Femtosecond inscription in borosilicate glass by CPO

The family of borosilicate optical glasses with its best known and most common representative member, BK7 glass, is one of the widely used optical materials due to the well developed fabrication technology, excellent mechanical, thermal and optical properties and uniformity as well as its low cost; it can also be made chemically stable, and has quite low absorption and a wide transparency window. Thus the establishment of inscription conditions in BK7 glass represents an important benchmark for the direct fs method. Additionally, as a multi-component glass, BK7 has a much lower glass transition temperature than pure fused silica. So its thermal properties are in the middle of the range for the majority of glasses, and this makes this glass an ideal candidate/host for the study of various thermal effects, which turned out to form the basis for the direct femtosecond fabrication method.

Preliminary trials on BK7 glass samples by *UQG* (UK) allowed us to determine an extended list of critical experimental parameters to explore. These are:

- laser pulse energy;

- translation speed;

- depth of inscription;

- polarisation state;

- direction of the sample translation;

- temporal distortions of the pulse;

- spatial distortions of the beam shape, e.g chirp, wavefront tilt etc.;

- other parameters, such as pulse duration, inscription wavelength, laser repetition rate, amplified background radiation, etc.;

- which optical layout and components are used, especially for beam focusing.

We tried to limit the list to the first five, while either keeping the rest of the parameters fixed or making their influence insignificant. For each set of parameters we had to use both forward and backward scanning directions. It helped us with an easy control over the compressor alignment and also eliminated issues with the tilt of a micro-objective, as it may

cause a wavefront distortion especially for the fs pulse [209]. This allowed us to avoid mixing all these reasons with the fundamental instability of the wavefront (even for an axially symmetric beam) when the pulse peak power approaches or exceeds P_{cr}, the critical power for self-focusing.
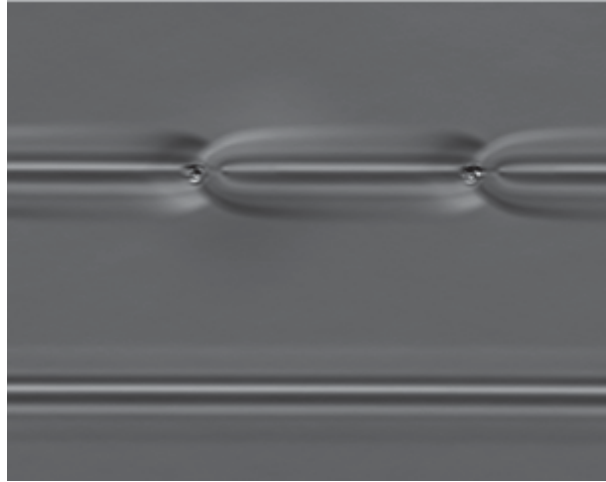
Figure 5.11: Demonstration of beam self modulation with poor micro-objective alignment: the waveguide is self-modulated when scanned in one direction only.

The presence of various aberrations, which are difficult to control, could manifest itself in different ways, for example as damage-like tracks appearing at one direction of scan only [209], or as self-started, stochastic modulation of tracks [25]. Overall the number of combinations of experimental parameters to explore was huge. However, there are only three (sometimes - just two) possible outcomes of experiments: i) weak or no inscription at all, ii) "good" structures, which might be useful, and iii) damage region (all depend on the task and criteria used). We performed extensive preliminary trials with as broad range of parameters as possible, based initially on simple estimates of the inscription threshold as described in section 3.2.5. Once approximate margins were found we selected narrower regions of interest for more thorough investigations.

In the next Section we present results for a reduced number of parameters, namely: sample translation speed varied from 20 to 60 mm/s with 5 mm/s step (9 values), pulse energy from 17 nJ to 30.7 nJ with a step of 3.5 nJ (5 values), focusing depth of 50, 60 and 70 micrometers (3 values), polarisation states (min 2 values) and two directions of scan. Even with two states of polarisation (X and Y, which are perpendicular and parallel to the direction of scan respectively) an enormous number of tracks had to be characterized: $9 \times 5 \times 3 \times 3 \times 2 = 900$.

So an express diagnostics method such as QPm (see Sections 5.2.3, 4.6) was vital for success.

5.2.1 Waveguide cross-sections

The inscription of a number of tracks was done using the setup shown in Figure 4.6. The microscopic view of fs track obtained is shown in Figure 5.12. Note that there is no dependence on the direction of scan whatsoever.

Brighter areas on Fig. 5.12, a) correspond to increased refractive index (positive laser-induced RI contrasts) or larger phase retardation or accumulated phase. The waveguides inscribed by HRR femtosecond laser have a characteristic W-shape, with the accumulated phase profile presented in Fig. 5.12, b).

a)   b)
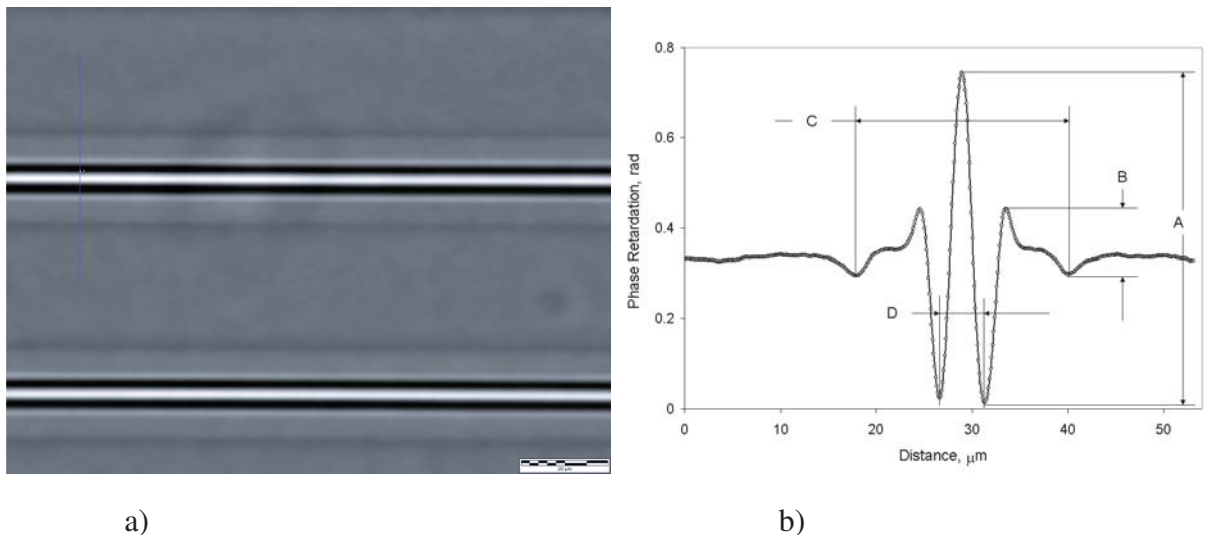
Figure 5.12: Phase retardation measured by QPm (a) for the waveguide inscribed with the laser pulse energy of 27.3 nJ, and 40 mm/s sample translation speed, when scanned in opposite directions. Scale bar is 20 μm. A cross-section of the accumulated phase map (b) in the direction perpendicular to waveguides. The parameters A and B represent peak-to-peak RI contrasts for core and cladding respectively, parameters D and C define the dimensions of the structure.

Using the analogy with the dispersion-compensated fibre index profile (also W-shaped), we suggest the following terms: the central area of the waveguide is called a core, and the peripheral or surrounding part is a cladding.

To characterize core and cladding quantitatively, the peak-to-peak values are used as explained in Figure 5.12. The analogy with step-index fibres is not perfect, as the waveguides are gradient rather than step-index.

a)   b)
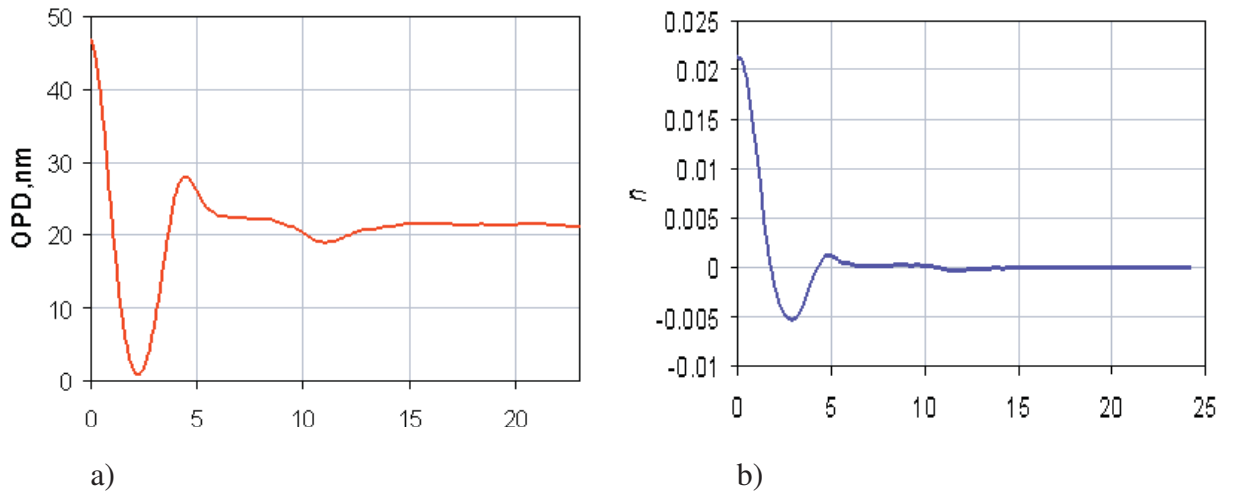
Figure 5.13: Cross-section of a phase retardation map obtained by QPm (a), and example of the reconstruction of the refractive index distribution using Abel inversion (b).

Using the accumulated phase map and Abel inversion procedure (described in Section 4.6) we reconstruct RI profiles for all of the inscribed tracks (Fig.5.13). Maximum measured RI contrast was found to be above 2.5×10^{-2}, which is about 5 times more than in the telecom fibre *SMF-28*.

Then BK7 samples were cut into two halves using a wire saw Model-15, lapped or grounded and polished from both edges to optical quality. After that they were explored under the microscope again, this time from the edges. The resultant micro-photographs for one of the the groups of tracks obtained with different sample translation velocities are shown in Figure 5.14. Indeed one can note the almost circular outer area of the waveguide, which we

20 mm/s   25   30   35   40   45   50   55   60
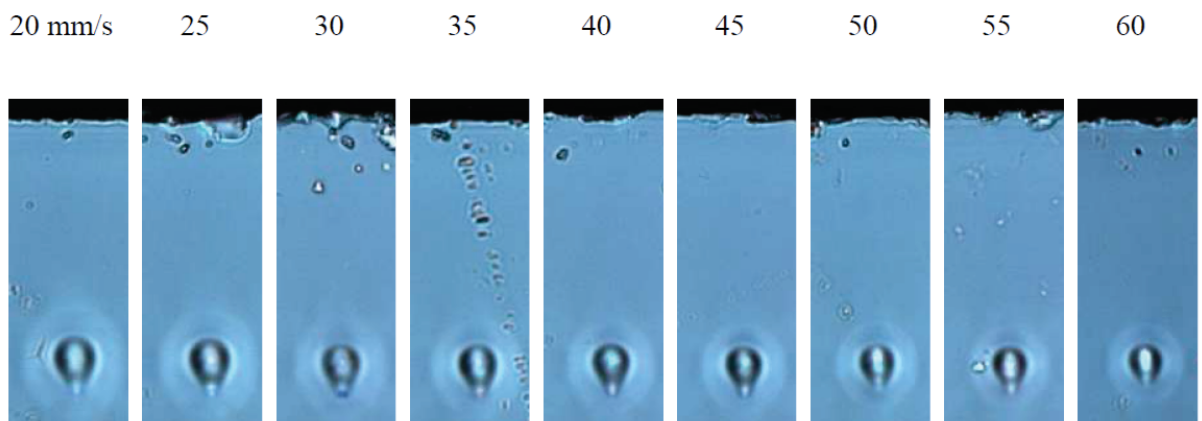
Figure 5.14: Cross-sections of the guides obtained by HRR fs inscription. All of the tracks were inscribed with different translation speed, which are shown above. Other inscription conditions are: laser pulse energy is 30.7 nJ; all tacks are at the depth of about 60 μm, which corresponds to 40 μm inward shift of the micro-objective.

called cladding. Its cylindrical shape is typical for the heat accumulation regime [130], [167]. The inner part (or "core") of the waveguide is slightly elliptical, with the minimum ratio of two axes being 0.8~0.9.

5.2.2 Waveguide dimensions

The dimensions of waveguides measured by the microscope are presented in Figure 5.15, where the following hierarchial structure of parameters is encoded into the serial number of the track: the lowest level of hierarchy refers to the direction of sample translation. This is used for internal control of wavefront quality, which we might not refer to in future as both directions of translation were identical. So first we change the value of the translation speed V. The next level corresponds to different focusing depths S or equivalent Z-axis shifts of the MO, after which we change the laser pulse energy E. Finally, the whole experiment was reproduced but with a different state of polarisation: **X**, **Y**, or circular polarisation. The tracks we inscribed were numbered *sequentially*, using the abovementioned hierarchy. The graphical explanation can be found in the insert as well as in captions to Figure 5.15 and in the text below.

The combined results for core and cladding diameters (or parameters C and D defined in Figure 5.12, b), are presented in Figure 5.15, where we put tracks for both polarisations **Y** - collinear and **X** - perpendicular to the track. As one can see there is practically no difference in the results for the two polarisations; however the irradiation with **X**-polarisation produces slightly larger cores when the laser pulse energy is at maximum and sample translation speed is at minimum. This may be attributed to the fact that the reflection from last three mirrors in our optical setup is slightly better for **X** polarisation due to the design of the broad-band multilayer dielectric coatings of those mirrors. Other possibilities include:

1. possible ellipticity in the laser beam with its longer axis positioned perpendicular to the direction of scan, **Y**;

2. additional elongation of a symmetric beam into slightly elliptic one, as predicted by the Fresnel refraction formula: the energy flow penetrates more fully for **p**-polarisation ray;

3. self-influence, and this can be understood from the fact that induced RI contrast may
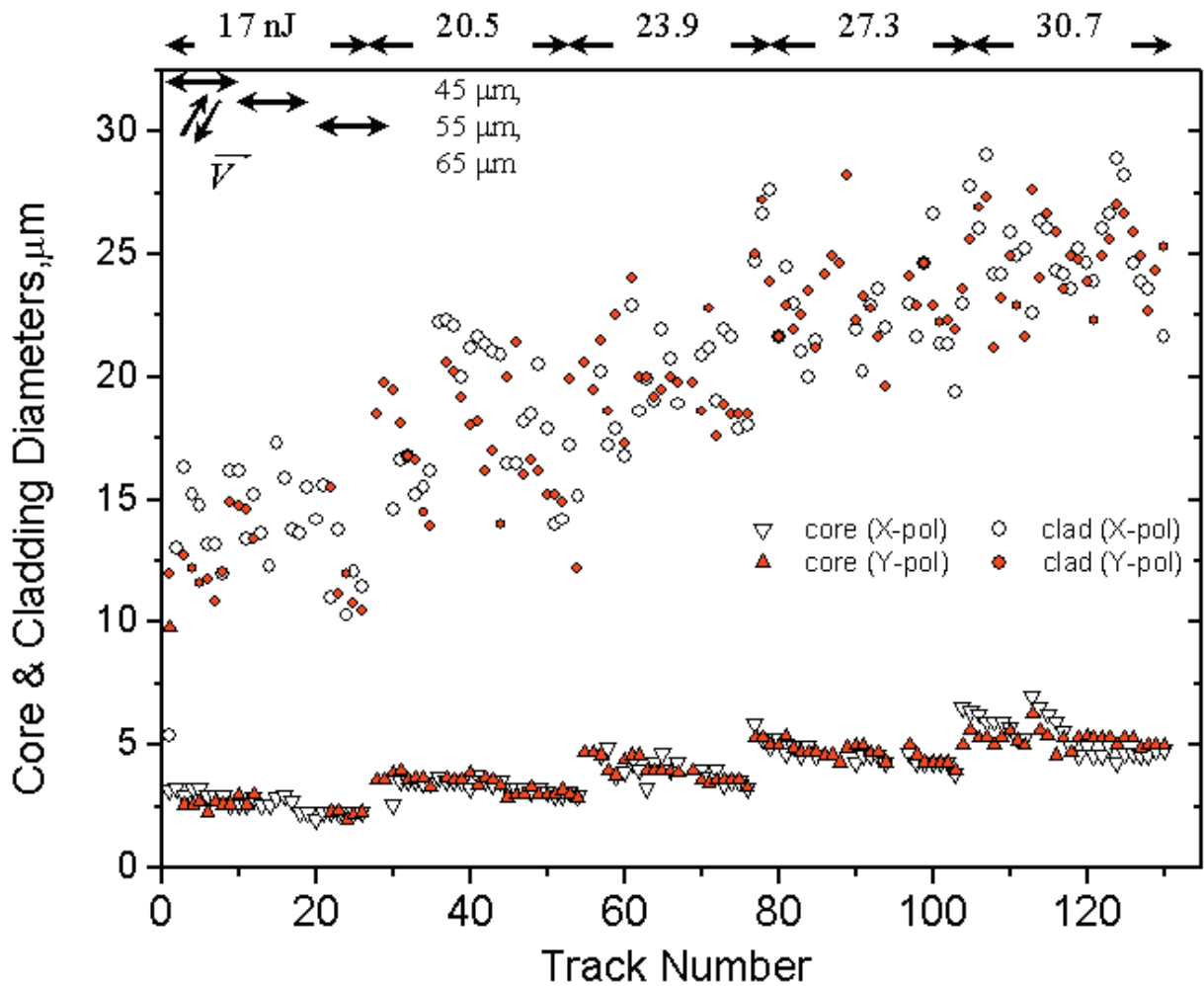
Figure 5.15: Core ($\triangle$) and cladding ($\bigcirc$) diameters for $X-$ (open) and Y-polarisations (solid). The hierarchy of numbering is explained graphically. The sequence of parameters change starting from the lowest level is explained graphically on top of the plot (see also text below). All data presented are for the same (forward) direction. Some points were dropped off - these are tracks with damage signatures.

be considered as a lens, which affects the focusing. The stronger the lens the shorter its focal distance. Inverse focus $1/f$ or the optical power of the lens, which is proportional to the ratio of $\Delta n/\rho$, where ρ is a characteristic radius of curvature of the modified area and Δn - induced RI contrast. A simple estimate reveals that fs-induced lens is about three times stronger than the sharpest MO used.

A proper analysis of the effect of femtosecond laser self-influence requires numerical solution of the system of Equations 3.1 and 3.2, which have to include the equation(s) for induced RI change of the media in response to the deposited energy. Such RI is the function of the illumination protocol, speed and amount of energy absorbtion, and it is not necessarily local, as for example a stress in the glass can induce a change in the RI surrounding this volume.

As can be seen in Figures 5.15 and 5.16, the decrease in core diameters (with increasing translation speed) is more pronounced at higher laser pulse energies. The drop in the core diameter with increasing speed was found to be more for deeper focusing.
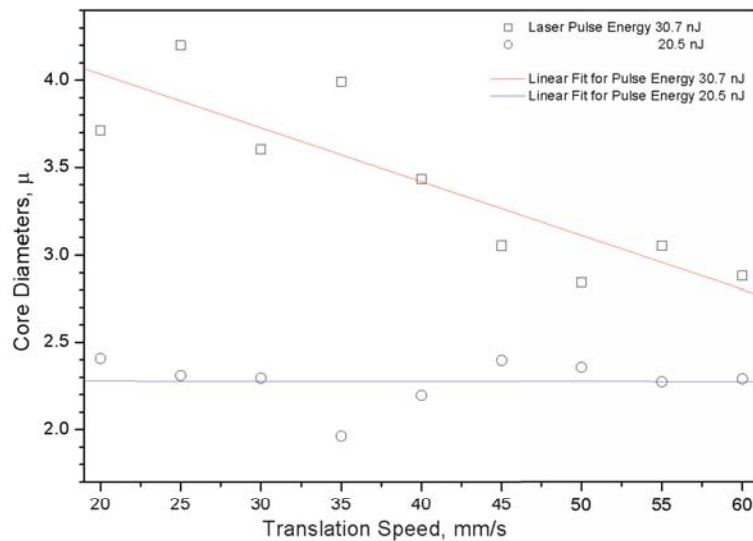
Figure 5.16: Dependence of diameters vs increasing translation speed of the sample for laser pulse energies of 20.5 nJ and 30.7 nJ at the depth (shift) of 55 μm.

Similar dependencies have been observed and reported in the paper by Eaton, et al (see Fig. 2b, 3 in paper [167]), but at slightly different average powers, perhaps due to the fact that in this paper there was no distinction between different parts of the waveguide. Both in

our and Eaton's experiments (see Fig. 5.15) the effect of reduction of the dimensions of WG was stronger at a higher repetition rate.

In contrast to the above cited paper, we explored a wider range of translation speeds. This seems to be possible only due to the much higher repetition rate of our CPO system. There is another effect, possibly related to the core-size shrinkage, namely that the refractive index contrast for the core increases with increasing speed of sample translation.

5.2.3 Core and cladding refractive index contrasts

Having measured the phase retardation maps for all tracks, we performed a reconstruction of the refractive index distributions with the help of the Abel inversion, as was described in Section 4.6. All these data are summarised in Figure 5.17 using the same hierarchy as was introduced in Figure 5.15. Such detailed information on waveguide parameters is often missing from other reports [167], perhaps due to the fact that the RNF-profilometry method they used is very time- and labour-consuming. Thus, in the paper by Eaton et al. an intuitive assumption was made that increasing the speed of sample translation, which decreases the energy dose absorbed per unit volume, should also reduce the induced contrast of the RI, as the latter one was *assumed* to be connected with the irradiation dose.
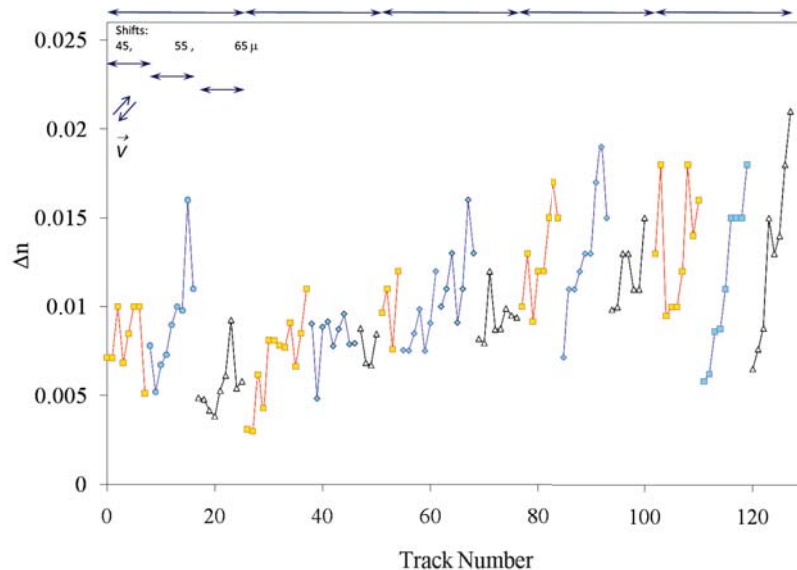
Figure 5.17: Induced contrast of refractive index for the core. The numbering of the tracks is in accordance with the hierarchy as on Fig. 5.15

As one can see in Figure 5.17, in our experiments we observed increasing index contrast for faster inscription in contrast to the assumption in [167]. Thus induced RI contrast is not connected to the irradiation dose.
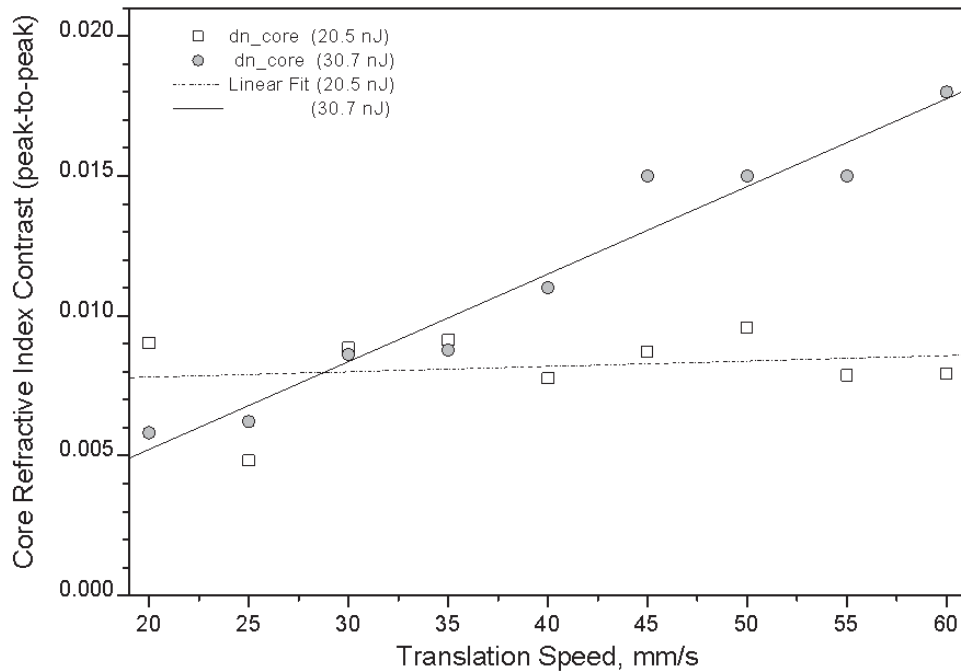
Figure 5.18: Induced refractive index contrast as a function of the sample translation speed. Laser pulse energies are: 20.5 nJ (dash-dot line, open squares) and 30.7 nJ (solid line, filled circles), the depth of inscription is about 84 μm in both cases.

The core RI contrasts increase with the *translation speed*, and in particular this effect is very clear for the highest laser pulse energy used - 30.7 nJ - and when the depth of focusing was at maximum (of about 100 μm; it should be recalled that the shifts of 45, 55 and 65 μm correspond to inscription depths of 68, 84 and 100 μm respectively). Detailed comparisons between the induced RI contrasts for core region vs the translation speed, for two cases of the laser pulse energies 20.5 nJ and 30.7 nJ, both at the inscription depth of 84 μm, are presented in Figure 5.18.

One would also note larger deviations of the induced refractive index contrast in the core, for example in the case of higher laser pulse energies (the third group of points from the end, which correspond to pulse energy 30.7 nJ and a focusing depth 64 μm). The variation could be attributed to a self-modulation of the core RI, as we will discuss later in the section related

to propagation losses.

This is the most important result, as it enabled us to increase significantly the contrast of RI (sometimes by more than 500%), as compared with other methods, including the ones listed in Table 2.4. The increase in RI occurs without damage of any kind, thus preserving the high WG quality and low losses. There was no damage in the form of periodic and a-periodic modulations, as for example can be observed in Figure 5.10.

In general, there are no quantitative models for the HRR inscription process as such, and thus no explanation for the effect of increasing RI with translation speed. Thus one can try to explore such effects experimentally. To probe the limits of the unusual effect (of increasing RI with increasing speed of sample translation) we made inscriptions at higher laser pulse energies and quicker sample translation speeds (up to 100 mm/s, the hardware limit of the Aerotech stage). The results, presented in Section 5.2.6, demonstrate the appearance of self-modulation of the RI but initially only in the central (core) area.
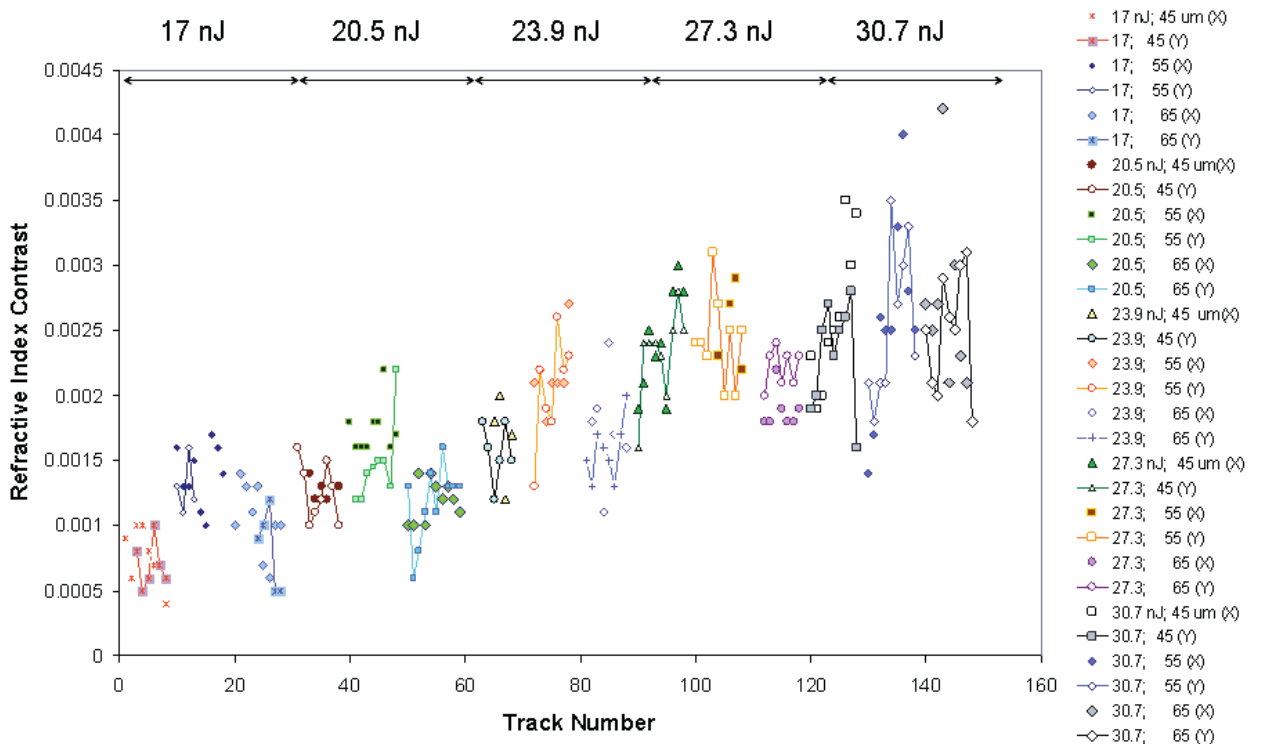
Figure 5.19: Cladding refractive index contrast (parameter B on Fig.5.15, b). The hierarchy of the track numbering is the same as in Fig.5.15. The points for groups with various translation speeds inscribed with Y-polarization of laser are connected by solid line for illustration purposes.

Another important parameter is the peak-to-peak RI contrast in cladding (defined in Fig.

5.12). Figure 5.19 provides cumulative experimental data for cladding RI contrasts using notations and style similar to the ones in Fig. 5.15. A comparison of Figures 5.17 and 5.19 leads to the conclusion that there is much less deviation in RI contrasts for cladding within the same group than in the case of core RI contrasts. There is also a different tendency with increasing sample translation speed. For example, quicker translation lowers the cladding RI contrasts, especially when the pulse energy is lower (see, for example, the case of 17. nJ, and for deeper inscription, e.g. at 100 μm).

Overall, there is no such dependence for cladding RI as was observed for the core indices when sample translation speed increased. Also we did not observe significant differences in the induced RI contrasts between the two polarisations, apart perhaps from the last two groups, (when E=30.7 nJ and shifts were 55 and 65 μm).

5.2.4   V-parameters and mode-field profiles

When the refractive indices and dimensions of femtosecond-inscribed WGs were measured, one can qualitatively characterize the waveguide strengths by calculating the corresponding V-parameters. It should be recalled that for a step-index fibre the V-parameter is defined as [210]:

$$V(\lambda) = \frac{2\pi r_{core}}{\lambda} \sqrt{n_{core}^2 - n_{clad}^2}, \tag{5.1}$$

where the last square-root in Eq. (5.1) is called the numerical aperture of the fibre.

To evaluate the V-parameter in our case (a gradient waveguide), one has to use the exact profile of the RI for each of the waveguides. In order to do this, we used reconstructed RI distributions, obtained as described by Eq. 4.3. As an estimate, one can use the data for cladding RI only, assuming a step index profile with the index contrast defined by cladding RI only and neglecting the contribution by the core. Surprisingly, this provides good estimations, and agrees well with V-parameters calculated by Eq. (5.2), which we derived earlier [8]. The exact expression for the V-parameter of a circular gradient waveguide is:

$$V = \frac{2\pi}{\lambda} \sqrt{\int_0^\infty 2 \left(n(r)^2 - n_0^2\right) r dr}, \tag{5.2}$$

where n_0 is a background refractive index. This expression includes as a limit the case of a step-index profile, as well as other cases described in [210].

Figure 5.20 presents calculated V-parameters at the wavelength of 1550 nm using gradient profiles of the refractive indexes we have determined above (Eq. 5.2).
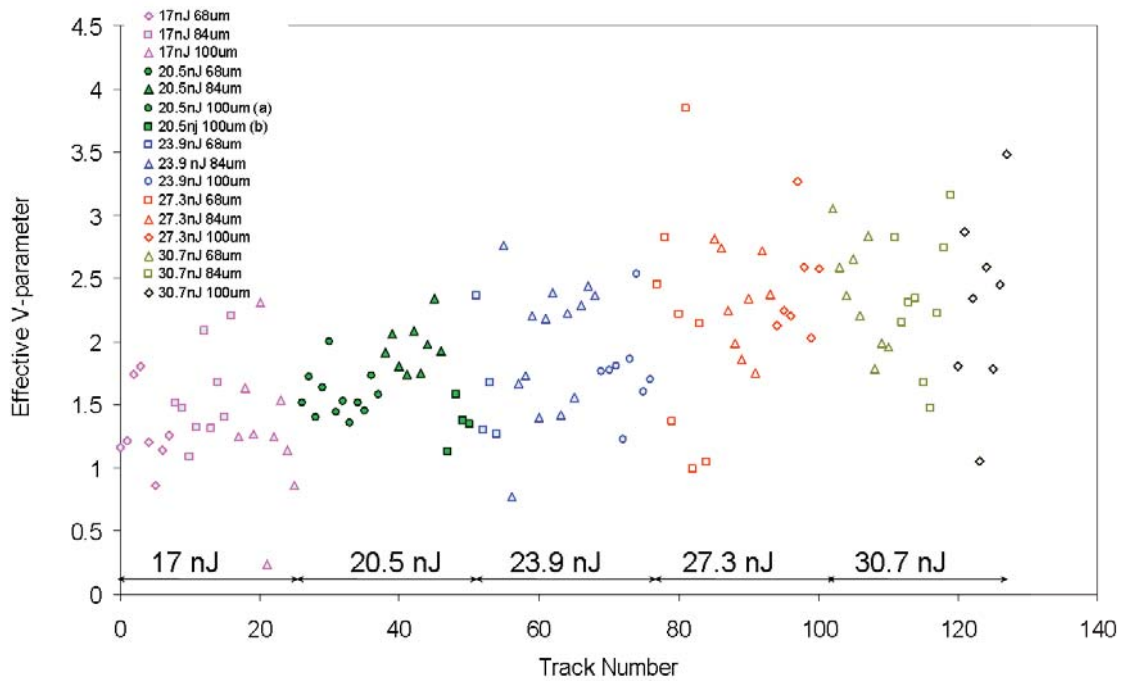
Figure 5.20: Calculated V-parameters for femtosecond waveguides for $\lambda = 1550nm$.

Slightly lower V-parameters can be obtained using a simplified expression for cladding RI data and its diameters, however such an estimate also predicts qualitatively a single-mode nature of the WG at telecom and existence of multiple core modes at the wavelength in the visible range (e.g. at 633 nm - He-Ne laser). This is shown in Figure 5.21, where the V-parameters both for 1550 nm (diamonds) and 633 nm (crosses) are plotted.

Indeed, in the experiments we did observe multiple modes for visible wavelengths, but never for NIR. The examples of intensity distributions at 633 nm are given in Section 5.2.7, in line with the results of numerical simulation of mode-field distributions by finite element method (*COMSOL*).

Figure 5.22 provides a combined picture of a few modes at 1550 nm for different waveguides. For comparison the mode-field intensity distribution for *SMF-28* fibre is given. One can conclude that the mode-field diameter of the femtosecond-inscribed waveguide can be done almost to match the one for *SMF-28* fibre, thus enabling potentially very low coupling losses. The coupling of the fs WG to some other commonly used fibres can also be optimised.
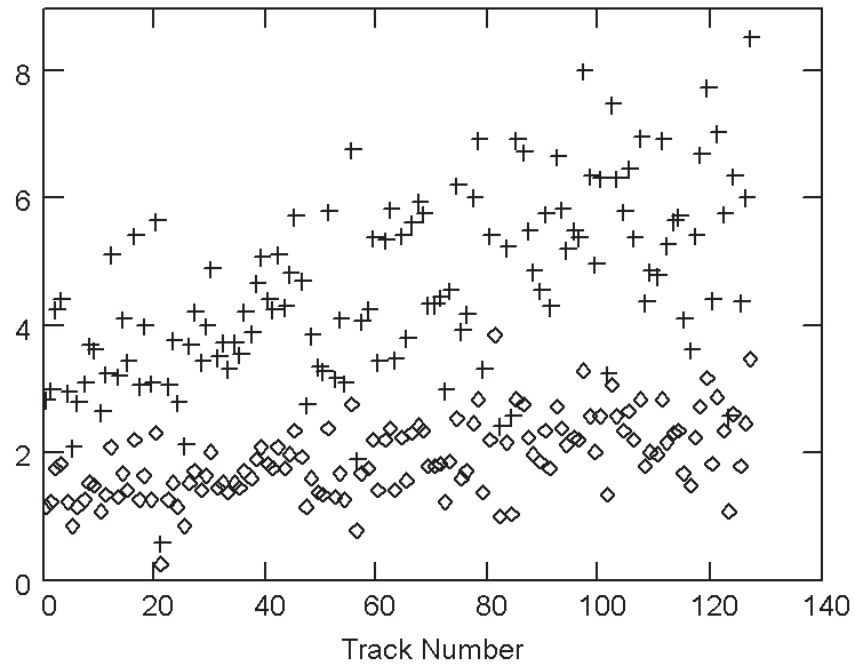
Figure 5.21: The upper group (crosses) corresponds to a V-parameter for a simplified step-index waveguide at the wavelength of 633 nm, and the lower group (diamonds) is for 1550 nm.
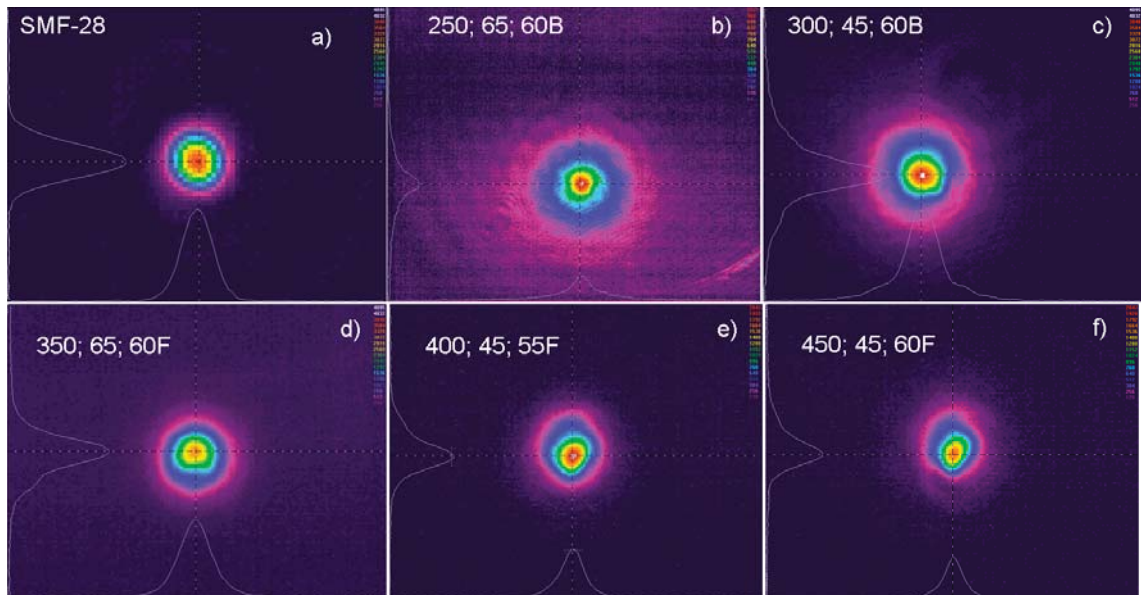
Figure 5.22: Mode-Field intensity distributions at 1550 nm for a number of WGs. The top left profile, a), corresponds to the output from *SMF-28* fibre. Note that the MFD of fs WG can be even more compact than in *SMF-28* fibre (for example, in figures e and f).

5.2.5 Waveguide Losses

After we have measured mode-field distributions (MFD) for all fundamental modes and for the fibre of interest, coupling losses to/from (SMF-) fibre can be calculated by the following equation:

$$CL = \frac{\int \int_S dS(E_M^* \cdot E_0)}{\sqrt{\int \int_S dS|E_0^2|}\sqrt{\int \int_S dS|E_M^2|}} \, , \tag{5.3}$$

When presented on a graph, the numerical integration by Eq. 5.3 of measured MFDs gives a coupling loss below 1dB at the regime, which is close to the optimum or to the middle of the scanning range, as defined in Section 5.2.1.
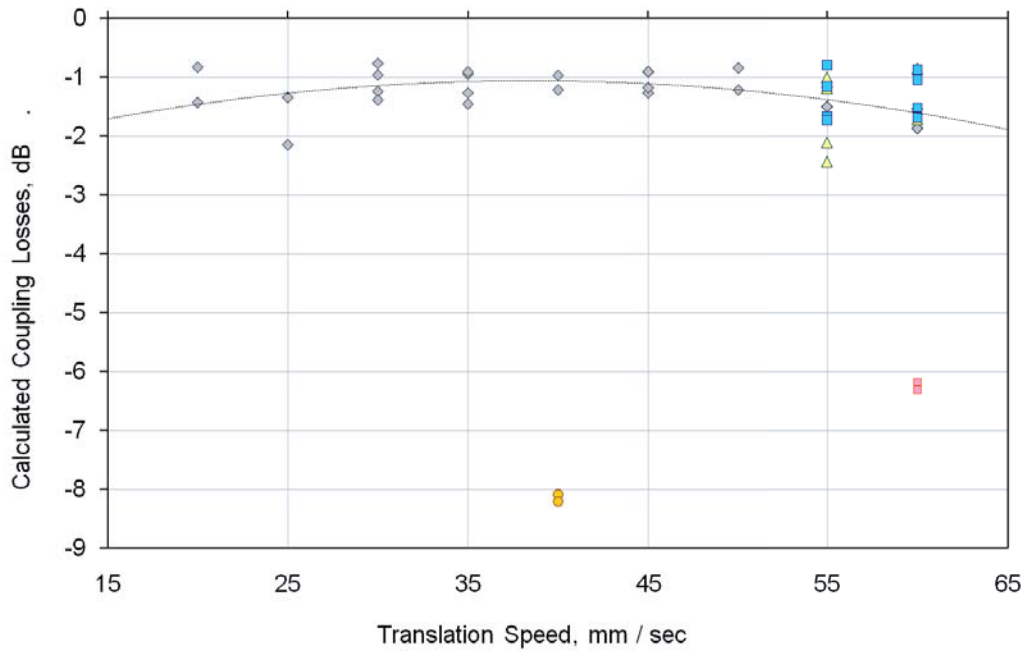
Figure 5.23: Dependence of the coupling losses on sample translation speed at laser pulse energy of 20.5 nJ (gray diamonds).

Total propagation losses for all tracks were measured as described in Section 4.7. They can be presented on 2D contour maps following the idea of a presentation from papers [167], [72]. This map defines the so called *inscription window*, using the terminology from these papers.

The abscissa denotes average laser power or pulse energy, shown in the bottom or top of the graph respectively; while the ordinate marks different translation speeds. We found that the appearances of these windows depend on focusing depth and, to a lesser extent, on a polarisation of the laser, and not much on the scan directions. The Figure below pro-

vides a few inscription windows under different experimental conditions and reveals that the inscription window may change with depth.
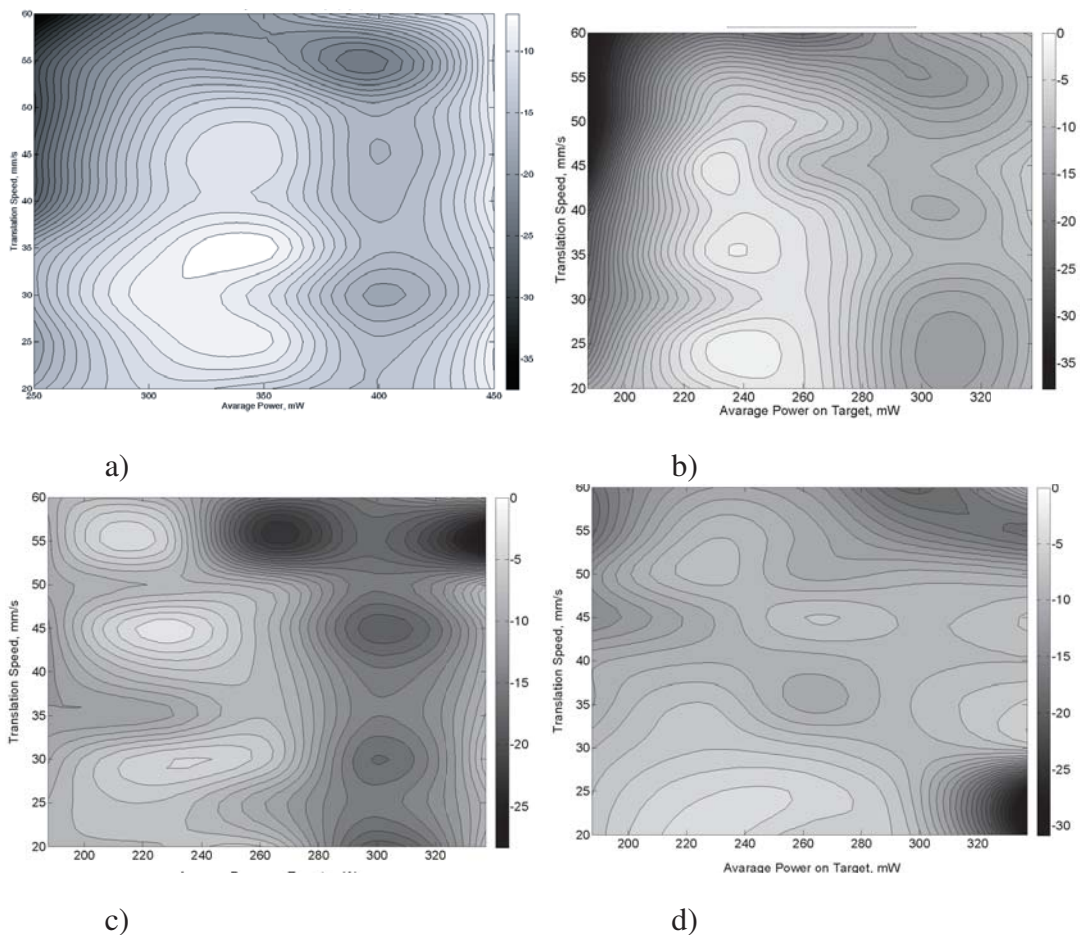
Figure 5.24: The first two graphs (a, b) are to compare the forward and backward direction of inscription at the depth of 68 μm; the last two (c, d) are for different inscription depths of 84 and 100 μm and backward direction of sample translation.

The comparison of losses at 633 and 1550 nm revealed that they may remain offset by approximately 1 or 2 dB, which we attributed to a coupling loss.

The minimum for total losses among the whole set of waveguides was 43% or -2.4 dB for a 2 cm track. Given the Fresnel losses to be -0.36 dB (or 8%), and coupling losses of about -1.0 dB (see Figure 5.23), total propagation losses for a 2 cm track are $(2.4 - 0.35 - 1)/2$ cm ≈ 0.5 dB/cm. This is a rough estimate as the coupling losses may be underestimated.

The NIR insertion losses are much harder to measure due to poor visualisation of the waveguides on our setup (thus hard to couple-in) and semi-manual translation of the sample into a perpendicular direction when switching to the next track. For this reason some tracks were missed/misinterpreted and thus dropped due to uncertainty. Only the last few tracks
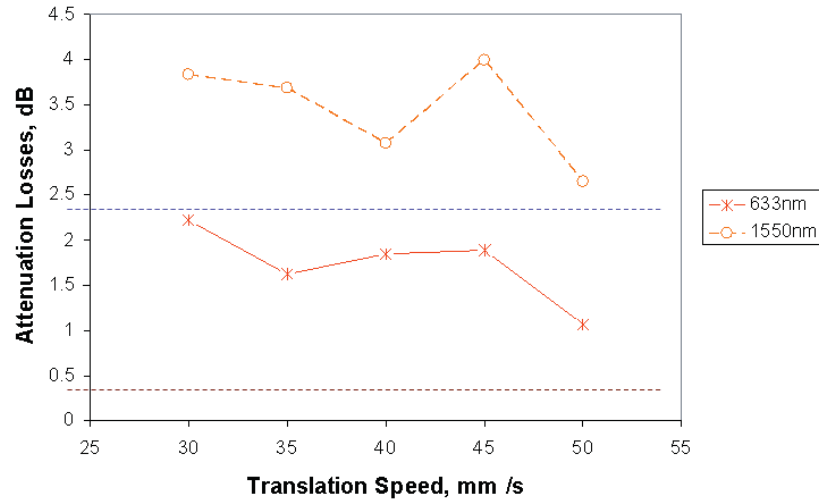
Figure 5.25: The dependence of total losses for both 633 and 1550 nm.

in each group were measured with confidence. These total NIR losses at the wavelength of 1550 nm for two orthogonal polarisations are presented in Figure 5.26. The level for Fresnel losses (0.355 dB), which is plotted by a dashed black line, was estimated using Sellmeier Equation for BK7 glass, which produced n_{1550}=1.5007. The minimum detected losses were

a)   b)
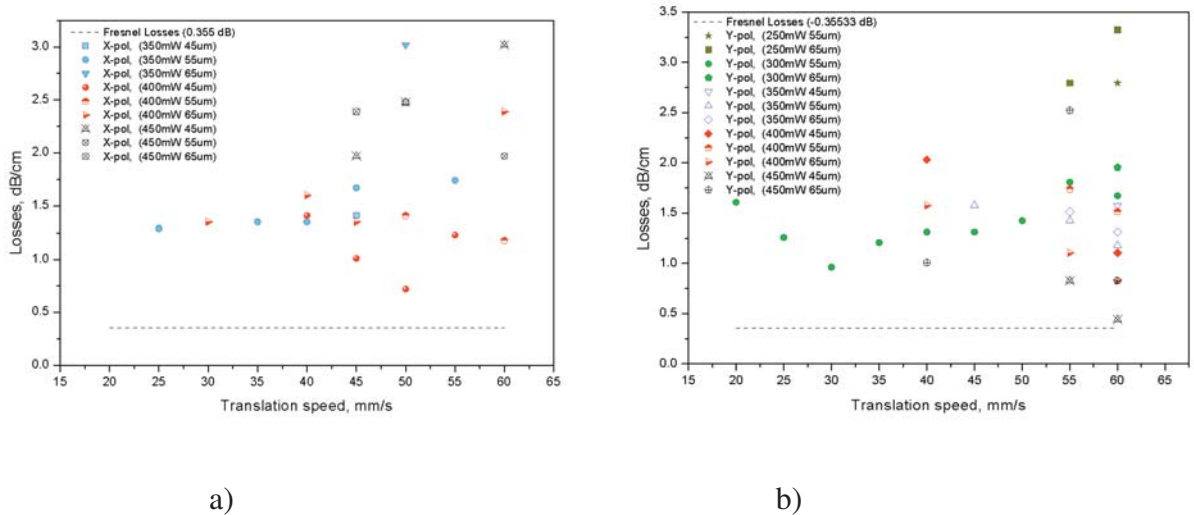
Figure 5.26: Total losses at 1550 nm (in dB/cm) for two samples of 1.8 and 2.2 cm long and two polarisations: X and Y.

found for **Y**-polarisation, laser pulse energy 30.7 nJ, depth of 45 μm and translation speed of 60 mm/s. The output power was 1120±20 μW when total power from *SMF-28* fibre was 1400±20 μW, which corresponds to 0.97 *dB* total loss. The Fresnel reflection gives 0.355 dB

loss for both facets, and with a sample length of 2.2 mm the upper limit of propagation losses is 0.28 dB/cm (assuming zero coupling losses). In the case of zero propagation losses, this corresponds to a 0.61 dB coupling loss, which is in reasonable agreement with what was estimated from mode-field distributions (see Figure 5.23).

With an assumption of a roughly 50:50 splitting between these two, we could estimate the coupling losses to be 0.31 dB (per joint) and propagation losses 0.14 dB/cm.

Exploring the graph for X and Y polarisations one can find that the latter produces slightly lower losses. Also there is a tendency to increased losses with increasing speed, which, can perhaps be attributed to the change in the waveguide geometry. This complex interplay between RI contrast (see sect. 5.2.3) and WG dimensions (see sect. 5.2.2) demands further thorough experiments and a complete data set for each track.

At X polarisation one can also observe an increase in total losses, say, above the average (or what may be expected). We explored again the tracks inscribed at the highest laser pulse energies. Although they look "perfect" under the microscope, the numerical processing of the accumulated phase map revealed that there is spontaneous RI modulation which occurs at highest energies, mostly for X polarisation of the inscribing laser. Also self-modulation was observed for the lowest laser pulse energies (20.5 nJ or below), with a tendency to occur more often for deeper positioned waveguides. We attribute this instability to a lower local temperature, when it drops below perhaps T_g - the glass transition temperature.

Comparison of our results with the results of Eaton et al [130], [167] revealed remarkable consistency in optimal conditions for femtosecond inscription obtained, despite the fact that *all* the experimental conditions for fs inscription were different in the two cases. This indicates the purely thermal nature of the RI modification mechanism of direct fs inscription, and perhaps little difference in how this energy deposition was done.

5.2.6   Losses at higher laser pulse energies

The losses at 633 nm presented in Figure 5.24 demonstrate an increase when both laser pulse energy and sample translation speed are increasing or when these two parameters are above their "optimal" values. The minimum losses were obtained in the middle of the diapason of parameters explored. This was expected, as before making a detailed search within a narrow range of parameters we explored a much wider diapason. However, in previous

Sections 5.2.3, 5.2.2 we found that the strength of the waveguide grows towards the end of this diapason, as both diameters of inner/outer parts of the WG and the induced RI contrast are higher towards the high end of the parameters' range. Thus, one can expect stronger waveguides here, as well as reduction of the coupling, and so the total losses.

There must be a reason why it appears at high energy or at higher translation speeds. An experimental observation made during the exploration of a much wider range of parameters revealed that stochastic (as well as almost periodic) RI modulations may occur both at high energies and at high translation speeds. So before the pronounced modulation there might be a modulation of RI, which may increases the propagation losses.

To confirm this, we explored the tracks inscribed with the pulse energy just above what was thought to be the optimal range, where they exhibit slightly higher losses than neighboring groups. We found that fs waveguides still look smooth both under the microscope and on QPm phase map, so they could be considered as good and not damaged.

To reveal RI variations we used numerical processing of the phase map, that is, we differentiated it in the direction parallel to the track. Such a numerical procedure imitates the properties of DIC microscopy, which is proven to be the best technique to reveal the smallest RI variations along the direction of differentiation, while it is almost insensitive to variations in the perpendicular direction. This numerical treatment indeed revealed modulations, which occurred only in the core of the WG but not in its cladding, as one can see in Figure 5.27.

It is this modulation which leads to a higher scattering and thus to higher propagation losses. We believe that such modulations facilitate the formation of self-arranged periodic structures as well.

5.2.7 Numerical simulations of mode-field profiles

Commercial software (by *COMSOL*) was used to explore the modes of gradient waveguides fabricated by HRR direct inscription at He-Ne and telecom laser wavelengths, and confirmed their multi-mode and single-mode nature respectively. The existence of multiple modes may affect coupling efficiency by a small change to the coupling angles and input fibre positions at the interface. In the experiment the structures produced have rather complex RI distribution, which was assumed to be circular for the Abel inversion. If we could measure true RI distribution, rigorous calculations with measured 2D RI profile may make sense.

a)   b)
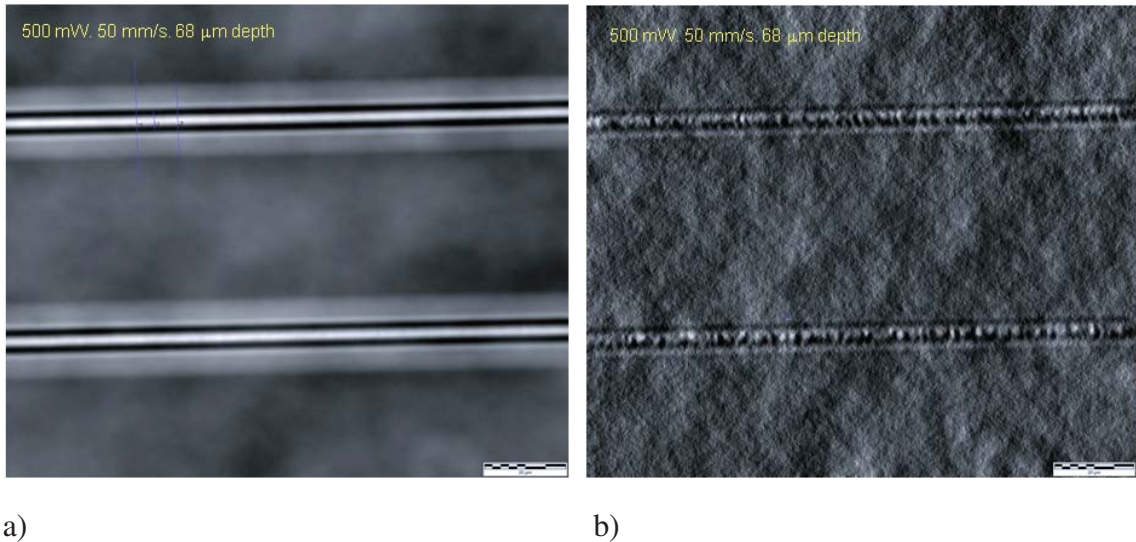
Figure 5.27: At higher pulse energies, when the WG still looks perfectly smooth on a phase retardation map (a), the core becomes stochastically modulated. Image on (b) obtained from the image presented on (a) by numerical differentiation of the accumulated phase along the waveguide direction. Note absence of such modulation in the cladding.

The structure for the simulation has a geometry which is presented schematically in Figure 5.28. Instead of true 2D RI distribution we approximated its gradient profile by a step-index one, matching the magnitudes of the RI used in simulations with ones obtained in the experiment, and manually introducing an ellipticity.

Peak-to-peak RI contrasts were moderate, just 4×10^{-3} for the core area, and 5×10^{-4} for the cladding, while their diameters were 4 and 25 μm respectively. The central part of the WG was chosen to be slightly elliptical, and a small feature was added near the bottom, to imitate the symmetry observed in experiments (see Figure 5.14).

It was confirmed by numerical simulations that even such weak waveguides demonstrate multiple core modes at the wavelength of He-Ne laser. The simulation results support (qualitatively) the shape of the modes which we observed in experiments. Most often the "donut-shape" mode was excited, as can be seen on right picture(s) in Figure 5.28.

The numerical modelling also confirms the single-mode nature of the fs WGs at the wavelength of 1550 nm, thus this providing further validation for our technique of RI reconstruction based on the combination of the QPm method and inverse Abel transform, as was described in Section 4.6.

It is noteworthy that experimentally observed mode-field profiles at 1550 nm can be reproduced almost exactly by numerical simulation even by the model with a stepwise refrac-
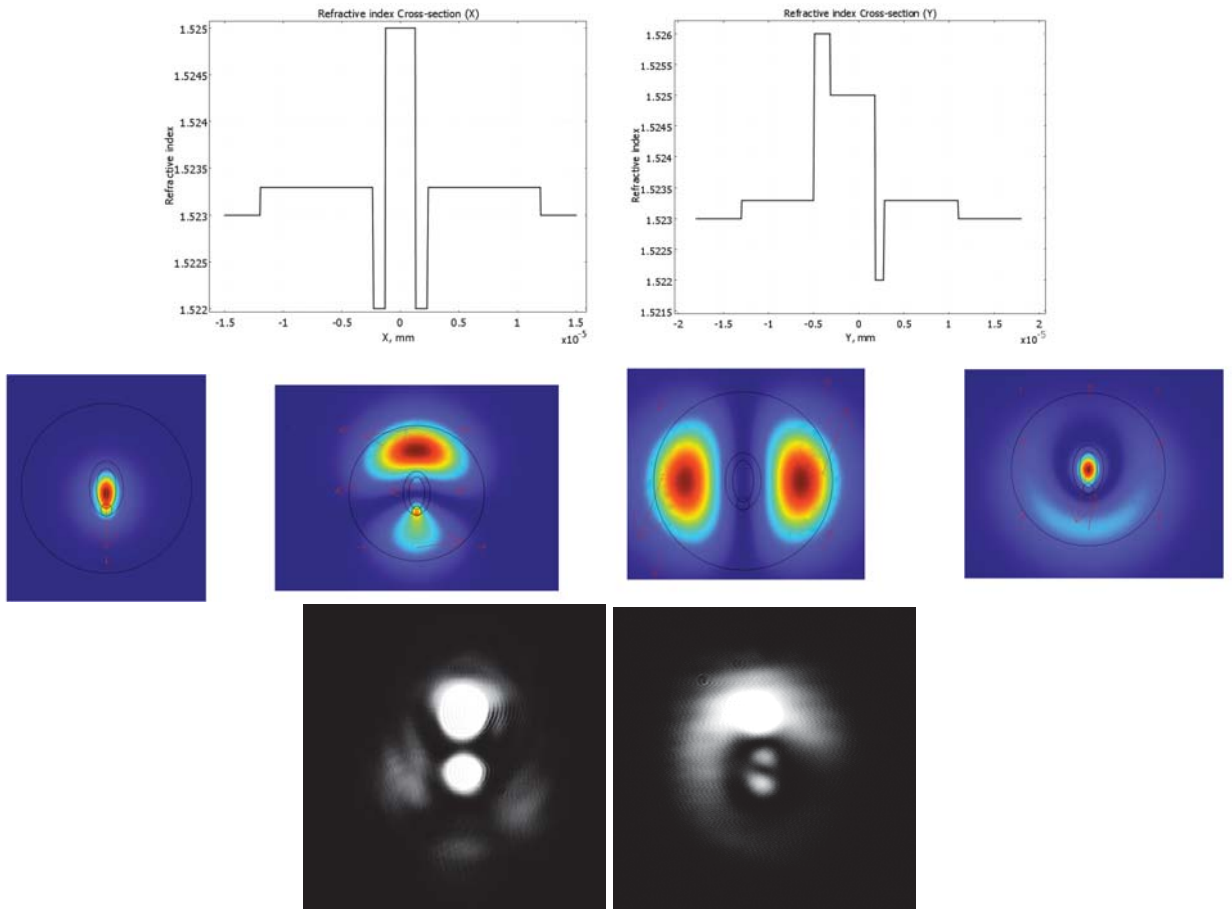
Figure 5.28: Simulated refractive index distribution and Mode-Fields at the wavelength of 633 nm and two examples of mode-field distribution observed in experiment.

tive index profile.

5.2.8 Bend losses in curvilinear waveguides

Any integrated optic circuits except for trivial ones require curvilinear tracks. Having obtained record high RI contrast one may expect low bend losses for curvilinear waveguides. In order to measure the losses induced by bends, one has to separate them from other types of losses.

A set of tracks was fabricated with variable radii of curvature (R) but with identical lengths, using the inscription parameters close to optimal inscription regimes, as was found before. In the design we added straight parts to make the lengths of all tracks equal. At the beginning and end of each structure we added small straight sections as well, so that the total lengths of waveguide would always remain the same after a polishing stage. This enables us to subtract the coupling and propagation losses (which are, presumably, due to scattering and linear absorption), as the lengths of all tracks were equal. Finally, our design enabled us to separate out the dependence of losses on radii of curvatures.

Total losses were measured on the characterisation setup described above in Section 4.7. These include:

- coupling losses from input fibre to the waveguides. These remain the same, as all inscription regimes were identical for all guides.

- propagation losses, which are presumably due to scattering and absorption. We ignored possible dependence of propagation losses on curvature, so these must be identical due to design.

- Fresnel losses due to reflection from un-coated front and back surface. Again, these are the same for all structures, provided no damage has been introduced during the polishing.

- transitional losses [210], p.23.5, which are essentially the coupling losses between straight and curvilinear parts, so they depend on the radius of curvature R;

- finally, radiation bend losses, which also depend on the radii.

The first three reasons are considered to be identical for all tracks regardless of radius of curvature, due to the chosen design. To subtract these, we assumed the following: coupling

plus Fresnel losses to be -1.4 dB; propagation losses of -1.0 dB/cm with total length of each structure of about 7.1 cm. This is really an estimate as we did not measure propagation losses for a straight track under experimental conditions used to process this sample. The value -1 dB/cm is justified by previous measurements of NIR losses. Finally, we obtained

a)   b)
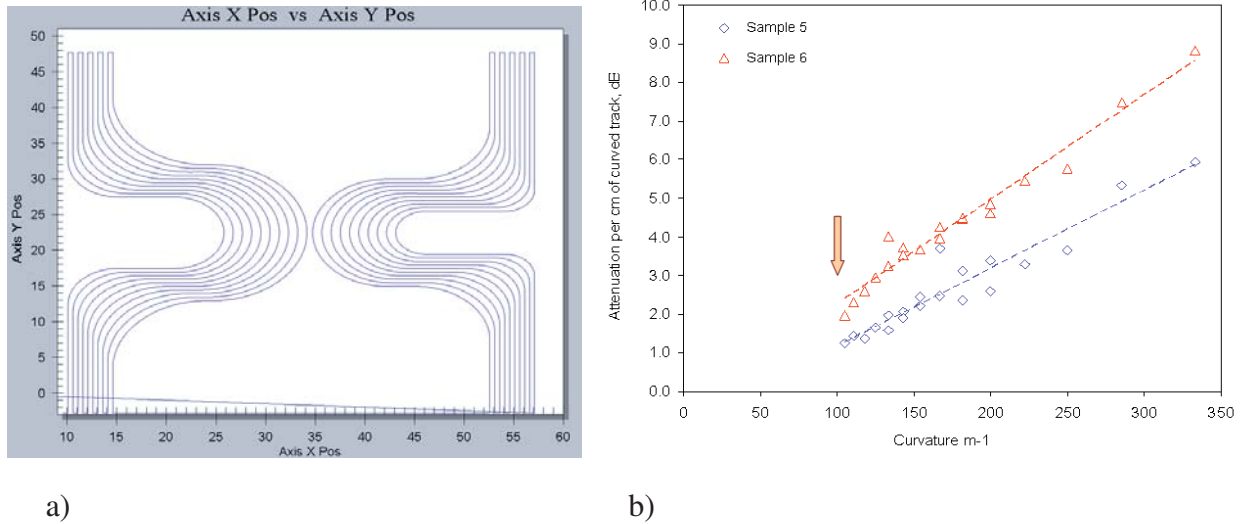
Figure 5.29: Waveguide geometry, (a) and Bend losses, (b) obtained for femtosecond waveguide fabricated using optimal inscription regime.

bend losses, which are normalized on the length of curved section (Figure 5.29).

Analysis of Figure 5.29 reveals that each centimeter of curvilinear track brings additional losses of $1\sim2$ dB per centimeter, for the waveguide with the radius of curvature of just 10 mm. This is in addition to the 1 dB/cm propagation losses we assumed above. When the radius is reduced to 3 mm the bend losses increase to $9\sim10$ dB/cm for a curvilinear part of track.

When compared with theoretical predictions for a step-index cylindrical waveguide [210] more factors should be considered. First of all we have to separate transitional losses from radiation bend losses (our estimates using the formula for a model step-index, cylindrical fibre show the domination of transitional losses over the radiation ones).

If compared with one of the best reported results by other groups [128], where losses of the order of 23 dB/cm were measured for R=10 mm tracks using a shorter wavelength (of 633 nm), our fs waveguides demonstrate much lower bend losses of about 1 dB/cm at the wavelength of 1550 nm.

So far the most comprehensive study on bend properties in femtosecond-written waveg-

145

uides has been carried out by Eaton et al. [211]. The geometry described in paper [211] makes the lengths of the curved parts comparable with ours. More importantly, the number of inflection points in each arm is exactly the same as in our design (namely, 6), so our results are comparable with the ones presented in [211]. Their results for a double S-bend structure with an offset of just a 50 μm reveal the bend losses of 2 dB for R=30 mm and about 14∼15 dB for R=10 mm. This should be compared with 7 dB total losses, as can be *estimated* for similar structures produced by our HRR system.

5.2.9 Shallow waveguides

There is a problem with shallow waveguide fabrication, which has only recently been resolved. The problem is that the waveguides at a shallow depth are always weaker than in the bulk, say at depths of a few tens of micrometers and more. It is not always possible to make a waveguide close to the surface, which always has a lower damage threshold than the bulk. It turned out that the WGs can only be fabricated when a micro-objective which is corrected against spherical aberration is used.

The necessity of using high-NA micro-objective is dictated by the need to avoid damage on a surface, which in practice can be achieved only by spatial localisation of the energy deposition, and thus high-NA focusing.

A second problem associated with such fabrication arises due to a stress build-up around the modified region. It turned out that the "thin" covering layer of the material often cannot withstand the stress generated, which causes cracks and may even affect the inscription process.

Figure 5.30 presents the results of experiments on such inscription.

We experimented on multiple successive scans over the same path in order to compensate for reduction of the induced RI contrast. The image in Fig. 5.30, a) revealed significant differences in the results of a multi-scan approach as compared to LRR inscription and HRR inscription in the bulk cases. First, there is no cross-talk due to the locked stress which proved that the heat accumulation regime also provides an annealing (higher temperatures). Second, the waveguides can be positioned as close as required, which allows in principle some flexibility in designing their cross-section. The last allowed us to compensate for the *lowering* of the RI in the central area. Third, weaker WGs demonstrate larger mode-field diameters (Fig.

a)   b)   c)
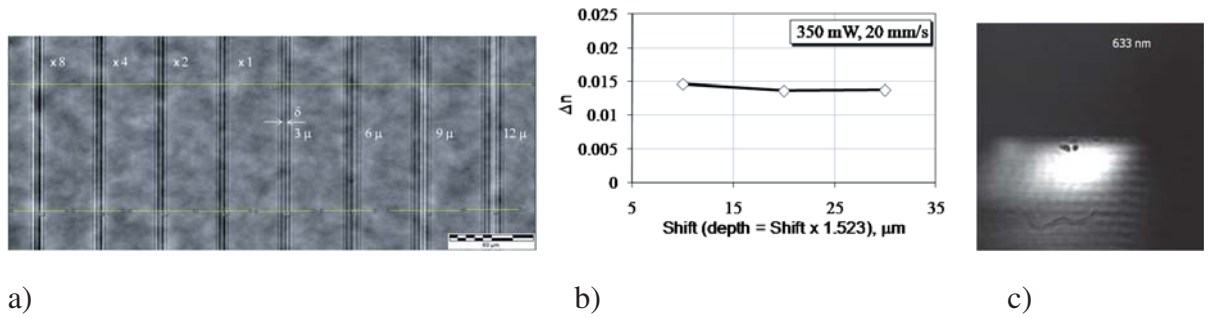
Figure 5.30: The shallow waveguides fabricated at the depth of 15 μm (a) revealed both reduced RI contrasts and lowering of a central (positive) RI spike. The inscription depth can be as low as 10 μm (b). Guiding of He-Ne laser radiation in one of the shallow waveguides (c).

5.30, c), which is essential for a number of sensing and plasmonics applications, as they require, for example, good coupling of the evanescent field with surface-plasmon modes. The inscription regimes and the strengths of the waveguides strongly depend on focusing depths, thus making the fabrication of shallow waveguides a challenging engineering task.

Finally, we would like to note that the problem of shallow waveguide fabrication at even lower depths has been addressed by the hybrid method, described in Chapter 8.

5.2.10   Discussion

To explain a counter-intuitive experimental fact, described in Section 5.2.3, one may appeal to a thermo-elastic mechanism [160] which has to be involved in post-deposition scenarios [212]. The ultra-fast glass heating and quenching of the overheated volume of glass take place shortly after the energy deposition stage. The overheated glass must be under high pressure at the same time, as the rest of the sample does not feel any "heat source" yet.

Theoretical description of the direct femtosecond modification process has to include a few stages (and various physical effects). Faster translation of the sample produces higher heating and cooling rates [13]. An estimate of such rates from paper [14] gives very high cooling rate, approaching $10^{8 \sim 9}$ K/sec. To the best of our knowledge there are no techniques (apart from some explosions) which can produce such rates. This is true for heating, but not for the cooling rate. The record-high cooling rate is due to the microscopic volumes involved in direct laser micro-fabrication: the more the surface area, proportional to R^2, the quicker the cooling. At the same time the total energy to be dispersed is proportional to the volume,

147

or $\cong R^3$. Thus the cooling speed depends on the characteristic dimensions of the volume, R as $\cong 1/R$, so it becomes very high for a microscopic volumes.

Faster cooling typically ends with a glass state which has a higher topological disorder [213] or, in other words, a glass with a less dense local arrangement of atoms, which are "frozen" in non-uniform states. The entropy of such a system differs from the equilibrium one, which is often reflected by the term the "fictive temperature" of glass [213, 214]. The deviation of entropy is an additional parameter of order for such a state, and this process may be considered as a phase transition of the second order.

There is a complication: such expansion of glass takes place inside the bulk of cold, solid matrix, which means that the surrounding material counteracts with a compressive stress onto an overheated volume. Such compressive stress (up to a few GPa) may and does change the conditions in which phase transitions occur [212], and leads to a different final state as compared with the thermal cycle involving uniform and slow heating and cooling of a bulk glass as a whole.

If the stress is above a certain value the deformation is no longer elastic and the material is said to be in a plastic deformation region, where the strain can take place without a change in stress [160], [215], provided the latter is constant. This has to be considered as a first-order phase transition in melted or super-heated solid glass, as the structure of the matrix has to be changed [216].

There is also other experimental evidence to support the consequences following from the thermo-elastic model: various self-started instabilities; the re-diffusion of light atoms out of the focal region or generation of various defects in the volume surrounding the focal spot; pressure build-up from the surrounding material, which balances the expansion of quenched glass and leads to a residual "locked" stress [193].

We believe that the proper model of femtosecond modification of glass should include self-influence of the beam as well, through both thermal lensing and due to a refraction on already modified area, which may work as a strong "lens". This self-influence is most likely to affect both the energy deposition process for subsequent pulses and later material modification stages. As laser beam focusing is affected by the aberrations, the interplay between thermal lens, non-linear self-focusing, and all other self-influence effects may be compensated by a thermal lens at some translation speed. The reason is that the gradient of the

thermal lens strongly depends on translation speed, and may change when the temperature distribution changes, while the aberrations introduced in the beam by the optics are assumed to be constant. Due to this interplay, at some speeds the energy deposition per unit volume may increase, which could elevate the local temperature, and also the associated heating and cooling rates, and consequently the induced contrasts of the refractive index.

For example, such self-influence, say from an already modified region onto beam focusing, may change the *shape* of the focal spot from the spherical to a slightly "elliptical" (see for example Fig. 5.14), which may affect the cooling speed (as this may decrease the cooling time), as well as 3D distribution of the induced mechanical stress.

Further complications may come with continuum generation and other effects. Hot and dense laser plasma created in the focal volume [217], [215] is always accompanied by a continuum-like radiation. The spectrum and intensity of such radiation suggests that strong UV light may be generated with the wavelengths, perhaps shorter than the absorption edge (or the band-gap) of the glass, and thus this could create an additional, non-local, compact source of ionisation. Altogether with a shrinkage of the band gap due to a high pressure (Franz-Keldysh effect) and high temperatures [218], the radiation energy transfer may also be a function of the glass local conditions (pressure and temperature).

As another aspect of this, let us consider the possibility of thermal diffusion of electrons out of focus. The Fermi speed can be estimated for a known electron concentration (in our case $n_e \approx 10^{21}$ cm^{-3}), this is about $v_F \approx 0.5$ nm/fs; and it may be compared with an average thermal velocity for electrons when they have an average energy of about $\mathcal{E}_{osc} \approx 20$ eV: $v_{T_e} \approx 2.7$ nm/fs. The last one scales linearly with intensity, I and is quicker than Fermi speed. To escape from focus during the time of the laser pulse, the last one has to be longer than 100 fs. It is essentially that electrons which have already escaped can be trapped on various defects and then generate local electric fields, the last ones can lower the band-gap and/or induce a polarisation around the focal volume, as was assumed in the "forest fire" model of femtosecond ionisation in papers by Petrov et.al. [219].

Also a steep gradient of electron density and/or temperature changes the symmetry of media, which may cause a higher harmonics generation. This has been observed in experiments on laser damage in various solids, especially near the surfaces as well as harmonics generation in gases. Note that the third harmonics of 800 nm laser radiation, if generated,

has the wavelength of 267 nm, which almost falls into the absorption band of BK7 and some other, narrower-band glasses.

All of the abovementioned makes a self-consistent model of direct femtosecond inscription practically impossible especially with HRR laser system.

However, a forecast for future development seems to be possible. As follows from the above, the parameters of waveguides achieved by HRR fs system are superior to what can be obtained by LRR systems. We have also mentioned similarities in "optimal regimes" for two completely different laser HRR systems, when average absorbed laser power was about 200∼300 mW.

In view of the experimental results presented, further increases in both sample translation speed and pulse repetition rate may be desirable. It is likely that the average laser power is to be kept at the same level, thus a two-fold increase in laser repetition rate would demand a 50% reduction in laser pulse energy. But in order to initiate the inscription with lower pulse energy the pulse duration has also to be shorter. This seems to be feasible, as pulses with the duration of 26 fs were achieved in CPO system [25], almost identical to ours.

A further reduction in pulse duration seems to be difficult due to practical problems with focusing and reflecting such broadband radiation. In order to initiate fs inscription with even lower pulse energy and even higher repetition rate one can use a tighter focusing, which is limited by the numerical aperture of the available micro-objectives and their quality. Such an approach has been already demonstrated by Tong et al. in [128], where they focused 800 nm laser radiation by the MO with maximum available NA≈ 1.4 into a focal area of ≅0.6 μm^2. The pulse train of 60 fs pulses at 25 MHz RR delivered an average power of 175 mW to the sample. The experimental threshold of 7nJ reported in the paper [128] can be compared with the pulse energy which can be obtained by Equation 3.49; such an estimate gives 8 nJ, which is in good agreement with their experimental findings.

Any further increase in repetition rates of the laser would require even tighter focusing. This seems to be possible only by using exotic beam shapes, such as a doughnut-mode, radially polarized beam, as described in [220], with the diameters of the focal spot around a few hundred nanometers. Alternatively, one has to use a combination of different wavelengths of higher harmonics of NIR femtosecond laser.

5.3 Examples of inscription in other hosts

The unique property of the direct fs inscription method lies in its application to different transparent dielectrics.

The first two examples are for inscription in narrow-band-gap glasses: the **oxyfluoride glass-ceramics**, which has $T_g \cong 390^oC$, $n \cong 1.6$, and **phosphate glass**: $T_g \cong 485 \sim 530\ ^oC$, $n = 1.52 \sim 1.538$) of QX type, with 2%wt. of Er, 4%wt. Yb, and a refractive index n_{800} of $\cong 1.52$ (by *Kigre*). These narrow-band-gap materials are of interest for a number of telecom and mid-IR applications, however no thorough optimisation has been done in terms of the quality of waveguide, magnitude of the induced RI contrast, or WG losses.

First, the writing of waveguides was demonstrated inside the oxyfluoride glass ($32SiO_2$, $9Al_2O_3$, $31.5CdF_2$, $18.5PbF_2$, $5.5ZnF_2$), doped by Er with the concentration of ErF_3 of 3.5 mol%, at a depth of 160 μm, where smooth tracks can be obtained. Note that such high concentration is not possible in silicate-based glasses without a clustering of Er^{3+}.

The WGs were written at pulse energies from 13.5 nJ to 30.7 nJ, while the modification threshold in terms of the laser pulse energy was about 10 nJ. The inscription was accompanied by bright continuum, similar to that which has been observed in the case of BK7 glass. The sample translational velocity varied between 1 mm/s and 60 mm/s. At higher translation speeds self-modulation appeared in the smooth track. The influence of translational velocity and pulse energy on the cross-sectional shape and integrity of the written tracks revealed similar behavior as in the BK7 case, but with larger diameters of inscribed structures. The shape of induced RI was similar to the W-shape observed in BK7 glass. However maximum RI contrast was estimated to be 1 order of magnitude lower, or just +0.003.

Tracks tend to be narrower, with weaker RI contrast as the pulse energy is lowered or translational velocity is decreased. Above the pulse energy of 22.9 nJ, tracks tend to crack upwards, up to the surface of the sample, especially for the WGs at shallower depths, signalling high locked stress around them. The light-guiding at both 651 nm and 973 nm wavelengths, as well as up-conversion, were observed in all tracks.

The interest in these glasses was due to the fact that they may form nano-glass ceramics after a heat treatment at or just above the glass transformation temperature (T_g) [20], [221]. However, in our experiments no evidence of appearance of nano-ceramics was observed when fs-treated samples were explored by NIR Fourier-transform spectrometry. This result
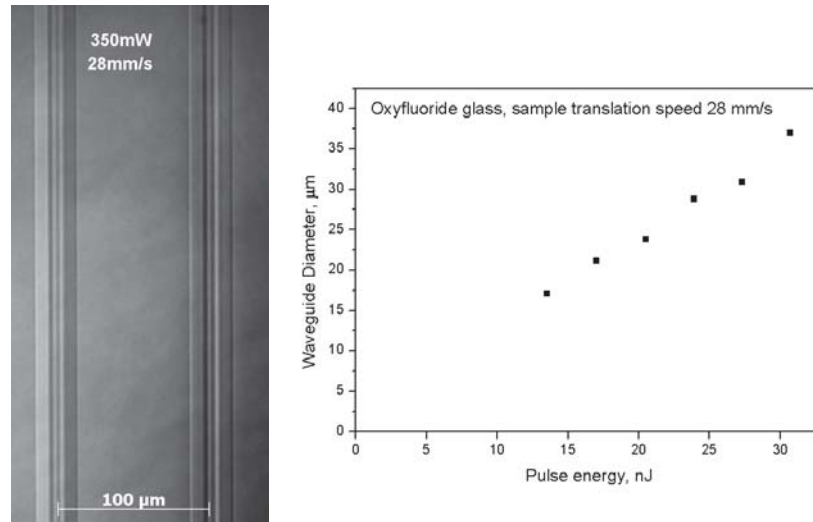
Figure 5.31: Example of a smooth track inscribed in oxyfluoride glass with 27.3nJ and 28mm/s (a); waveguide outer diameter as a function of laser pulse energy (b).

may be due to the fact that the heating and cooling rates were too high to allow any matrix rearrangements at the translation speed used (even at nanometer scale). A slower translation speed causes clear visible glass darkening (brownish colour) signalling a large number of defects created, and, additionally, this regime often produced tracks that were not smooth.

The heat-treatment results in the case of borosilicate glass were reported in [130]. When BK7 was heated above the glass *annealing* temperature, the outer part of the fs-waveguide was not visible under a microscope. In the case of oxyfluoride glass, the annealing at a temperature slightly above T_g also removed a light-guiding peripheral region of the fs-written tracks, suggesting again that this region may have been fs-modified by stress alone [20]. Due to a higher refractive index (n=1.6) and deeper inscription than in BK7, we observed more ellipticity in all tracks [20] as compared to the BK7 case [18].

It should be noted that these glasses are very unstable as regards self-arrangement when under fs inscription. A wide variety of a-periodic and periodic instabilities has been observed. Figure 5.32 provides typical examples of almost perfectly periodic structures, which appeared in a self-reproducible manner. It seems these periods can be controlled simply by changing major inscription conditions: the laser pulse energy and the translation speed of the sample as illustrated in Figure 5.32, where the short-period modulation (down to 0.76μm) occurred with inscribing laser pulse energy of 14.4 nJ and sample translation speed 40 mm/s when we focused at a depth of 160 μ m; (b) a period of 1.88 μm appeared at 20 nJ and V=30 mm/s;
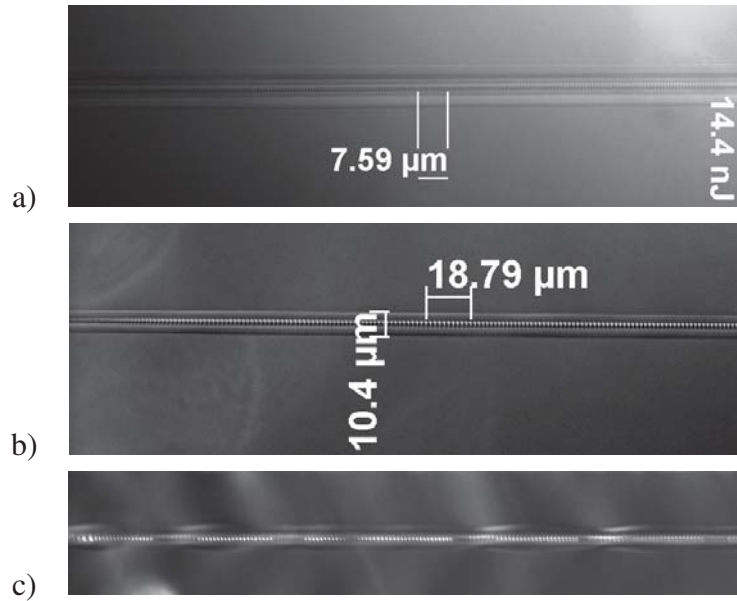
Figure 5.32: Self-modulation instabilities during fs inscription in oxyfluoride glass: (a) periodical self-modulation in the core of the waveguide; (b) bubble formation at higher energies; (c) beam "wobbling" at maximum energies before damage occurs.

and (c) at a high pulse energy the depth of the track is also varied with a period of about 20 μm.

Similar results were observed in doped **phosphate glass** ($T_g \cong 485 \sim 530$, $n = 1.52 \sim 1.538$) [222], when we compared low- and high- repetition rate inscription regimes. When compared to BK7 glass we observed both lower index contrasts, of about $5.4 \cdot 10^{-4}$, and narrower tracks. Note good RI matching of phosphate and BK7 glasses. We also observed two new effects: i) the refractive index *sign* changed from negative to positive when the laser pulse energy increased; ii) a new type of instability, i.e. sinusoidal "wobbling" of the direction of the track, has been observed.

The waveguides guide light at both visible and telecom wavelengths, although no optimisation of inscription regimes has been made in this work.

The next example of HRR inscription is illustrative: HRR direct femtosecond inscription has been demonstrated through the region of thermally (diffusion) bonded **laser crystals**: $Nd^{3+} : YAG$ and $Cr^{4+} : YAG$. The melting temperature of $Nd^{3+} : YAG$ is T_m=1950 ^oC, its refractive index is $n_{800} = 1.8245$. The inscription was obtained at maximum available laser pulse energy (of about 80 nJ), however this may not be the optimum. When the beam crossed the border of the bonding region between two crystals, a modulation of the track was

observed (see top part of the track (a) in Figure 5.33), perhaps due to the increased linear absorption in the $Cr^{4+} : YAG$ section. A small difference in the refractive index between the two sections may be another reason for this, especially in the region where the mechanical stress can occur due to different thermal expansion coefficients for these two materials.

a)   b)   c)
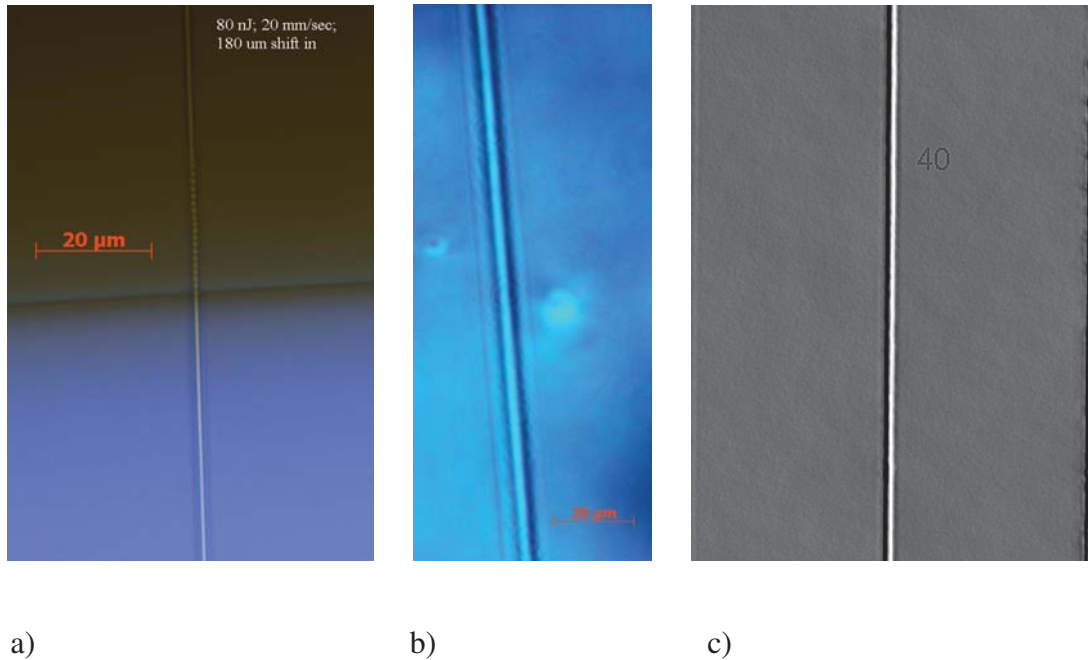
Figure 5.33: Examples of inscription with HRR laser in crystals: thermal-diffusion bonded YAG:Nd^{3+}+YAG:Cr^{4+} (a), in Z-cut LiNbO$_3$ crystal (b), and (c) - in Yb^{3+} :KY(WO$_4$)$_2$.

A completely unexpected observation was made when we explored this sample under the microscope and after we measured induced refractive indices with QPm: the induced RI contrast can be both negative, which was believed to be the usual case, and *positive* [223]. After exploring the dependence on inscription pulse energy we found that the change in the sign of the induced RI remains positive if translation speeds, and thus a cooling and heating rates, are above a certain value.

The refractive index change in doped laser crystals under fs irradiation is thought to be associated with some rearrangement of local defect structures. Experimental observations (by Okhrimchuk et. al., unpublished) of the saturation level of the induced RI contrast revealed that induced RI contrasts seem to be proportional to the concentration of dopant ions, and thus defects. It is thought that the mechanism of the RI change is associated with the increase or a shift in the absorption bands, or changes in the imaginary part of permittivity. Shifts in the absorption, typically observed in experiment correspond to a negative RI

a)   b)
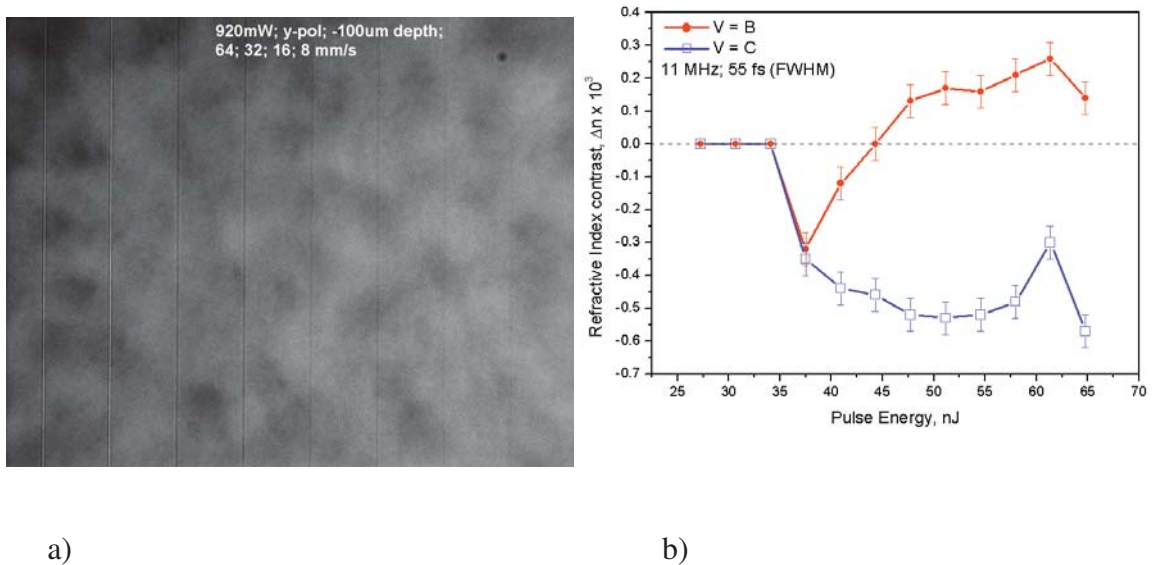
Figure 5.34: Visual change in the sign of the induced RI (a). Dependence of the refractive index on inscribing pulse energy (b) for two different sample translation velocities: 32 mm/s (red circles, trace B) and 64 mm/s (open squares, blue trace C).

change (or to a decrease of the refractive index in the irradiated area). It is not clear how a slower translation speed can change this mechanism. Perhaps a slower translation increases the internal irradiation of the crystal by the UV part of the super-continuum, generated during the process of fs writing. This may lead to an increased dose of UV irradiation and thus to the generation of additional defect bands, while at a slower scan the continuum is weaker. Also regimes of thermal annealing may be different at different translation speeds.

Conclusions

In conclusion to this Chapter, we compared the results of direct femtosecond inscription for LRR and HRR femtosecond systems in BK7 glass in Table 5.3 below.

At least one order of magnitude enhancement was found for the most critical parameters: induced refractive index contrast and insertion losses.

For other parameters, which are important for practical usage of the method of direct fs laser fabrication, such as fabrication time, laser pulse energy utilisation, and waveguide dimensions the HRR system enabled an enhancement (of up to three orders of magnitude) in all corresponding parameters.

Given the LBF time for modern laser systems of about 4×10^7 sec, with a lifetime value

| Femtosecond system | 1 KHz, 100 fs | 11 MHz, 50 fs | Enhancement |
| | (E_{max}=800 μJ) | (E_{max}=100 nJ) | factor |
Parameter			
Efficiency of utilization of laser pulse energy	80$\sim$800 nJ (10^{-4})	20$\sim$90 nJ (0.2$\sim$0.9)	$>10^3$
Induced RI contrast, Δn	2$\sim$3$\times10^{-3}$	2$\sim$3$\times10^{-2}$	>10
Sample translation speed, mm/s	0.01$\sim$0.1	10$\sim$100	$\gtrsim 10^3$
Waveguide dimensions (diameter), μm	<2	20	>10
Propagation losses, dB/cm	>3	$\approx$0.2	>10

Table 5.3: Comparison of LRR and HRR regimes for fs inscription.

of about $4\cdot10^7$ pence, the cost of waveguide writing is about 0.5 per meter (excluding the cost of substrates) when manufacturing speed is just 20 mm/sec. This is comparable with 0.1 per meter for the most commonly used optical fibre SMF-28e (by Corning).

Chapter 6

Inscription of periodic structures

Most integrated optics circuits for wavelength-selective applications demand periodic perturbations in the core/cladding of some waveguide or fibre. Such periodic elements are much easier to fabricate in fibres, as a fibre itself is already a perfect waveguide. In fibres a periodic (and sometimes not quite periodic) variation of the refractive index is usually referred to as a grating [224, 225]. Short-period ones are often called Bragg gratings. Fibre Bragg gratings (FBGs) provide resonant reflection/deflection on wide angles, up to 180 degrees or back reflection. Long-period gratings (LPG) usually couple light from the core to (a number of) co-propagating cladding modes. Direct femtosecond inscription is a very attractive method as it allows the problem of inscription in non-photosensitive materials to be overcome, brings geometrical flexibility and enables one to fabricate devices which were not previously possible.

A short-period RI perturbation can be induced by one of the following methods: i) an interferometric fringe pattern created by a phase-mask or a combination of phase masks; this seems to be the most reliable and practical method, despite the relatively high cost for a good phase mask; ii) interferometric methods, using various types of beam-splitters; this method has distinct flexibility in period choice, but requires excellent stability from the optical setup, especially when CW UV laser is used, and thus long time exposure is involved. Its revival is anticipated with high-power pulsed laser sources; and iii) Point-by-Point (PbP) inscription, where inscription of every pitch of the grating occurs in a single (or sometimes, multiple) shot(s), and then a focal pattern or fibre is being translated on a pre-selected distance between these shots; iv) there are also several examples of self-arranged (self-build) periodic struc-

tures, from which we mention pioneering work by Hill [226], chain of voids formed in the direction perpendicular to the laser beam when the last one is translated [25], and chain of voids formed as a result of multiple fs pulse irradiation in the direction opposite to the laser beam propagation (similar to what is observed in the case of fibre fuse) [227,228], and finally, frozen plasma waves enriched or with depleted oxygen concentration, which are left after a high-power femtosecond pulse, for example, in the bulk of fused silica [229], [230], [231]. This last method is not likely to be used for Bragg reflectors fabrication, but it has immense importance for post-inscription chemical treatment (etching in the diluted HF acid). At the same time these planes separated by a few hundred nanometers define the shortest achievable periods.

PbP inscription [232], [28] offers the most flexibility and control of the various methods, as it enables arbitrarily complex chirp and apodisation profiles to be simply programmed and realised by high-resolution translation stages. This flexibility comes with a cost for precision translation and alignment of the focal spot to the fibre core.

We also demonstrate other methods, for example micro-holographic inscription which may be considered as an extension of the point-by-point method.

In 2004, two groups independently reported on direct femtosecond PbP inscription of fibre Bragg grating (FBG) in standard non-photosensitive (and not hydrogenated) fibers [29], [233], [28]. Both groups used fs laser radiation at 800 nm tightly focussed into the fibre core, and precision positioning systems. The FBG-s produced were of multiple orders: either 4th order (Λ = 2.14 μm) [233] or from 1st to 4th orders, with the second order to be the strongest (period of about 1.07 μm) [29], [28]. For telecom applications at 1550 nm a period around 535 nm is required. Since that time, this PbP technique has evolved and become a standard method for the fabrication of FBG, with typical values of the inscribed period of 1070 nm [28], [91], [133], [94], [234], [9] or 1.12 μm (third-order grating for the reflection at 1080 nm [235]).

In 2005 we demonstrated first-order gratings for 1550 nm wavelength with the period Λ=0.535 nm. This was manufactured for the first time [39], [6] by 800 nm fs laser, when tightly focused inside the slab of pure fused silica, using a reflective micro-objective with NA=0.36. The key is in aberration-free focusing. Soon afterwards, this enabled us to inscribe the FBG with the same period of 535 nm by introducing an index-matching fluid between the

planar microscope cover slip and the fibre. So first order FBG became possible in standard fibres, including doped ones [133, 236], with periods that were already below the diffraction limit. In 2006 [50], the introduction of index-matching oil and a cover slip also enabled us to fabricate micro-holes, drilled through the fibre, which would otherwise be impossible due to the influence of a fibre cladding, which itself acts as a strong cylindrical lens.

For applications at shorter wavelengths (e.g. 1060 nm) shorter periods of about 360 nm are required, with the grating pitch being approximately half of this or 180 nm. This seems to be unlikely to be fabricated by 800 nm laser radiation. Numerical simulations performed by our group revealed that tight focusing could still produce such compact plasma clouds.

The challenge was to make them.

6.1 Point-by-point method for micro-fabrication of periodic structures by NIR fs laser

NIR PbP FBG inscription was carried out for the first time at the end of 2003. The setup for inscription in fibres had two additional 3D-stages of 17MAX303 type (by *Melles-Griot*) installed on top of the Y-stage of the 2D air-bearing stage (by *Aerotech*).

The key for PbP inscription was in the ability to align the position of the focus to the arbitrary point of the fibre core (usually a core has a radius of a few μm). The idea for the alignment method came from observation of the laser plasma discharge in air (see Figure 6.1) on the screen of the monitor or a computer. Using two CCD-cameras with high magnification optics for observation in the vertical and horizontal planes it was possible to find the position of the focus in air in the "reference system" of the optical table. Then next thing that required was the fibre core alignment to the plasma spot.

We used fibre illumination by coupling green/blue laser light into the fibre core, and on doing so the core was clearly seen on the monitor. So it was possible to bring it to the *same position* as the plasma spot. After alignment on one end of the travel range with the help of mechanical 3D-stage, the fibre was translated to the other end using the top axis (Y-) of the 2D air-bearing stage. At the other end the fibre was again manually aligned by another 3D-stage. By repetitive iterations, with this procedure one can eliminate an inclination of the fibre during translation. After vertical alignment the fibre was aligned in the horizontal

Figure 6.1: Plasma in air observed with top-view CCD camera. The length of the filament, obtained by $100\times$ MO when E$\cong 15\mu$J, is about $20\,\mu$m.

plane, using the diffraction pattern observed on the second ("horizontal") CCD-camera with highly attenuated laser light (sometimes with CPA output switched off by SDG-1 controls), or observing just a spontaneous emission from the amplifier.

This non-destructive procedure allows us to align the fibre without introducing any change at all to the material in the core/cladding areas. A similar method can be implemented both for polymer coated fibres, as well as for some "exotic" types of fabrication: pre-stretched, offset and twisted FBGs.

In the last case, the twisting of the fibre was using rotational clamps (by *Thorlabs*) mounted on top of each 3D-stage. Note that this method is suitable only for small twists, with a maximum available rotation per 70 mm fibre span of just a single twist (before the fibre breaks). This gives approximately the same range of periods as in *SPUN* silica fibres, where the twist is usually obtained by rotating the preform during the drawing of the fibre.

The spatially overlapped FBG (for example, at slightly different wavelengths) can also be fabricated if the fibre is rotated between two inscriptions [139]. We found that gratings can be offset from the center of the core, thus opening access to their polarisation properties. Examples of highly birefgingent gratings fabricated by the NIR fs PbP method are given in Section 7.1 and 7.2.

In our setup the lower (X-) stage is used to control the focusing distance from the micro-objective to the fibre. We found that it was more difficult to achieve good Bragg grating when the lower stage was used for scanning the fibre without a vibration isolation of the optical table. The mean-square deviation of (or error in) the position for Y-axis scan is less
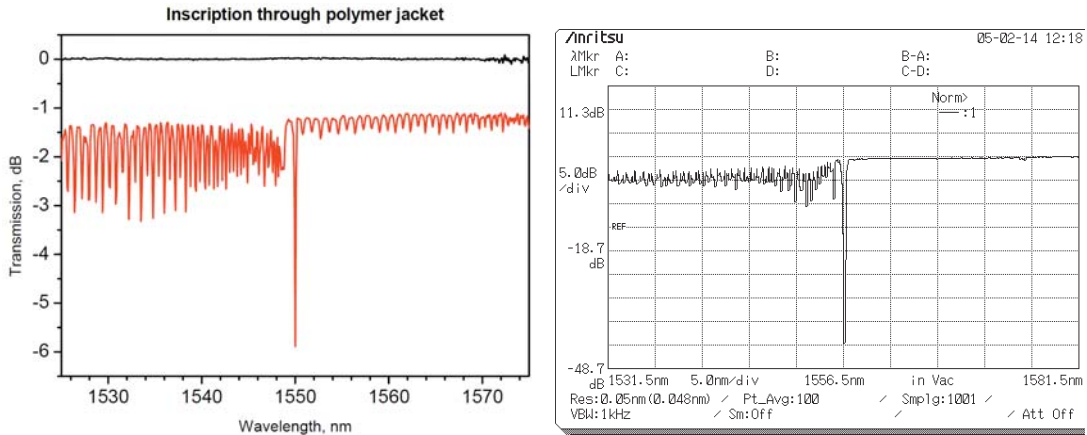
Figure 6.2: PbP FBG of the second order in a pre-twisted *SMF-28* fibre, inscribed without removing the polymer acrilic coating (a). For comparison a second order FBG was inscribed in DCF fibre (b). Note the absence of cladding mode resonances at longer wavelengths in the last case.

than 50 nm, while for X-axis it is three times greater.

Our observation on NIR inscription in planar poly-methyl methacrylate (PMMA) sample revealed that it is possible to introduce RI change without surface damage. Later, this observation allowed NIR PbP inscription of the strongest FBGs (-60 dB transmission deep when a second order grating was inscribed [94]) through the polymer coating of the fibre. The acrylic coating works here as a solid index-matching layer, but it demands high quality and uniform layers.

Once we had obtained the possibility of aligning the fibre under femtosecond laser, a number of inscriptions of various types of gratings in various optical fibres, both passive and active, were demonstrated [16, 139]. Some of them were described in the PhD thesis by Amos Martinez "Inscription of in-fibre photonics devices by an infrared femtosecond laser".

Meanwhile, NIR PbP fibre Bragg gratings suffer from a few serious drawbacks. While attempting to make first order gratings by using precise control of laser pulse energy, we observed simultaneously with the reduction in grating period reductions in the transverse dimensions of the grating pitch and in the RI contrast induced (due to the lower laser energy used). The effect is further enhanced for shorter periods [36]. This shrinkage of transverse dimensions has a twofold effect: i) due to smaller overlap of the modified RI area with the fibre mode and *lower* RI contrast these FBGs are *weaker*; ii) more localized (or compact) variations of RI create parasitic scattering, which manifests itself as off-resonance (gray)

losses, as well as parasitic resonances with higher order cladding modes (especially for multiple order gratings), which may create problems in multi-channel systems. Note that these resonances can be used for some sensing applications [237], [238]. Both gray losses and grating strength can be significantly improved if one can control the transverse shape and dimensions of the grating pitch.

6.2 UV point-by-point inscription of periodic structures

As mentioned in the previous section, it is difficult to fabricate FBGs with periods shorter than 530 nm by NIR fs laser. However, shifting the wavelength of the inscribing laser into the UV range, e.g. to 267 nm, with a simultaneous decrease in the order of absorption process from five-photon to two-photon, would immediately allow structures with even smaller periods to be recorded. Such a development is very important for a number of applications at the wavelength of about 1 μm. Since the achieved size of the pitch of the grating at telecom wavelengths (assuming 50:50 duty cycle) is about 270 nm and is already much smaller than the inscribing wavelength of 800 nm, further pitch size reduction using 800 nm wavelength would appear to be highly unlikely. It should be noted that before 2006 previous investigations on point-by-point micro-fabrication employed 800 nm femtosecond laser pulses, which excite the glass samples via five-photon absorption. A multi-photon approach can employ different wavelengths and different numbers of photons in one elementary act of absorption [239, 240], thus facilitating inscription inside various non-photosensitive optical materials.

It is also known that the propagation of a femtosecond pulse inside a bulk dielectric (e.g. fused silica glass) with a peak power above the threshold (critical power) results in self-focusing. Remarkably, this regime is characterized by a reduction of the spatial dimensions of the photoinduced material modifications below the diffraction limit [9]. Note that the reduction of focal spot can also occur below critical power, as was shown in Chapter 3.2.

There are two considerations which lie in the background of UV fs inscription. First, it is well known that the minimal spot size *linearly* scales down with the wavelength. The second is not so obvious and it is related to the fact that the non-linear properties of material may differ significantly when fs UV laser is used: the critical power for self-focusing scales
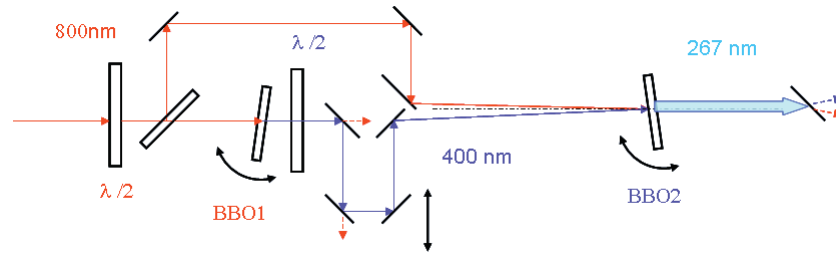
Figure 6.3: The setup for second and third harmonics generation. Second (and third) harmonics are obtained through collinear (non-collinear) Type-I (o-o-e) sum frequency generation, in 1 mm thick BBO crystals. First zero-order half wave-plate (HWP) is used to split the beam in two parts, using a 45-degrees polarisation beam-splitter, the second HWP is for 400 nm beam polarisation rotation. Note that by using first HWP the output power of second and thus third harmonics can be controlled.

down as a *square* of laser wavelength, thus for third harmonics this guarantees almost an order of magnitude reduction in critical power for self-focusing. The experimental setup for III harmonics generation is presented in Figure 6.3.

There is a problem with femtosecond laser power attenuation in the UV range, where there are few components which could withstand high peak and average power.

To address this issue we suggested using i) the Diffractive Optics variable attenuator [241], realized as a thin phase mask made of pure fused silica substrate. As was experimentally proven, this approach can cope with fs pulses as short as 50 fs with a spectral width of about 30 nm; ii) instead one can attenuate US fs radiation by simply rotating the first half-wave plate shown in Figure 6.3, which can be used to re-distribute the energy of 800*nm* pulses between two channels. This allowed us to manipulate the energy at the entrance of second-harmonics generator and thus the energy of the output radiation at 267 nm.

The CPA laser system delivered up to 0.85 mJ pulses with $\approx$150 fs duration and 1 kHz repetition rate. The diameter of the NIR laser beam was 2.5 mm. Second harmonic (400 nm) is produced in a 1 mm thick BBO crystal cut for type-I collinear SH generation ($\theta = 29.2$, $\varphi = 90$) [32]. A second zero-order half-wave plate was used for the 90° polarization rotation of the 400 nm beam. Using three "blue" mirrors, with high reflectance at 400 nm, the SH beam was separated from the fundamental. The 400 nm and a (partially) 800 nm beams were then directed onto a 1.0 mm thick second BBO crystal, cut for type-I sum-frequency generation ($\theta = 44.3$, $\varphi = 90$) [32]. The angle between the 800 nm and 400 nm beams was less than 2 degrees in the horizontal plane. Again, by using high-reflecting UV mirrors and the non-collinear geometry of THG, we easily separated the 267 nm radiation. The UV

pulse energy was monitored by a PD10 head and single shot energy-meter (USBU, Ophir Optronics). The maximum energy of the third harmonic pulses can be as high as 84 μJ with pump energy of 800 μJ at fundamental 800 nm. By varying the optical delay and measuring the cross-correlation function between the fundamental pulse and its second harmonic, we estimated the width of both 400 nm and 267 nm pulses to be about 350 fs. Maximum conversion efficiency into third harmonics was 12%.

The UV laser beam was sent in a strictly perpendicular direction on to the surface of the fused silica sample from the top, using a setup similar to the one presented on Fig. 4.5. Fused silica samples of 50×20 mm size and 1 mm thickness (by *Schott Glas*) were used in the experiments. They were moved in the horizontal plane in two perpendicular directions by the ABL10050 air-bearing translation stages. The translation speed varied in the range of 0.1∼5. mm/s. The absolute and relative micro-positioning accuracies were both better than 50 nm.

The UV fs beam could be focused to any selected depth between 0 and 600 μm below the surface with the accuracy of 1 μm. For focusing we used a reflective microscope objective (by *Ealing*), which has enhanced-Al UV coating and numerical aperture of 0.65, manipulated by a manual 3D-micro-positioning translation stage 17MAX303 (*Melles-Griot*). This objective has a correction ring to correct a spherical aberration of a sharply focused beam − for different sample (or cover glass) thicknesses or focusing depths up to 1 mm. The optimal correction was found as a result of multiple thorough experiments for the smallest period of the grating. The remote CCD-camera (with filters and protection windows removed,as these are non transparent for UV) was used for alignment and on-line monitoring of the inscription process. The inscription energy values varied between 15 and 400 nJ, whilst the length of inscribed tracks was usually between 0.5 and 4 cm. Due to the specific design of MO the central part in this objective is always blocked. The objective has an obscuration of about 15%, and a working distance of 8.6 mm. The period can be varied by tuning the translation speed. For example, for the inscription of the 535 nm period the stage was moved with a speed of 0.535 mm/sec while the laser had a repetition rate of 1 kHz.

We also tested "classic" UV glass objectives (by *OFR*) which produced much worse results, possibly due to self focusing inside the glass lenses.

In our first set of experiments, described in [32], the use of 267 nm femtosecond pulses

with 82 nJ energies of 360 fs pulses led us to the inscription of 300-nm-period structures. Subsequently, the optimisation of the inscription depth has allowed us to decrease the inscription energy down to 30 *nJ* and to inscribe the $250 - nm$-period. The quality of the nanostructures was also significantly improved in comparison with the first report [32].

To establish optimal conditions for femtosecond inscription, in general, one should adjust at least three parameters, including particularly the laser pulse energy, the focus depth inside the sample, and the polarization of the inscribing light with respect to the direction of sample movement. The combination of the speed of translation stage movement together with the pulse repetition rate defines the period one wants to obtain, which is why it is not a free parameter. Often the inscription depth is not a free parameter either. Other parameters which can be hard to change in experiment include: the numerical aperture of the microscope objective, and laser parameters such as the repetition rate of the laser, the wavelength and the duration of the inscribing pulses, which could also be variables. One parameter we have not discussed so far is a spherical aberration, which would inevitably occur due to the high numerical apertures of the micro-objectives involved. Experimentally, this parameter can be controlled by a correction ring, which in fact enables precision shifts of a lens (or a group of lenses) in the objective. Overall, the resulting number of experimental tracks could easily reach some thousands: thus, an express diagnostics method is important for such optimisation. We perform the characterisation of the irradiated samples using Axioscope-2 MOT+ (*Zeiss*) optical microscope, which was equipped for both transmitted light and Differential Interference Contrast (DIC) measurements. The resolution d of (or minimum spot diameter obtained with) an optical microscope is considered to be of the order of the illumination wavelength, and can be estimated using this practical formula:

$$d \approx C \cdot \frac{\lambda}{NA}, \tag{6.1}$$

where NA is the numerical aperture of the objective used, and C typically between 1.22 and 1.5 depending on the shape of the beam.

In our microscope (with NA=1.4 oil immersed, $100\times$ objective), even with the use of halogen lamp illumination and a blue filter ($\lambda \approx 0.4\mu$m) it was rather difficult to distinguish the 400-nm-period perturbations induced in the bulk of the material. However, the use of DIC technique enabled us to monitor structures with periods down to 250 nm. In the experiments, we used the combination of the Plan-Apochromat oil immersed objective (100/1.40/DIC)

and the Achromatic-Aplanatic condenser (1.4H/PH/DIC) with NA=0.6 (or even higher!). A DIC-prism (III/1.4) and DIC-slider (100/1.40III) were also used; such a combination seems to be the best one commercially available (all by *Zeiss*).

The refractive index variation was of the order of 10^{-4}, which corresponds to a few times more than the level of sensitivity for our microscope, based on comparable experiments conducted with known samples. It is important to remember that DIC microscopy does not present the real image; rather, the resulting picture contains the information on the intensity distribution and the derivative of the optical phase between two orthogonally polarised beams, spatially separated by a distance *shorter* than the resolution of the $100\times$, NA=1.4 microscope objective (which is about 400 nm in our case). Thus, periods down to about few hundred nanometers can be detected. Finally, the visibility (contrast) of the pictures was higher when additional interference filters 380 or 405 nm were used (by *Semrock*).

For the independent calibration of the microscope, some tracks also exhibiting topographic changes of the surface were characterized with atomic-force microscopy (AFM) [36], when the commercial instrument Dimension Nanoscope III (by VEECO) working in the tapping mode was used. We begin our inscription experiments by focussing the MO on the surface of the fused silica sample. With pulse energy as small as 38 nJ, we were able to ablate nanostructures with a translation speed of 1 mm/s. Taking into account the repetition rate of 1 kHz, it is easy to deduce that the recorded grating possesses a 1000 nm period (Fig. 6.4, a, b). The DIC microphotography taken at the surface of our fused silica sample makes us suspect that the laser beam cross-section in the focal plane has a non-Gaussian profile and may also vary in size from pulse to pulse. This was revealed by the AFM technique (Fig. 6.4, b) as topographic changes in the sample surface. The asymmetry seen in individual voxels may be related to the light diffraction (of an imperfectly circular beam) on the wire holders of a small mirror inside the micro-objective. From further consideration it will be evident that such diffraction becomes unimportant while focussing inside the slab of fused silica. Calibration of our microscope was also confirmed. Thus, Figure 6.4, (b) (cross-section of the image along the grating) shows that 10 periods of our nanostructure inscribed on the surface of a sample correspond exactly to 10 μm length, confirming our calibration (the scale bar is 10 μm). The cross-section in the perpendicular direction, presented in (c), which is an ablation profile or cross-section, gives an upper estimate of 400 nm for the diameter of
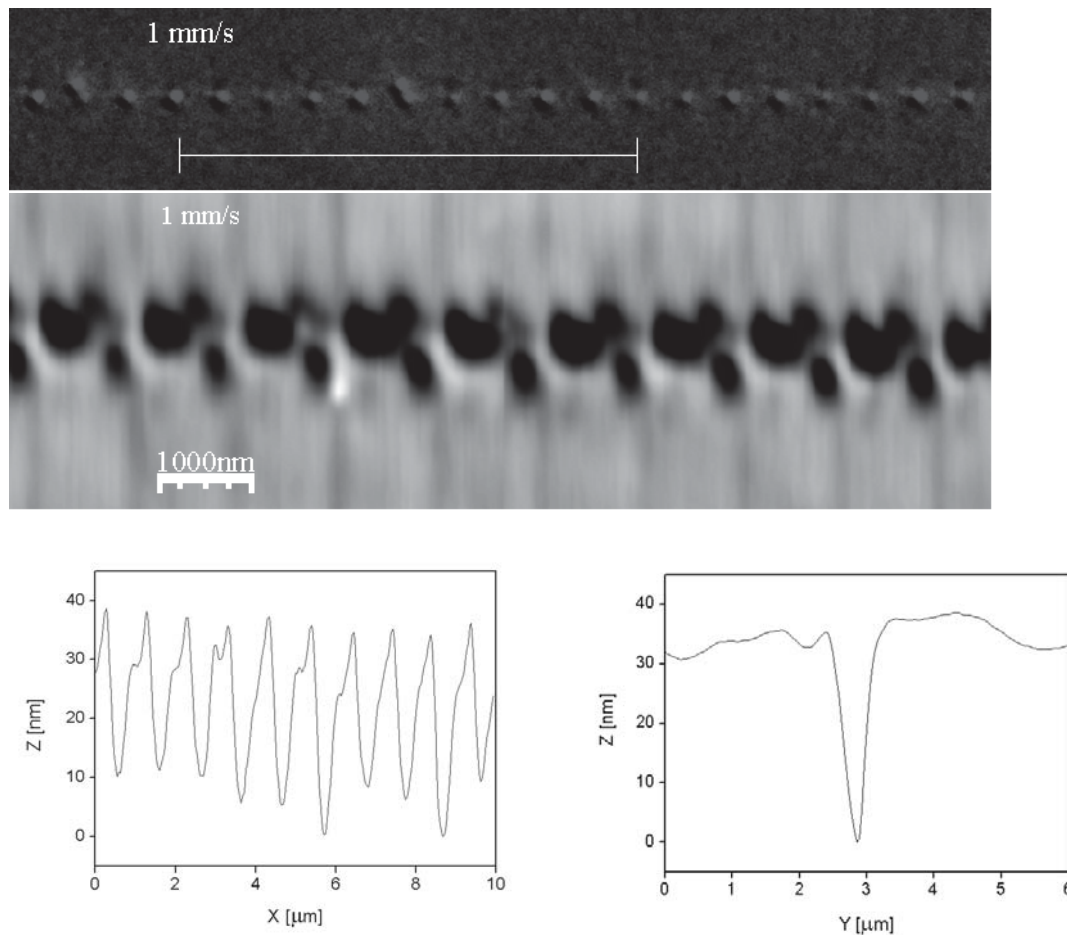
Figure 6.4: DIC microphotograph (a) of the 1000-nm-period nanostructure, fabricated on the surface of a fused silica sample. The energy of the inscribing pulses was 38 nJ. The size of the bar corresponds to 10 μm. Topography (b) of the same 1000-nm-period nanostructure from (a), investigated by AFM. Cross-section (c) of the image presented in (b), along the inscription direction. Cross-section of the image presented in (b), perpendicular to the inscription direction (d).

167

the laser beam cross-section at FWHM at the surface of our sample, which agrees with the spot sizes deduced from the figure (300~360 nm). To estimate the beam-waist diameter in the focal plane, we use the Eq. 6.1, where for a diffraction-limited focusing, C is ≈1.22. Substituting λ=267 nm and NA=0.65 gives a beam-waist diameter of 500 nm, which agrees reasonably well with the experimental values given above. Much better results - inscription at smaller translation speed values down to 0.25 mm/s - were obtained with the inscribing light tightly focussed to a depth of 170 μm below the surface of a fused silica sample. Figure 6.5 demonstrates the periodic structures obtained using 30 *nJ* pulses with sample translation speed values of 1.0, 0.5, 0.4, 0.3, and 0.25 mm/s, i.e. with periods 1000, 500, 400, 300, and 250 nm respectively. The polarisation of the light was parallel to the direction of the scan.

The good quality of the gratings obtained (Figure 6.5) should be emphasized (cf. structures with similar periods obtained in our first experiment [32] and depicted in Fig. 6.4). Furthermore, the irregularity in spot size was strongly reduced.

It is interesting to note that measurements of the diameter of spots presented in Fig. 6.5 show that the decrease of the translation speed value from 1.0 mm/s to 0.5 mm/s and further to 0.4 mm/s leads to the simultaneous decrease of a (single pitch) diameter from 630 nm to 300 nm and then to 230 nm (with an accuracy of about 10%). A similar feature was seen in the tracks with similar periods presented in our paper [32] (Fig. 6.4). This effect could be related to the change in glass properties (e.g., induced absorption and refractive index change) performed by the previous inscription pulse (pulses). These changes increase the absorption or destroy the wavefront for the following laser pulse (pulses) and hence change laser pulse energy arriving at the focus, and perhaps the self-focusing scenario. The decrease of the translation speed value should increase the probability of such effect(s). Thus the deterioration of quality of these gratings may be connected with overlapping between neighbouring spots if the size of a spot exceeds half of the nanostructure period, i.e., 150 nm.

Note that the structures with the shortest period of 250 nm were observed only at a depth of 170 μm. This perhaps reflects the fact that 100× NA=1.4 MO is designed to give the best resolution at this depth. The importance of using the optimal focus depth and optimal energy can be illustrated by experiments conducted at 330 μm below the sample surface. At this focus depth, using 89 nJ pulses, we managed to record structures only with periods down to 500 nm; at the optimal inscription depth of 170 μm, with almost the same pulse energy of

10 µm
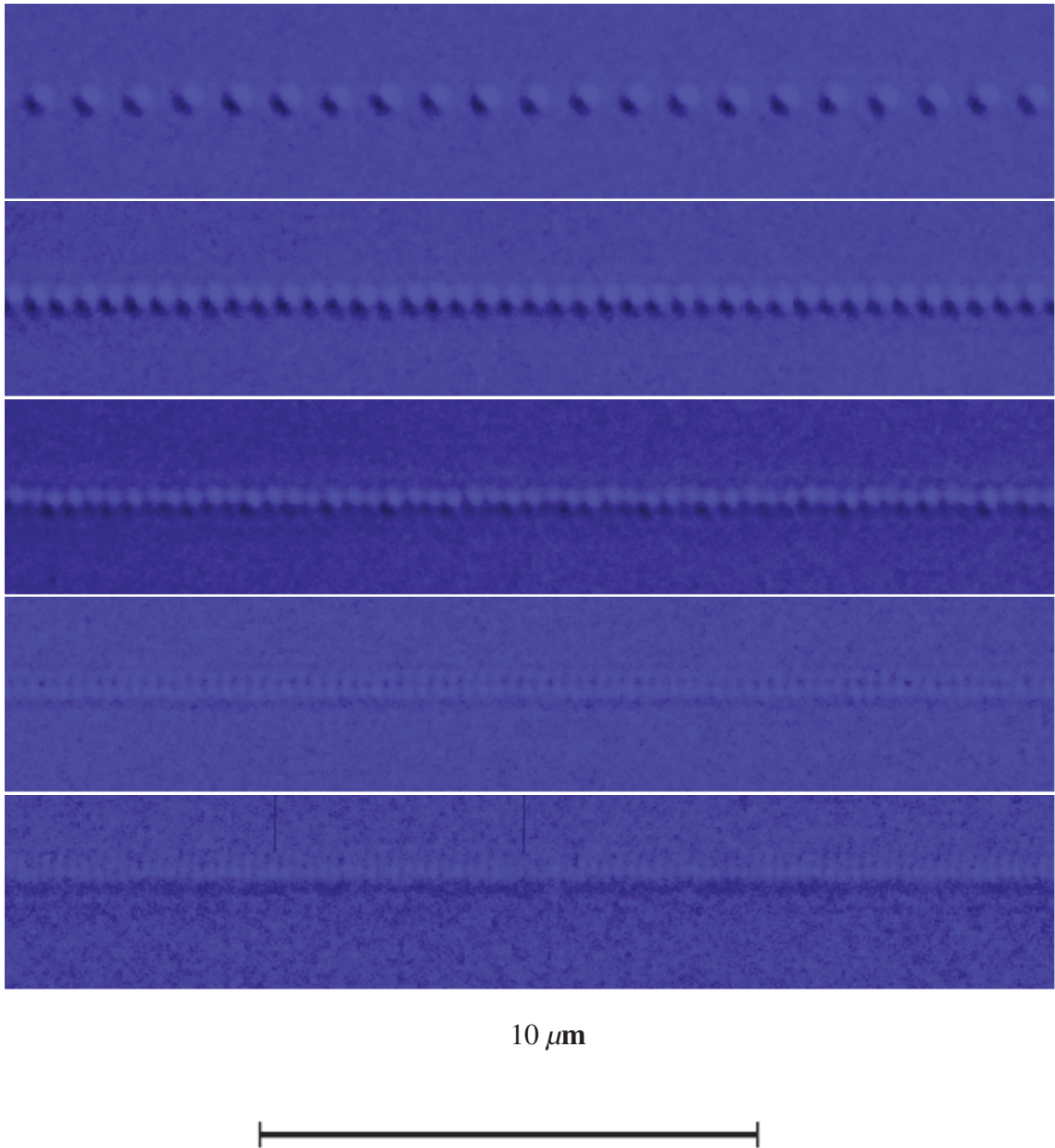
Figure 6.5: Results of optimisation - record short-period (250 nm) structures were created in the bulk of pure fused silica at the depth of 170 µm, using the point-by-point method and 267 nm femtosecond laser radiation, laser pulse energy of 30 nJ and a pulse duration (FWHM)- 330 $\pm$ 50 fs. Focusing by reflecting micro-objective 74$\times$ with *NA* =0.65 (*Davin Optronics*) and enhanced *Al* UV-coating, and a correction ring set to 0 µm. Polarization of laser beam was linear, parallel to the tracks.

92 nJ, it was possible to record both 400 and 300 nm periods [36], [32].

It is likely that femtosecond PbP inscription might be able to provide even shorter periods, down to the physical limit defined by the dimensions of a plasma cloud, which seems to be about 200 nm, as was observed in experiments by [242], [231]. This effect may also occur due to the spatial compression of the electromagnetic field coupled to plasma waves. Unfortunately the model, based on paraxial NLSE coupled to plasma, does not allow us to simulate all these effects accurately.

The minimal pulse energy value of 30 nJ used for inscription can be compared with the pulse energy value of 600 nJ used earlier for NIR PbP nanostructure fabrication [139]. Such a decrease in the inscription energy is in line with the decrease in the order of the absorption process, from five-photon to two-photon. It should be emphasized that the laser pulse peak power values used in our experiments (up to 300 kW) correspond to (or are above) the critical power for self-focusing in fused silica, which at 267 nm is estimated to be 250 kW (see below). The importance of the 170 μm-thick glass layer for the substantial decrease of the focal beam spot is undoubtedly related to nonlinear effects, as was revealed by numerical modelling [38] (see also Figure 6.6 below).

The estimate of the critical role of non-linear effects is based on the fact that critical power at the wavelength of third harmonics:

$$P_{cr} \simeq 0.93 \cdot \frac{\lambda_{TH}^2}{2\,\pi\,n_0\,n_2} \approx 250\,kW, \tag{6.2}$$

is about one order of magnitude less than at 800 nm (2.3 MW). In our experiments on UV PbP inscription the pulse peak power was almost always above P_{cr}. The estimation of the inscription threshold by using formula (3.47),

$$I_{MPA} = \left(\frac{K\,E_{ph}\,\rho_{BD}}{\tau_P\,\beta^{(K)}} \right)^{1/K} \tag{6.3}$$

where $K \cdot E_{ph}$ is the energy of K=2 photons at 267 nm ($\approx$9 eV), ρ_{BD} =1.6·10^{22} cm^{-3} is the critical (breakdown) plasma density at this wavelength, τ_P is the laser pulse duration, $\beta^{(2)}$ is two-photon absorption coefficient 2·10^{-11} cm/W [82]). The calculation gives for the threshold of femtosecond inscription at 267 nm the value of about 7.7×10^{13} W/cm^2.

Once the I_{th} is determined, using the pulse duration t$_{FWHM}$ =350 fs or $\tau_p = \frac{350\,fs}{2\,\sqrt{\ln 2}} \approx$ 200 fs - a pulse-width at 1/e-level, the threshold energy can be estimated intuitively as:

$$E_{th} = I_{th}^{(267)} \cdot \sqrt{\pi}\,\tau_p \cdot S_l \approx 53.7\,nJ, \tag{6.4}$$
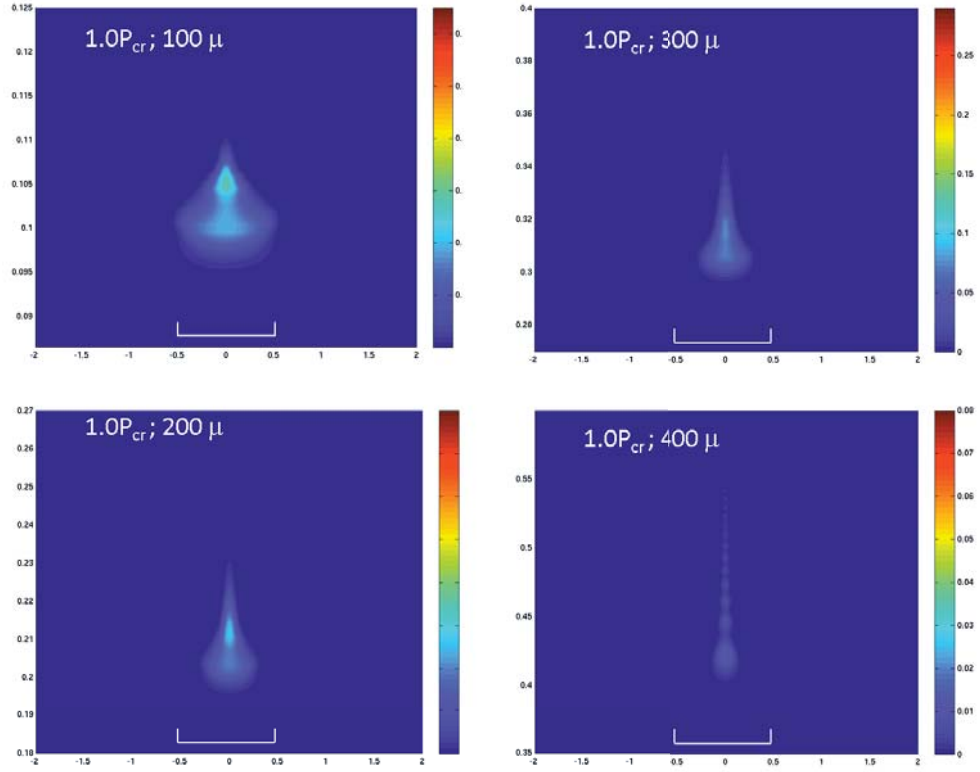
Figure 6.6: Numerical simulations of the plasma distribution at different depths. The scale-bar on all graphs corresponds to 1 μm, all plasma densities were normalized to ρ_{BD}.

Alternatively, we can use Eqs. (3.32), (3.49). The needed area of the focal spot in the linear case is $S_l = \pi \left(0.61\frac{\lambda}{NA}\right)^2 \approx 0.192\,\mu m^2$, and the "critical area" $S_{cr} = P_{cr}/I_{th} \approx 0.4\,\mu m^2$ for the case of Gaussian beam (note that it is two times larger for the ring beam of the first order, as follows from Eq.3.32 in the case of M=1).

$$E_{th}^{(lin)} \approx \xi \cdot P_{cr}^{(267)} \sqrt{\pi}\,\tau_p \qquad (6.5)$$

the factor ξ represents the ratio of the pulse peak power at threshold to the critical power of self-focusing. It equals to 0.377 for the case of Gaussian beam and 0.233 for the case of ring beam of the lowest order of M =1 (as follows from Eq. 3.32, 3.49).

The estimate by Eq.6.5 produces 3.3 nJ or 4.1 nJ threshold for UV fs inscription in the case of Gaussian or ring beams respectively. This simple estimate well agrees with experimental results (the detected threshold for inscription was about 10 nJ, however this did not produce the best periodical structure), and also was confirmed by numerical simulations (by H. Schmitz) and published in our paper [38].

A few pictures from the paper [38] are reproduced in Figure 6.6, where the following

171

parameters have been used for calculations: $NA = 0.45$, $n_0 = 1.4993$, $\tau = 175$ fs, $n_2 = 2.72 \cdot 10^{-16}$ cm^2/W, $\beta^{(K)} = 2.0 \cdot 10^{-11}$ cm/W - TPA coefficient, $\tau_e = 1.7$ fs - electron collision time, $\sigma^{(2)} = \beta^{(2)}/(2 \cdot \hbar \cdot \omega \cdot \rho_{at})$.

One can see that at the depth of 200 μm the plasma generated has maximum density and the most compact distribution.

Thus both the analytic results developed in Chapter 3 and the results of numerical simulation using the semi-phenomenological NLSE model (equations 3.1, 3.2) are in good agreement with the experimental findings. Note that this was possible after careful alignment of the micro-objective, the optimisation of the correction ring and using a laser beam of good quality (M^2-parameter less than 1.1). These experimental findings set an important benchmark for the short-period limit one could achieve for periodic pattern inscription.

6.3 Micro-holographic inscription method

The PbP method offers the greatest flexibility, as well as outstanding high temperature and high energy performance of FBG; however lengthening of the grating pitch in the direction of light propagation (perpendicular to the fibre core axis) and shrinkage in lateral dimension leads to a birefringence in reflection/transmission spectra as well as high off-resonance losses, which may or may not be desirable.

As was demonstrated in the previous section, the point-by-point method can possibly be implemented even for visible range applications. Having obtained the shortest period by UV PbP inscription, the issue of low overlap integral has not been addressed, neither has the problem of high off-resonant losses. There are also other issues associated with the stochastic nature of the PbP gratings: any pulse-to-pulse energy variations of the laser and/or positional errors (e.g due to the translation stage or vibrations) may be converted into stochastic variation of the grating parameters. These could broaden the reflection resonance and decrease the maximum reflection, so a beam-shaping technique which takes all these factors into account should be found.

Ideally, the laser radiation should be focused into a focal area of few micrometers, which has to be patterned in such a way as to produce the short-period intensity distribution along the core of the waveguide (as with the phase mask method). If this interference pattern is

translated between laser shots exactly over its period, then it may inscribe the grating along the whole translation length.

First we considered a simple model, sketched below, where we calculated intensity distribution as a result of the interference of two tilted Gaussian beams. The expression for the Gaussian beam in the reference frame when the beam axis is collinear to Z-axis reads:

$$E(x,y,z) = E_0 \frac{\omega_0}{\omega(z)} \cdot exp\left[-i \cdot \left(k\,z - arctg\left(\frac{z}{Z_r}\right)\right) - (x^2 + y^2) \cdot \left(\frac{1}{\omega(z)^2} + \frac{i\,k}{2\,R(z)}\right)\right].$$
(6.6)

When the propagation axes of two beams are tilted (symmetrically, around the y-axis), then the following variable substitution:

$$\{ \ \widetilde{\mathbf{x}}_\pm \ \leftrightarrow \ \cos(\alpha)\,\mathbf{x} \ \pm \ \sin(\alpha)\,\mathbf{z}; \quad \widetilde{\mathbf{y}} \leftrightarrow \mathbf{y}; \ \ \widetilde{\mathbf{z}}_\pm \ \leftrightarrow \ \pm \ \sin(\alpha)\,\mathbf{x} + \cos(\alpha)\,\mathbf{z} \ \}$$

allows the intensity distribution to be found. With two identical monochromatic Gaussian beams, without any temporal delay between them, when both are tilted at equal angles $\pm\alpha$ to the vertical axis and focused into the same focal spot, the intensity distribution in the plane ($\widetilde{\mathbf{z}} = 0$), which is perpendicular to the bisectrices of the angle between two beams can then be written as:

$$I(\widetilde{\mathbf{x}}, \widetilde{\mathbf{y}}, \widetilde{\mathbf{z}}) \ = \ \int_\lambda \left[\left|\overrightarrow{E}(\widetilde{\mathbf{x}}_{+\alpha}, \widetilde{\mathbf{y}}, \widetilde{\mathbf{z}}_{+\alpha}) + \overrightarrow{E}(\widetilde{\mathbf{x}}_{-\alpha}, \widetilde{\mathbf{y}}, \widetilde{\mathbf{z}}_{-\alpha})\right|^2\right] d\lambda$$
(6.7)

Two beams have nearly plane wavefronts near their foci, so one may expect that the interference will form a set of parallel lines, in any plane perpendicular to the bisectrices of the angle between two beams; and these lines could be separated approximately by the distance $\lambda/(2 \cdot sin(\alpha))$, where α is the angle between the bisectrices and the corresponding beam axis. In Eq. 6.7 the arrows above the electric field indicate that the expression takes their polarisations into account. Obviously maximum contrast can be achieved in the case of S-polarisation (perpendicular to the plane of incidence). This case was calculated numerically, and the results are presented in Figure 6.7. Indeed the results obtained support intuitive considerations.

In experiment, these two beams could be produced in different ways. To illustrate experimental feasibility, we have chosen three optical layouts, inspired by work of Maznev et al. [243]. All our designs are based on transparent phase masks (such as binary diffractive gratings) with relatively coarse periods. Such masks themselves can be fabricated by fs lasers [244]. We intended to use third harmonic (267 nm), produced on the fs LRR CPA setup
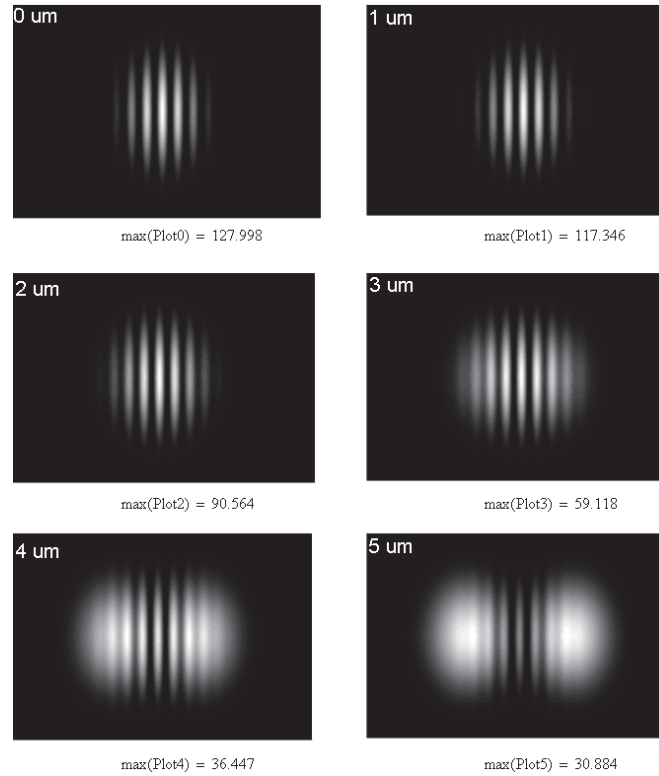
Figure 6.7: Calculated intensity distributions for two beams interfering at some angle. The distance from focal plane is indicated on the figures. The laser spectral width is 12 nm.

as was described above, and sharp focusing by one of the reflective micro-objectives. Sharp focusing is a "must have" option in order to reach the threshold intensity ($> 10^{13}\ W/cm^2$). The idea of using phase masks is not new, however it has not been done in combination with the MO, so we named this approach Micro-Holographic method.

In Table 6.1 we present the results of calculations of the interference angle in a symmetrical configuration, required for inscription of the first order Bragg grating for application at different wavelengths, using the formula: $sin(\alpha) = \lambda/(2 \cdot \Lambda_B)$, where Λ_B is the required period for a Bragg grating. These values demand certain apertures of the objective (NA) to be used in each case.

Considering the apertures of the MO we have, the best choice seems to be the $74\times$ reflecting one with a maximum *NA* of 0.65. This MO should allow us to fabricate periods as short as 200 nm: from the third line of Table 6.1 we found that III-harmonic combination with such reflecting MO offers greatest flexibility for FBG inscription for applications ranging from 650 nm to 1650 nm.

Phase masks (with nulled zero-orders, from 50 to 100 *l/mm*) were fabricated specially to

Inscription / Application Wavelengths (Period), nm	1560 (538)	1050 (362)	980 (338)	808 (279)	650 (224)
800 nm (Fundamental)	0.74	> 1	> 1	> 1	> 1
400 nm (SH)	0.37	0.55	0.59	0.72	> 1
267 nm (TH)	0.25	0.37	0.40	0.48	0.60

Table 6.1: Minimum numerical aperture of MO required to inscribe 1st order FBG in standard fibre, depending on application wavelength (and Bragg period required). The first, second and third rows of the table correspond to fs inscription made by NIR laser radiation with the wavelength of λ=800 nm, its 2nd (400 nm) and 3rd (267) harmonics respectively.

match our UV, 74×, reflecting MO. Three examples of optical layouts, are considered below. In all cases we use the MO and mask(s), to split incident beam into two ($\pm$1) diffraction orders. These two beams are then focused by the same MO and spatially overlapped in the focal plane (or beyond, as for example in the first layout), so the interference pattern is produced. Other diffraction orders are blocked due to the design of the MO. The modification of the refractive index in the maxima of the interference pattern leads to the inscription of a periodic structure (grating). If the sample is translated perpendicularly to the interference fringes with a speed V equals $\Lambda_B \cdot N \cdot f$, where f is the pulse repetition (or modulation) rate and N is an integer, a periodic structure or grating will be inscribed over the whole length of the translation. The optical schemes we tested with the micro-holographic method are presented in Fig. 6.8.

The first version of the optical layout (Fig. 6.8, a) consists of a pair: a phase mask (PM) and the MO. As these two beams are not parallel to the optical axis of MO, they will be focused at different points in the focal plane. However, the beams intersect beyond the focal plane and will interfere regardless of how short the laser pulse is [243, 245]. In the area of intersection an interference pattern is produced. This scheme works well for surface structures even in the case of a few fs pulses, but it is not possible to use it to make an inscription in the bulk. This is caused by the fact that intensity around the focal points is higher than in the maxima of interference fringes. When the beam power is sufficient for inscription to begin, modifications (or even damage) are produced first in the focal plane, thus these start to scatter light and interference will be distorted or may be even destroyed. Scheme A is very easy to align, as it has only two elements. This layout guarantees pulse overlapping and the generation of an interference pattern in large areas, even with small tilts
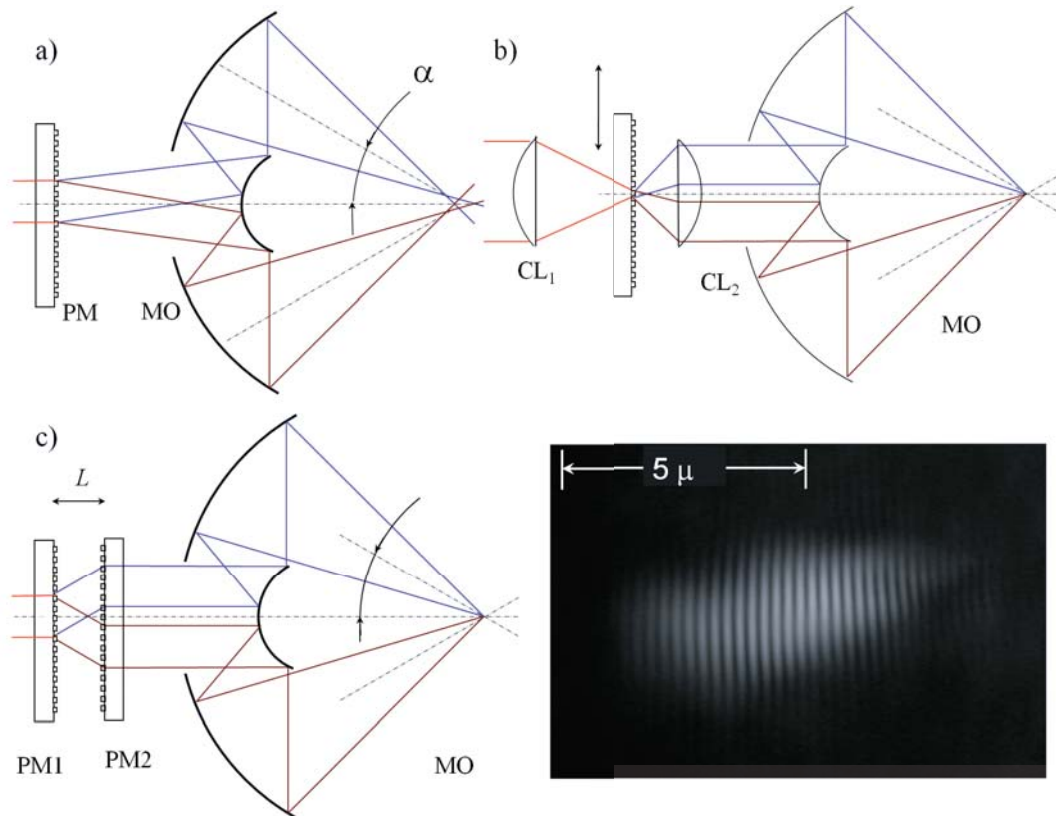
Figure 6.8: Optical layouts for micro-holographic inscription: a) PM and MO pair, b) two cylindrical lenses (CL1 and CL2), PM and MO, c) two phase-masks and MO. The shortest period obtained by using the longest focal distance CL2 in the layout b) is about 260 nm.

of the mask. The geometry is suitable for inscription of micro-gratings on the surface of any sample, for example by means of direct femtosecond laser ablation, and also in the bulk of thin samples - for example, layered, say, by UV absorbtion.

The second version of the optical layout (Fig. 6.8, b) includes two cylindrical lenses, the PM and the MO. The beam focused by the first cylindrical lens CL1 on PM, after diffraction creates multiple diffracted beams with the same origin, which are then collimated by the second cylindrical lens CL2. The position of the phase mask and the distance between CL1 and CL2 were adjusted so that the PM was placed in the focal plane of both lenses. Two collimated beams after CL2 fall onto the objective MO and, ideally, focus at the same point, where the interference pattern is produced. The application of cylindrical lenses is critical, as CL1 focuses light on the PM surface forming the focal line with the length up to the input pupil of the MO or the input beam diameter. If a conventional lens is used, a laser light will be focused in smaller spot, which could damage the phase mask. With CL1 the intensity is much lower and the mask is not affected. On a sample the laser light is focused into a much smaller spot, thus the intensity in fringe maxima is sufficient to initiate material modification, even if the sample and the PM are made from the same material. When CL1 and CL2 are different, the beam (as well as the focal spot) may lengthen. The greatest disadvantage of this scheme is in its complex adjustment, because of the small diameters of the two focal spots. If the two beams are not quite parallel, they do not overlap, so no interference pattern will be created. Furthermore the diffraction stretches the femtosecond pulse and also tilts the direction of the wave front. So the stretching and the space chirp may cause the intensity contrast at focus to decrease, so the beam power may need to be increased. High power can damage optical components used in this optical layout. Even without damage, we observed that strong red luminescence occurred when an 8 mm thick phase mask made of pure fused silica was used. Scheme (b) allows simple period tuning by translating chirped phase mask (the mask with variable period) perpendicular to the laser beam.

The third version of the optical layout (Fig. 6.8, c) incorporates two phase masks PM1, PM2 and the MO. After diffracting on the first *and* second phase masks (both are identical), the two beams become parallel. This layout (known as the Talbot interferometer [246]), produces two parallel beams if the masks PM1 and PM2 are identical. The chirp introduced by two diffractions cannot be easily compensated for in our setup. The only available mech-
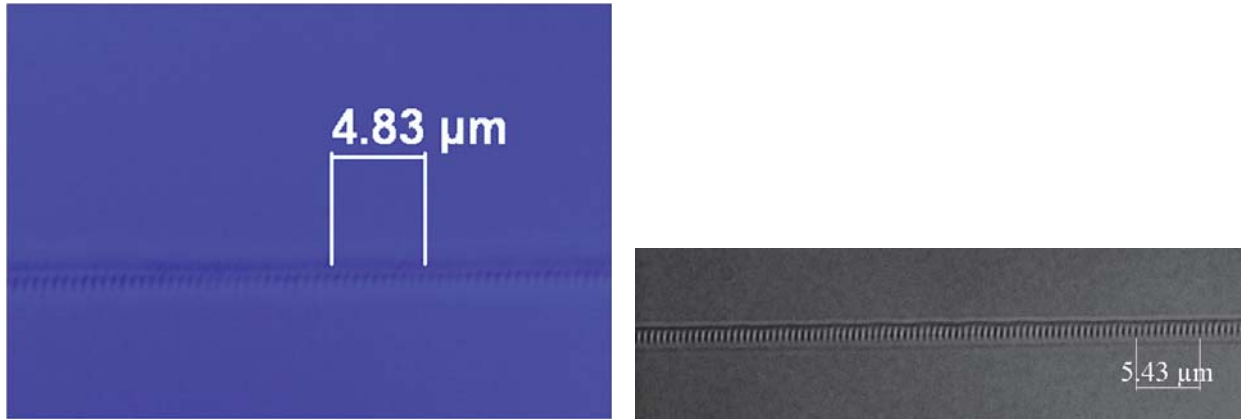
Figure 6.9: Examples of 483 nm period in the bulk, at a depth of 100 μm (a) and periodic pattern directly ablated on a fused silica sample surface (b) with the period of 543 nm. Both structures are made with the optical layout (b) of Figure 6.8.

anism for chirp pre-compensation has already been used for optimisation of the harmonics generation, so this is no longer a free parameter. It was much easier to align two masks made of a plane-parallel substrates, than layout (b) in Figure 6.8, which involves two cylindrical lenses.

A third scheme offers the possibility of continuously tuning the period of the fringe pattern by simply changing the distance between the two masks. It is worth noting that all of the schemes above allow fine interference fringe period tuning by changing the wavelength of the fs laser light. All of the layouts suffer from spatial chirp. More sophisticated designs seem to be possible to compensate for this.

An example of a periodic interference pattern is shown in Figure 6.7, while the examples of periodic structures generated in fused silica are in Figure 6.9

The periods down to 450 nm were obtained in the bulk of fused silica at a depth of about 80~100 μm, with the UV fs pulse energy below 80~100 nJ [37]. Unfortunately, our current setup does not allow inscription in an optical fibre due to strong absorption in index matching liquids.

In conclusion, more than one order of magnitude enhancement in the lateral length of the focal spot and the lateral dimensions of the structures produced were demonstrated. The shortest period which can be achieved with such a technique is about 250 nm, currently limited by the maximum NA of the reflecting MO. The Micro-Holographic method paves the way to a hundred-nm pitch inscription using the non-lithographic direct fs inscription tech-

nique. For a demonstration of the micro-holographic inscription in optical fibres a new setup has to be designed and built, which would address several issues of our current experimental facility, including absorption in index matching oil. The most problematic was the alignment of two spots together, with equal optical paths for two interfering beams. Surprisingly, it was easier to balance OPD in scheme (b) with two cylindrical lenses, and much more difficult for scheme (c), with two phase masks, perhaps due to the fact that the masks were made on thick and *wedged* substrate.

6.4 Periodic structures creation by direct modulation of the femtosecond pulse train

The most attractive possibility for practical usage would be the simultaneous inscription of both smooth waveguides and periodic structures using the HRR system. This non-trivial approach was suggested for HRR systems in 2006 [247] and it could be realised if the output pulse train is being modulated by an external modulator (AO or EO). Surprisingly, the heat accumulation effect does not prevent such short periods from occuring (the period 500 nm, which we demonstrate below, is 50 times smaller than the WG cladding diameter and 5 times smaller than the core). We incorporated such a modulator into the HRR system layout, before the prism compressor. Our modulator (by *Magdich*) has the following parameters: max aperture 4 mm; material Quartz, with BB AR-coating on both surfaces; input polarisation - horizontal; ON/OFF switch time - better than 1μs for beam diameter of about 4 mm. It was driven by 80 MHz RF-amplifier (by *Intra-Action Corp.*), and provided up to 98% of laser beam attenuation. The duty cycle in all our experiments was 50% with a maximum available intensity modulation contrast. We implemented the following trick for searching for inscription regimes with such modulation. While driving the stage with a sample (at a constant laser power or pulse energy) at an increasing speed of translation, the modulation frequency applied to the AO modulator also increased proportionally, so the expected period was kept the same in the range around 500 nm, which would define the periods suitable for applications at around 1550 nm. The speed was varied around a few tens of mm/sec, as this allows us to use optimal inscription parameters. We found that arbitrary periods starting from 480 nm and up to $\approx$2,200 nm can be obtained at maximum available pulse energy from our
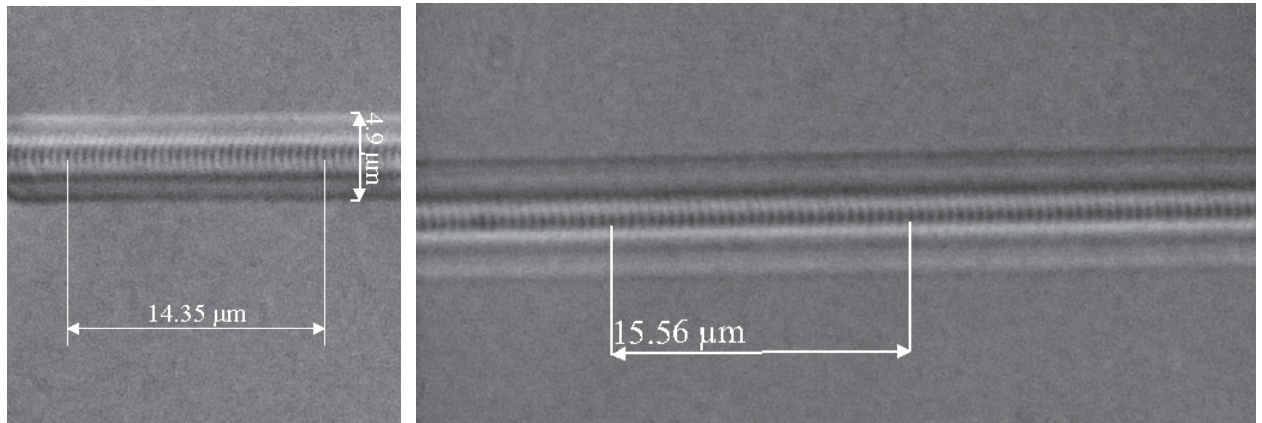
Figure 6.10: Direct modulation allowed the fabrication of first-order period waveguide Bragg gratings: a) 480 nm; b) 520 nm.
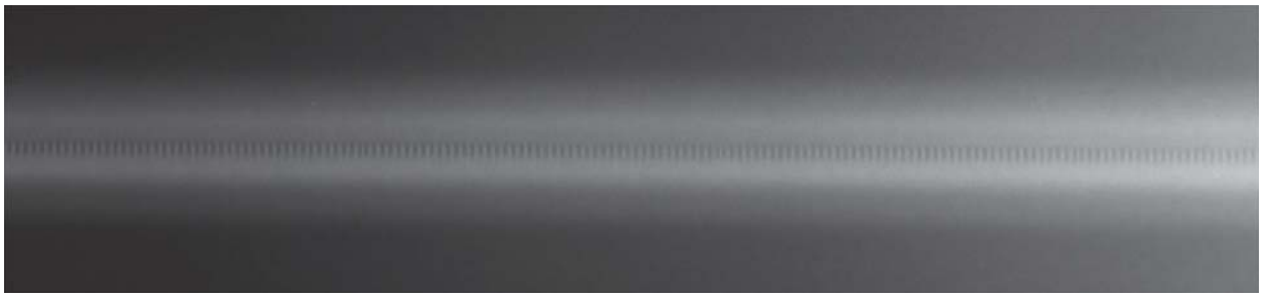
Figure 6.11: HR DIC microscopic image revealed no modulation in the waveguide cladding, but only in the core. Note the high quality of such self-arranged structures.

oscillator (65 nJ on target). The range of periods demonstrated is far above what is required for the whole C-band. Note that we have not observed any modulations in the cladding region, perhaps due to heat diffusion, while the core region was extremely responsive to the modulation. Figure 6.11 illustrates the high quality of such self-arranged periodic structures. Note that to cover whole C-band (1530 to 1565 nm) one should be able to fabricate periods from 500 to 542 nm (assuming n_{eff} =1.52).

Thus we managed to incorporate the direct AO modulation technique into the HRR femtosecond inscription setup. Following this step, we demonstrated the high quality periodically modulated waveguides with periods shorter than could possibly be achieved by the PbP NIR method [132]. This technique, which is based on self-arranged periodical modulations, should be applicable to fibre Bragg grating fabrication as well. The range of periods demonstrated is far beyond what is required for C-band. This enabling technique may be further developed for a single-stage fabrication of integrated optics WDM-components. In view of the high-temperature stability of such gratings [72], [167], this seems to be a very attractive

future project.

Chapter 7

Novel components by direct femtosecond inscription in fibres

Since the first demonstration of direct femtosecond inscription in glass, fibre devices have attracted a lot of attention. In this Chapter we provide examples of direct femtosecond inscription in fibres.

7.1   Vectorial bend sensors fabricated in a standard optical fibres

A Long Period Grating is formed as a result of periodic RI variations in the core of a single-mode optical fibre, and it couples light from the fundamental mode into one or more co-propagating resonant cladding modes. Among many applications, a promising one is an LPG for bend sensors [224, 225]. However, there is a problem associated with this, as the direction of the bend obviously cannot be determined if the sensor is inscribed symmetrically and in axially symmetric fibre. Special multi-core fibres could solve this problem, but there are further problems associated with the higher cost of sensors and more difficult interconnections with standard fibres, which are usually used to couple light in and out for monitoring.

We suggested [41, 248] modifying part of the fibre by femtosecond laser [138], thus removing the inherent symmetry and creating what could be a truly directional or vectorial

a)   b)
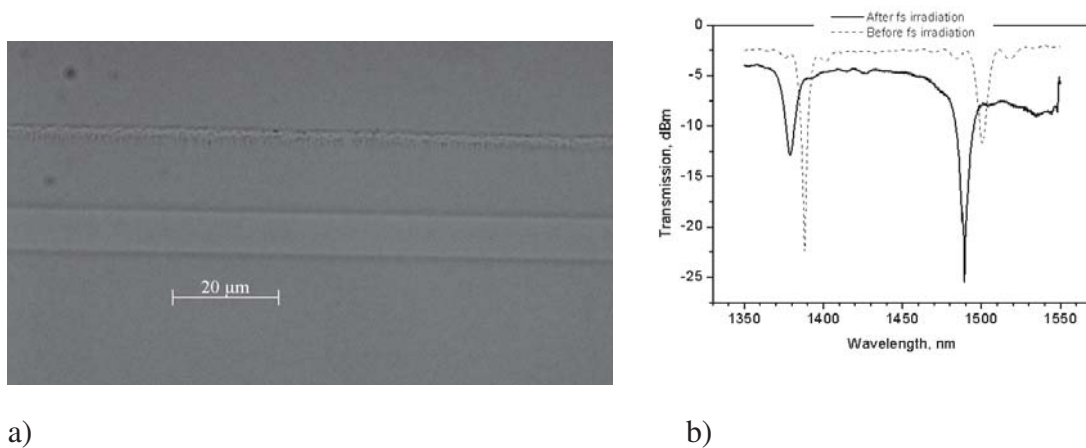
Figure 7.1: Example of the modification in the fibre cladding (a) and the observed change in a spectral response of the LPG with cladding modified by fs laser (b).

bend sensor. Obviously there are a few ways of breaking symmetry: any inscription (even in the cladding) made asymmetrically should do it. In the next section we considered the example of such asymmetrisation coming from a side offset of the longitudinal LPG grove. Here we provide an example of such modification being done in the cladding region, in proximity to the fibre core. Obviously when the modification is too weak or positioned too far away from the core it may be not possible to detect such changes. Thus control of laser pulse energy and the position of the modified area may be used to control sensor sensitivity.

For this a standard LPG (period $\Lambda=400\mu$m, and 50 mm length), inscribed with UV laser radiation in H_2 loaded step-index fibre (previously without any vectorial properties), was exposed to the fs laser radiation so that three tracks were inscribed in the cladding at distances of $+2$, -2 and $+20$ μm from the end of the core-cladding boundary, all in the same plane. The length of all tracks was about the length of the LPG. The geometry of inscription was chosen based on experimental monitoring of the LPG transmission spectra during the modification, so if the track did not produce any change in the spectrum of the grating, we shifted the focus inwards and did the inscription again. All tracks were made continuously with the LPG-sample translation speed of 0.1 mm/s in the direction perpendicular to the fs laser beam and the inscription laser pulse energy of 1 μJ. A cylindrical lens was put in proximity to the 100$\times$ ($NA = 0.55$) micro-objective, in such a way that the astigmatic beam produced a wider track in the transverse dimensions. The visible diameter of the track was $4 \sim 5$ μm. The final results however were qualitatively insensitive both to positioning errors

183

and to intensity variations, thus showing the robustness of the method suggested. An example of modification is presented in Figure 7.1, together with the spectral responses before and after fs treatment.

For experimental characterisation, the LPG device was inserted into a 4 mm diameter flexible rubber tube to prevent the fibre flipping to another orientation, and both the fibre and the rubber tube were clamped between two towers, with one of the clamps mounted on a translation stage. To determine bending direction, marks were put on the LPG sensor before femtosecond inscription. We describe the bending as convex when the written structure is on the outermost side of the fibre axis, and concave when it is on the inside. In this arrangement the LPG was midway between the two clamps, with the sensor's curvature, C, and radius of curvature, R, given by $C = 1/R = 2d/(d^2 + L^2)$, where L is half the distance between the edges of the two clamps and d is the bending displacement at the centre of the LPG. The characterisation of the LPGs' transmission bands was made using an optical spectrum analyser with a resolution of 0.1 nm and a broadband light source. No clear birefringence was detected at this stage.
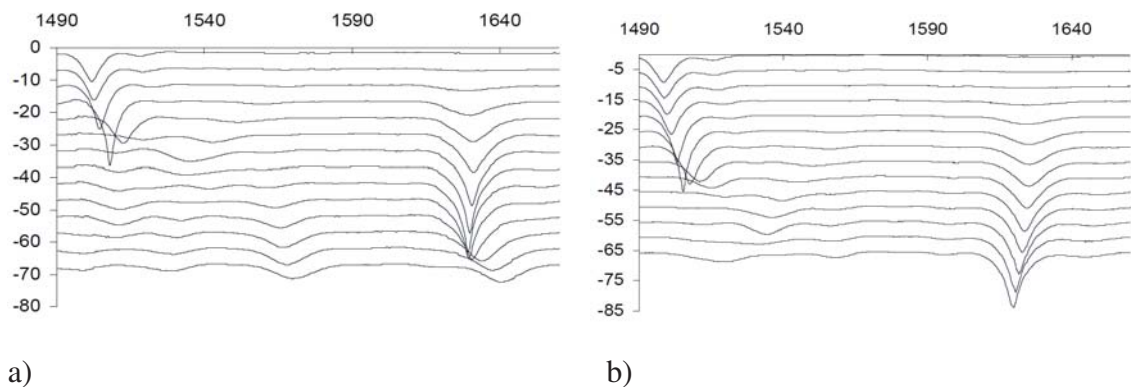
Figure 7.2: Transmission spectra of the LPG before (a) and after (b) femtosecond inscription. The curvature increases from the top to the bottom.

The change in transmission spectra can be observed in Fig. 7.2, a) where the figure clearly demonstrates shift in the *induced* attenuation bend at about 1630 nm. The induced attenuation bands have indeed demonstrated direction sensitivity during bending as plotted on the following Figure 7.3. When cases of both concave and convex bending are combined on one graph, there is a clear change in the response characteristics of such sensors.

From the last graph one could also derive the sensitivity ($d\lambda/dC, nm \cdot m$ to be about $1\, nm \cdot m$ and almost monotonic.
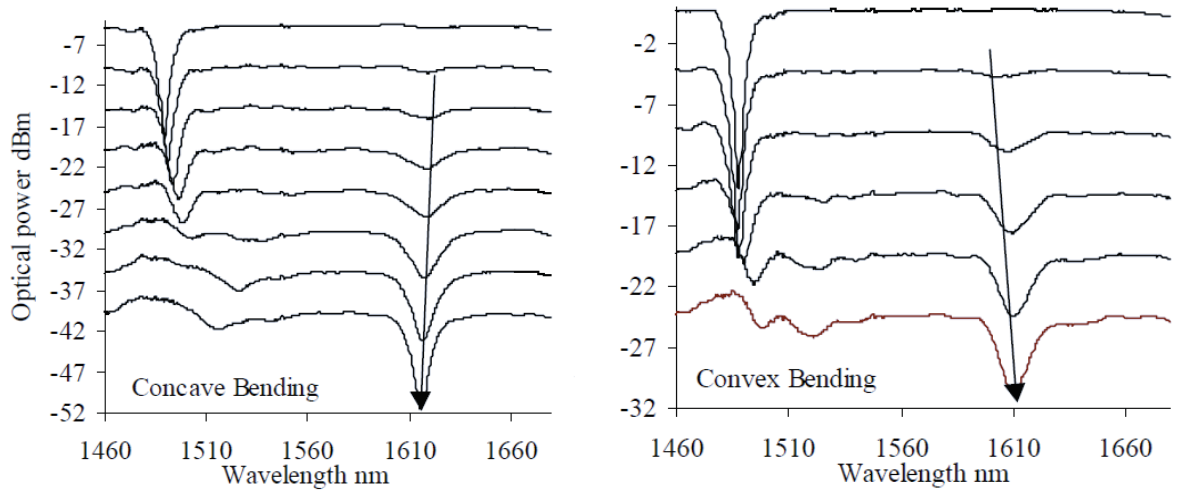
a)   b)

Figure 7.3: Transmission spectra of the LPG bend sensor after the fs treatment for concave (a) and convex (b) bending for induced attenuation bend at about 1600 nm. The curvature increases from the top to the bottom.
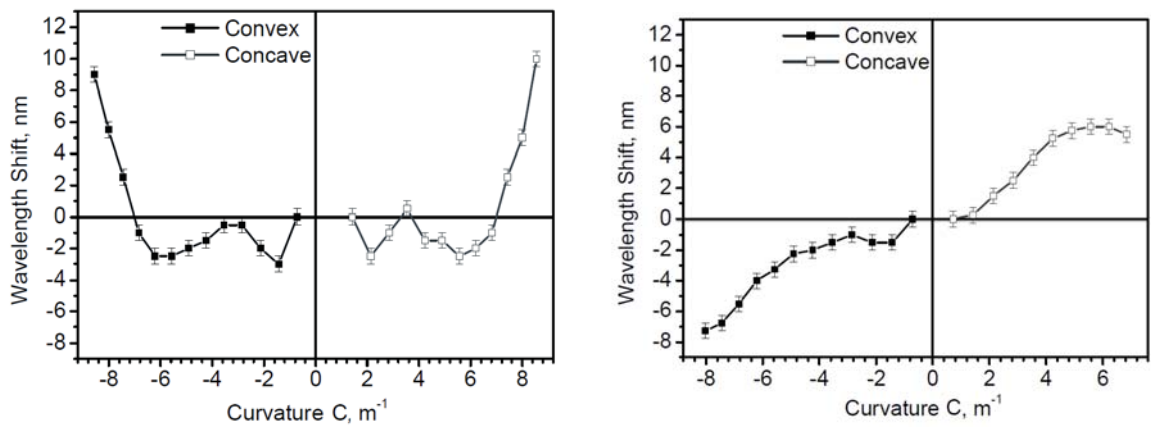
a)   b)

Figure 7.4: Response characteristics for bend sensor before (a) and after (b) the fs-laser treatment for induced attenuation band at 1600 nm.

The appearance of the induced attenuation bands does indicate a change in the selection rules for cylindrically-symmetric LPG, as follows from the theory of fibre gratings developed by Erdogan in his paper [249]. Both numerical and theoretical analysis may be required, as more cladding modes have to be taken into consideration.

For the practical application of a bend sensor, the problem of cross-talk between at least two parameters, affecting wavelength shift, has to be estimated. These represent the response to temperature and bend. The crosstalk coefficients between these two parameters have been derived [250] from the study of a similar sensor − the LPG with a similar period Λ=380 nm in a D-shaped fibre. Due to the crosstalk, an error of about 0.4%/^{o}C may occur [250]. For some applications, e.g. monitoring of the deformations of the structural elements of an airplane, a much better stability over a wide range of temperature (minimum $\pm$50 ^{o}C) variations may be required.

a)   b)
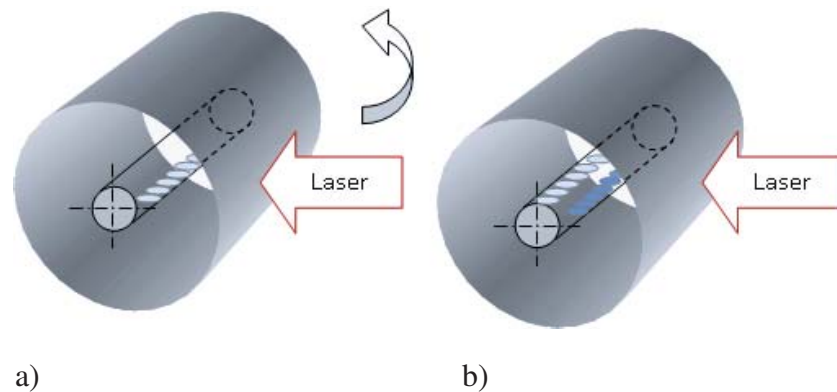
Figure 7.5: Principle of FBG directional bend sensor. First 2nd order FBG (a) is fabricated with the offset as regards to the fibre core. After that a fibre is rotated by 180 degrees and another FBG with slightly different resonant wavelength is inscribed with the same offset (b).

We came up with the idea of a bend sensor, based on spatially separated FBGs rather than LPG [138]. In order to probe bend(s) *two* (or more) FBGs have to be superimposed in the same section of the fibre core; however, they should be separated in space. Such a design in principle allows a fully vectorial bend sensing, as a single sensor can probe the bend in two orthogonal planes. This can only be achieved in standard fibres by direct fs inscription using sharp focusing of a fs laser beam. The idea was proven to work [48, 49].

The sensor consists of two Bragg gratings (of the second order), with slightly different resonant wavelengths, each of the gratings being offset by about 3 μm. The second FBG

was fabricated after rotating the fibre through 180 degrees in rotational clamps. The required wavelength shift was beyond the precision of the translation stage, so we had to change the *stretch* of the fibre and monitor the wavelength shift (when the first FBG was inscribed) on the OSA screen. After that the fibre was aligned for the second FBG inscription, which was done with *the same* translation speed. In principle, this universal method of fine tuning of the FBG period allows one to vary it (even online!) by the tension of the fibre during inscription. However, this method would require a complete redesign of the FBG inscription setup.

The sensitivity to the bend was found to be $0.7 \cdot 10^{-3}$ nm·m [48], or more than three orders of magnitude lower than for the one based on LPG, which was described above. While the sensitivity to the bend is much lower in the case of FBG, the thermal drifts in both gratings should be identical. In contrast to previous types, FBG sensor could work both in the reflection mode and in the transmission mode of operation.

In theory it could provide a direct THz-signal as a result of beating between two reflected wavelengths, as these two might be positioned quite close to each other; the optical amplifier can boost the power at these two wavelengths and thus enable a difference-frequency generation in a non-linear crystal. The frequency tuning does not require anything other than a mechanical or piezoelectric bending device.

To conclude this section, we demonstrated experimentally a universal concept for the LPG and FBG based bend sensors vectorisation in a single-mode step-index telecom fibre. The LPG bend sensor demonstrated has a sensitivity of about 1 nm·m, while the FBG based one had $0.7 \cdot 10^{-3}$ nm·m. The first type is much more sensitive for small bend radii, while the second type may be potentially much less sensitive to parasitic cross talk due to temperature changes. Both devices utilise the geometrical flexibility of the direct fabrication method and cannot be fabricated by other means. The concept of selective modification of the fraction of the core or cladding turned out to be robust and is applicable to any fibres, including non-photosensitive ones.

7.2 Long Period Gratings with high birefringence by direct modulation method

Since the early demonstrations of grating inscription with femtosecond NIR laser [80], much effort has been spent on improving the quality of fibre gratings and on understanding the mechanisms of the residual changes of the refractive index [239]. As was described in the previous Section 7.1, femtosecond post-processing of LPGs, fabricated by means of standard UV inscription, may result in a new type of fibre device: a directional bend sensor [40]. In this section we describe another example for such sensor fabrication in a single-step process. We also describe unique polarisation properties for off-set femtosecond LPGs. These all-fibre devices can be fabricated in standard telecommunication *SMF-28* fibre. Such elements may be of interest, for example, for high-power fibre lasers and for ultrafast all-optical processing/switching, for example when used as polarisers.

A novel approach to fibre grating fabrication has been suggested in [16, 27–29, 138], when a sharply focused femtosecond laser is used for inscription, as opposed to the longer focal distance focusing optics used previously. It allows accurate positioning of the compact area with modified RI within either the fibre core or the cladding, literally in any position with respect to the fibre axis. Hence well controlled asymmetry may be introduced in the resulting device. The geometry now plays the role of a new parameter which has not been used before. We demonstrate below how this parameter allows us to control the properties of such devices.

Another advantage of our approach, described in this section, consists of combining both inscription of the bend sensor (or LPG) and possible post-processing or asymmetrisation, if required, as was described in the previous section and in publications [41, 44]. The capability to withstand high-temperature annealing was found to be better than for a standard UV LPG [91, 105]. However, thermal behavior of fs-inscribed LPGs is far more complex, as it involves more parameters, such as residual stress distribution [45]. We have also found that asymmetrically fabricated LPGs have better sensitivity to bending at lower curvatures (0.3 m^{-1}) as compared to a standard UV-LPG, modified by fs inscription in cladding in the same fibre (2.0 m^{-1}) - see paper [44]. This suggests that such gratings have higher polarization sensitivity [251], which is the main focus of the following section.

The experimental arrangement was similar to what is described in Chapter 4 and presented schematically in Figure 4.5. The TTL-output of the electrical pulse generator with square-wave amplitude was applied as a trigger to an electronic shutter (Uniblitz), thus producing a 50% duty cycle filled by bursts of 1 kHz fs pulses. A standard *SMF-28e* fibre was moved with a typical speed of 70 μ/s by the air-bearing translation stage. Thus, an electrical pulse with the period of 5 sec enabled fabrication of a series of LPG groves with the period Λ=350 μm. The inscription of the grating was done after careful positioning of the focal spot with respect to the centre of the fibre core (better than $\pm0.5\mu$m) on both ends of the travel range, followed by fibre offset using precision shift in the direction of laser beam propagation (with the accuracy ±50 nm). The power level was kept above the threshold for super-continuum generation, as was observed on the screen of an analogue monitor receiving the signal from two CCD-cameras. As a result, a damage groove visible under microscope was typically produced inside the core of the fibre. A series of gratings all with the same period (of 0.35 mm) and lengths of up to 46 mm were inscribed with variable laser pulse energies. The inscription stopped just after the next period when the attenuation strength (deep) reached its maximum. This was monitored on-line by an OSA and a broad-band (1200$\sim$1750 nm) light source. The resolution of the optical spectrum analyzer was better than 0.1 nm.

After that, microscopic images of all gratings were inspected with respect to their position in fibre, by rotating the fibre around its optical axis, using the setup as shown on the insert of Figure 4.9. All gratings were offset by approximately the same distance of 3±0.5 μm from the center of the fibre core, as can be seen in Figure 7.6, b).

The transmission spectrum of one of the fs-LPGs is shown in Fig. 7.6, a). For comparison, there is a typical spectrum for standard UV inscribed LPG in the insert of Fig. 7.6, a). As one can see in Fig. 7.6, the attenuation band can reach -16 dB for a relatively short device (of $\approx$25 mm), which is more than for (or comparable with) the best UV inscribed LPGs with the same length. Secondly, the LPG produced by direct fs inscription had very strong dependence of the positions of the transmission dips on laser pulse energy used for inscription, and these positions were also well separated for two orthogonal polarizations compared to standard UV-written LPG (where the maximum difference observed was typically below 0.5 nm).
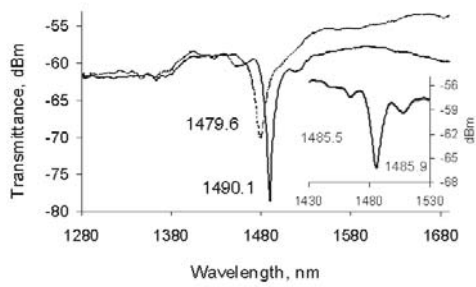
a)

b)   c)

Figure 7.6: a). Example of transmission spectrum of the fs-LPG inscribed with $E_0 = 370\,nJ$. b). The microscopic photograph of a single period of such LPG. c). Strong birefringence observed under crossed polarisers in the area of the grove.

(a)
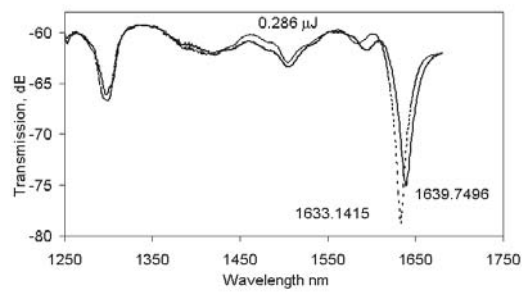
(b)
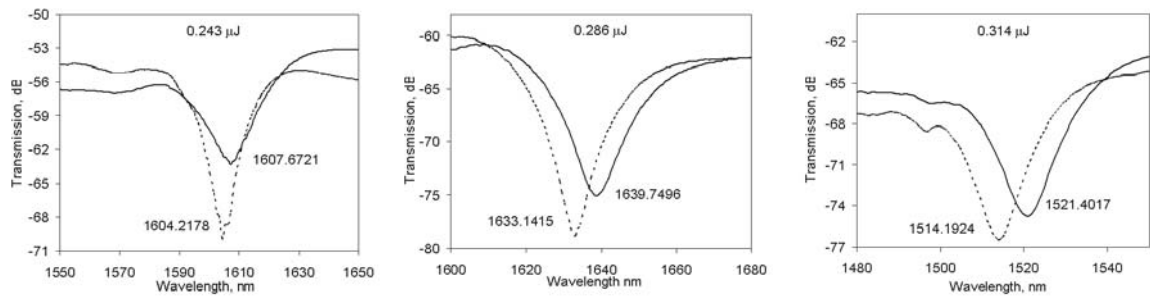
Figure 7.7: (a) Example of transmission spectrum of femtosecond Long Period Grating, including 1550 *nm* range. (b) Transmission bands of the femtosecond LPGs, inscribed at different laser pulse energies.

Another distinctive result was obtained when we checked the dependence of such polarization splitting as a function of the fs pulse energy used for inscription. It is clear that femto-LPG tends to be much more birefringent when higher pulse energies are used. Thus, by tuning the energy of the inscribing pulses, we could control their polarisation properties.

The birefringence might be attributed to the stress induced in the material around the damaged area [194], as modified structures are most likely to be damaged waveguides as one can see in Fig. 7.6 c), where fs-LPG is explored under crossed polarisers. It seems that the visible size of the fs-induced grove is much less than the stress affected area, surrounding the grove.

We believe this could explain the high overlap integral and thus strong attenuation bands observed. This conclusion may be confirmed by the results of thermal annealing of femto-LPGs. Additionally, we observed strong blue shift in the position of the attenuation dip, as presented in Figure 7.8, a). Figure 7.8, b) summarises the experimental data on birefringence (or PDL) induced by off-axis inscription at variable laser pulse energies.
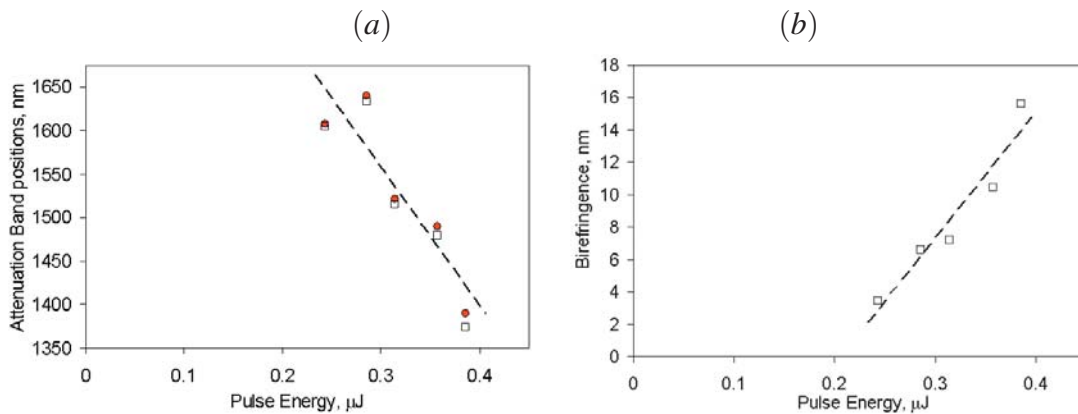
Figure 7.8: (a) Attenuation Band positions and (b) Birefringence (or PDL) observed, as a function of laser pulse energy used for inscription.

In the rest of this section we describe the numerical simulation of fs-LPGs using the FEMLAB package (by *COMSOL*). We chose for the grove of the LPG to be modelled as having a circular cross section, with its center to be offset at 3 μm from the fibre axis. The diameters of the fibre core and cladding were 8.2 μm and 125 μm respectively. The diameters of the *cylindrical* void (with n=1) is dependent on laser pulse energy, for example, it may be taken as $d \sim \sqrt{E_{in}}$. Figure 7.9 below has a sketch of the geometry used for simulations.

Following our experimental investigations on point-by-point inscribed fibre Bragg grat-
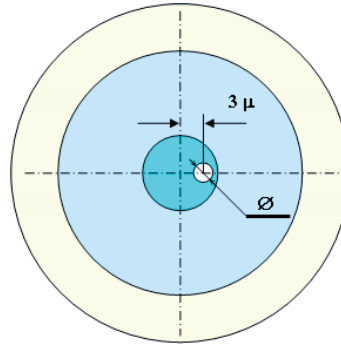
Figure 7.9: Geometry for fs-LPG modelling. The cladding is surrounded by air, the void is positioned at a distance of 3 μm from the fibre axis, its diameter depends on fs-laser pulse energy used for LPGs inscription.

ings [9], we assumed that a femtosecond laser creates a *cylindrical* area with decreased refractive index (n=1). The simulation procedure included the following steps: first the geometry and RI parameters were set, then both core and cladding eigenmodes (propagation constants) were found, both for unexposed fibre and for the fibre, which has a *cylindrical* hole in the core, with the center of this hole always being kept at a distance of 3 μm from the fibre axis and variable diameters. It was this diameter that was linked to a variable inscription laser pulse energy. It is known from other studies [104, 252] that the diameter of a spherical micro-void created by the fs pulse is proportional to the cubic root of laser pulse energy $E^{1/3}$. This dependence reflects the energy conservation law, as the number of broken bonds inside the material scales as a cube of the diameter. This conclusion has been validated (both experimentally and theoretically) for spherical voids, but not for a cylindrical one.

The wavelength of resonant coupling for LPG is calculated in accordance with the following equation [249]:

$$\lambda = \Lambda \cdot (n_{eff}^{(co)} - n_{eff}^{(cl)}) \tag{7.1}$$

Figure 7.10 presents the distributions of intensity for fundamental modes at different void diameters. We found that both propagation constants and shapes for fundamental mode are most dependent on (or sensitive to) void diameters. This tendency remains also for lower cladding modes, as illustrated in Figure 7.11, where lower cladding modes suffer from significant symmetry distortion (see, for example, the mode with three rings, the top one on the insert).

The 7-rings cladding mode turned out to be responsible for the attenuation dip at about 1600 nm (see Figure 7.11, a) - this is the bottom one on the insert). The effective refractive
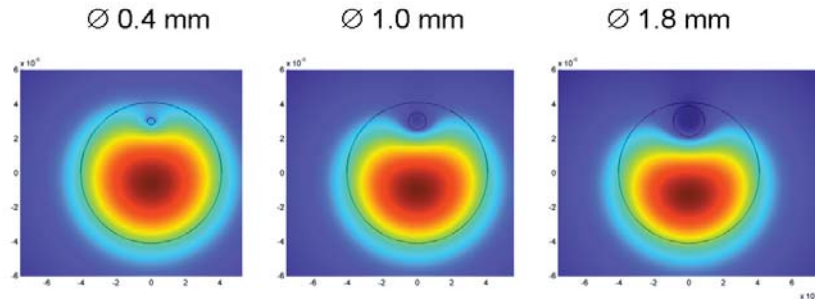
Figure 7.10: (a) Fundamental modes for different diameters of induced voids ($\lambda = 1550nm$), and (b) several cladding modes, which may be responsible for attenuation dips of the LPG. Note the much greater influence on mode shape for lower order symmetrical cladding modes.
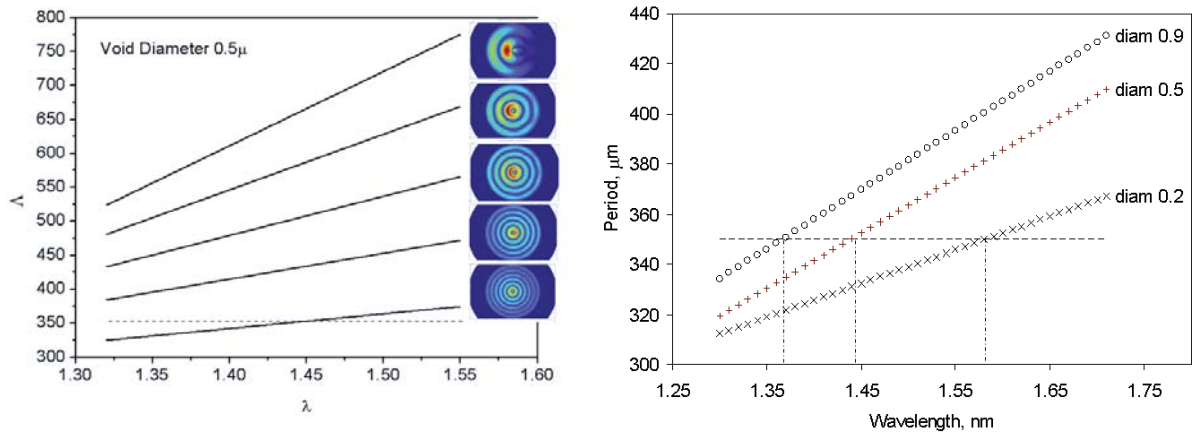
Figure 7.11: a) Effective index dependence for 3 to 7-rings cladding modes at 1550 nm. For LPG with the period of 350 μm and void diameter of 0.5 μ the resonance with the 7-ring mode (no. 185) occurs at about 1450 nm. b) Dependence of the effective index for resonant 7-ring mode (#185) as a function of the void diameter.

indexes for the fundamental mode are equal to the average of the unexposed and exposed parts of the fibre. Then we calculated the cladding modes with characteristic N-ring structures, as they must have the highest coupling coefficients with the fundamental mode [249]. All other modes were neglected at this stage, however without rigorous justification. We assumed that for fs-LPG the selection rules derived in the above-mentioned paper still hold, in spite of the broken circular symmetry of the fibre.

After all symmetrical cladding modes of interest were identified, we calculated the dispersion of their effective indexes. Finally, we repeated these calculations for a number of different diameters created in the core by femtosecond laser, to reveal the dependence of the attenuation dip vs laser pulse energy.

Even such a simple analysis correctly predicts one of the main tendencies observed in the experiment: the blue shift of resonant wavelength with increasing laser pulse energy used for inscription. One can see a reasonable quantitative agreement between the experiment and the calculations.

It seems that non-monotonic behaviour (e.g. between the first and second devices, as well as third third and fourth ones) may signal strong perturbation of the family of fibre eigenmodes, induced by femtosecond laser. Attempts to explain these experimental results by the perturbation approach were made by J. Petrovic in her PhD thesis [253]. These perturbations may not be treated as small, if the modal structure of the resulting waveguide has been, for example, re-arranged (the perturbation theory applicability is limited by the condition that induced change in propagation constant should be much less than the mode separation ($\delta\beta \ll \Delta\beta$). For the fundamental mode this condition may be valid, as the gap to the next propagation constant of the (cladding) mode is maximal. For higher order cladding modes, these separations are much narrower, so the perturbation approach may not be applicable. Thus the fs laser inscribed structures may change significantly the mode structure of the fibre, especially for cladding modes.

Numerical simulations confirm the birefringence: the dependence of the effective refractive indexes on two orthogonal polarizations, even for two fundamental modes at orthogonal polarisations. However our model does not reproduce quantitatively the results of the experiments.

Possible reasons could be: elevated RI surrounding the fs-created grove due to material

redistribution, as was considered in detail in Chapter 4 of the PhD Thesis "Modelling of Long Period Gratings in PCFs Inscribed by an Electric Arc and Gratings in SMF Inscribed by Femtosecond Laser Pulses" by J.Petovich (2006) [253]. It was found that both perturbation theory [210], and numerical simulations could not produce sufficient birefringence for quantitative agreement.

In conclusion, we have produced strong long period gratings using the direct modulation method and sharply focused femtosecond laser pulses. These gratings reveal strong dependence upon the irradiation dose in attenuation band positions and its birefringence. Such polarization sensitive LPGs can be used in directional bend sensors, polarisation controllers, fast switches and other devices based on these in a range of applications both in telecommunication and in fibre-lasers.

Chapter 8

Hybrid techniques for photonics device fabrication

For a number of sensing applications, a waveguide positioned near the surface, or shallow waveguide, is in high demand. There is a challenge in fabricating such waveguides by direct fs inscription. It originates from the fact that such inscription (at depths from a few and up to dozens of micrometers) will have to use an almost collimated beam, as the depth of focus $\approx \lambda \cdot n_0 / NA^2$ might be a few micrometers even for high-NA objectives. This makes intensity at the sample surface almost the same as in the bulk. But any surface always has a lower damage threshold due to a larger concentration of defects. Also, in accordance with our analysis of reduced NLSE in Section 3.2 (see formula 3.18, 3.19) this significantly reduces the parameter C_s, which is related to the number of Fresnel zones on a surface. Then a non-linear beam compression becomes inevitable - in accordance with Eq. 3.21 in Section 3.2. This may further reduce the threshold of fs inscription. Finally, locked stress surrounding the fs waveguide may cause surface cracks.

We have undertaken a number of experiments in order to test the minimal inscription depth and the properties of shallow waveguides, and managed to fabricate shallow WGs at a minimum inscription depth of 15 μm, as one can see in Figure 8.1. The graph on b) presents the results of refractive index measurements as described in section 4.6 after multiple overlapping (namely, two) scans. Neither multiple scans (up to 16 times) nor parallel writing could improve induced RI contrast in such conditions. At the maximum we observed RI
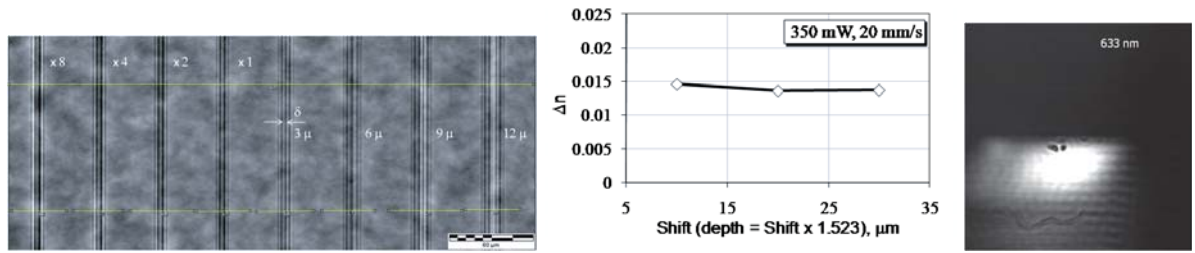
Figure 8.1: Shallow waveguides by direct femtosecond inscription. Due to low RI contrast we attempted multiple scans. Maximum RI contrast achieved is 0.014 at minimum depth of 15 μm (b); near-field profile of the coupled-in mode at $\lambda = 633$ nm (c).

contrast approximately twice as low as can be achieved with direct fs inscription in the bulk of the same glass. However, the structures do exhibit light guiding, especially at visible wavelengths - see Figure 8.1 c), where the output facet of the sample is projected onto the CCD camera. Further progress in shallow WG fabrication would require even higher NA focusing optics, perhaps by use of oil-immersion objectives. It is not clear what would be possible, due to the fact that surface cracks were quite frequent.

To address the issue of shallow WGs fabrication we suggested a flexible, hybrid method for fabricating by using femtosecond laser direct ablation of pre-determined patterns on a metal coated glass substrate followed by an ion-exchange stage. In our method we overcome not only the complexity of traditional approaches using multi-stage photoresist processings, but also the drawbacks of low index contrast, which direct fs inscription suffers from, in particular for shallow waveguides writing. Our approach also eliminates the major problem of surface cracking due to induced stress. When compared to conventional lithography, the technique turned out to be much simpler and has advantages in terms of flexibility as regards the types of structures which can be fabricated. Also it is worth mentioning that the ion-exchange method is very general and quickly became dominant for example for waveguides fabrication in $LiNbO_3$ and other materials.

8.1 Mask-less lithography

In this section we describe a combinational (or hybrid) technology for the production of shallow, 2D-arbitrary-shaped, high refractive index contrast waveguides with moderate propagation losses.

In general, commonly used technologies involve the design of a mask and delineation (image transfer) using standard photolithographic techniques in a clean room, the sole exception being direct fs-laser writing. The most competitive technology for waveguide fabrication available, to our knowledge, is the ion-exchange method [56]. In addition to being low-cost, the ion-exchange method produces low-loss (typically below 0.1 dB/cm) optical waveguides which have low sensitivity to polarisation, well controlled mode shape, and, possibly, controlled depth of positioning by virtue of electric field assisted ion in-diffusion. Compared with polymers these WGs are more stable. The only problem that remained was the lithography required. We use femtosecond direct laser ablation as a substitute conventional lithography.

This can provide a sub-micrometer resolution similar to standard UV lithography and is also flexible and can be used to make and correct masks in real time. Furthermore, this approach can be used to create periodic structures with sub-micrometer periods and offers the possibility of inscribing both waveguide and a sub-micrometer periodic perturbation simultaneously. If not, there are publications on post-inscription of Bragg reflectors on top of the ion-exchanged waveguides, re-discovered recently by Grobnic et. al. [254], where a 1.6 μm period structure was inscribed by fs-phase-mask method, but it requires a time-consuming additional sample alignment. The results on surface ablation presented in Figure 6.7 clearly demonstrate that surface ablation could be used for this, but it would require simply the insertion of a mask in front of the MO, thus saving time on sample alignment.

To the best of our knowledge, there has been little work reported using a combination of ion-exchange with direct fs laser writing. Here we would mention work done in 1998 by Salguerio et al. [255], and in 2006 by Koch et al [256]. In the first paper, they employed conventional photolithography to create masks, but with the aid of direct laser writing on *photoresist* coating deposited on top of a metal layer. This method still requires consumables, such as photoresist, as well as auxiliary equipment (dryers, ovens, spin-coater, mask-aligner, clean room etc), and would result in higher costs and longer processing times especially for low volume production or prototyping. There is also the problem associated with direct exposure of a photoresist with lasers due to photoresist heating by the laser pulse train, described for example in paper [256]. Higher repetition rate exposures can significantly raise the local temperature, so the problems of resist adhesion as well as its thermal stability

have also to be addressed.

The direct laser ablation of a thin metal *Al*-layer, deposited on a glass surface (combined with the ion-exchange method), seems to be a possible solution. In our work, a focused NIR laser beam is used to ablate a metal layer of *Al* along a pre-defined path leaving the glass beneath exposed area to subsequent post-treatments. The *Al*-layer was deposited in a clean-room environment using the *Kurt Lesker* thermal (resistive) evaporation or plasma deposition setup. The pressure in the vacuum chamber during the deposition was 10^{-5} Pa. Before deposition the glass was systematically cleaned in an ultrasonic bath to remove dirt, grease, organic and inorganic impurities. The deposition rate was about 0.1 *nm/sec*. After the *Al*-deposition the samples were stored in a vacuum/at low pressure of N_2 before they were processed by fs-laser in a normal laboratory environment. Note that such coated slides are available commercially in large quantities, once the optimum deposition conditions are established.

Ideally, the surface of the glass beneath the mask should not be affected by femtosecond laser ablation. This is possible due to the uniqueness of ultrashort pulse interaction with the materials or the fact that surrounding material was not exposed to thermal load at all, and to the fact that there is no need to specially treat the substrate with a photoresist or other photosensitive layer. This significantly reduces the processing steps and the need for additional consumables, and thus time for device prototyping (assuming that glass slides with a pre-coated metal layer are available).

Then the whole manufacturing process consists of the following stages: i) sample alignment and femtosecond laser ablation of the desired pattern; ii) possibly, post-laser-inscription cleaning in the ultrasonic bath to remove debris, if any - but this often can be omitted, if the ablation protocol has already been optimised; iii) ion-exchange in a melt of salt(s), containing, for example, Ag^+-ions; iv) finally, removal of metal coating, followed by, v) edge-polishing or cleaving for butt coupling and testing.

Most of the time-consuming and delicate polishing for the coupling stage could be removed if the PLC is designed for other than butt-coupling interconnection, or is to be integrated into the photonics device. Post-treatments such as E-field assisted shaping and deepening (positioning) of the light guiding core at the designed depth or the introduction of additional surface corrugations by a laser on another run are, in principle, possible.

The issues relating to direct femtosecond laser ablation of metal films, such as burr formation around the hole, microbumps and nanojets for lower laser pulse energies [256], highly nonlinear or even bi-stable absorption regimes with the dependence of the ablation depth on the protocol of laser illumination [257] (see also other papers on so-called "black metals"), and, of course, film and its adhesion non-uniformity, have been addressed in this work.

A number of approaches, such as using back and front illumination were tested, with the best results obtained using multiple scans and front illumination. These scans were made using the same air-bearing stages capable of sub-micrometer precision repetitive movements and laser pulse energies successively decreasing with each scan. The exposure was synchronised with stage motion (using *Uniblitz* electronic shutter) to obtain sharp sub-micron scale features comparable to what is achievable in standard lithography.

Several trial runs were carried out to determine the optimum laser energy, number of scans and writing speed for laser ablation of metal films with different thicknesses. We found that it was difficult to generate a good quality, clean ablation track while leaving the glass surface untouched at any laser pulse energy when a thick coating (about 1000 nm) was used. In our experiments we used a CCD-camera to monitor the NIR transmitted laser light below the sample, which allowed us to optimize manually the parameters of the ablation process: laser energy, Z-position of focal spot, sample translation speed, etc. However, the implementation of a fully automatic feedback system could significantly improve the quality, robustness and precision of the ablation stage.

In experiments, while higher energies produced deeper ablation spots, the speed had to be increased in order to avoid damage, while with lower energies there was insufficient penetration of the beam into the metal, even at much lower speeds. Furthermore, when the speed was sufficiently high ($> 2\, mm/s$), it resulted in a discontinuous line as the ablated areas of the Al coating did not adequately overlap. Other problems affecting direct laser ablation are variations in thickness of the metal film and the deviation in pulse to pulse energy of the laser (typically less than 3%), as no energy stabilisation system was used. These may result in non-ablated parts of the track, thus affecting ion exchange in those areas, or variable width of the ablated strips, leading to parasitic scattering and reflection for the guided light when the waveguide is formed, and thus to higher propagation losses.

In the end we arrived at the following protocol for the ablation stage, which included an
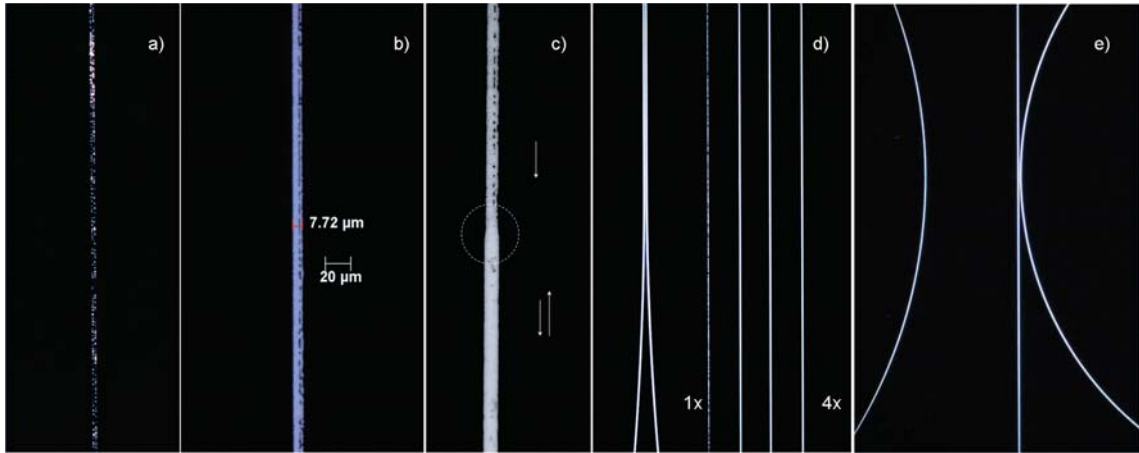
Figure 8.2: The results of the ablation stage of the aluminium film, when: a) laser pulse energy is too small; b) laser pulse energy is too high, as structuring of the glass surface underneath may be seen; c) second scan of the laser removes re-deposited/residual metal and leaves a clean trace behind; d) the lines from 1 to 4 represent the influence of the number of scans with the same energy, from 1 to 4 respectively. Y-coupler from the left no (d) was made with two scans; e) the result of ablation of the ring-resonator structure with the optimised parameters.

initial scan with laser pulse energy in the range of 50 to 150 nJ, followed by a few successive scans with gradually decreasing energy - down to 20 or 30 nJ. These are optimal parameters for a $\approx$100 nm thick Al-coating and scanning speed in the range of 0.1 - 0.2 mm/sec. The proper choice of laser energy at a suitable velocity enables consistently reproducible line widths for a given aluminium thickness (see Fig. 8.2, d). Our technique was proven to produce uniform and reliable ablation patterns even on non-uniform metal layers, with poor adhesion and even some defects in coating. Perhaps this is where the advantage of the multi-layer coating approach [255, 256, 258] becomes obvious, or alternative laser sources (say, UV, which is absorbed in most of multi-component glasses) might be advantageous.

Finally, to form waveguides, an ion-exchange was then performed by immersing the delineated patterned substrate in a dilute melt of salts: $AgNO_3 + NaNO_3$. The relative concentration of silver ions was about 10^{-3}. This allowed for better control over diffusion rates, and thus a smoother index contrast, for producing single mode waveguides, as against using a pure melt of $AgNO_3$. The diffusion process in our case makes smoother short scale structures, however we found it is sensitive to the surface uniformity, both natural (on uncovered parts of substrate) and induced by femtosecond laser ablation of the near-surface region.

After the ion-exchange, the metal layer was then removed and the samples were cut
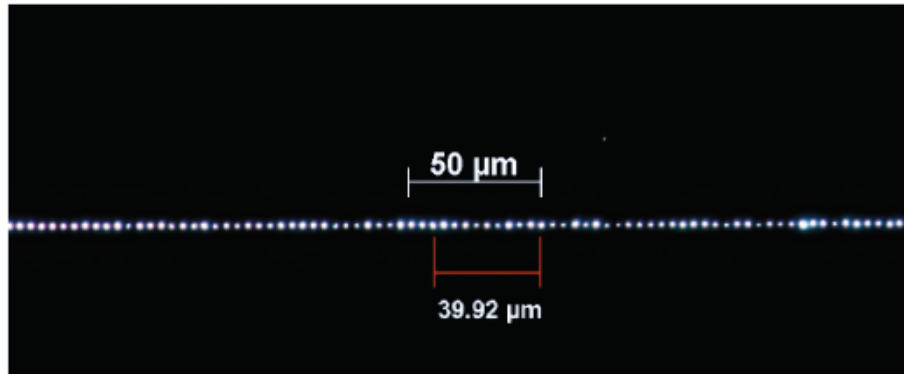
Figure 8.3: Periodic perforation of a line of holes with 4 μm period on aluminium film. Note a non-uniformity after a single pass.

and edge-polished to couple light. An alternative design of input/output ports for optimal coupling with fibres is under consideration, which might significantly reduce this time-consuming stage. The ion-exchanged structure has formed near the substrate surface and therefore can be used for a variety of sensing applications which involve an evanescent field. If necessary, some additional processing (such as coating) could also be used, for example in the case of various plasmonic sensors. Special packaging of these devices can tailor their environmental sensitivity. Standard soda-lime glass microscopic slides (by *Menzel Glaser*) as well as borosilicate optical B270 glass (analogue of BK7, by *UQG Optics*) were used in all our experiments for the fabrication of ion-exchange waveguides. Other hosts, including RE doped ones, may be considered as well.

Periodic structures can also be fabricated (see Fig. 8.3) with this technique either by introducing a periodic perforation in the metal film and thus index variation after ion-exchange or by creating groves on the glass surface (before or after the IE stage). It was demonstrated in single shot laser ablation experiments [157], that clear holes as small as ≈ 40 nm can be fabricated. These experimental findings seem currently to hold the world record for smallness of diameter of NIR-laser perforations. Note that the thickness of the metal coating in the above cited paper was of the order of the hole diameter, and the diameter obtained is approximately 20 times smaller than the laser wavelength used.

In single shot experiments we have also been able to ablate holes, with diameters estimated from relative transmission measurements under the microscope, as small as 100 nm. The femtosecond pulses were focused using a long working distance NIR 36($\times$) reflecting microscope objective with a numerical aperture of $NA = 0.5$. The diameter of the focused

beam was estimated to be about 2 μm. One could expect that such a large focal spot may be a limiting factor for sub-micrometer periodic pattern ablation on a metal film; it was however possible to ablate (in a single shot) a hole of about 100nm in diameter using this arrangement, which is 1/20 of the focal spot diameter. The limiting factors here are the spot size (the minimum is about laser wavelength) and the thickness of the metal layer used. While in our experiments the focal spot can be successfully tailored down to a sub-micrometer region, the metal layer has to be sufficiently thick to offer its protective function during the ion-exchange stage.

We did try a micro-holographic approach [200, 245, 259] well fitted for short-period pattern formation. Note that post-IO stage inscription is also available, as described in [254]. Remarkably the photo-sensitivity for inscription with 800 nm fs laser was observed only in the ion-exchanged part of the substrate. This significantly reduces the time and cost for the setup for such post-WBG fabrication, as it makes alignment trivial.

a)   b)
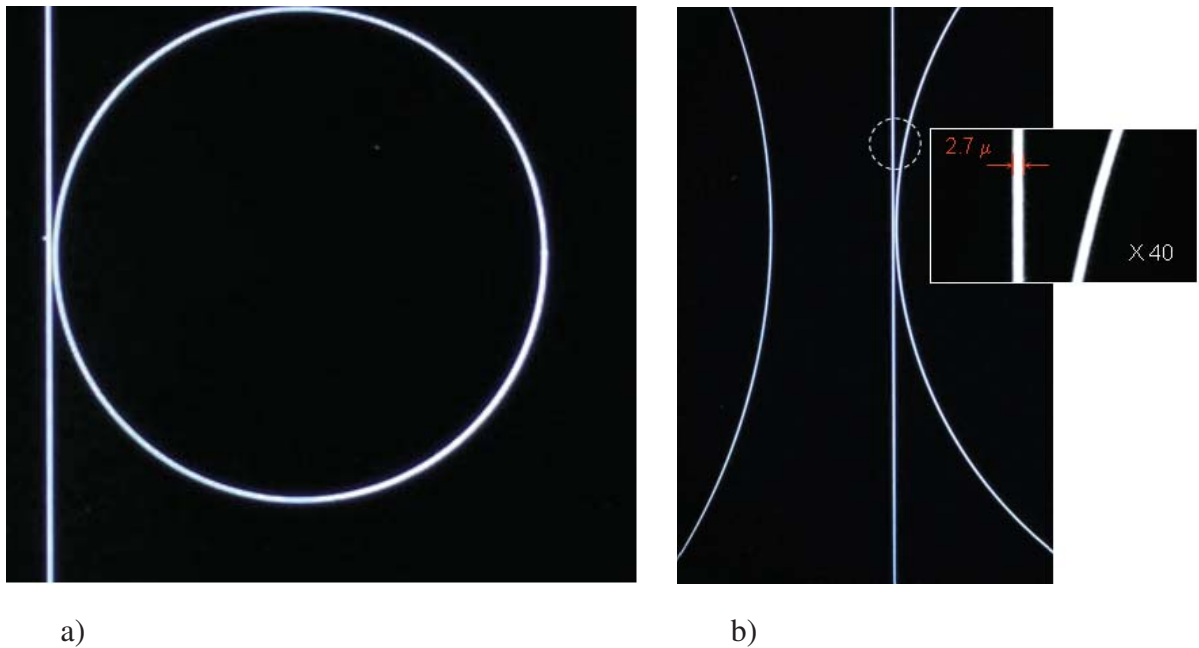
Figure 8.4: a). Ring-resonator made with optimised ablation parameters: Al-layer thickness - 100nm; translation speed V = 0.13 mm/s; pulse energies during successive scans are E_1= 100 nJ (threshold: 25-40 nJ); E_2 = 80 nJ. b). Demonstration of control over the width of the ablated tracks - pulse energies during successive scans are E_1= 60 nJ; E_2 = 40 nJ; E_3 = 25 nJ

The adhesion of the metal film and thus its ability to withstand the elevated temperatures are of great importance. As ion-exchange is a diffusion process, one may expect that minor defects of ablation are significantly washed out. At the same time, tiny and almost invisible

under the microscope micro-pores on a metal film become much clearer, especially in the area adjacent to the track, as the film here experienced more thermal load. We believe that the reason for this is imperfect adhesion of the *Al*-film in our samples. After the ion-exchange stage those spots adjacent to the waveguide became much more pronounced.

In Figure 8.5, b) the DIC examination of the resulting waveguide (after the ion-exchange and polishing) revealed the following characteristic faults of the process: i) overexposure of the glass surface, as the track has parallel lines on it because of differing diffusions in pristine and illuminated glass; ii) the bumps adjacent to the waveguide, due perhaps to bad adhesion, will cause high propagation losses; iii) the cracked edge of the sample may cause high coupling losses; iv) other defects in the metal coating, where no laser ablation took place, probably due to poor cleaning. These defects are a major contribution to the observed high propagation losses in the waveguide. Although in our work we have mostly used soda-lime glass (by Menzel), it is possible to use other hosts, such as lithium niobate and other speciality glasses.

Prior to ion-exchange, the patterned structures were examined under an optical microscope to estimate their linewidths as well as to check for any defects. Linewidths of the ablated track measured on some of the patterned structures are shown in Fig. 8.4. Typically, for a 6 μm slit a waveguide width becomes between 6 μm to 10 μm, depending on the duration of the ion-exchange stage. This allows fine tuning of the diameter of the waveguide to match those of the majority of telecom fibres. After ion-exchange, the aluminium mask was removed and the sample was again examined under the microscope (Fig. 8.5). A DIC-microscope was used to identify the regions of higher refractive index obtained after the ion-exchange stage from the rest of the glass. After that the refractive index contrast of the waveguides was measured using the QPm method, as described earlier. The results are presented on the insert on Fig. 8.5, b). The temperature of the exchange was carried out in a furnace at 360 ^{o}C typically for 45 minutes.

For devices of interest the optimal values were expected to be in the region of 0.005 to 0.008. With some modifications of the ion-exchange parameters, it is possible to produce an index contrast at least one order of magnitude higher than that which has been demonstrated in this work. The exact value can be verified only from reconstruction of the refractive index profile from the near-field intensity distribution measurements.
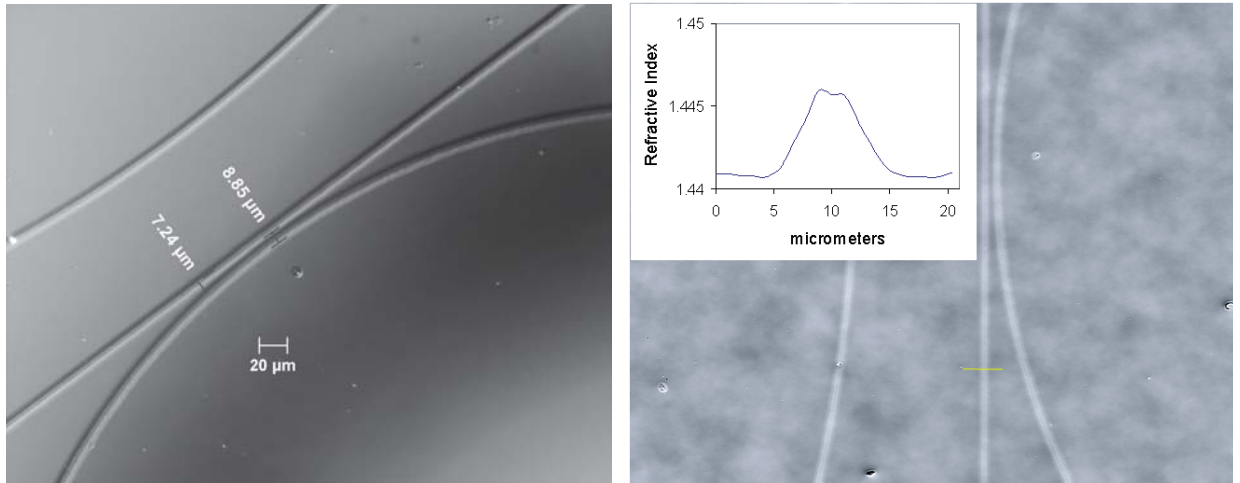
Figure 8.5: QPm map of the accumulated phase after ion-exchange stage, image of the ring resonator. Refractive index profile is shown on the insert.

The V-parameter of the straight waveguide was estimated (assuming a step-index profile with the contrast of 0.005 and *radius* of the waveguide of about 3.5 μm) to be up to 3.7 at He-Ne laser wavelength, i.e. it might be multimode. The V-parameter is about 1.8 at the wavelength of 1550 nm, which is good for various applications in the NIR region. In order to couple light into the waveguide, the edges of the sample were polished. The sample was then bonded along with dummy slides and polished until the surface produced no significant defects on the waveguide edges as was observed under the optical microscope.

The setup used for butt-coupling of the waveguides was used. The near-field pattern of the edge was captured on the screen at the output end.

The transmission losses were measured using the side scattering technique and found to be below 6 dB/cm at the wavelength of 532 nm for the waveguide of approximately 20 μm in width. Coupling losses were estimated to be up to 6 dB per surface, because of the mismatch of the modes diameter between the *SMF-28e* fibre and the test waveguide (these had a $20 \times 5\mu$m cross section in our first experiments). There is surely room to obtain a waveguide with much lower coupling and propagation losses. We believe that the main sources of propagation losses are stochastic variation of the waveguide cross-section and the surface corrugation left after the laser ablation stage. It should be possible to have a two stage ion-exchange process with the field assisted Ag^+ in-diffusion in another salt melt being the second stage with the aim of achieving better performance for the ion-exchange waveguides. Currently the best propagation losses of a single-mode WG are less than 0.01 dB/cm, it has
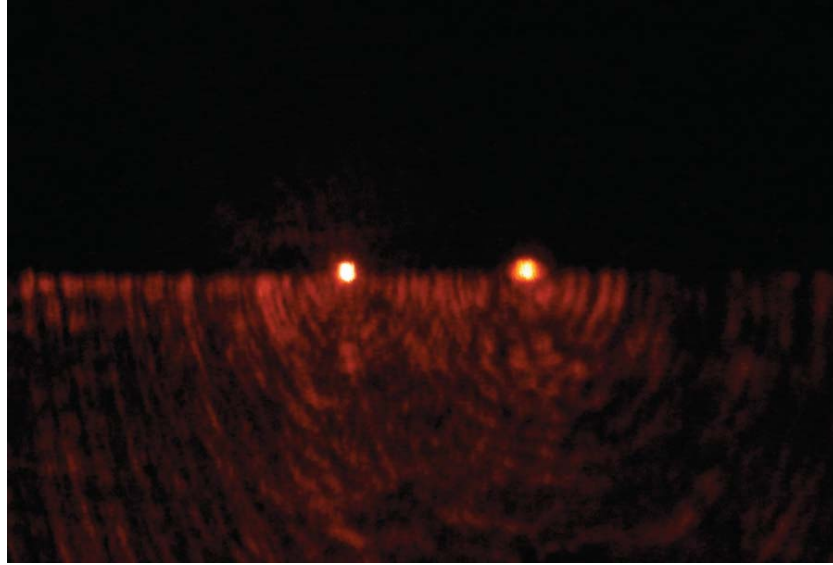
Figure 8.6: Photo of the output ports of 50:50 Y-coupler when 633 nm laser was butt-coupled to the structure input port.

a circular mode-field distribution, matching exactly the mode of a standard SMF fibre and positioned at a depth of up to 20 micrometers.

To conclude this section, we have successfully fabricated optical waveguides by combining direct femtosecond laser ablation with ion-exchange method. The laser energy level and speed of writing have been optimised for our system to produce consistently reproducible patterns that can be used for fabrication of ion-exchange waveguides in glass. Optimal index contrasts in the region of 0.005~0.008 have been obtained by this combination technique which allows flexibility and ease of prototyping of photonics devices, as compared to exclusive use of the direct laser writing method or conventional lithography. Potentially, low-loss and high contrast waveguides can be achieved by this method and would have numerous applications in sensing and telecommunication wavelengths range as well as at mid-IR.

8.2 Possible developments

The hybrid method described in the previous section is most suitable for sensing applications demanding shallow waveguides. This imposes some additional problems for in- and out-coupling and propagation losses, as well as isolation of the device from the environment. Ion-exchange is routinely being used in a number of applications (like, for example, $LiNbO_3$ based Mach-Zander modulators and interferometers) where the waveguide's proximity to

the surface is not so critical, or it would even be desirable to embed it deeper in the bulk of material. Then field-assisted ion-in-diffusion is one of the options worth trying. As a reference, there are commercially available waveguides with almost circular cross-sections, optical losses of less than 0.1 dB/cm, mode-matching with standard fibres, and positioned at the required depth (a few dozens of micrometers) which were obtained by this approach. In principle, it might be possible to vary the depth of various sections of waveguide to match application demands. A possible continuation of this work seems to be the exploration of the phenomenon of induced photosensitivity in ion-exchanged glasses. As was demonstrated experimentally [260], femtosecond inscription through the phase mask can occur on near-surface regions only where ion-exchange took place. This opens up the possibility of added functionality on demand, where MZ-interferometers created by first (IO) stage will be customized to be wavelength-selective, depending on the application demands. Photosensitivity is not the only thing that can be affected by the IO-process; other properties, for example, selective chemical etching may also change.

Finally, and interesting from our point of view, is the aggregation of metal nano-clusters inside glass. This allows for fascinating engineering of the material properties. Examples, which one can find in literature, include modification of the non-linear properties of glass with the inclusion of metal nano-particles or their aggregates; local changes in the crystallisation properties; or triggering even quicker metal clustering.

Chapter 9

Conclusions and future work

We explored the possibilities of the direct femtosecond laser micro-fabrication method to produce basic components for integrated photonics devices in transparent dielectrics. The main focus of this work was on improving the most critical parameters for any application or device, namely: the maximum induced refractive index contrast in straight and curvilinear waveguides; minimum coupling, propagation and bending losses; short-period perturbation for wavelength-selective structures, such as gratings directly inscribed into the core and/or cladding of already existing or newly inscribed waveguides.

Comparison of the experimental results achieved by different laser systems revealed the undoubted advantages of high-repetition rate inscription for fabrication of both smooth and periodic structures, as we highlighted when appropriate. In order to conduct the experiments we identified relevant equipment, designed and built a few laboratories. For the first time we deployed the method of Quantitative Phase microscopy for express measurements of the induced RI contrast in the femtosecond laser written waveguides and periodic structures in a variety of transparent dielectrics including fibres. The QPm method was calibrated using telecom fibres and later used for express characterisation of all fs-inscribed structures, both in fibre and planar samples. Numerical procedures for index reconstruction in the case of axially symmetric waveguides were developed and tested experimentally. This method enabled us to explore a multi-dimensional space of parameters of fs inscription in the case when HRR laser was used, and allowed us to identify the optimal regimes for waveguide inscription in borosilicate optical glass (BK7) in order to achieve minimum coupling and propagation losses.

A practical method for on-line diagnostics of the results of femtosecond inscription has also been demonstrated. The method is based on the numerical solution of the inverse scattering problem in first order Born approximation. The method does not use any assumptions on the scalar nature of the electro-magnetic fields involved; instead special design of the cuvette enabled us to reduce the reconstruction to a scalar case. Cross-calibration of the scattering method with the QPm method allowed us to identify potential problems with QPm measurements. These are related to the imaginary part of the permittivity in the volume of material, modified by femtosecond laser. To the best of our knowledge, our scattering method is the only method which allows one to measure 3D distribution of induced absorption from a single volume of a few cubic micrometers, with the temporal resolution of the order of a picosecond. Its potential applications are not limited by the laser damage/modification phenomenon, but could be useful for in-vivo diagnostics at a cell or a macro-molecular level, physics of non-equilibrium phase transitions, meta-materials, as well as others.

We demonstrated that a chirped-pulse oscillator femtosecond laser system with a higher repetition rate than is commonly used enables one to achieve record-high induced RI contrasts, and also much quicker inscription protocols, which makes the method of direct femtosecond inscription very attractive.

Maximum induced RI contrast can reach $2.5 \cdot 10^{-2}$, or approximately 5 times more than in standard telecommunication fibre. Record-high induced refractive index contrast in a curvilinear track with the radius of curvature of 1 cm enabled bend losses of about 1 dB/cm. This level of losses is already acceptable for integrated photonics devices of medium and low complexity. Further optimisation and reduction of the bend losses seems to be possible, mainly due to optimum design of the curvilinear parts. Total losses, including coupling and propagation losses at the wavelength of 1550 nm in a 2 cm long BK7-glass sample, can be about 0.6 dB. This demonstrates that both coupling and propagation losses can be on the level of Fresnel losses or even below.

The Point-by-Point method was suggested for fibre Bragg gratings and other devices fabrication by NIR and UV fs lasers. The key alignment procedure was developed, based on the monitoring of the position of a plasma discharge in the air in a reference frame of coordinate. Such simple procedure can produce accurate alignment of fibres. A number of devices were fabricated by direct femtosecond NIR inscription in various fibres: Bragg and

long-period gratings with controlled birefringence, as well as various vectorial band sensors.

Some of the limitations of the NIR PbP method for short-period structures fabrication were addressed. Periods shorter than 500 nm can be inscribed, for example in a moving slab of fused silica (or fibre) by using 3rd harmonic of NIR laser at the wavelength of 267 nm. For the first time, periods as short as 250 nm were experimentally demonstrated at the depth of 170 μm in a silica sample, which to the best of our knowledge is the shortest period produced by PbP method. Such a reduction in the period leads to a further reduction of the modified area in transverse dimensions and thus to a poorer overlap integral with fibre modes.

In order to increase this overlap we suggested and demonstrated experimentally the micro-holographic method. In this method a patterned focal spot may be created in a simple optical configuration based on a combination of a diffractive-optic element (or phase mask) and a sharp focusing UV micro-objective. Interference fringe patterns were demonstrated in the vicinity of MO focus, with periods ranged from 250 nm to 500 nm and above, with the overall diameter of the patterned focal spot of up to a few μm. Inscription with such a periodically patterned focal spot should allow a much stronger overlap with fibre modes, enabling us to inscribe much shorter periods and stronger reflectors than is possible by NIR PbP method. This method still has to find its applications for inscription of strong fibre Bragg gratings in the visible and NIR range.

High-quality periodically modulated waveguides were demonstrated by the direct modulation method on the HRR laser system as well, with the periods shorter than can possibly be achieved by NIR PbP method and LRR fs system. This technique is capable of generating a waveguide Bragg grating alongside a smooth waveguide fabrication on the same setup. This possibility significantly expands the direct fs micro-fabrication method by HRR systems. The range of periods demonstrated is already sufficient for various applications in telecommunications' both C- and L-bands.

A new and powerful concept of selective spatial modification of the refractive index in the core or cladding of standard fibres was suggested and experimentally demonstrated. This approach enables one to trim various properties of standard fibres to the required application; for example, we demonstrated experimentally the vectorisation of the LPG- and FBG-based bend sensors. The LPG-based vectorial bend sensor has a sensitivity of about 1 nm·m, while the FBG-based one demonstrates $0.7 \cdot 10^{-3}$ nm·m. The first type of sensor is much more sen-

sitive for small bend curvatures, while the second type of sensor is potentially less sensitive to the change in ambient temperature. Both devices demonstrated exploit the geometrical flexibility of the direct laser micro-fabrication method and cannot be fabricated by other means.

Strong long-period gratings fabricated by sharply focused femtosecond laser pulses with controlled offset provide another example of this universal concept. The irradiation dose can be used to control the attenuation band positions and their birefringence, as we demonstrated experimentally. Such polarization sensitive LPGs with tunable polarisation properties offer a variety of applications, such as: polarization controllers, directional bend sensors and ultra-fast all-optical switches. These novel highly birefringent LPG devices may be in demand for high-power fibre lasers, for example as a non-linear mode-locker, based on the effect of non-linear polarisation rotation. The general concept of managing the birefringence in a well-controlled manner seems also to be applicable for modification of birefringent properties of standard fibres, which are initially circular-symmetric.

This proves that the concept of selective modification of the fraction of the core and/or cladding is universal and robust, and that this approach is applicable for any fibres, including non-photosensitive ones.

All these demonstrations are to be considered as a "proof of principles" with more efforts needing to be made in order to bring the technology to the industrial level. Challenging experimental problems have to be addressed for this, namely: managing the quality of laser radiation focusing at arbitrary depth; synchronisation of laser firing with the motion of the translation stage; on-line feedback based on the final result of the inscription process, which implies the ability of in-situ measurement of parameters of interest.

Finally, a method for shallow waveguide fabrication was suggested by combining the direct femtosecond laser ablation of a thin metal layer with the following ion-exchange. Optimal thicknesses of Al-film were determined, and the laser energy and the speed of ablation were optimised experimentally to create consistently reproducible patterns that can be used as masks, for example, for fabrication of waveguides by ion-exchange in multicomponent glasses. As for the mask fabrication itself this seems to be the quickest method, suitable for application in a normal laboratory environment. Optimal index contrasts in the region of 0.005~0.008 have been obtained in ion-exchanged waveguides by using diluted melt of

salts. This combination or hybrid technique resolves the issue of shallow waveguides fabrication, allows the flexibility and ease of prototyping of photonics sensors and other devices as compared to exclusively using the direct laser writing method or by other methods based on conventional lithography. Potentially, very low-loss and high contrast waveguides can be achieved by this method and could have numerous applications in sensing using wavelengths from visible to the mid-IR.

References

[1] V. K. Mezentsev, S. K. Turitsyn, M. P. Fedoruk, M. Dubov, A. M. Rubenchik, and E. V. Podivilov, "Modelling of femtosecond inscription in fused silica," in *2006 International Conference on Transparent Optical Networks*, **4**, pp. 146–149, Institute of Electrical and Electronics Engineers Inc.(IEEE), 2006.

[2] S. Turitsyn, V. Mezentsev, M. Dubov, A. Rubenchik, M. Fedoruk, and E. Podivilov, "Nonlinear diffraction in sub-critical femtosecond inscription," in *Conference on Lasers and Electro-Optics Europe - Technical Digest*, pp. –, Institute of Electrical and Electronics Engineers Inc., 2007.

[3] S. K. Turitsyn, V. K. Mezentsev, M. Dubov, A. M. Rubenchik, M. P. Fedoruk, and E. V. Podivilov, "Sub-critical regime of femtosecond inscription," *Optics Express* **15**, pp. 14750–14764, Oct. 2007.

[4] V. Mezentsev, M. Dubov, A. Martinez, Y. Lai, T. P. Allsop, I. Khrushchev, D. J. Webb, F. Floreani, and I. Bennion, "Micro-fabrication of advanced photonic devices by means of direct point-by-point femtosecond inscription in silica," in *Proceedings of SPIE - The International Society for Optical Engineering*, **6107**, p. 61070C, SPIE, 2006.

[5] V. Mezentsev, M. Dubov, J. S. Petrovic, I. Bennion, J. Dreher, and R. Grauer, "Role of plasma in femtosecond laser pulse propagation," *Physics of Ionized Gases* **876**, pp. 169–180, 2006.

[6] V. Mezentsev, J. S. Petrovic, M. Dubov, I. Bennion, J. Dreher, H. Schmitz, and R. Grauer, "Femtosecond laser microfabrication of subwavelength structures in photonics - art. no. 64590b," *Laser-based Micro- and Nanopackaging and Assembly* **6459**, p. B4590, 2007.

[7] I. S. Petrovi, V. Mezentsev, M. Dubov, A. Martinez, and I. Bennion, "Plasma assisted femtosecond laser inscription in dielectrics," *Physics of Ionized Gases* **876**, pp. 216–223, 2006.

[8] M. Dubov, V. Mezentsev, and I. Bennion, "Method for characterisation of weakly guiding waveguides by measuring mode field diameter," in *Conference on Lasers and Electro-Optics Europe - Technical Digest*, p. 565, Institute of Electrical and Electronics Engineers Inc., 2005.

REFERENCES

[9] A. Martinez, M. Dubov, I. Khrushchev, and I. Bennion, "Photoinduced modifications in fiber gratings inscribed directly by infrared femtosecond irradiation," *IEEE Photonics Technology Letters* **18**(21-24), pp. 2266–2268, 2006.

[10] A. V. Turchin, M. Dubov, and J. A. R. Williams, "In situ measurement and reconstruction in three dimensions of femtosecond inscription-induced complex permittivity modification in glass," *Optics Letters* **35**(17), pp. 2952–2954, 2010.

[11] A. V. Turchin, M. Dubov, and J. A. Williams, "3-D reconstruction of complex dielectric function of the glass during the femtosecond micro-fabrication," in *Bragg Gratings, Photosensitivity, and Poling in Glass Waveguides*, p. BWD7, Optical Society of America, 2010.

[12] M. Dubov, L. Krushchev, I. Bennion, A. Okhrimchuk, and A. Shectakov, "Waveguide inscription in YAG:Cr4+ crystals by femtosecond laser irradiation," in *Conference on Lasers and Electro-Optics/International Quantum Electronics Conference and Photonic Applications Systems Technologies*, p. CWA49, Optical Society of America, 2004.

[13] M. Dubov, T. D. P. Allsop, S. R. Natarajan, V. K. Mezentsev, and I. Bennion, "Low-loss waveguides in borosilicate glass fabricated by high-repetition-rate femtosecond chirp-pulsed oscillator," in *CLEO-Europe and EQEC 2009 Conference Digest*, p. CEP4, Optical Society of America, 2009.

[14] M. Dubov, T. Allsop, S. R. Natarajan, V. K. Mezentsev, and I. Bennion, "Curvilinear low-loss waveguides in borosilicate glass fabricated by femtosecond chirp-pulse oscillator," in *Femtosecond Laser Microfabrication*, p. LMTuC6, Optical Society of America, 2009.

[15] I. Khruschev, A. Okhrimchuk, A. Shestakov, M. Dubov, and I. Bennion, "Laser inscription of optical structures in crystals (Patent WO 2005040874-A2)," 2005.

[16] I. Khruschev, A. Okhrimchuk, A. Shestakov, M. Dubov, I. Bennion, and A. Martinez, "Laser inscribed structures (Patent WO 2005111677-A2)," 2005.

[17] I. Khrushchev, A. Okhrimchuk, A. Shestakov, M. Dubov, and I. Bennion, "Laser inscription of optical structures in crystals, (Patent EP 1678535)," 2006.

[18] T. Allsop, M. Dubov, V. Mezentsev, and I. Bennion, "Inscription and characterization of waveguides written into borosilicate glass by a high-repetition-rate femtosecond laser at 800 nm," *Applied Optics* **49**(10), pp. 1938–1950, 2010.

[19] I. Bennion, V. Mezentsev, M. Dubov, A. Okhrimchuk, T. Allsop, and H. Schmitz, "Single process femtosecond microfabrication of key components for integrated optics," in *Bragg Gratings, Photosensitivity, and Poling in Glass Waveguides*, p. BWB3, Optical Society of America, 2010.

[20] Y.-L. Wong, D. Furniss, V. K. Tikhorairov, E. A. Romanova, M. Dubov, T. D. P. Allsop, V. Mezentsev, I. Bennion, T. M. Benson, and A. B. Seddon, "Femtosecond

laser writing of buried waveguides in erbium iii-doped oxyfluoride glasses and nano-glass-ceramics," in *Proceedings of 2008 10th Anniversary International Conference on Transparent Optical Networks, ICTON*, **3**, pp. 234–238, IEEE, 2008.

[21] A. G. Okhrimchuk, V. K. Mezentsev, H. Schmitz, M. Dubov, and I. Bennion, "Cascaded nonlinear absorption of femtosecond laser pulses in dielectrics," *Laser Phys.* **19**(7), pp. 1415–1422, 2009.

[22] A. Okhrimchuk, V. Mezentsev, M. Dubov, H. Schmitz, and I. Bennion, "Cascaded nonlinear absorption of laser pulse energy in femtosecond microfabrication: Experiment, numerics, and theory," in *OSA Trends in Optics: Femtosecond Laser Microfabrication*, p. LMTuA6, Optical Society of America, 2009.

[23] A. Okhrimchuk, V. Mezentsev, H. Schmitz, M. Dubov, and I. Bennion, "Characterization of nonlinear absorption in femtosecond laser inscription," in *CLEO-Europe and EQEC 2009 Conference Digest*, p. EFP15, Optical Society of America, 2009.

[24] M. Ams, G. D. Marshall, P. Dekker, M. Dubov, V. K. Mezentsev, I. Bennion, and M. J. Withford, "Investigation of ultrafast laser-photonic material interactions: Challenges for directly written glass photonics," *IEEE Journal on Selected Topics in Quantum Electronics* **14**(5), pp. 1370–1388, 2008.

[25] R. Graf, A. Fernandez, M. Dubov, H. Brueckner, B. Chichkov, and A. Apolonski, "Pearl-chain waveguides written at megahertz repetition rate," *Applied Physics B: Lasers and Optics* **87**(1), pp. 21–27, 2007.

[26] I. Khrushchev, M. Dubov, A. Martinez, Y. Lai, and I. Bennion, "Point-by-point femtosecond laser inscribed structures in optical fibres and sensors using the same, (Patent EP 1759229)," 2007.

[27] A. Martinez, M. Dubov, I. Khrushchev, and I. Bennion, "Point by point FBG inscription by a focused NIR femtosecond laser," in *Lasers and Electro-Optics, 2004. (CLEO). Conference on*, **1**, p. 2, 2004.

[28] A. Martinez, M. Dubov, I. Khrushchev, and I. Bennion, "Direct writing of fibre Bragg gratings by femtosecond laser," *Electronics Letters* **40**(19), pp. 1170–1172, 2004.

[29] A. Martinez, M. Dubov, I. Khrushchev, and I. Bennion, "Point by point FBG inscription by a focused NIR femtosecond laser," in *OSA Trends in Optics and Photonics Series*, **96 A**, pp. 393–394, Optical Society of America, 2004.

[30] A. Martinez, M. Dubov, I. Y. Khrushchev, and I. Bennion, "Direct femtosecond inscription of fiber Bragg gratings," in *Materials Research Society Symposium Proceedings*, **850**, pp. 137–142, Materials Research Society, 2005.

[31] A. Martinez, M. Dubov, I. Khrushchev, and I. Bennion, "Structure of fiber gratings directly written by infrared femtosecond laser," in *Conference on Lasers and Electro-Optics and 2006 Quantum Electronics and Laser Science Conference, CLEO-QELS 2006*, pp. –, IEEE, 2006.

REFERENCES

[32] M. Dubov, V. Mezentsev, I. Bennion, and D. N. Nikogosyan, "UV femtosecond laser inscribes a 300 nm period nanostructure in a pure fused silica," *Measurement Science & Technology* **18**(7), pp. L15–L17, 2007.

[33] M. Dubov, V. Mezentsev, I. Bennion, and D. Nikogosyan, "Inscription of a 300-nm-period nanostructure in a pure fused silica," in *Conference on Lasers and Electro-Optics Europe - Technical Digest (Post-deadline papers)*, **1**, p. 1, Institute of Electrical and Electronics Engineers Inc., 2007.

[34] M. Dubov, V. Mezentsev, I. Bennion, and D. Nikogosyan, "Demonstration of possibility of 300-nm-period Bragg grating inscription in a pure fused silica," in *Bragg Gratings, Photosensitivity, and Poling in Glass Waveguides*, p. BTuD5, Optical Society of America, 2007.

[35] M. Dubov, V. Mezentsev, I. Bennion, and D. Nikogosyan, "Inscription of a 300-nm-period nanostructure in a pure fused silica," in *CLEO-Europe and IQEC 2007 Conference Digest*, pp. CP2–4, Optical Society of America, 2007.

[36] M. Dubov, I. Bennion, D. Nikogosyan, P. Bolger, and A. Zayats, "Point-by-point inscription of 250 nm period structure in bulk fused silica by tightly focused femtosecond uv pulses," *J. Opt. A: Pure Applied Optics* **10**(6), p. 025305, 2008.

[37] M. Dubov, R. K. Nasyrov, D. N. Nikogosyan, A. G. Poleshchuk, V. Mezentsev, and I. Bennion, "Micro-holographic methods for sub-micrometer grating fabrication in fused silica with UV femtosecond laser - art. no. 71000t," *Optical Design and Engineering Iii, Pts 1 and 2* **7100**, pp. T1000–T1000, 2008.

[38] D. N. Nikogosyan, M. Dubov, H. Schmitz, V. Mezentsev, I. Bennion, P. Bolger, and A. V. Zayats, "Point-by-point inscription of 250-nm-period structure in bulk fused silica by tightly-focused femtosecond uv pulses: experiment and numerical modeling," *Cent. Eur. J. Phys.* **8**(2), pp. 169–177, 2010.

[39] M. Dubov, V. Mezentsev, and I. Bennion, "Femtosecond inscription of the first order Bragg gratings in pure fused silica," in *2006 NSTI Nanotechnology Conference and Trade Show - NSTI Nanotech 2006 Technical Proceedings*, **3**, pp. 229–232, Nano Science and Technology Institute, 2006.

[40] T. Allsop, M. Dubov, A. Martinez, F. Floreani, I. Khrushchev, D. Webb, and I. Bennion, "Directional bend sensor based on an asymmetric modification of the fiber cladding by femtosecond laser," in *2005 Conference on Lasers and Electro-Optics, CLEO*, **3**, pp. 2179–2181, Optical Society of America, 2005.

[41] T. Allsop, M. Dubov, A. Martinez, F. Floreani, I. Khrushchev, D. J. Webb, and I. Bennion, "Long period grating directional bend sensor based on asymmetric index modification of cladding," *Electronics Letters* **41**(2), pp. 59–60, 2005.

[42] T. Allsop, M. Dubov, A. Martinez, F. Floreani, I. Khrushchev, D. J. Webb, and I. Bennion, "A long period grating directional bend sensor incorporating index modification of the cladding," *17th International Conference on Optical Fibre Sensors, Pts 1 and 2* **5855**, pp. 98–101, 2005.

REFERENCES

[43] T. D. Allsop, M. Dubov, A. Martinez, F. Floreani, I. Khrushchev, D. J. Webb, and I. Bennion, "Directional bend sensor based on an asymmetric modification of the fiber cladding by femtosecond laser," in *Conference on Lasers and Electro-Optics/Quantum Electronics and Laser Science and Photonic Applications Systems Technologies*, p. CFG6, Optical Society of America, 2005.

[44] T. Allsop, M. Dubov, A. Martinez, F. Floreani, I. Khrushchev, D. Webb, and I. Bennion, "Bending characteristics of fiber long-period gratings with cladding index modified by femtosecond laser," *J. Lightwave Technol.* **24**(8), pp. 3147–3154, 2006.

[45] T. Allsop, M. Dubov, H. Dobb, A. Main, A. Martinez, K. Kalli, D. Webb, and I. Bennion, "A comparison of the spectral properties of high temperature annealed long period gratings inscribed by fs laser, uv and fusion-arc," in *Proceedings of SPIE - The International Society for Optical Engineering*, **6193**, p. 61930M, SPIE, 2006.

[46] T. Allsop, K. Kalli, K. Zhou, Y. Lai, G. Smith, M. Dubov, D. J. Webb, and I. Bennion, "Long period gratings written into a photonic crystal fibre by a femtosecond laser as directional bend sensors," *Optical Communications* **281**(20), pp. 5092–5096, 2008.

[47] A. Martinez, Y. Lai, M. Dubov, I. Y. Khrushchev, and I. Bennion, "Vector bending sensors based on fiber Bragg gratings inscribed by an infrared femtosecond laser," in *Conference on Lasers and Electro-Optics/Quantum Electronics and Laser Science and Photonic Applications Systems Technologies*, p. CFH1, Optical Society of America, 2005.

[48] A. Martinez, Y. Lai, M. Dubov, I. Khmshchev, and I. Bennion, "Vector bending sensors based on fibre Bragg gratings inscribed by infrared femtosecond laser," *Electronics Letters* **41**(8), pp. 472–474, 2005.

[49] A. Martinez, Y. Lai, M. Dubov, I. Khrushchev, and I. Bennion, "Vector bending sensors based on fiber bragg gratings inscribed by an infrared femtosecond laser," in *2005 Conference on Lasers and Electro-Optics, CLEO*, **3**, pp. 2185–2187, Optical Society of America, 2005.

[50] Y. Lai, K. Zhou, M. Dubov, L. Zhang, and I. Bennion, "Fabrication of micro-channels in optical fibers using femtosecond laser pulses and selective chemical etching," in *Optical Fiber Communication Conference and Exposition and The National Fiber Optic Engineers Conference*, *Optical Fiber Communication Conference and Exposition and The National Fiber Optic Engineers Conference* , p. OTuL4, Optical Society of America, 2006.

[51] M. Dubov, S. R. Natarajan, J. A. R. Williams, and I. Bennion, "Mask-less lithography for fabrication of optical waveguides - art. no. 688110," *Commercial and Biomedical Applications of Ultrafast Lasers Viii* **6881**, pp. 88110–88110, 2008.

[52] M. Dubov, S. Natarajan, J. Williams, and I. Bennion, "Optical structures (Application for Patent WO 2009007712)," 2009.

[53] Y. Vlasov, "Silicon photonics for next generation computing systems." Tutorial given at Conference on Optical Communications, available online at: $http://www.research.ibm.com/photonics/publications/ecoc\_tutorial\_2008.pdf$, 2008.

REFERENCES

[54] C. Honninger, R. B. Doua, E. P. Mottay, and F. Salin, "High energy, 40 fs compact diode-pumped femtosecond laser for nanostructuring applications - art. no. 61000i," *Solid State Lasers XV: Technology and Devices* **6100**, pp. I1000–I1000, 2006.

[55] H. Nishihara, M. Haruna, and T. Suchara, *Optical Integrated Circuits*, McGraw-Hill Professional, 454 pages, 1988.

[56] S. I. Najafi, *Introduction to Glass Integrated Optics*, Artech House, Boston, 1992.

[57] E. Murphy, *Integrated Optical Circuits and Components: Design and Applications*, CRC Press, 1999.

[58] L. Eldada, "Polymer integrated optics: promise vs. practicality," *Proc. SPIE, Organic Photonic Materials and Devices IV, Bernard Kippelen; Donal D. Bradley; Eds.* **4642**, pp. 11–22, 2002.

[59] C. Brinker and G. Scherer, *Sol-Gel Science: The Physics and Chemistry of Sol-Gel Processing*, Academic Press, 912 pages, 1990.

[60] H. Misawa and S. Juodkazis, *3D Laser Microfabrication. Principles and Applications*, Wiley-VCH Verlag GmbH & Co. KGaA, Weinheim, 2006.

[61] M. E. Fermann, A. Galvanauskas, and G. E. Sucha, *Ultrafast Lasers: Technology and Applications (Optical Science and Engineering)*, CRC Press, 1-st ed., 800 pages, 2002.

[62] D. Strickland and G. Mourou, "Compression of amplified chirped optical pulses," *Optical Communications* **55**(6), pp. 447 – 449, 1985.

[63] D. Strickland and G. Mourou, "Compression of amplified chirped optical pulses," *Optical Communications* **56**(3), pp. 219 – 221, 1985.

[64] K. M. Davis, K. Miura, N. Sugimoto, and K. Hirao, "Writing waveguides in glass with a femtosecond laser," *Optics Letters* **21**(21), pp. 1729–1731, 1996.

[65] K. Miura, J. R. Qiu, H. Inouye, T. Mitsuyu, and K. Hirao, "Photowritten optical waveguides in various glasses with ultrashort pulse laser," *Applied Physics Letters* **71**(23), pp. 3329–3331, 1997.

[66] K. Miura, H. Inouye, J. R. Qiu, T. Mitsuyu, and K. Hirao, "Optical waveguides induced in inorganic glasses by a femtosecond laser," *Nuclear Instruments & Methods In Physics Research Section B-beam Interactions with Materials and Atoms* **141**(1-4), pp. 726–732, 1998.

[67] R. R. Gattass and E. Mazur, "Femtosecond laser micromachining in transparent materials," *Nature Photonics* **2**, pp. 219–225, Apr. 2008.

[68] K. Hirao and K. Miura, "Writing waveguides and gratings in silica and related materials by a femtosecond laser," *Journal of Non-Crystalline Solids* **239**(1-3), pp. 91–95, 1998.

REFERENCES

[69] O. Efimov, L. Glebov, K. Richardson, E. Van Stryland, T. Cardinal, S. Park, M. Couzi, and J. Bruneel, "Waveguide writing in chalcogenide glasses by a train of femtosecond laser pulses," *Opt. Mater.* **17**(3), pp. 379–386, 2001.

[70] M. Ams, G. D. Marshall, D. J. Spence, and M. J. Withford, "Slit beam shaping method for femtosecond laser direct-write fabrication of symmetric waveguides in bulk glasses," *Optics Express* **13**(15), pp. 5676–5681, 2005.

[71] R. Osellame, S. Taccheo, M. Marangoni, R. Ramponi, P. Laporta, D. Polli, S. De Silvestri, and G. Cerullo, "Femtosecond writing of active optical waveguides with astigmatically shaped beams," *Journal of the Optical Society of America B-optical Physics* **20**(7), pp. 1559–1567, 2003.

[72] S. Eaton, H. Zhang, and P. Herman, "Heat accumulation effects in femtosecond laser-written waveguides with variable repetition rate," *Optics Express* **13**(12), pp. 4708–4716, 2005.

[73] M. Will, S. Nolte, B. Chichkov, and A. Tunnermann, "Optical properties of waveguides fabricated in fused silica by femtosecond laser pulses," *Applied Optics* **41**(21), pp. 4360–4364, 2002.

[74] A. Streltsov and N. Borrelli, "Fabrication and analysis of a directional coupler written in glass by nanojoule femtosecond laser pulses," *Optics Letters* **26**(1), pp. 42–43, 2001.

[75] C. Florea and K. Winick, "Fabrication and characterization of photonic devices directly written in glass using femtosecond laser pulses," *J. Lightwave Technol.* **21**(1), pp. 246–253, 2003.

[76] R. R. Thomson, H. T. Bookey, N. D. Psaila, A. Fender, S. Campbell, W. N. MacPherson, J. S. Barton, D. T. Reid, and A. K. Kar, "Ultrafast-laser inscription of a three dimensional fan-out device for multicore fiber coupling applications," *Optics Express* **15**(18), pp. 11691–11697, 2007.

[77] S. Nolte, M. Will, J. Burghoff, and A. Tuennermann, "Femtosecond waveguide writing: a new avenue to three-dimensional integrated optics," *Applied Physics A-Materials Science & Processing* **77**(1), pp. 109–111, 2003.

[78] S. M. Eaton, W.-J. Chen, H. Zhang, R. Iyer, J. Li, M. L. Ng, S. Ho, J. S. Aitchison, and P. R. Herman, "Spectral loss characterization of femtosecond laser written waveguides in glass with application to demultiplexing of 1300 and 1550 nm wavelengths," *J. Lightwave Technol.* **27**(9), pp. 1079–1085, 2009.

[79] F. Dreisow, M. Ornigotti, A. Szameit, M. Heinrich, R. Keil, S. Nolte, A. Tu andnnermann, and S. Longhi, "Octave spanning 50x50 beam splitting via interrupted stirap," in *Lasers and Electro-Optics (CLEO) and Quantum Electronics and Laser Science Conference (QELS), 2010 Conference on*, pp. 1 –2, May 2010.

[80] Y. Kondo, K. Nouchi, T. Mitsuyu, M. Watanabe, P. G. Kazansky, and K. Hirao, "Fabrication of long-period fiber gratings by focused irradiation of infrared femtosecond laser pulses," *Optics Letters* **24**(10), pp. 646–648, 1999.

REFERENCES

[81] Y. Kondo, K. Nouchi, T. Mitsuyu, M. Watanabe, P. G. Kazansky, and K. Hirao, "Long-period fiber grating fabricated by focused irradiation of femtosecond laser pulses," *Optical Devices For Fiber Communication* **3847**, pp. 34–41, 1999.

[82] A. Dragomir, D. N. Nikogosyan, K. A. Zagorul'ko, and P. G. Kryukov, "Inscription of long-period fibre gratings by femtosecond UV radiation," in *Proceedings of SPIE - The International Society for Optical Engineering*, **4876**(1), pp. 313–320, 2002.

[83] T. Fujii, T. Fukuda, S. Ishikawa, Y. Ishii, K. Sakuma, and H. Hosoya, "Characteristics improvement of long-period fiber gratings fabricated by femtosecond laser pulses using novel positioning technique," in *OSA Trends in Optics and Photonics Series*, **95 B**, pp. 53–55, Optical Society of America, 2004.

[84] M. Dubov, I. Bennion, S. A. Slattery, and D. N. Nikogosyan, "Strong long-period fiber gratings recorded at 352 nm," *Optics Letters* **30**(19), pp. 2533–2535, 2005.

[85] K. Oi, F. Barnier, and M. Obara, "Fabrication of fiber bragg grating by femtosecond laser interferometry," in *Conference Proceedings - Lasers and Electro-Optics Society Annual Meeting (LEOS-2001)*, **2**, pp. 776–777, Institute of Electrical and Electronics Engineers Inc., 2001.

[86] A. Dragomir, D. N. Nikogosyan, K. A. Zagorulko, P. G. Kryukov, and E. M. Dianov, "Inscription of fiber Bragg gratings by ultraviolet femtosecond radiation," *Optics Letters* **28**(22), pp. 2171–2173, 2003.

[87] S. Mihailov, C. Smelser, P. Lu, R. Walker, D. Grobnic, H. Ding, G. Henderson, and J. Unruh, "Fiber Bragg gratings made with a phase mask and 800-nm femtosecond radiation," *Optics Letters* **28**(12), pp. 995–997, 2003.

[88] D. Grobnic, C. Smelser, S. Mihailov, R. Walker, and P. Lu, "Fiber Bragg gratings with suppressed cladding modes made in smf-28 with a femtosecond ir laser and a phase mask," *IEEE Photonics Technology Letters* **16**(8), pp. 1864–1866, 2004.

[89] G. Marshall and M. Withford, "Rapid production of arbitrary fiber Bragg gratings using femtosecond laser radiation," in *Conference Proceedings - Lasers and Electro-Optics Society Annual Meeting-LEOS*, **2005**, pp. 935–936, Institute of Electrical and Electronics Engineers Inc., 2005.

[90] D. Grobnic, S. Mihailov, C. Smelser, and H. Ding, "Sapphire fiber Bragg grating sensor made using femtosecond laser radiation for ultrahigh temperature applications," *IEEE Photonics Technology Letters* **16**(11), pp. 2505–2507, 2004.

[91] A. Martinez, I. Khrushchev, and I. Bennion, "Thermal properties of fibre Bragg gratings inscribed point-by-point by infrared femtosecond laser," *Electronics Letters* **41**(4), pp. 176–178, 2005.

[92] K. Zhou, C. Mou, M. Dubov, L. Zhang, and I. Bennion, "Line by line fiber Bragg grating by femtosecond laser," *Bragg Gratings, Photosensitivity, and Poling in Glass Waveguides* , p. JThA24, Optical Society of America, 2010.

REFERENCES

[93] M. Bernier, Y. Sheng, and R. Vallee, "Ultrabroadband fiber Bragg gratings written with a highly chirped phase mask and infrared femtosecond pulses," *Optics Express* **17**(5), pp. 3285–3290, 2009.

[94] A. Martinez, I. Y. Khrushchev, and I. Bennion, "Direct inscription of Bragg gratings in coated fibers by an infrared femtosecond laser," *Optics Letters* **31**, pp. 1603–1605, June 2006.

[95] G. D. Marshall, P. Dekker, M. Ams, J. A. Piper, and M. J. Withford, "Directly written monolithic waveguide laser incorporating a distributed feedback waveguide-bragg grating," *Optics Letters* **33**, pp. 956–958, May 2008.

[96] M. Bernier, R. Vallée, X. Pruneau-Godmaire, M. andré Lapointe, and B. Morasse, "Writing of fiber Bragg gratings using 400 nm femtosecond pulses and its application to high power fiber laser," in *Bragg Gratings, Photosensitivity, and Poling in Glass Waveguides*, p. BWC5, Optical Society of America, 2010.

[97] M. Bernier, M. andré Lapointe, R. Vallée, X. Pruneau-Godmaire, and B. Morasse, "High-power splice-free ytterbium fiber laser based on femtosecond-written fiber Bragg gratings," in *Conference on Lasers and Electro-Optics*, p. CTuC3, Optical Society of America, 2010.

[98] M. Bernier, D. Faucher, N. Caron, and R. Vallée, "Highly stable and efficient erbium-doped 2.8 μm all fiber laser," *Optics Express* **17**(19), pp. 16941–16946, 2009.

[99] R. Osellame, G. Cerullo, S. Taccheo, M. Marangoni, D. Polli, P. Laporta, and R. Ramponi, "Femtosecond lasrwriting of symmetrical optical waveguides by astigmatically shaped beams," *Proceedings of the Society of Photo-Optical Instrumentation Engineers (SPIE)* **5451**, pp. 360–368, SPIE-INT SOC OPTICAL ENGINEERING, 2004. Conference Optics and Photonic Integrated Circuits, Strasbourg, FRANCE, APR 27-29, 2004.

[100] N. Jovanovic, M. Aslund, A. Fuerbach, S. D. Jackson, G. D. Marshall, and M. J. Withford, "Narrow linewidth, 100 W CW Yb3+-doped silica fiber laser with a point-by-point Bragg grating inscribed directly into the active core," *Optics Letters* **32**(19), pp. 2804–2806, 2007.

[101] N. Jovanovic, M. Aslund, A. Fuerbach, S. D. Jackson, G. D. Marshall, and M. J. Withford, "100 w cw yb3+ -doped silica fiber laser utilizing an active-core inscribed point-by-point Bragg grating," in *Bragg Gratings, Photosensitivity, and Poling in Glass Waveguides*, p. BWB7, Optical Society of America, 2007.

[102] R. Osellame, V. Maselli, R. M. Vazquez, R. Ramponi, and G. Cerullo, "Integration of optical waveguides and microfluidic channels both fabricated by femtosecond laser irradiation," *Applied Physics Letters* **90**(23), p. p2747194, 2007.

[103] S. Juodkazis, K. Nishimura, S. Tanaka, H. Misawa, E. G. Gamaly, B. Luther-Davies, L. Hallo, P. Nicolai, and V. T. Tikhonchuk, "Laser-induced microexplosion confined in the bulk of a sapphire crystal: Evidence of multimegabar pressures," *Physical Review Letters* **96**, p. 166101, Apr. 2006.

REFERENCES

[104] E. G. Gamaly, S. Juodkazis, H. Misawa, B. Luther-Davies, A. V. Rode, L. Hallo, P. Nicolai, and V. T. Tikhonchuk, "Formation of nano-voids in transparent dielectrics by femtosecond lasers," *Curr. Appl Phys.* **8**, pp. 412–415, May 2008.

[105] M. Dubov, T. D. Allsop, A. Martinez, V. Mezentsev, and I. Bennion, "Highly bire-fringent long period gratings fabricated with femtosecond laser," in *Optical Fiber Communication Conference and Exposition and The National Fiber Optic Engineers Conference*, p. OWI50, Optical Society of America, 2006.

[106] Y. Lai, K. Zhou, M. Dubov, L. Zhang, and I. Bennion, "Fabrication of micro-channels in optical fibers using femtosecond laser pulses and selective chemical etching," *2006 Optical Fiber Communication Conference/National Fiber Optic Engineers Conference, Vols 1-6* **1-6**, pp. 286–288, 2006.

[107] R. Hunsperger, *Integrated Optics*, Springer-Verlag, 2002.

[108] T. Miya, "Silica-based planar lightwave circuits: Passive and thermally active devices," *IEEE Journal of Selected Topics in Quantum Electronics* **6**(1), pp. 38–45, 2000.

[109] L. Eldada, "Optical communication components," *Rev. Sci. Instrum.* **75**(3), pp. 575–593, 2004.

[110] Y. Vlasov and S. McNab, "Losses in single-mode silicon-on-insulator strip waveg-uides and bends," *Optics Express* **12**(8), pp. 1622–1631, 2004.

[111] S. Smirnov and S. Kobtsev, "Review of methods for waveguide fabrication." private communication, 2006.

[112] A. G. Okhrimchuk, A. V. Shestakov, I. Khrushchev, and J. Mitchell, "Depressed cladding, buried waveguide laser formed in a yag : Nd3+ crystal by femtosecond laser writing," *Optics Letters* **30**, pp. 2248–2250, Sept. 2005.

[113] H. Zhang, S. Eaton, and P. Herman, "Low-loss type ii waveguide writing in fused silica with single picosecond laser pulses," *Optics Express* **14**(11), pp. 4826–4834, 2006.

[114] H. Zhang, S. M. Eaton, J. Li, A. H. Nejadmalayeri, and P. R. Herman, "Type ii high-strength Bragg grating waveguides photowritten with ultrashort laser pulses," *Optics Express* **15**(7), pp. 4182–4191, 2007.

[115] T. Fukuda, S. Ishikawa, T. Fujii, K. Sakuma, and H. Hosoya, "Improvement on asym-metry of low-loss waveguides written in pure silica glass by femtosecond laser pulses," **5279**, pp. 21–28, 2003.

[116] M. Dubov, G. Klishevich, V. Sergienko, I. Obukhov, A. Turchin, and M. Cher-nomorets, "An astigmatic wavelength meter," *Pribory i Tekhnika Eksperimenta* **44**(4), pp. 124–131, 2001.

[117] T. Fukuda, S. Ishikawa, T. Fujii, K. Sakuma, and H. Hosoya, "Low-loss optical waveg-uides written by femtosecond laser pulses for three-dimensional photonic devices," *Photon Processing In Microelectronics and Photonics Iii* **5339**, pp. 524–538, 2004.

REFERENCES

[118] andrés Ferrer, A. R. de la Cruz, D. Puerto, W. Gawelda, J. A. Vallés, M. A. Rebolledo, V. Berdejo, J. Siegel, and J. Solis, "In situ assessment and minimization of nonlinear propagation effects for femtosecond-laser waveguide writing in dielectrics," *J. Opt. Soc. Am. B* **27**(8), pp. 1688–1692, 2010.

[119] C. B. Schaffer, A. Brodeur, J. F. Garcìa, and E. Mazur, "Micromachining bulk glass by use of femtosecond laser pulses with nanojoule energy," *Optics Letters* **26**, pp. 93–95, 2001.

[120] L. Shah, F. Yoshino, A. Arai, S. Eaton, H. Zhang, S. Ho, and P. Herman, "MHz-rate ultrafast fiber laser for writing of optical waveguides in silica glasses," *Commercial and Biomedical Applications of Ultrafast Lasers V* **5714**, pp. 253–260, 2005.

[121] R. Osellame, N. Chiodo, G. Della Valle, G. Cerullo, R. Ramponi, P. Laporta, A. Killi, U. Morgner, and O. Svelto, "Waveguide lasers in the c-band fabricated by laser inscription with a compact femtosecond oscillator," *IEEE Journal of Selected Topics in Quantum Electronics* **12**(2), pp. 277–285, 2006.

[122] G. Della Valle, R. Osellame, and P. Laporta, "Micromachining of photonic devices by femtosecond laser pulses," *Journal of Optics A - Pure and Applied Optics* **11**(1), p. 013001, 2009.

[123] A. Streltsov and N. Borrelli, "Study of femtosecond-laser-written waveguides in glasses," *Journal of the Optical Society of America B - Optical Physics* **19**(10), pp. 2496–2504, 2002.

[124] V. Bhardwaj, E. Simova, P. Corkum, D. Rayner, C. Hnatovsky, R. Taylor, B. Schreder, M. Kluge, and J. Zimmer, "Femtosecond laser-induced refractive index modification in multicomponent glasses," *J. Appl. Phys.* **97**(8), 2005.

[125] R. An, Y. Li, D. Liu, Y. Dou, F. Qi, H. Yang, and Q. Gong, "Optical waveguide writing inside foturan glass with femtosecond laser pulses," *Applied Physics A - Materials Science & Processing* **86**(3), pp. 343–346, 2007.

[126] K. C. Vishnubhatla, S. V. Rao, R. S. S. Kumar, R. Osellame, S. N. B. Bhaktha, S. Turrell, A. Chiappini, A. Chiasera, M. Ferrari, M. Mattarelli, M. Montagna, R. Ramponi, G. C. Righini, and D. N. Rao, "Femtosecond laser direct writing of gratings and waveguides in high quantum efficiency erbium-doped baccarat glass," *Journal of Physics D - Applied Physics* **42**(20), p. p205106, 2009.

[127] R. Osellame, N. Chiodo, V. Maselli, A. Yin, M. Zavelani-Rossi, G. Cerullo, P. Laporta, L. Aiello, S. De Nicola, P. Ferraro, A. Finizio, and G. Pierattini, "Optical properties of waveguides written by a 26 MHz stretched cavity Ti:Sapphire femtosecond oscillator," *Optics Express* **13**, pp. 612–620, Jan. 2005.

[128] L. M. Tong, R. R. Gattass, I. Maxwell, J. B. Ashcom, and E. Mazur, "Optical loss measurements in femtosecond laser written waveguides in glass," *Optical Communications* **259**, pp. 626–630, Mar. 2006.

REFERENCES

[129] V. Maselli, R. Osellame, N. Chiodo, G. Cerullo, P. Laporta, P. Ferraro, S. De Nicola, and A. Finizio, "3d photonic devices at telecom wavelengths fabricated by a femtosecond oscillator - art. no. 61080w," *Commercial and Biomedical Applications of Ultrafast Lasers VI* **6108**, p. 61080W, 2006.

[130] S. M. Eaton, M. L. Ng, J. Bonse, A. Mermillod-Blondin, H. Zhang, A. Rosenfeld, and P. R. Herman, "Low-loss waveguides fabricated in bk7 glass by high repetition rate femtosecond fiber laser," *Applied Optics* **47**(12), pp. 2098–2102, 2008.

[131] S. M. Eaton, M. L. Ng, T. Rafique, and P. R. Herman, "High refractive index contrast in fused silica waveguides by tightly focused, high-repetition rate femtosecond laser," in *Conference on Lasers and Electro-Optics/International Quantum Electronics Conference*, p. CFT3, Optical Society of America, 2009.

[132] Y. Lai, K. Zhou, K. Sugden, and I. Bennion, "Point-by-point inscription of first-order fiber Bragg grating for c-band applications," *Optics Express* **15**, pp. 18318–18325, Dec. 2007.

[133] Y. Lai, A. Martinez, I. Khrushchev, and I. Bennion, "Distributed Bragg reflector fiber laser fabricated by femtosecond laser inscription," *Optics Letters* **31**, pp. 1672–1674, June 2006.

[134] K. Zagorul'ko, P. Kryukov, E. Dianov, A. Dragomir, and D. Nikogosyan, "Fibrebragg-grating writing in single-mode optical fibres by uv femtosecond pulses," *Quant. Electron.* **33**(8), pp. 728–730, 2003.

[135] K. Zagorul'ko, P. Kryukov, E. Dianov, A. Dragomir, and D. Nikogosyan, "Fbg writing in single-mode fibers by uv femtosecond pulses," *Kvantovaja Electronica (in Russian)* **33**(8), pp. 728–731, 2003.

[136] S. Mihailov, D. Grobnic, and C. Smelser, "Efficient grating writing through fibre coating with femtosecond ir radiation and phase mask," *Electronics Letters* **43**(8), pp. 442–443, 2007.

[137] S. Mihailov, C. Smelser, D. Grobnic, R. Walker, P. Lu, H. Ding, and J. Unruh, "Bragg gratings written in all-sio2 and ge-doped core fibers with 800-nm femtosecond radiation and a phase mask," *J. Lightwave Technol.* **22**(1), pp. 94–100, 2004. Conference on Optical Fiber Communications Conference (OCF), ATLANTA, GEORGIA, 2003.

[138] I. Khrushchev, Y. Lai, M. Dubov, A. Martinez, and I. Bennion, "Laser inscribed structures (Patent US 2007230861-A1)," 2007.

[139] A. Martinez, *Inscription of in-fibre photonic devices by an infrared femtosecond laser*. PhD thesis, School of Engineering and Applied Science, Aston University, Birmingham, UK, 2005.

[140] M. Aslund, N. Jovanovic, J. Groothoff, N.and Canning, G. Marshall, S. Jackson, A. Fuerbach, and M. Withford, "Large diffractive scattering losses in the visible region produced by femtosecond laser written bragg gratings," in *2008 Joint Conference of the Opto-Electronics and Communications Conference and the Australian Conference on Optical Fibre Technology (OECC/ACOFT-2008)*, p. 1, IEEE, 2008.

REFERENCES

[141] M. Aslund, N. Jovanovic, J. Groothoff, N.and Canning, G. Marshall, S. Jackson, A. Fuerbach, and M. Withford, "Optical loss mechanisms in femtosecond laser-written point-by-point fibre Bragg gratings," *Optics Express* **16**(18), pp. 14248–14254, 2008.

[142] L. Keldysh, "Ionization in the field of a strong electromagnetic wave," *Zh. Eksperim. i Teor. Fiz.* **47**, pp. 1945–1957, 1964.

[143] J.-C. Diels and W. Rudolph, *Ultrashort Laser Pulse Phenomena*, (Optics and Photonics Series), Academic Press; 2-nd ed., 680 pages, 2006.

[144] S. A. Akhmanov, V. A. Vysloukh, and A. S. Chirkin, *Optics of Femtosecond Laser Pulses*, AIP Press, 388 pages, 1991.

[145] G. Agrawal, *Nonlinear Fiber Optics (Optics and Photonics)*, Academic Press, 3 ed., 467 pages, 2001.

[146] T. Brabec and F. Krausz, "Nonlinear optical pulse propagation in the single-cycle regime," *Physical Review Letters* **78**, pp. 3282–3285, 1997.

[147] M. D. Feit and J. A. Fleck, "Effect of refraction on spot-size dependence of laser-induced breakdown," *Applied Physics Letters* **24**(4), pp. 169–172, 1974.

[148] J. K. Ranka and A. L. Gaeta, "Breakdown of the slowly varying envelope approximation in the self-focusing of ultrashort pulses," *Optics Letters* **23**, pp. 534–536, 1998.

[149] A. L. Gaeta, "Catastrophic collapse of ultrashort pulses," *Physical Review Letters* **84**, pp. 3582–3585, 2000.

[150] S. Tzortzakis, L. Sudrie, M. Franco, B. Prade, A. Mysyrowicz, A. Couairon, and L. Bergé, "Self-guided propagation of ultrashort ir laser pulses in fused silica," *Physical Review Letters* **21**, p. 213902, 2001.

[151] M. Kolesik, J. V. Moloney, and M. Mlejnek, "Unidirectional optical pulse propagation equation," *Physical Review Letters* **89**, p. 283902, 2002.

[152] S. Tzortzakis, L. Bergé, M. Franco, B. Prade, andré Mysyrowicz, and A. Couairon, "Infrared femtosecond light filaments in air: simulations and experiments," *J. Opt. Soc. Am. B* **19**, pp. 1117–1129, 2002.

[153] M. Kolesik, G. Katona, J. Moloney, and E.M.Wright, "Physical factors limiting the spectral extent and band gap dependence of supercontinuum generation," *Physical Review Letters* **91**, p. 043905, 2003.

[154] R. Nuter, S. Skupin, and L. Bergé, "Chirp-induced dynamics of femtosecond filaments in air," *Opt. Lett* **30**, pp. 917–919, 2005.

[155] Q. Feng, J. V. Moloney, A. C. Newell, E. M. Wright, K. Cook, P. K. Kennedy, D. X. Hammer, B. A. Rockwell, and C. R. Thompson, "Theory and simulation on the threshold of water breakdown induced by focused ultrashort laser pulses," *IEEE J. Quantum Electron.* **33**, pp. 127–137, 1997.

REFERENCES

[156] M. D. Feit and J. J. A. Fleck, "Beam nonparaxiality, filament formation, and beam breakup in the self-focusing of optical beams," *J. Opt. Soc. Am. B* **5**(3), pp. 633–640, 1988.

[157] A. P. Joglekar, H. H. Liu, E. Meyhofer, G. Mourou, and A. J. Hunt, "Optics at critical intensity: Applications to nanomorphing," *Proc. Nat. Acad. Sci. U.S.A.* **101**(16), pp. 5856–5861, 2004.

[158] V. Mezentsev, J. Petrovic, J. Dreher, and R. Grauer, "Adaptive modeling of the femtosecond inscription in silica," in *Laser-based Micropackaging*, F. G. Bachmann, W. Hoving, Y. Lu, and K. Washio, eds., *Proc. SPIE* **6107**, p. 61070R, 2006.

[159] K. Germaschewski, R. Grauer, L. Bergé, V. K. Mezentsev, and J. J. Rasmussen, "Splittings, coalescence, bunch and snake patterns in the 3D nonlinear schrodinger equation with anisotropic dispersion," *Physica D* **151**, pp. 175–198, 2001.

[160] X. Zhang, X. Xu, and A. Rubenchik, "Simulation of microscale densification during femtosecond laser processing of dielectric materials," *Appl. Phys. A* **79**, pp. 945–948, 2004.

[161] S. Vlasov, V. Petrishchev, and V. Talanov, "Averaged description of wave beams in linear and nonlinear media," *Radiophys. Quantum Electron.* **14**, pp. 1062–1070, 1971.

[162] J. H. Marburger, "Self-focusing: theory," *Prog. Quantum Electron.* **4**, pp. 35–110, 1975.

[163] S. K. Turitsyn, V. K. Mezentsev, M. Dubov, A. M. Rubenchik, M. P. Fedoruk, and E. V. Podivilov, "Nonlinear diffraction in sub-critical femtosecond inscription," in *CLEO-Europe and IQEC 2007 Conference Digest*, p. CM2.2, Optical Society of America, 2007.

[164] H. C. Guo, H. B. Jiang, Y. Fang, C. Peng, H. Yang, Y. Li, and Q. H. Gong, "The pulse duration dependence of femtosecond laser induced refractive index modulation in fused silica," *Journal of Optics A - Pure and Applied Optics* **6**, pp. 787–790, Aug. 2004.

[165] C. Hnatovsky, R. S. Taylor, P. P. Rajeev, E. Simova, V. R. Bhardwaj, D. M. Rayner, and P. B. Corkum, "Pulse duration dependence of femtosecond-laser-fabricated nanogratings in fused silica," *Applied Physics Letters* **87**, p. 014104, July 2005.

[166] P. P. Rajeev, M. Gertsvolf, E. Simova, C. Hnatovsky, R. S. Taylor, V. R. Bhardwaj, D. M. Rayner, and P. B. Corkum, "Memory in nonlinear ionization of transparent solids," *Physical Review Letters* **97**, p. 253001, Dec. 2006.

[167] S. M. Eaton, H. Zhang, M. L. Ng, J. Li, W.-J. Chen, S. Ho, and P. R. Herman, "Transition from thermal diffusion to heat accumulation in high repetition rate femtosecond laser writing of buried optical waveguides," *Optics Express* **16**(13), pp. 9443–9458, 2008.

REFERENCES

[168] K. Minoshima, A. M. Kowalevicz, E. P. Ippen, and J. G. Fujimoto, "Fabrication of coupled mode photonic devices in glass by nonlinear femtosecond laser materials processing," *Optics Express* **10**(15), pp. 645–652, 2002.

[169] A. M. Kowalevicz, V. Sharma, E. P. Ippen, J. G. Fujimoto, and K. Minoshima, "3d photonic devices fabricated in glass by a femtosecond oscillator," *Ultrafast Phenomena XIV* **79**, pp. 801–803, 2005.

[170] A. Fernandez, T. Fuji, A. Poppe, A. Furbach, F. Krausz, and A. Apolonski, "Chirped-pulse oscillators: a route to high-power femtosecond pulses without external amplification," *Optics Letters* **29**, pp. 1366–1368, June 2004.

[171] S. Naumov, A. Fernandez, R. Graf, P. Dombi, F. Krausz, and A. Apolonski, "Approaching the microjoule frontier with femtosecond laser oscillators," *New Journal of Physics* **7**, p. 216, Oct. 2005.

[172] V. L. Kalashnikov and A. Apolonski, "Chirped-pulse oscillators: A unified standpoint," *Physical Review A* **79**, p. 043829, Apr. 2009.

[173] A. Fernandez, A. Verhoef, V. Pervak, G. Lermann, F. Krausz, and A. Apolonski, "Generation of 60-nj sub-40-fs pulses at 70 MHz repetition rate from a Ti:Sapphire chirped pulse-oscillator," *Applied Physics B-lasers and Optics* **87**, pp. 395–398, May 2007.

[174] Y. Deng, C.-Y. Chien, B. G. Fidric, and J. D. Kafka, "Sub-50 fs pulse generation from a high power Yb-doped fiber amplifier," in *Conference on Lasers & Electro-Optics/Quantum Electronics and Laser Science Conference (CLEO/QELS-2009), vols.1-3*, pp. 1779–1780, IEEE, 2009.

[175] T. Eidam, S. Hanf, E. Seise, T. V. andersen, T. Gabler, C. Wirth, T. Schreiber, J. Limpert, and a. Tuennermann, "Femtosecond fiber cpa system emitting 830 w average output power," *Optics Letters* **35**(2), pp. 94–96, 2010.

[176] Z. Bor, "Distortion of femtosecond laser-pulses in lenses and lens systems," *Journal of Modern Optics* **35**(12), pp. 1907–1918, 1988.

[177] Z. Bor and Z. Horvath, "Distortion of femtosecond pulses in lenses - wave optical description," *Optics Communications* **94**(4), pp. 249–258, 1992.

[178] D. Fittinghoff, A. Millard, J. Squier, and M. Muller, "Frequency-resolved optical gating measurement of ultrashort pulses passing through a high numerical aperture objective," *IEEE Journal of Quantum Electronics* **35**(4), pp. 479–486, 1999.

[179] D. Fittinghoff, J. der Au, and J. Squier, "Spatial and temporal characterizations of femtosecond pulses at high-numerical aperture using collinear, background-free, third-harmonic autocorrelation," *Optics Communications* **247**(4-6), pp. 405–426, 2005.

[180] M. R. Teague, "Deterministic phase retrieval - a green-function solution," *Journal of the Optical Society of America* **73**(11), pp. 1434–1441, 1983.

[181] K. Nugent, "Wave field determination using 3-dimensional intensity information," *Physical Review Letters* **68**(15), pp. 2261–2264, 1992.

REFERENCES

[182] A. Barty, K. A. Nugent, D. Paganin, and A. Roberts, "Quantitative optical phase microscopy," *Optics Letters* **23**(11), pp. 817–819, 1998.

[183] A. Barty, K. A. Nugent, A. Roberts, and D. Paganin, "Quantitative phase tomography," *Optical Communications* **175**(4-6), pp. 329–336, 2000.

[184] D. Paganin and K. Nugent, "Noninterferometric phase imaging with partially coherent light," *Physical Review Letters* **80**(12), pp. 2586–2589, 1998.

[185] C. Bellair, C. Curl, B. Allman, P. Harris, A. Roberts, L. Delbridge, and K. Nugent, "Quantitative phase amplitude microscopy iv: imaging thick specimens," *Journal of Microscopy-Oxford* **214**(Part 1), pp. 62–69, 2004.

[186] E. Ampem-Lassen, S. Huntington, N. Dragomir, K. Nugent, and A. Roberts, "Refractive index profiling of axially symmetric optical fibers: a new technique," *Optics Express* **13**(9), pp. 3277–3282, 2005.

[187] A. Horn, I. Mingareev, J. Gottmann, A. Werth, and U. Brenk, "Dynamical detection of optical phase changes during micro-welding of glass with ultra-short laser radiation," *Measurement Science & Technology* **19**(1), 2008.

[188] A. Gopal, S. Minardi, and M. Tatarakis, "Quantitative two-dimensional shadow-graphic method for high-sensitivity density measurement of under-critical laser plasmas," *Optics Letters* **32**(10), pp. 1238–1240, 2007.

[189] E. Cuche, P. Marquet, and C. Depeursinge, "Simultaneous amplitude-contrast and quantitative phase-contrast microscopy by numerical reconstruction of fresnel off-axis holograms," *Applied Optics* **38**(34), pp. 6994–7001, 1999.

[190] E. Cuche, P. Marquet, and C. Depeursinge, "Spatial filtering for zero-order and twin-image elimination in digital off-axis holography," *Applied Optics* **39**(23), pp. 4070–4075, 2000.

[191] M. Liebling, T. Blu, and M. Unser, "Complex-wave retrieval from a single off-axis hologram," *Journal of the Optical Society of America A-optics Image Science and Vision* **21**, pp. 367–377, Mar. 2004.

[192] V. V. Bukin, S. V. Garnov, V. V. Strelkov, T. V. Shirokikh, and D. K. Sychev, "Spatio-temporal dynamics of electron density in femtosecond laser microplasma of gases," *Laser Physics* **19**(6), pp. 1300–1302, 2009.

[193] F. Durr, H. Limberger, R. Salathe, F. Hindle, M. Douay, E. Fertein, and C. Przygodzki, "Tomographic measurement of femtosecond-laser induced stress changes in optical fibers," *Applied Physics Letters* **84**(24), pp. 4983–4985, 2004.

[194] H. G. Limberger, C. Ban, R. P. Salathe, S. A. Slattery, and D. N. Nikogosyan, "Absence of uv-induced stress in Bragg gratings recorded by high-intensity 264 nm laser pulses in a hydrogenated standard telecom fiber," *Optics Express* **15**(9), pp. 5610–5615, 2007.

REFERENCES

[195] W. Gawelda, D. Puerto, J. Siegel, A. Ferrer, A. R. de la Cruz, H. Fernandez, and J. Solis, "Ultrafast imaging of transient electronic plasmas produced in conditions of femtosecond waveguide writing in dielectrics," *Applied Physics Letters* **93**, p. 121109, Sept. 2008.

[196] I. Blonskyi, V. Kadan, O. Shpotyuk, and I. Dmitruk, "Manifestations of sub- and superluminality in filamented femtosecond laser pulse in fused silica," *Optics Communications* **282**(9), pp. 1913–1917, 2009.

[197] A. Horn, E. Kreutz, and R. Poprawe, "Ultrafast time-resolved photography of femtosecond laser induced modifications in bk7 glass and fused silica," *Applied Physics A - Materials Science & Processing* **79**(4-6), pp. 923–925, 2004.

[198] T. Kubota, K. Komai, M. Yamagiwa, and Y. Awatsuji, "Moving picture recording and observation of three-dimensional image of femtosecond light pulse propagation," *Optics Express* **15**(22), pp. 14348–14354, 2007.

[199] S. M. Eaton, H. Zhang, M. L. Ng, J. Li, W.-J. Chen, S. Ho, and P. R. Herman, "Transition from thermal diffusion to heat accumulation in high repetition rate femtosecond laser writing of buried optical waveguides," *Optics Express* **16**(13), pp. 9443–9458, 2008.

[200] M. Dubov, R. Nasyrov, D. Nikogosyan, A. Poleshchuk, V. Mezentsev, and I. Bennion, "Micro-holographic methods for sub-micrometer grating fabrication in fused silica with UV femtosecond laser," in *Proceedings of SPIE - The International Society for Optical Engineering*, **7100**, p. paper7100, 2008.

[201] K. Zhou, Y. Lai, X. Chen, K. Sugden, L. Zhang, and I. Bennion, "A refractometer based on a micro-slot in a fiber Bragg grating formed by chemically assisted femtosecond laser processing," *Optics Express* **15**(24), pp. 15848–15853, 2007.

[202] C. Schaffer, J. Garcia, and E. Mazur, "Bulk heating of transparent materials using a high-repetition-rate femtosecond laser," *Applied Physics A-Materials Science & Processing* **76**(3), pp. 351–354, 2003.

[203] M. Ams, G. D. Marshall, J. A. Piper, and M. J. Withford, "Femtosecond laser writing of symmetric, low loss waveguides in active glasses," *2005 IEEE LEOS Annual Meeting Conference Proceedings (LEOS)* **1-3**, pp. 676–677, 2005.

[204] M. Ams, *Fabrication of Optical Waveguide Devices in Bulk Material Using femtosecond Laser Pulses*. PhD thesis, Macquarie University, Sydney, Australia, 2008.

[205] A. G. Okhrimchuk, A. V. Shestakov, I. Khrushchev, and I. Bennion, "Waveguide laser formed in yag : Nd3+ crystal by femtosecond laser," *Solid State Lasers XIV: Technology and Devices* **5707**, pp. 258–264, 2005.

[206] K. Zhou, M. Dubov, C. Mou, L. Zhang, V. K. Mezentsev, and I. Bennion, "Line-by-line fiber Bragg grating made by femtosecond laser," *IEEE Photonics Technology Letters* **22**(16), pp. 1190–1192, 2010.

REFERENCES

[207] V. Mezentsev, M. Dubov, A. Martinez, Y. Lai, T. P. Allsop, I. Khrushchev, D. J. Webb, F. Floreani, and I. Bennion, "Micro-fabrication of advanced photonic devices by means of direct point-by-point femtosecond inscription in silica," in *Laser-based Micropackaging*, F. G. Bachmann, W. Hoving, Y. Lu, and K. Washio, eds., *Proc. SPIE* **6107**, p. 61070C, 2006.

[208] S. M. Eaton, H. Zhang, P. R. Herman, F. Yoshino, L. Shah, and A. Y. Arai, "Writing optical waveguides with a 0.1 - 5 MHz repetition rate femtosecond fiber laser," in *Conference on Lasers and Electro-Optics/Quantum Electronics and Laser Science and Photonic Applications Systems Technologies*, p. CFG4, Optical Society of America, 2005.

[209] P. G. Kazansky, W. J. Yang, E. Bricchi, J. Bovatsek, A. Arai, Y. Shimotsuma, K. Miura, and K. Hirao, ""Quill" writing with ultrashort light pulses in transparent materials," *Applied Physics Letters* **90**, p. 151120, Apr. 2007.

[210] A. Snyder and J. Love, *Optical Waveguide Theory*, Springer, 1-st edition, 734 pages, 1983.

[211] S. M. Eaton, W. Chen, L. Zhang, H. Zhang, R. Iyer, J. S. Aitchison, and P. R. Herman, "Telecom-band directional coupler written with femtosecond fiber laser," *IEEE Photonics Technology Letters* **18**, pp. 2174–2176, Sept. 2006.

[212] J. S. Petrovic, V. Mezentsev, H. Schmitz, and I. Bennion, "Model of the femtosecond laser inscription by a single pulse," *Optical and Quantum Electronics* **39**, pp. 939–946, Aug. 2007.

[213] M. I. Ozhovan, "Topological characteristics of bonds in sio2 and geo2 oxide systems upon a glass-liquid transition," *Journal of Experimental and Theoretical Physics* **103**(5), pp. 819–829, 2006.

[214] A. K. Varshneya, *Fundamentals of Inorganic Glasses*, Society of Glass Technology, 2-nd ed., 570 pages, 2006.

[215] C. W. Carr, H. B. Radousky, A. M. Rubenchik, M. D. Feit, and S. G. Demos, "Localized dynamics during laser-induced damage in optical materials," *Physical Review Letters* **92**(8), p. 087401, 2004.

[216] A. Pasquarello and R. Car, "Identification of raman defect lines as signatures of ring structures in vitreous silica," *Physical Review Letters* **80**(23), pp. 5145–5147, 1998.

[217] C. W. Carr, M. D. Feit, A. M. Rubenchik, P. D. Mange, S. O. Kucheyev, M. D. Shirk, H. B. Radousky, and S. G. Demos, "Radiation produced by femtosecond laser plasma interaction during dielectric breakdown," *Optics Letters* **30**, pp. 661–663, 2005.

[218] L. Glebov, O. Efimov, and G. Prtrovski, "An absence of below threshold ionization and an accumulation effect upon multiple exposure of glasses to the laser-radiation," *Kvantovaja Electronica (in Russian)* **13**(9), pp. 1897–1902, 1986.

REFERENCES

[219] G. M. Petrov and J. Davis, "Interaction of intense ultra-short laser pulses with dielectrics," *Journal of Physics B: Atomic, Molecular and Optical Physics* **41**(2), p. 025601, 2008.

[220] S. Quabis, R. Dorn, M. Eberler, O. Glckl, and G. Leuchs, "Focusing light to a tighter spot," *Optics Communications* **179**(1-6), pp. 1 – 7, 2000.

[221] V. Tikhomirov, D. Furniss, A. Seddon, I. Reaney, M. Beggiora, M. Ferrari, M. Montagna, and R. Rolli, "Fabrication and characterization of nanoscale, er3+-doped, ultra-transparent oxy-fluoride glass ceramics," *Applied Physics Letters* **81**(11), pp. 1937–1939, 2002.

[222] M. Ams, G. D. Marshall, P. Dekker, M. Dubov, V. K. Mezentsev, I. Bennion, and M. J. Withford, "Investigation of ultrafast laser-photonic material interactions: Challenges for directly written glass photonics," *IEEE Journal of Selected Topics in Quantum Electronics* **14**(5), pp. 1370–1381, 2008.

[223] A. Okhrimchuk, M. Dubov, V. Mezentsev, and I. Bennion, "Permanent refractive index change caused by femtosecond laser beam in yag crystals," in *abstracts of the 3rd EPS-QEOD Europhoton Conference (Europhoton-2008)*, (TUp.15), p. TUp.15, EPS, 2008.

[224] A. Othonos and K. Kalli, *Fiber Bragg Gratings*, Artech House, 422 pages, 1999.

[225] R. Kashyap, *Fiber Bragg Gratings (Optics and Photonics Series)*, Academic Press, 2-nd ed., 632 pages, 2009.

[226] K. O. Hill, Y. Fujii, D. C. Johnson, and B. S. Kawasaki, "Photosensitivity in optical fiber waveguides - application to reflection filter fabrication," *Applied Physics Letters* **32**(10), pp. 647–649, 1978.

[227] S. Kanehira, J. H. Si, J. R. Qiu, K. Fujita, and K. Hirao, "Periodic nanovoid structures via femtosecond laser irradiation," *Nano Lett.* **5**(8), pp. 1591–1595, 2005.

[228] S. Kanehira, K. Miura, K. Fujita, and K. Hirao, "Nano-sized modification of transparent materials using femtosecond laser irradiation - art. no. 64130m," *Smart Materials IV* **6413**, pp. M4130–M4130, 2007.

[229] P. G. Kazansky, J. Mills, E. Bricchi, H. Inouye, J. Qiu, and K. Hirao, "Photoinduced anisotropy and related phenomena in glass irradiated with ultrashort pulses," *International Symposium on Photonic Glass (ISPG-2002)* **5061**, pp. 77–83, 2003.

[230] P. G. Kazansky, E. Bricchi, Y. Shimotsuma, and K. Hirao, "Self-assembled nanostructures and two-plasmon decay in femtosecond processing of transparent materials," *2007 Conference on Lasers & Electro-optics/quantum Electronics and Laser Science Conference (CLEO-QELS2007), Vols 1-5* **1-5**, pp. 1169–1170, 2007.

[231] C. Hnatovsky, R. S. Taylor, E. Simova, V. R. Bhardwaj, D. M. Rayner, and P. B. Corkum, "Polarization-selective etching in femtosecond laser-assisted microfluidic channel fabrication in fused silica," *Optics Letters* **30**, pp. 1867–1869, July 2005.

REFERENCES

[232] B. Malo, K. O. Hill, F. Bilodeau, D. C. Johnson, and J. Albert, "Point-by-point fabrication of micro-bragg gratings in photosensitive fiber using single excimer pulse refractive-index modification techniques," *Electronics Letters* **29**(18), pp. 1668–1669, 1993.

[233] E. Wikszak, J. Burghoff, M. Will, S. Nolte, A. Tunnermann, and T. Gabler, "Recording of fiber Bragg gratings with femtosecond pulses using a "point by point" technique," in *Lasers and Electro-Optics, 2004. (CLEO). Conference on*, **2**, pp. 2 pp. vol.2–, 2004.

[234] G. D. Marshall, M. Ams, and M. J. Withford, "Direct laser written waveguide-bragg gratings in bulk fused silica," *Optics Letters* **31**, pp. 2690–2691, Sept. 2006.

[235] N. Jovanovic, A. Fuerbach, G. D. Marshall, M. J. Withford, and S. D. Jackson, "Stable high-power continuous-wave yb3+-doped silica fiber laser utilizing a point-by-point inscribed fiber Bragg grating," *Optics Letters* **32**, pp. 1486–1488, June 2007.

[236] I. Bennion, V. Mezentsev, M. Dubov, D. Nikogosyan, J. Petrovic, Y. Lai, G. Smith, K. Zhou, and K. Sugden, "Device fabrication by femtosecond laser inscription," in *Bragg Gratings, Photosensitivity, and Poling in Glass Waveguides*, p. BWB6, Optical Society of America, 2007.

[237] C. X. Z. K. Z. L. B. I. R. Suo, "800 nm WDM interrogation system for strain, temperature, and refractive index sensing based on tilted fiber bragg grating," *IEEE Sensors Journal* **8**(7), pp. 1273–1279, 2008. cited By (since 1996) 1.

[238] R. Suo, X. Chen, K. Zhou, L. Zhang, and I. Bennion, "In-fibre directional transverse loading sensor based on excessively tilted fibre Bragg gratings," *Measurement Science and Technology* **20**(3), 2009. cited By (since 1996) 2.

[239] D. Nikogosyan, "Multi-photon high-excitation-energy approach to fibre grating inscription," *Measurement Science and Technology* **18**(1), pp. R1–R29, 2007.

[240] C. Smelser, S. Mihailov, and D. Grobnic, "Formation of type I-IR and type II-IR gratings with an ultrafast IR laser and a phase mask," *Optics Express* **13**(14), pp. 5377–5386, 2005.

[241] A. G. Poleshchuk, R. K. Nasyrov, V. V. Cherkashin, M. V. Dubov, V. M. Mezentsev, and I. Bennion, "Diffractive variable attenuator for femtosecond laser radiation control," *Applied Optics* **48**(4), pp. 708–711, 2009.

[242] Y. Shimotsuma, K. Hirao, J. R. Qiu, and K. Miura, "Nanofabrication in transparent materials with a femtosecond pulse laser," *Journal of Non-Crystalline Solids* **352**(6-7), pp. 646–656, 2006.

[243] A. A. Maznev, T. F. Crimmins, and K. A. Nelson, "How to make femtosecond pulses overlap," *Optics Letters* **23**(17), pp. 1378–1380, 1998.

[244] G. N. Smith, K. Kalli, I. Bennion, and K. Sugden, "Demonstration of inscription and ablation of phase masks for the production of 1-st, 2-nd and 3-rd order FBG gratings using a femtosecond laser," *Proceedings of SPIE - The International Society for Optical Engineering* **7205**, p. 720511, 2009.

REFERENCES

[245] A. A. Maznev, K. A. Nelson, and T. A. Rogers, "Optical heterodyne detection of laser-induced gratings," *Optics Letters* **23**(16), pp. 1319–1321, 1998.

[246] H. Knuppertz, J. Jahns, and R. Grunwald, "Temporal impulse response of the Talbot interferometer," *Optics Communications* **277**(1), pp. 67 – 73, 2007.

[247] H. Zhang, S. M. Eaton, J. Li, and P. R. Herman, "Type II femtosecond laser writing of Bragg grating waveguides in bulk glass," *Electronics Letters* **42**, pp. 1223–1224, Oct. 2006.

[248] T. Allsop, M. Dubov, A. Martinez, F. Floreani, I. Khrushchev, D. J. Webb, and I. Bennion, "Directional bend sensor based on an asymmetric modification of the fiber cladding by femtosecond laser," *2005 Conference on Lasers & Electro-Optics (CLEO), vols.* **1-3**, pp. 2179–2181, 2005.

[249] T. Erdogan, "Cladding-mode resonances in short- and long-period fiber grating filters," *Journal of the Optical Society of America A-Optics Image Science and Vision* **14**(8), pp. 1760–1773, 1997.

[250] T. Allsop, T. Earthrowl, H. Dobb, V. Mezentsev, A. Gillooly, D. Webb, and I. Bennion, "The spectral sensitivity of long period gratings fabricated in elliptical core D-shaped optical fibre," in *Fiber Optic Sensor Technology and Applications - III*, M. Marcus, B. Culshaw, and J. Dakin, eds., **5589**, pp. 266–277, 2004.

[251] M. Dubov, T. D. P. Allsop, A. Martinez, V. Mezentsev, and I. Bennion, "Highly birefringent long period gratings fabricated with femtosecond laser," *Optical Fiber Communication Conference/National Fiber Optic Engineers Conference, (OFC-2006), vol.* **1-6**, pp. 663–665, 2006.

[252] T. Hashimoto, S. Juodkazis, and H. Misawa, "Void formation in glasses," *New Journal of Physics* **9**, p. 253, Aug. 2007.

[253] J. Petrovic', *Modelling of Long Period Gratings in PCFs Inscribed by an Electric Arc and Gratings in SMF Inscribed by Femtosecond Laser Pulses*. PhD thesis, School of Engineering and Applied Science, Aston University, 2006.

[254] D. Grobnic, S. Mihailov, C. Smelser, M. Becker, and M. Rothhardt, "Femtosecond laser fabrication of Bragg gratings in borosilicate ion-exchange waveguides," *IEEE Photonics Technology Letters* **18**(13), pp. 1403–1405, 2006.

[255] J. Salgueiro, J. Roman, and V. Moreno, "System for laser writing to lithograph masks for integrated optics," *Optical Engineering* **37**, pp. 1115–1123, Apr. 1998.

[256] J. Koch, E. Fadeeva, M. Engelbrecht, C. Ruffert, H. H. Gatzen, A. Ostendorf, and B. N. Chichkov, "Maskless nonlinear lithography with femtosecond laser pulses," *Applied Physics A - Materials Science & Processing* **82**(1), pp. 23–26, 2006.

[257] A. Y. Vorobyev and C. L. Guo, "Shot-to-shot correlation of residual energy and optical absorptance in femtosecond laser ablation," *Applied Physics A - Materials Science & Processing* **86**(2), pp. 235–241, 2007.

REFERENCES

[258] B. N. Chichkov, E. Fadeeva, J. Koch, A. Ostendorf, A. Ovslanikov, S. Passinger, and C. Reinhardt, "Femtosecond laser lithography and applications - art. no. 610612," *Photon Processing in Microelectronic and Photonics V* **6106**, pp. 10612–10612, 2006.

[259] T. Kondo, S. Matsuo, S. Juodkazis, and H. Misawa, "Femtosecond laser interference technique with diffractive beam splitter for fabrication of three-dimensional photonic crystals," *Applied Physics Letters* **79**(6), pp. 725–727, 2001.

[260] D. Grobnic, S. Mihailov, C. Smelser, F. Genereux, G. Baldenberger, and R. Vallee, "Bragg gratings made in reverse proton exchange lithium niobate waveguides with a femtosecond ir laser and a phase mask," *IEEE Photonics Technology Letters* **17**(7), pp. 1453–1455, 2005.